Lawrence Berkeley National Laboratory

Recent Work

Title

Properties and applications of doped Ge thermistors

Permalink

https://escholarship.org/uc/item/9qz9t9ts

Author

Grannan, Sabrina Marie

Publication Date

1996-12-01

eScholarship.org Powered by the California Digital Library
University of California

LBNL-39874
UC-406

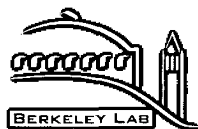

ERNEST ORLANDO LAWRENCE BERKELEY NATIONAL LABORATORY

Properties and Applications of Doped Ge Thermistors

Sabrina M. Grannan

Materials Sciences Division

December 1996
Ph.D. Thesis

REFERENCE COPY
Does Not
Circulate
Bldg. 50 Library - Ref.
Lawrence Berkeley National Laboratory
Copy 1
LBNL-39874

DISCLAIMER

This document was prepared as an account of work sponsored by the United States Government. While this document is believed to contain correct information, neither the United States Government nor any agency thereof, nor the Regents of the University of California, nor any of their employees, makes any warranty, express or implied, or assumes any legal responsibility for the accuracy, completeness, or usefulness of any information, apparatus, product, or process disclosed, or represents that its use would not infringe privately owned rights. Reference herein to any specific commercial product, process, or service by its trade name, trademark, manufacturer, or otherwise, does not necessarily constitute or imply its endorsement, recommendation, or favoring by the United States Government or any agency thereof, or the Regents of the University of California. The views and opinions of authors expressed herein do not necessarily state or reflect those of the United States Government or any agency thereof or the Regents of the University of California.

LBNL-39874
UC-406

Properties and Applications of Doped Ge Thermistors

Sabrina Marie Grannan
Ph.D. Thesis

Department of Physics
University of California, Berkeley

and

Materials Sciences Division
Ernest Orlando Lawrence Berkeley National Laboratory
University of California
Berkeley, CA 94720

December 1996

This work was supported in part by the Director, Office of Energy Research, Office of Basic Energy Sciences, Materials Sciences Division, of the U.S. Department of Energy under Contract No. DE-AC03-76SF00098. S.G. was supported by fellowships from the National Science Foundation and the Department of Education.

Properties and Applications of Doped Ge Thermistors

by

Sabrina Marie Grannan

B. A. (University of California at Berkeley) 1989
M. A. (University of California at Berkeley) 1994

A dissertation submitted in partial satisfaction of the

requirements for the degree of

Doctor of Philosophy

in

Physics

in the

GRADUATE DIVISION

of the

UNIVERSITY of CALIFORNIA at BERKELEY

Committee in charge:

Professor P. L. Richards, Chair
Professor E. E. Haller
Professor A. Zettl

1996

Properties and Applications of Doped Ge Thermistors

Copyright © 1996

by

Sabrina Marie Grannan

The U.S. Department of Energy has the right to use this document
for any purpose whatsoever including the right to reproduce
all or any part thereof

Abstract

Properties and Applications of Doped Ge Thermistors

by

Sabrina Marie Grannan

Doctor of Philosophy in Physics

University of California at Berkeley

Professor Paul L. Richards, Chair

In the first half of this thesis, we discuss the importance of doped semiconductors for studies of disordered systems and review impurity conduction in the Ohmic limit. We then review the previous theoretical and experimental studies of non-Ohmic impurity conduction and discuss many contradictions between the existing studies. In particular, the dependence of the non-Ohmic conductivity on impurity concentration and temperature has not been established.

We describe three experimental studies of non-Ohmic impurity conduction in neutron transmutation doped germanium samples which have an extremely homogeneous, random impurity distribution. We find several new phenomena including a universal curve which describes the non-Ohmic behavior of lightly doped Ge:Ga samples, and a dramatic change in the non-Ohmic conductivity as the impurity concentration nears the critical concentration for a metal-insulator transition. We include a qualitative discussion of the effects of stress.

The second half of this thesis is concerned with various applications of doped Ge semiconductors. We present numerical methods for the global optimization of bolometric infrared detectors which use current-biased semiconducting thermistors. We explicitly include both the electric field dependence of the thermistor resistance and amplifier noise.

We present data from a novel low temperature particle detector which uses doped Ge thermistors as calorimeters. This detector uses a quasiparticle trapping mechanism to

funnel athermal phonon energy from a large Ge absorber into a small doped Ge thermistor via a superconducting Al film.

We conclude with a description of an experiment which uses a doped Ge thermistor as part of a conventional low temperature bolometer for far infrared studies of the novel materials $Sc_2@C_{84}$ and $Er_2@C_{82}$. This is the first study of the far infrared properties of metallofullerenes and may help in the determination of their structural and electronic properties.

In the appendix we present measurements of the NJ132L JFET voltage noise as a function of temperature, drain voltage, and current. We discuss the fabrication of small, cooled JFET packages which can bolt to a helium cold plate and self-heat to a selected operating temperature, and we present an ultra-low noise voltage preamplifier design for room temperature operation.

For my parents. Ralph and Patricia

Table of Contents

Chapter 1 Introduction

1.1 Motivation for studying non-Ohmic impurity conduction in doped semiconductors 1
1.2 Outline of thesis 3
1.3 Impurities in semiconductors 6
1.3.1 Compensation 10
1.4 Structure of the impurity band 10
1.4.1 The Fermi energy 11
1.4.2 Fermi level in the limit of weak compensation 12
1.4.3 Position of the Fermi level for intermediate and strong compensation 13
1.4.4 Density of states in the impurity band 14
1.4.5 The upper Hubbard band and the D- state 15
1.5 Impurity conduction in doped semiconductors 15
1.5.1 Transitions between localized states in an aperiodic solid 15
1.5.2 Temperature dependence of the impurity conductivity 17
1.5.2.1 Variable range hopping conduction 19
1.6 Anderson localization 21

Chapter 2 Theory of non-Ohmic impurity conduction in doped semiconductors

2.1 Bulk non-Ohmic impurity conduction 26
2.1.1 Poole-Frenkel Effect 27
2.1.2 Impact ionization breakdown 28
2.1.3 Non-Ohmic conduction in the impurity band 30
2.1.3.1 Impurity conduction in weak electric fields 31
2.1.3.2 Negative differential conductance 36
2.1.3.3 Impurity conduction in moderate electric fields 38
2.1.3.4 Impurity conduction in strong electric fields 41
2.1.3.5 Non-Ohmic impurity conduction in moderately and heavily doped semiconductors 43
2.1.3.6 Summary of non-Ohmic impurity conduction in doped semiconductors 44

2.2 Contact effects 46
2.2.1 The Schottky barrier 46
2.2.2 Ohmic contacts 50
2.2.3 Contact resistance for the samples studied in this work 51
2.3 Hot electron effects 55
2.3.1 Definition of the hot electron regime 55
2.3.2 Hot electron effects in metals 57
2.3.2 Hot electron effects in semiconductors 59
2.3.2.1 Hot electron effects and ε_1 impurity conduction 59
2.3.2.2 Hot electron effects and hopping conduction 60
2.3.2.3 Discrepancies in the existing hopping conduction data which are analyzed using a hot electron model 65

Chapter 3 Experimental studies of non-Ohmic impurity conduction in neutron transmutation doped Germanium
3.1 Overview 68
3.2 Experimental procedure 69
3.2.1 Semiconductor doping 70
3.2.2 Neutron transmutation doping 71
3.2.3 Sample preparation 73
3.2.4 Measurement technique 75
3.3 Experimental results 77
3.3.1 Experiment 1 77
3.3.1.1 Motivation for a new method of analyzing the non-Ohmic impurity conductivity 81
3.3.1.2 Universal curve describing the field dependence of the conductivity in lightly doped ^{nat}Ge:Ga 84
3.3.2 Experiment 2 88
3.3.3 Effect on an electric field on the impurity wavefunctions 92
3.3.3.1 Wannier-Stark localization in a regular crystal lattice 92
3.3.3.2 Disordered systems 93
3.3.3.3 Proposed model of Anderson localization in an electric field 94
3.3.4 Experiment 3 95
3.3.4.1 ^{74}Ge:As, Sample 1: N = 0.17 Nc 99
3.3.4.2 ^{74}Ge:As, Sample 2: N = 0.51 Nc 102

Chapter 4 Effect of stress on non-Ohmic impurity conduction

4.1 Effect of stress on impurity states 108

4.1.1 Effect of uniaxial stress on acceptor ground state in p-type germanium 109

4.1.2 Effect of uniaxial stress on donor ground state in n-type germanium 110

4.2 Effect of stress on non-Ohmic hopping conduction 111

Chapter 5 Numerical optimization of bolometric infrared detectors including optical loading, amplifier noise, and electrical nonlinearities

5.1 Introduction 114

5.2 Bolometer model 116

5.3 Bolometer responsivity and NEP 119

5.4 Numerical optimization program 121

5.5 Implications for bolometer design 123

5.6 Conclusion 133

Chapter 6 Collection of athermal phonons into doped Ge thermistors using quasiparticle trapping

6.1 Introduction 135

6.2 Principles of operation 137

6.3 NTD Ge thermistors 138

6.4 Aluminum film properties 140

6.5 Experimental procedure 142

6.6 System time constants 145

6.7 Pulse height spectra 147

6.8 Conclusion 151

Chapter 7 Far infrared transmittance of $Sc_2@C_{84}$ and $Er_2@C_{82}$

7.1 Introduction 153

7.2 Sample preparation 155

7.3 Experimental technique 156

7.4 Experimental results 159

7.5 Discussion and conclusion 164

Appendix A JFET noise

A.1 JFET noise minimization: NJ132L JFET 167
A.1.1 Voltage noise 167
A.1.2 Current noise 172
A.2 Construction of cooled JFET packages 174
A.3 Low noise preamplifier circuit 177
A.4 Calibration of a diode thermometer 181

Appendix B Details of numerical optimization program

B.1 Instructions for using the numerical optimization program 183
B.2 Constants and partial derivatives used in the Davidon-Fletcher-Powell algorithm 185
B.2.1 Constants 185
B.2.2 Partial derivatives 186

References 189

List of Tables

Table 2.1 Theoretical predictions for the electric field dependence of the conductivity at various electric field strengths 45

Table 3.1 Neutron capture reactions which take place in natural germanium to produce dopant isotopes 71

Table 3.2 Parameters describing the NTD ^{nat}Ge:Ga samples studied in Experiment 1 78

Table 3.3 Parameters describing the NTD ^{70}Ge:Ga samples studied in Experiment 2 88

Table 3.4 Measured conductivity parameters of the two ^{74}Ge:As samples studied in Experiment 3 97

Table 5.1 Neutron transmutation doped Ge thermistor parameters 125

Table 5.2 Results of numerical optimization program 128

Table 6.1 Low temperature mean free path of a number of Al films with different deposition conditions 141

Table 7.1 Absorption features in $Sc_2@C_{84}$ 163

Table 7.2 Absorption features in $Er_2@C_{82}$ 163

List of Figures

Fig. 1.1 Donor and acceptor states in Group IV semiconductors 7
Fig. 1.2 One-dimensional band diagram of a Ge semiconductor doped with As and Ga 8
Fig. 1.3 Effect of increasing impurity concentration on the density of states in the impurity band and on impurity wavefunctions 9
Fig. 1.4 Compensation in a doped semiconductor 10
Fig. 1.5 Donor electrons can be excited into the conduction band, the upper Hubbard band, or into an empty donor state 18
Fig. 1.6 Structure of the impurity band of an n-type semiconductor with a small number of compensating acceptors 18
Fig. 1.7 Illustration of two impurity sites separated in distance and energy 19
Fig. 1.8 Electrons hop between localized states by the variable range hopping mechanism at low temperatures 20
Fig. 1.9 Localization in a random potential V(x) 22
Fig. 1.10 Potential wells in the Anderson model, adapted from Shklovskii and Efros [1984] 24
Fig. 1.11 Density of states in the impurity band in the Anderson model 24
Fig. 2.1 The Poole-Frenkel effect 28
Fig. 2.2 Weak, moderate, and strong field regimes for hopping conduction in an applied electric field F 30
Fig. 2.3 Electric field dependence of the conductivity of neutron transmutation doped Ge:Ga 33
Fig. 2.4 Electric field dependence of the conductivity of a Ge bicrystal, adapted from Zavaritskaya *et al.* [1985] 34
Fig. 2.5 Electric field dependence of the conductivity of ion-implanted Si:As, adapted from Gang *et al.* [1989] 35
Fig. 2.6 Illustration of the transition from isotropic to directed hopping conduction under an applied electric field, using the model of a random resistor network between impurity sites 37
Fig. 2.7 "Dead ends" in the random resistor network 37
Fig. 2.8 As the impurity concentration increases, the doped semiconductor is modelled by a network of nonlinear triodes rather than by a network of nonlinear resistors 43
Fig. 2.9 Formation of a Schottky barrier between a metal and a semiconductor 47

Fig. 2.10 Contact resistances to a bulk semiconductor 50
Fig. 2.11 Formation of a low resistance contact by additional doping 52
Fig. 2.12 Measured temperature dependence of the resistance of two ^{74}Ge:As samples used to place an upper limit on the contact resistance 53
Fig. 2.13 Sample geometry used for four-probe and two-probe measurements of the sample resistance 55
Fig. 2.14 Thermal model for the theory of hot electron behavior 56
Fig. 2.15 Hopping in the band tail of an amorphous semiconductor under an applied electric field, adapted from Marianer and Shklovskii [1992] 62
Fig. 2.16 Two fitting functions for the temperature dependence of the resistance of ^{70}Ge:Ga-1.65 64
Fig. 3.1 Phase space diagram of the electric field dependence of the conductivity for various impurity concentrations and electric field strengths 69
Fig. 3.2 Doped semiconductor produced by the melt doping process 70
Fig. 3.3 Illustration of the neutron transmutation doping process for the germanium isotope ^{74}Ge 72
Fig. 3.4 Schematic diagram of the measurement circuit used to measure the electric field dependence of the resistance 75
Fig. 3.5 Measured low field resistance at 1.2 K of a ^{70}Ge:Ga sample, showing that the relative error in the resistance measurement is a part in 10^4 76
Fig. 3.6 Phase space diagram showing the impurity concentrations and compensations of the samples studied in this work 76
Fig. 3.7 Measured temperature dependence of the conductivity of the NTD ^{nat}Ge:Ga samples studied in Experiment I 79
Fig. 3.8 Measured dependence of the variable range hopping parameter T_0 on impurity concentration for the samples in Experiment I 80
Fig. 3.9 Electric field dependence of the resistance of a lightly doped ^{nat}Ge:Ga sample with an impurity concentration $N \approx 0.046\ N_c$ 80
Fig. 3.10 Data from Fig. 3.9 replotted using several fitting functions 82
Fig. 3.11 Dependence of the hop length parameter L on temperature measured for $F < 10$ V/cm and $F > 10$ V/cm 82
Fig. 3.12 Measured temperature dependence of L for three lightly doped ^{nat}Ge:Ga samples 84
Fig. 3.13 Electric field dependence of the conductivity of six ^{nat}Ge:Ga samples, plotted using a new method 85
Fig. 3.14 Measured dependence of the parameter L_0 on $FT^{-1.5}$ in ^{nat}Ge:Ga

with an impurity concentration $N = 0.34\ N_c$ 87

Fig. 3.15 Measured dependence of the parameter L_0 on $FT^{-1.5}$ in ^{nat}Ge:Ga with an impurity concentration $N = 0.50\ N_c$ 87

Fig. 3.16 Temperature dependence of the resistance of a ^{70}Ge:Ga sample 89

Fig. 3.17 Electric field dependence of the conductivity of a ^{70}Ge:Ga sample with an impurity concentration $N = 0.16\ N_c$ 90

Fig. 3.18 Electric field dependence of the conductivity of a ^{70}Ge:Ga sample with an impurity concentration $N = 0.42\ N_c$ 90

Fig. 3.19 Electric field dependence of the conductivity of a ^{70}Ge:Ga sample with an impurity concentration $N = 0.50\ N_c$ 91

Fig. 3.20 Electric field dependence of the conductivity of a ^{70}Ge:Ga sample with an impurity concentration $N = 0.77\ N_c$ 91

Fig. 3.21 Anderson localization in an applied electric field 94

Fig. 3.22 Proposed model for the effect of an electric field on the impurity wavefunctions 94

Fig. 3.23 Measured temperature dependence of the conductivity as a function of temperature of two ^{74}Ge:As samples 96

Fig. 3.24 Measured electric field dependence of the resistance of ^{74}GeAs Sample 2 97

Fig. 3.25 Data from Fig. 3.24 replotted in a different form 98

Fig. 3.26 Measured electric field dependence of the conductivity for ^{74}GeAs Sample 1 at various temperatures 99

Fig. 3.27 Temperature dependence of the parameter x from Equation 3.12 100

Fig. 3.28 Measured dependence of $\ln \sigma$ on $F^{1.5}$ 101

Fig. 3.29 Exponent x from Equation 3.12 as a function of electric field 101

Fig. 3.30 Temperature dependence of the parameter A from Equation 3.12 102

Fig. 3.31 Field dependence of the conductivity of Ge:Sb with an impurity concentration $N \approx 0.67\ N_c$, adapted from Matveev *et al.* [1993] 104

Fig. 3.32 Dependence of the length parameter L on electric field when the conduction is described by $\sigma(F,T) \propto \exp(AF^{3/2})$, calculated using Equation 3.13 106

Fig. 3.33 Proposed model for the effect of an electric field on non-Ohmic impurity conduction into extended states in the impurity band 106

Fig. 4.1 Effect of stress on the impurity wavefunctions 109

Fig. 4.2 Effect of stress on non-Ohmic impurity conduction when the applied stress is parallel to the electric field 112

Fig. 4.3	Effect of stress on non-Ohmic impurity conduction when the applied stress is perpendicular to the electric field	112
Fig. 4.4	Measured effect of stress on the non-Ohmic impurity conduction	113
Fig. 5.1	Schematic illustration of bolometer operation	116
Fig. 5.2	Measurements of the electrical nonlinearities in neutron transmutation doped Ge	125
Fig. 5.3	Optimized NEP as a function of heat sink temperature for several NTD Ge thermistor materials	127
Fig. 5.4	Variation of the NEP with ϕ as a function of β	129
Fig. 5.5	Variation of the bolometer NEP with background optical power Q	130
Fig. 5.6	Variation of responsivity with the bias parameter ϕ	131
Fig. 5.7	Variation of the NEP with thermal conductance parameter G_0	132
Fig. 6.1	Schematic diagram of the SLAPS device	136
Fig. 6.2	Principles of operation of the SLAPS device	138
Fig. 6.3	Temperature dependence of the resistance of the thermistors used in the SLAPS device	139
Fig. 6.4	Temperature dependence of the thermal conductivity of the epoxy bonds used in the SLAPS device	143
Fig. 6.5	Pulse height spectrum of γ-rays produced by a ^{241}Am source	144
Fig. 6.6	Linearity of the thermistor response	144
Fig. 6.7	Superimposed pulse height spectra obtained with quasiparticle trapping thermistor	148
Fig. 6.8	Ratio of athermal phonon to thermal phonon energy collected in the SLAPS thermistors	149
Fig. 6.9	Position dependence of the signal rise times observed in the thermistor with a quasiparticle trapping mechanism	151
Fig. 7.1	Schematic of the far infrared spectrometer	157
Fig. 7.2	Transmittance at 1.5 K of parafilm and crystal quartz	159
Fig. 7.3	Transmittance of $Sc_2@C_{84}$	160
Fig. 7.4	Frequency dependence of the absorption coefficient of $Sc_2@C_{84}$, $Er_2@C_{82}$, and C_{60}	162
Fig. A.1	Voltage noise measurement circuit	169
Fig. A.2	Voltage noise of the NJ132L JFET as a function of drain voltage	171
Fig. A.3	Voltage noise of the NJ132L JFET as a function of current	171
Fig. A.4	Voltage noise of the NJ132L JFET as a function of temperature	172
Fig. A.5	Measurement circuit used to measure JFET leakage current	173

Fig. A.6 Room temperature current noise of the NJ132L JFET as a function of drain-gate voltage 173
Fig. A.7 Schematic diagram of a small cooled JFET package 176
Fig. A.8 Low noise voltage preamplifier circuit diagram 178
Fig. A.9 Measured voltage noise of the circuit in Fig. A.8 180
Fig. A.10 Temperature dependence of the 1N4448 diode drop 182

Acknowledgements

I first wish to thank my parents, who have given me the strongest possible foundations upon which to build my life. I cannot thank them enough for their love and encouragement. They are my role models, as well as friends with whom I have spoken almost daily.

Under the guidance of my advisor, Paul Richards, I have learned how to conduct an experiment, how to collaborate with other scientists, how to present data clearly, and many other things which have transformed me from a student into a scientist. His personal integrity, his sincere regard for his students, and his continuing enthusiasm for experimental physics have been an inspiration to me. I am especially grateful to Professor Richards for allowing me the freedom and independence to pursue my own research ideas, and for his honesty which can be painful at times but is always helpful.

I have been extremely fortunate to have had the opportunity to collaborate with Eugene Haller, Kohei Itoh, Jeff Beeman, and John Emes. Professor Haller and his group have produced extremely high purity, well-characterized thermistor materials which they have generously shared with me, as well as sharing many useful ideas about the physics of these materials. I sincerely thank them for helping me to perform a comprehensive study of electric field effects in doped semiconductors; this work would not have been possible without them.

I owe many thanks to Andrew Lange who gave me such a positive introduction to laboratory research while still a Berkeley undergraduate. I am also grateful for having had the opportunity to collaborate with Don Bethune, Jens Kircher, Alex Zettl, and Jim Hone on various far infrared spectroscopy experiments, one of which is described in Chapter 7 of this thesis. Bernard Sadoulet and Simon Labov gave me sound advice and many useful physical insights during our collaboration on the quasiparticle trapping experiment described in Chapter 6. I especially want to thank Bertha Zambrano for her administrative assistance, without which research in the Richards group would not be possible.

I have enjoyed working with and learning from my labmates and classmates, many of whom have become good friends outside the lab, including Anita Barnes, Ted Bunn, Matt Craig, Warren Holmes, Bill Holzapfel, Keith Schwab, Tom Shutt, Stacy Tanaka, Thor Wilbanks, and Betty Young.

I particularly wish to thank the following people who have most influenced me and given me encouragement throughout graduate school. Nasreen Chopra is always a delight to be around, and is more gifted than anyone I know at enjoying the best aspects of life and seeing the best qualities in other people.

Thanks to my lab partner John Birmingham, I have spent many days in the spectrometer room laughing from morning until night, albeit usually at my own expense. I have wonderful memories of walking with John on the Strawberry Canyon fire trail, discussing the advantages of living in the Victorian age and the wisdom of Miss Manners. I will miss exploring these topics with him more than I can say.

My closest friend throughout graduate school has been Michael Hase, who has unfailingly supported and helped me in countless tangible and intangible ways. Knowing Mike is reason enough to have come to Berkeley. Without his computer expertise, Chapter 5 of this thesis would not have been possible.

Most of all I wish to thank my husband, Jason Feldman, who is not only the most accomplished person I have ever known but also the kindest. His thoughtfulness and generosity have meant the world to me as I have brought this project to a close.

Chapter 1
Introduction

1.1 Motivation for studying non-Ohmic impurity conduction in doped semiconductors

Traditional solid state physics is concerned with the properties of perfect crystalline solids. However, much recent research has focused on the properties of disordered systems which lack translational symmetry and exhibit many new properties. One of the central issues in solid state physics has been the metal-insulator transition (MIT) in disordered systems which corresponds to the transition from extended to localized states at the Fermi level. The theoretical importance of doped semiconductors arises from the fact that they provide the simplest and best-defined system for studying conduction processes between localized states and for exploring the properties of disordered systems and the MIT. Doped semiconductors offer numerous opportunities of tuning through the MIT by (1) variation of the overlap between impurity wavefunctions through changing the impurity concentration, by applying stress, or by applying a magnetic field, or by (2) varying the random impurity potential through changing the compensation [Chroboczek, 1987].

Despite numerous theoretical and experimental studies of doped semiconductors over the last few decades, many fundamental questions remain concerning the role of electron-electron interactions, the nature of the metal-insulator transition, the variation of impurity localization within the impurity band, and the structure of the impurity band. Many techniques have been used to study the properties of doped semiconductors including Knight shift, Raman, far-infrared reflectance, Hall effect, and transport at various pressures, magnetic fields, temperatures, impurity concentrations, and compensations [Kamimura and Aoki, 1989; Mott, 1993]. However, although studies of non-Ohmic effects in doped semiconductors are known to provide a probe of impurity localization and

mobility, both experimental and theoretical investigations of non-Ohmic behavior have been small in number.

Those few investigations which have been performed on the dependence of the impurity conductivity on an applied electric field have provided surprising and conflicting results on the effects of varying the electric field, the temperature, and the impurity concentration. For example, in low electric fields the theoretically predicted "Ohmic regime" is frequently not observed, or is observed at fields several orders of magnitude lower than predicted. Some authors have found that the non-Ohmic behavior becomes stronger with increasing impurity concentration, while others have found the opposite tendency. The dependence of the non-Ohmic conductivity on temperature has not yet been established.

The existing theories of non-Ohmic behavior in moderate electric fields have been developed assuming a lightly doped semiconductor. They predict a phonon-assisted non-Ohmic impurity conductivity of the form $\sigma(F,T) = \sigma(0,T) \times \exp(eFL/kT)$ where F is the applied electric field and L is a length factor related to the hop length R. As yet no theory has been developed which includes the effects of electron-electron interactions between impurities, the variation of localization throughout the impurity band, and the influence of the applied electric field on the impurity wavefunctions. All of these effects may become important as the impurity concentration increases and nears the critical concentration for a metal-insulator transition. The few experimental studies of non-Ohmic behavior in moderately and heavily doped semiconductors [Gang *et al.*, 1989; Matveev and Lonchakov, 1993; Rosenbaum *et al.*, 1980] have typically analyzed the moderate field data according to the expression developed for a lightly doped semiconductor, rather than used the data to test whether this expression remains valid.

It is plausible that at higher impurity concentrations for which carriers are no longer localized at individual impurities, a different electric field dependence should apply because Anderson localization cannot be assumed throughout the impurity band and L can no longer

be uniquely defined. The electric field may influence the impurity wavefunctions. leading to new behaviors. Non-Ohmic conductivity studies at higher impurity concentrations can conceivably provide an exciting probe of impurity localization. the position of the mobility edge in the impurity band. and the metal-insulator transition.

1.2 Outline of thesis

The outline for the rest of this thesis is as follows.

The remainder of Chapter 1 contains a brief outline of the general theory of impurity states in doped semiconductors, the structure of the impurity band. and impurity conduction in the Ohmic limit of small applied electric fields. We discuss the Mott-Hubbard model of localization of impurity states through electron-electron interactions. as well as the Anderson model of disorder-driven localization.

Chapter 2 contains a review of the previous experimental and theoretical work on non-Ohmic impurity conduction in doped semiconductors. We distinguish between (1) non-Ohmic conduction by impurities excited into the conduction band. which is well described by the Poole-Frenkel effect and impact ionization breakdown; and (2) non-Ohmic conduction in the impurity band. which remains poorly understood. We include a discussion of contact effects and hot electron effects which can also lead to significant non-Ohmic behavior.

In Chapter 3. we describe three experiments on non-Ohmic impurity conduction in both p-type and n-type Ge samples. The samples are extremely uniformly and randomly doped by the neutron transmutation doping process. in which ultra-pure germanium crystals are exposed to a thermal neutron source and impurities are created through the decay of germanium isotopes. In Experiment 1. we study the non-Ohmic conductivity of lightly and moderately doped Ge:Ga with a compensation K = 0.32. In Experiment 2. we study the non-Ohmic conductivity of moderately and heavily doped

$^{70}Ge:Ga$ with a compensation $K < 0.01$. In Experiment 3, we study the non-Ohmic conductivity of moderately doped $^{74}Ge:As$ with a compensation $K < 0.01$.

We show that the non-Ohmic hopping conductivity data for the lightly doped Ge:Ga samples in Experiment 1 can be collapsed onto a single universal curve. The length parameter L deduced from the universal curve does not depend on the impurity concentration N. As the impurity concentration nears the critical concentration N_c for a metal-insulator transition, we show that the non-Ohmic hopping conductivity of the samples in both Experiment 1 and Experiment 2 changes dramatically. We find the counter-intuitive result that the conductivity begins to depend more strongly on applied electric field in the weak field regime than in the moderate field regime as the impurity concentration increases. In Experiment 3, we perform the first study of the non-Ohmic behavior in the conduction regime intermediate between ε_2 conduction and hopping conduction. We find the unexpected result that the dependence of the conductivity σ on applied electric field F is $ln\,[\sigma(F,T)/\sigma(0,T)] \propto F^{1.5}$. This dependence has not been previously reported or predicted. The field dependence exponent 1.5 has been determined with a probable error of 2%, and the temperature dependence of the non-Ohmic conductivity is much stronger than seen in any other material to date. These results, though surprising, do not conflict with available theories which assume hopping conduction in a lightly doped semiconductor.

The qualitative effects of stress on the non-Ohmic hopping conductivity are discussed in Chapter 4. We present data showing that stress can either enhance or suppress the magnitude and temperature dependence of the hopping length parameter L, depending on the orientation of the applied stress relative to the measurement axis. The effects of stress have typically been ignored in the published literature. Our new result explains some of the contradictory experiments in the literature on the dependence of the non-Ohmic hopping conduction on impurity concentration and temperature.

We turn our attention from the non-Ohmic properties of doped semiconductors to their practical applications in Chapter 5. One important application of doped semiconductors at low temperatures is their use as very sensitive resistance thermometers, or thermistors. Doped semiconductor thermistors are widely used in the development of bolometers and heterodyne mixers for far infrared spectroscopy and astronomy, the development of dark matter detectors, and as all-purpose thermometers at temperatures below 4 K. In this chapter we present numerical methods for the global optimization of bolometric infrared detectors which use current-biased semiconducting thermistors. We extend the analysis of Griffin and Holland [1989] to explicitly include both the electric field dependence of the thermistor resistance and amplifier noise. We include a number of examples illustrating the uses of this program.

In Chapter 6, we describe the use of doped Ge thermistors as calorimeters in a novel low temperature particle detector, the Superconducting Large Area Phonon Sensor (SLAPS). This device uses a quasiparticle trapping mechanism to funnel athermal phonon energy from an large Ge absorber into a small doped Ge thermistor via a superconducting Al film. We show that by using a quasiparticle trapping mechanism, we can dramatically increase the sensitivity of a calorimetric detector to athermal phonons. The observed pulse shapes contain information on the position of a particle interaction in the large absorber for unprecedented interaction distances of up to 0.6 cm from the thermistor.

Chapter 7 contains a description of an experiment which uses a doped Ge thermistor as part of a conventional low temperature bolometer for far infrared studies of novel materials. We present measurements of the far infrared transmittance of $Sc_2@C_{84}$ and $Er_2@C_{82}$ at 1.5 K between 30 cm^{-1} and 200 cm^{-1}. This is the first study of the far infrared properties of metallofullerenes and may help in the determination of their structural and electronic properties.

Many applications of doped Ge thermistors require an extremely low noise in the readout electronics. We discuss the minimization of JFET noise in Appendix A. In

Section A.1 we describe voltage noise measurements and noise minimization of the NJ132L JFET at low frequencies (50 - 400 Hz) as a function of JFET temperature, drain voltage, and current. In Section A.2, we describe the fabrication of small, cooled JFET packages which can bolt to a helium cold plate and self-heat to a selected operating temperature. In Section A.3, we present an ultra-low noise voltage preamplifier design for room temperature operation which uses the NJ903L JFET. In addition, we describe how to convert a commercial diode into a calibrated thermometer for use between 77 K and 300 K in Section A.4.

Instructions for using the numerical optimization program described in Chapter 5 are presented in Appendix B, along with the constants and partial derivatives used in one of the minimization routines.

1.3 Impurities in semiconductors

In studying doped semiconductors, we begin with a description of the shallow impurity states of an isolated donor in silicon and germanium. Both of these Group IV elements have a diamond crystal structure, in which $(ns)^2(np)^2$ valence electrons form covalent bonds between sp^3 hybridized orbitals [Kamimura and Aoki, 1989]. When an atom from a Group V element such as As is doped into a Group IV crystal such as Ge as shown in Figure 1.1, four of the As valence electrons will form sp^3 bonds with the Ge atoms in the crystal. The fifth extra electron is weakly bound to the As nucleus by an attractive Coulomb potential. As a result, a hydrogen-like shallow impurity state with quantum number 1s is formed. The energy of the donor electron lies just below the conduction band edge as shown in Figure 1.2. At finite temperatures the 1s electron in the impurity state can be thermally excited into the conduction band with an energy ε_1. These impurities are called "donors" because they donate an electron to the conduction band. Similarly, atoms from a Group III element doped into a Group IV crystal will accept a

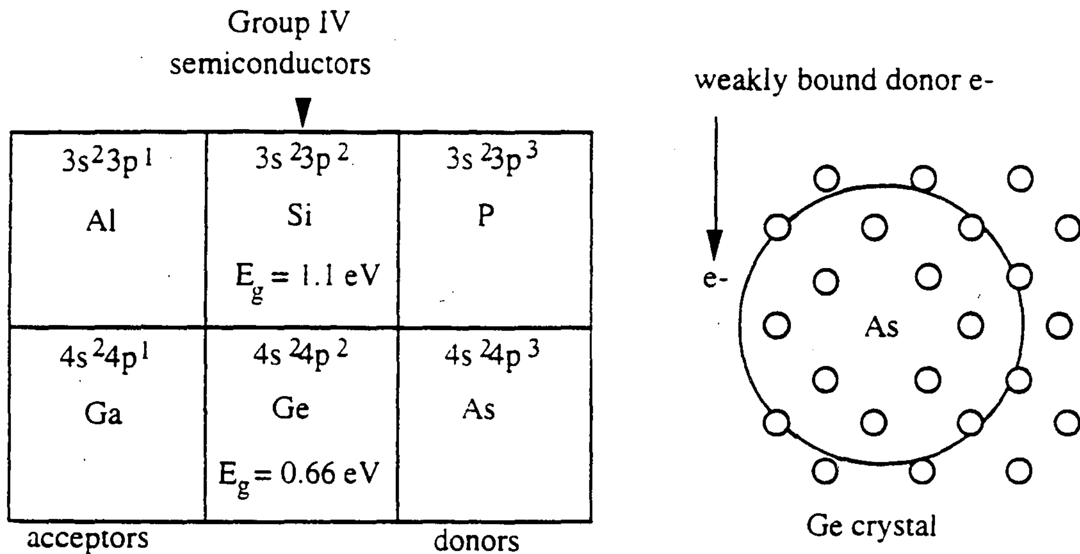

Fig. 1.1 Atoms from Group V elements such as As doped into a Group IV semiconductor crystal such as Ge will form a hydrogen-like impurity state with a weakly bound electron.

weakly bound extra electron from the crystal, creating a "hole" in the valence band. Group III impurities imbedded in Group IV crystals are therefore known as "acceptors". In the discussion that follows we consider the specific case of a donor impurity state; however the conclusions are equally applicable to acceptor states.

The binding energy of a donor impurity state can be approximated by the binding energy for a hydrogen atom imbedded in a homogeneous medium,

$$E_b = 13.6\ \text{eV}\left[\frac{m^*}{m_e}\frac{1}{\kappa^2}\right], \tag{1.1}$$

where κ is the dielectric constant κ and m^* is the electron mass corresponding to the effective mass of the conduction band minimum. The effective Bohr radius of the impurity state is

$$a = 0.5\ \text{Å}\left[\frac{\kappa m_e}{m^*}\right]. \tag{1.2}$$

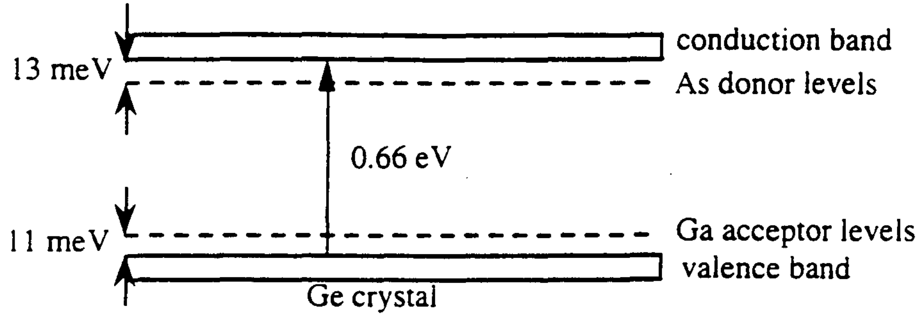

Fig. 1.2 One dimensional band diagram of a Ge semiconductor doped with As and Ga.

Since Ge and Si have anisotropic conduction band minima, m* is not uniquely defined. The dispersion relation around the conduction band minimum is described by an elliptic relation

$$E(\mathbf{k}) = E_o + \frac{h^2}{8\pi^2 m_t}(k_x^2 + k_y^2) + \frac{h^2}{8\pi^2 m_l} k_z^2 , \tag{1.3}$$

where m_t is the effective mass in the transverse direction and m_l is the effective mass in the longitudinal direction. The effective mass m* of the conduction band extremum is approximated by

$$m^* = (m_l\, m_t^2)^{1/3}. \tag{1.4}$$

For Ge, $\kappa \approx 16$ and $m^* \approx 0.2 m_e$. Figure 1.2 shows the shallow energy levels of As donor atoms and Ga donor atoms in Ge, estimated using Equation 1.1. The Bohr radius a of the impurity states is ≈ 40 Å.

As the impurity concentration N increases, the energy levels of the randomly located impurity sites form an impurity band as shown in Figure 1.3. For sufficiently large values of N, the impurity wavefunctions overlap and the average radius of the impurity wavefunctions increases from a to $\zeta \geq a$. For the remainder of this thesis we will use ζ to refer to the localization radius of the impurity wavefunctions. At the critical impurity concentration N_c such that $N_c^{-1/3}a \approx 0.25$, ζ become infinite and the sample undergoes a metal-insulator transition.

Impurity concentration	Density of states	Wavefunction ψ

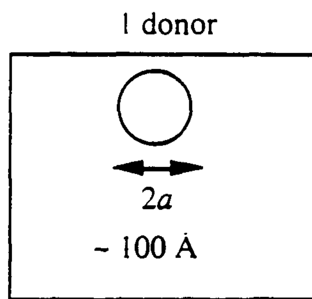

a = localization radius

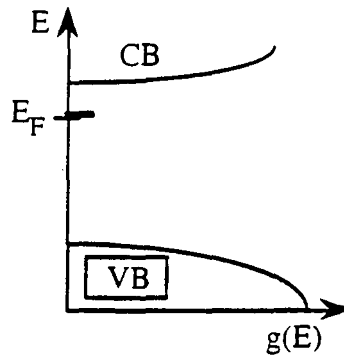

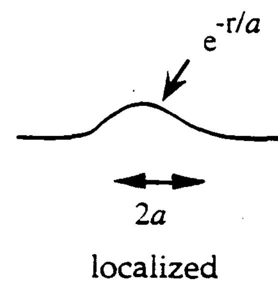

localized

many donors

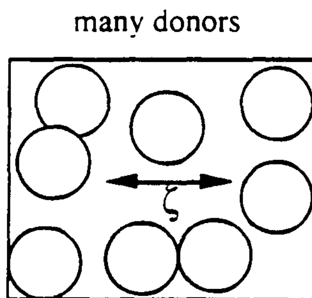

ζ = localization radius

$\zeta > a$

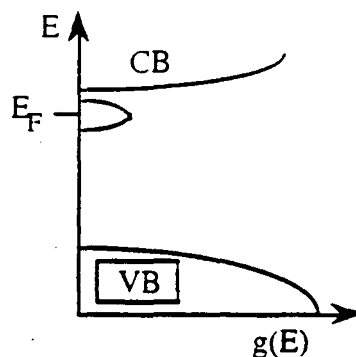

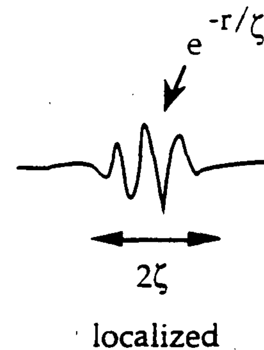

localized

metal-insulator transition

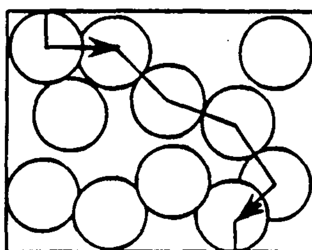

$\zeta = \infty$

$N = N_c = (4a)^{-3}$

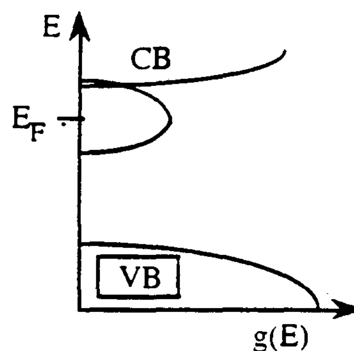

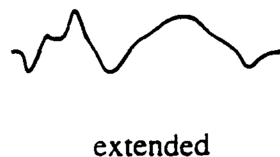

extended

Fig.1.3 As the impurity concentration increases, the doped semiconductor undergoes a metal-insulator transition corresponding to the transition between extended and localized states at the Fermi level.

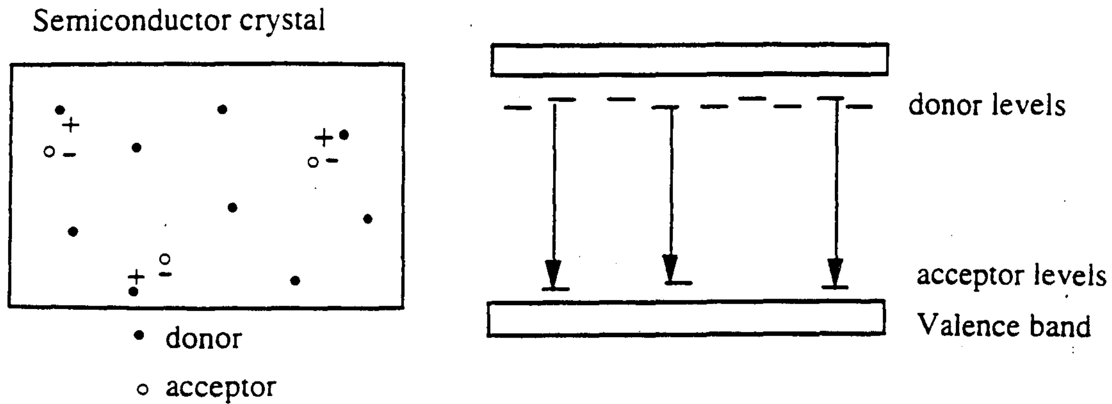

Fig. 1.4 In a semiconductor crystal containing both donors and acceptors, each acceptor will capture an electron from a donor until all the acceptor levels are filled or all the donor levels are depleted. This process is known as compensation.

1.3.1 Compensation

When a semiconductor is doped with both acceptor and donor species with concentrations N_A and N_D, each acceptor will capture an electron from a donor following the minimum energy principle until all the acceptor levels are filled or all the donor levels are depleted. This process is known as compensation and is illustrated in Figure 1.4. The concentration of uncompensated impurities is given by $|N_A - N_D|$. If $N_D > N_A$ then the donors are referred to as the majority dopant and the acceptors are referred to as the minority dopant. The compensation ratio K of a semiconductor is defined as

$$K = N_{min}/N_{maj}. \tag{1.5}$$

K always has a value between 0 (uncompensated) and 1 (fully compensated).

1.4 Structure of the impurity band

The detailed structure of the impurity band, notably the position of the Fermi level μ and the density of states g(E), is a function of the majority impurity concentration N_{maj} and the degree of compensation K. For a lightly doped semiconductor with a random distribution of impurities, μ and g(E) will be completely determined by N_{maj} and K. In

general the band structure cannot be solved for analytically. However, in the limiting cases of low and high compensation the Fermi level can be calculated. As we will explain, the density of states has two peaks corresponding to the typical energies of occupied and unoccupied majority dopant sites. The density of states function falls to zero at the Fermi energy due to long-range Coulomb interactions between impurities. The following discussion of the impurity band structure is adapted from Efros and Shklovskii [1972], Efros and Shklovskii [1975], and Shklovskii and Efros [1984].

1.4.1 The Fermi energy

Consider a semiconductor with a donor concentration N_D and an acceptor concentration $N_A < N_D$. At low temperatures each acceptor captures an electron from a donor and becomes negatively charged. Thus as T approaches zero there are $N_D - N_A$ neutral donors, N_A positively charged donors, and N_A negatively charged acceptors. Let us define our zero of energy as the energy of an isolated donor. Then the energy at donor site i is determined by Coulomb interactions with the charged impurities:

$$E_i = \frac{e^2}{\kappa}\left[\sum_j^{acc} \frac{1}{|r_i - r_j|} - \sum_{k \neq i}^{don} \frac{1 - n_k}{r_i - r_j}\right]. \tag{1.6}$$

For a neutral donor the electron occupation n_k is 1; for a compensated donor n_k is 0. At T equal to zero the set of occupation numbers $\{n_k\}$ is that for which the total electrostatic energy is a minimum; this is known as the ground state. The Fermi energy μ is defined as the energy below which all donor sites are filled and above which all donor sites are empty in the ground state. At nonzero temperatures the occupation probability P_i of a donor site in thermal equilibrium is given by:

$$P_i = \frac{1}{\exp\left(\frac{E_i - \mu}{kT}\right) + 1}. \tag{1.7}$$

The position of the Fermi level relative to the isolated donor energy can be determined analytically only in the limiting cases of weak and strong compensation $K = N_A/N_D$.

1.4.2 Fermi level in the limit of weak compensation

When $K \ll 1$ only a small fraction of donors are positively charged. In the ground state these ionized donors are all located as close as possible to a negatively charged acceptor. Since $N_A \ll N_D$, each acceptor can be treated as if it were immersed in a sea of donors. The most probable binding energy of an ionized donor-acceptor pair is given by the average energy required to move an electron from a remote site to the ionized donor site. This energy is $e^2/\kappa R_D$, where $R_D = 3/4\pi N_D^{-1/3}$ is the average separation between ionized and neutral donors in the ground state.

Most acceptors will compensate exactly one donor (this is known as a 1-complex). However, other configurations are possible in which an acceptor doesn't ionize any donors (0-complex) or may ionize two donors (2-complex). The condition for a 0-complex is that no donors exist within a sphere of radius $r_\mu = e^2/\kappa\mu$ from an acceptor site. The probability of this is given by $P_o(\mu) = \exp[-4\pi r_\mu^3 N_D/3]$. Thus the number of 0-complexes is given by $N_o(\mu) = N_A P_o(\mu) = N_A \exp[-4\pi e^6 N_D/3\kappa^3\mu^3]$.

Since the donor distribution is random, another possibility is that many donors are situated close to an acceptor. Consider the configuration below in which two ionized donors are an equal distance r from an acceptor:

The donor binding energy in this case will be $e^2/\kappa r - e^2/2\kappa r = e^2/2\kappa r$. Therefore a 2-complex is actually energetically more favorable than a 1-complex for which the nearest donor is located at a distance greater than 2r.

It can readily be shown [Shklovskii and Efros, 1984] that one acceptor cannot bind more than two ionized donors because the energy of an n-complex where $n \geq 3$ is always repulsive. Thus the three possible acceptor configurations are 0-, 1-, and 2- complexes.

Charge neutrality requires that $N_0(\mu) = N_2(\mu)$. This condition allows us to determine the Fermi energy μ. A complicated integral based on the probability of finding a pair of donors whose energies E_1 and E_2 exceed μ when both are ionized leads to an expression for $N_2(\mu)$ which is then set equal to $N_A \exp[-4\pi e^6 N_D/3\kappa^3\mu^3]$. In the limit of small K, we find that

$$\mu = \frac{0.99 e^2 N_D^{1/3}}{\kappa} . \tag{1.8}$$

The percentage of 0-complexes $N_0(\mu)/N_A$ is approximately $\exp[-4\pi/3] \approx 1.3\%$, and the number of two complexes is the same. Since 97.4% of acceptors form neutral 1-complexes, it is tempting to think that in a first approximation one need not consider other configurations. However, if every acceptor produced a 1-complex, then in a random impurity distribution sometimes the nearest ionized donor would be located far from its acceptor. The binding energy E for this ionized donor is almost zero, but we know that in the ground state $\mu < E$ so if only 1-complexes were possible, μ would be ≈ 0 for low compensation semiconductors.

1.4.3 Position of the Fermi level for intermediate and strong compensation

At high compensation ($1 - K \ll 1$) the concentration of neutral donors is much less than the concentration of ionized donors. This means that the Fermi level is located below the isolated impurity level and that as K varies from 0 to 1, μ varies from $0.99e^2N_D^{1/3}/\kappa$ through zero to a negative value located deep in the forbidden gap. Electrons therefore only occupy the states at the deepest energies. Each of these deep states is created by a pair of donors, one occupied and one empty, located very close together. If the pair separation is less than $-e^2/\kappa\mu$ then the donor-pair is energetically favorable. A calculation of the probability of finding such a donor pair and a consideration of long-range potentials gives the Fermi energy

$$\mu = -\frac{C e^2 N_D^{1/3}}{\kappa(1-K)^{1/3}} . \tag{1.9}$$

where $[N_D/(1-K)]^{1/3}$ is related to the average separation between donor sites and C is a numerical constant that depends on the details of the semiconductor.

Although the position of the Fermi level relative to the isolated impurity level cannot be determined analytically for intermediate compensation, computer simulations minimizing the energy of a random impurity distribution can be used to determine the dependence of μ on K for $0 \leq K \leq 1$. The results of such simulations are in good agreement with theoretical calculations in the limit of weak and strong compensation, and can be found in Shklovskii and Efros [1984].

1.4.4 Density of states in the impurity band

Pollak [1978] first showed that the density of states g(E) always has two peaks. The high energy peak is due to unoccupied donors which have formed complexes with nearby acceptors. The integral $\int g(E)dE$ from μ to ∞ is equal to N_A, the concentration of compensating sites. The low energy peak is due to occupied donor levels; the integral $\int g(E)dE$ from $-\infty$ to μ gives $N_D - N_A$.

Most theories predict a dip in the density of states at the Fermi level. Efros and Shklovskii [1975] first showed that that density of states at the Fermi level must vanish if long-range Coulomb interactions between impurity states are taken into account, or equivalently if electron screening is not effective on small length scales. The Coulomb gap arises in the following way: since in the ground state the occupation numbers minimize the total energy, any variation in occupation number leads to a positive energy increment ΔE. Thus, if we transfer an electron from one donor (j) to another donor (i) starting from the ground state configuration the change in energy is given by $\Delta E = E_j - E_i - e^2/\kappa r_{ij} > 0$ (here E_i and E_j are measured relative to the Fermi level μ). Since ΔE is positive, $r_{ij} > e^2/\kappa(E_i - E_j)$. As E_i and E_j approach the Fermi level, $E_i - E_j$ goes to zero and r_{ij} tends toward

infinity. The physical meaning of this is that states close to the Fermi level are located far apart. It follows that g(E) near the Fermi level is proportional to $(E - \mu)^2$. The Coulomb gap in the density of states has a strong effect on the low temperature variable range hopping conduction, as discussed in Section 1.5.4.

1.4.5 The Upper Hubbard band and the D^- state

In addition to the energy levels discussed above, an n-type semiconductor with a donor concentration N_D has N_D additional energy levels corresponding to the electronic states of a negative donor ion known as the D^- ion. The existence of the D^- ion was first suggested by Fritzsche [1958] and Lampert [1958] in analogy with the hydrogen ion H^- which is stable with a binding energy of 0.7 eV for the second electron. The D^- states are frequently described in terms of the Mott-Hubbard model. An extremely simplified model of electron-electron interactions was first developed by Hubbard. In the Hubbard model [Shklovskii and Efros, 1984; Mott, 1993], it is assumed that electrons repel each other only when they are located on the same site. The intra-atomic interaction between two electrons is measured by the Hubbard "U" and is defined as

$$U = \int\int \frac{e^2}{\kappa r_{12}} |\psi(x_1)|^2 |\psi(x_2)|^2 d^3x_1 \, d^3x_2 \, , \tag{1.10}$$

where ψ is the wavefunction for one of the donor centers. This interaction produces an energy gap between singly occupied and doubly occupied donor states.

1.5 Impurity conduction in doped semiconductors

1.5.1 Transitions between localized states in an aperiodic solid

We begin our discussion of impurity conduction in doped semiconductors with a general comparison of transition rates between localized states in an aperiodic solid with transition rates between band states in a crystal [Pollak, 1987]. Transitions between localized electron states in aperiodic solids are effected by phonons via a deformation

potential, and the dominant processes are single-phonon absorption and emission. Therefore, the "golden rule" can be used for evaluating transition rates. The localized states are described by wavefunctions of the form

$$\phi_i(r) = F(r) \exp\left[- \frac{|(r_i - r)|}{a} \right] , \qquad (1.11)$$

where F(r) is a rapidly varying function on the atomic scale, r_i is the position of the center of the localized state ϕ_i, and a is the localization radius. In comparison, band wavefunctions have the form

$$\phi_k(r) = f(r) \exp[i\mathbf{k}\cdot\mathbf{r}] , \qquad (1.12)$$

where f(r) is a periodic function varying rapidly on the atomic scale, and k is the usual wavevector. The perturbation Hamiltonian V to be used in the golden rule is

$$V = g\mathbf{p} \exp[i\mathbf{k}'\cdot\mathbf{r}] , \qquad (1.13)$$

where g is the amplitude of the strain tensor due to the phonon with wavevector k' and **p** is the deformation potential tensor. The rapidly varying functions F and f do not contribute to the matrix elements $< \phi_i | V | \phi_j >$, $< \phi_k | V | \phi_{k''} >$. The important part of the matrix element for transitions between localized states is

$$< \exp\left[- \frac{|(r_i - r)|}{a} \right] V \exp\left[- \frac{|(r_j - r)|}{a} \right] > . \qquad (1.14)$$

The square of this matrix element, needed for the golden rule, is proportional to exp [-$2r_{ij}/a$], where $r_{ij} = | r_i - r_j |$. The analogous matrix element squared for transitions between band states is unity, because conservation of crystal momentum requires that k + k' + k" = 0.

The transition rate W_{ij} between localized states i and j compared with the transition rate $W_{kk''}$ between band states k and k" is therefore reduced by a factor $\exp[-2r_{ij}/a]$ which can be extremely small. The small transition rate between localized states will be further discussed in Chapter 2, Section 2.3. Furthermore, the spread in W_{ij} is very large due to the spread in r_{ij}, which is typically several times larger than a.

The above discussion neglects consideration of the density of final states which is proportional to the number of phonons present that can effect a transition between i and j (or between k and k"). For transitions upward in energy the transition rate will be smaller by an additional factor of $\approx \exp(-E_{ij}/kT)$ where E_{ij} is the energy difference between the states i and j. For transitions downward in energy, a factor of unity must be introduced.

1.5.2 Temperature Dependence of the Impurity Conductivity

Electrical conduction in doped semiconductors is strongly dependent on temperature. At high temperatures *intrinsic conduction* occurs, in which carriers are thermally activated from the valence band into the conduction band. The intrinsic carrier concentration decreases rapidly with temperature until it becomes less than the concentration contributed by impurities. The conduction is then determined by the nature and doping density of impurities, and it is called *extrinsic conduction.*

As shown in Figure 1.6, impurity electrons be thermally excited into one of three states. A donor electron can be thermally activated into the conduction band with an energy ε_1, resulting in a positively charged donor site and a free electron. A donor electron can also be thermally excited from the band of ground states (termed the D^o band or the lower Hubbard band) to the band of doubly occupied impurity centers (termed the D^- band or the upper Hubbard band) with an activation energy ε_2, resulting in two donor atoms one with a positive and one with a negative charge. Finally, in a compensated semiconductor a donor electron can hop into a neighboring empty donor state with an energy ε_3, resulting in a positively charged donor site and a neutral donor site. This process is known as nearest neighbor hopping conduction. These conduction processes are indicated in Figure 1.6, which shows the impurity band structure of an n-type semiconductor with a small number of compensating acceptors. The impurity contribution to the electrical conductivity of a semiconductor can therefore be written as

(1) $kT \sim \varepsilon_1$: Activation into conduction band

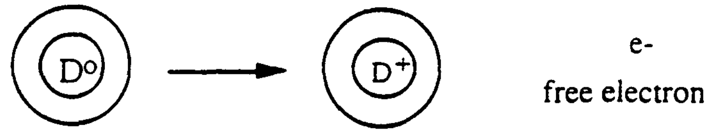

(2) $kT \sim \varepsilon_2$: Activation into upper Hubbard band

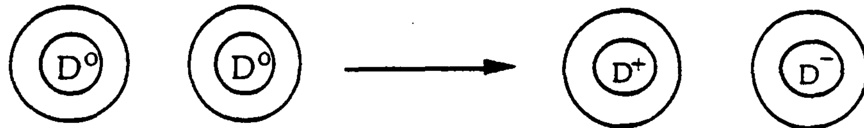

(3) $kT \sim \varepsilon_3$: Hopping into empty donor state

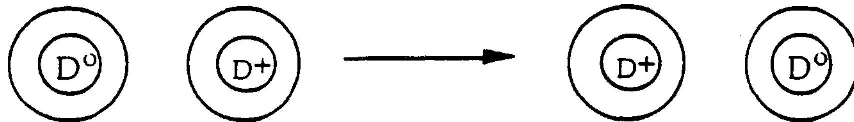

Fig. 1.5 Donor electrons can be excited into one of three states.

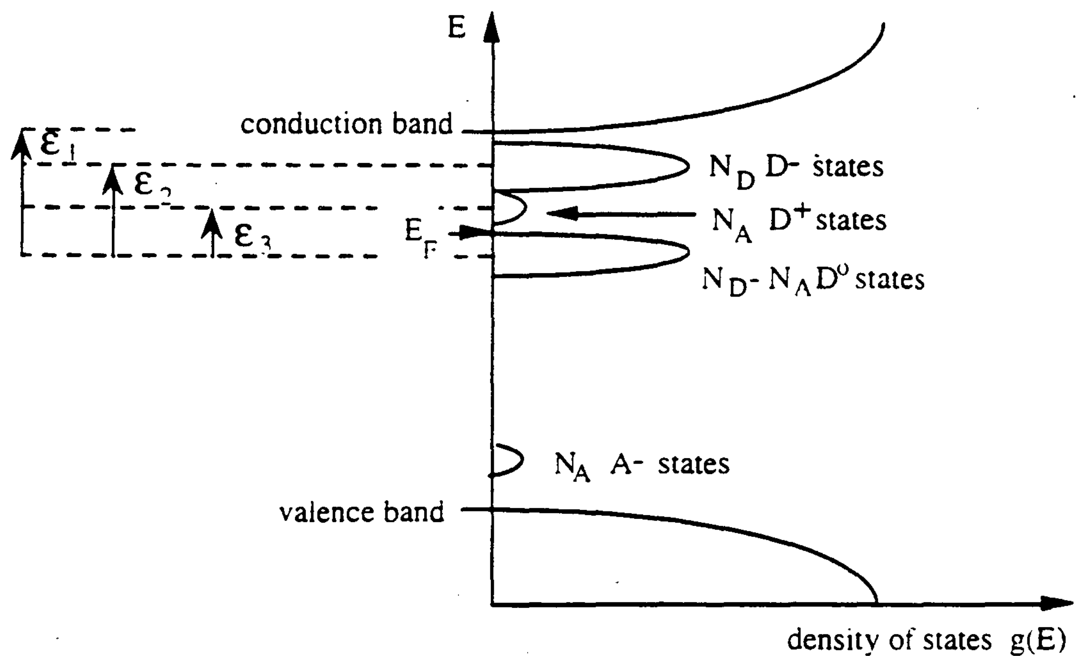

Fig 1.6 Stucture of the impurity band of an n-type semiconductor with a small number of compensating acceptors.

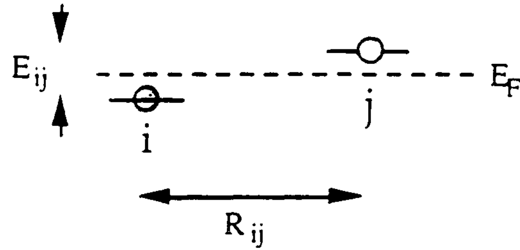

Fig. 1.7 An occupied impurity site i and an unoccupied impurity site j, separated by a distance R_{ij} and by energy E_{ij}.

$$\sigma(T) = \sigma_1 \exp(-\varepsilon_1/kT) + \sigma_2 \exp(-\varepsilon_2/kT) + \sigma_3 \exp(-\varepsilon_3/kT). \qquad (1.15)$$

As the temperature of the doped semiconductor is lowered, the dominant conduction mechanism ranges from ε_1 conduction at high temperatures to ε_3 conduction at low temperatures.

1.5.2.1 Variable range hopping conduction

As described in Section 1.4.1, the transition rate between localized impurity states i and j is given by

$$W_{ij} \propto \exp(-2r_{ij}/a) \exp(-E_{ij}/kT) \qquad (1.16)$$

where R_{ij} is the spatial separation between sites and E_{ij} is their energy separation as shown in Figure 1.7.

The equation for the conductivity as a function of average hopping distance R, average energy gap E, and temperature T is:

$$\sigma = \sigma_o \exp(-2R/a)\exp(-E/kT). \qquad (1.17)$$

The factor exp(-2R/a) may be understood as an exponential attenuation of the conductivity for distant impurity states, while exp(-E/kT) is the Boltzmann factor corresponding to the absorption and emission of phonons. When R is independent of temperature, this is just the nearest neighbor hopping formula and E is the activation energy ε_3. At very low temperatures the overlap integral between impurity states which is proportional to the factor

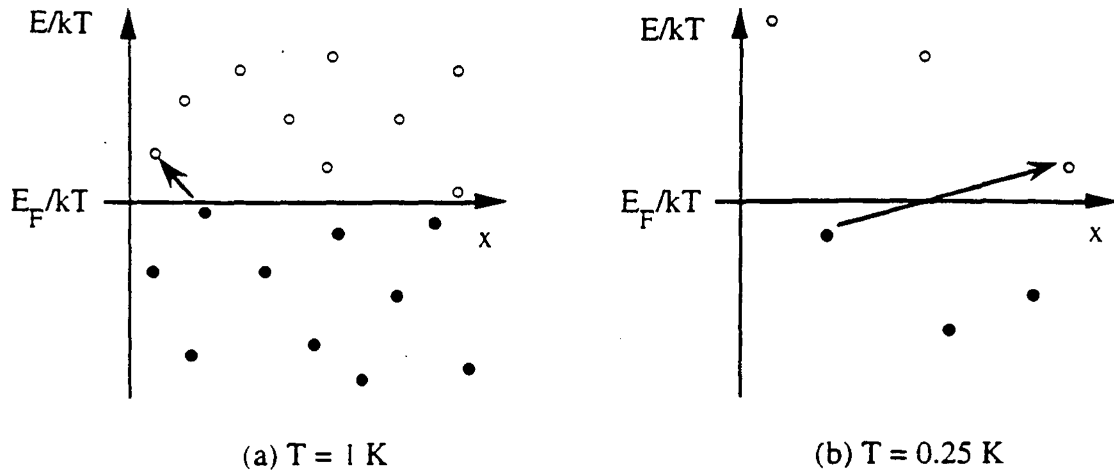

Fig. 1.8 As the temperature decreases, it becomes energetically favorable for a hopping electron to hop to a distant site which is closer in energy.

exp(-2R/*a*) becomes comparable to the Boltzmann factor exp(-E/kT). It then becomes energetically favorable for an impurity electron to hop to a distant impurity site which is close in energy as shown in Figure 1.8. The hopping length R then increases with decreasing temperature, and the conduction mechanism is known as variable range hopping (VRH). VRH conduction can be described by a conductivity of the form

$$\sigma(T) = \sigma_0 \exp[-(T_0/T)^n] \tag{1.18}$$

where T_0 and n depend on the density of states (DOS) in the impurity band.

Mott's theory of variable range hopping assumes a constant density of energy states $g(E) = N_0$ near the Fermi level and can be derived as follows [Shklovskii and Efros, 1984]. Consider the conductivity resulting from energy levels in a small band E_0 around the Fermi level: the concentration of states is given by $N = 2N_0E_0$. Since $R \sim N^{-1/3}$, the conductivity can be written as

$$\sigma = \sigma_0 \exp[-(2N_0E_0a^3)^{-1/3} - E_0/kT]. \tag{1.19}$$

The minimum of σ with respect to E_0 is when $1/3(gE_0a^3) = (kT)^{3/4}$. The energy band E_0 is called the "optimal band," and the conductivity of the system can be assumed to be determined by E_0. Since $E_0 \propto T^{3/4}$, σ is given by

$$\sigma = \sigma_0 \exp[(-T_0/T)^{1/4}] \tag{1.20}$$

for some constant T_0. Therefore the temperature exponent in Equation 1.18 is $n = 1/4$ for a constant density of states at the Fermi level. In Mott's theory the optimum hopping length $R \propto E_0^{-1/3} \propto T^{-1/4}$.

Mott's theory neglects Coulomb interactions between impurity sites. When Coulomb interactions become important [Shklovskii and Efros, 1984], then the density of states g is no longer constant but varies with energy as E^2 and is zero at the Fermi level. This is referred to as a "Coulomb gap", and the total number of states within energy E of the Fermi level is $N = \int g(E)dE = (cE)^3$ for some constant c. Therefore $R \approx N^{-1/3} = 1/cE$. The contribution to the conductivity from energy levels in a small band E_0 around the Fermi level can thus be written as

$$\sigma = \sigma_0 \exp(-1/cE_0 a - E_0/kT) \tag{1.21}$$

The maximum of the conductivity occurs when $E_0 \propto (kT)^{1/2}$. Assuming that the conductivity is determined by E_0 we have

$$\sigma = \sigma_0 \exp[(-T_0/T)^{1/2}] \tag{1.22}$$

for some constant T_0. Therefore the temperature exponent in Equation 1.18 is $n = 1/2$ for a constant density of states at the Fermi level. The optimum hopping length $R \propto E_0^{-1} \propto T^{-1/2}$ for the case of variable range hopping in the presence of a Coulomb gap.

1.6 Anderson Localization

The electronic states in non-crystalline solids can be either localized or extended, depending on the degree of disorder and the role of electron-electron interactions. This contrasts with periodic solids, for which electronic states are compelled by symmetry to be

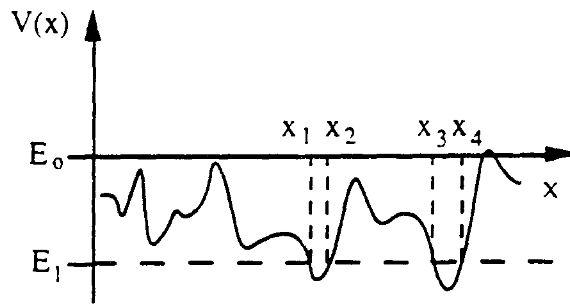

Fig. 1.9 Localization in a random potential.

delocalized Bloch states. The electron-electron interaction gives rise to a splitting of the impurity band, leading to localization of the impurity states as in the Mott-Hubbard model discussed in Section 1.4.5. In the Mott-Hubbard model the filled and empty levels are separated by a gap. Localization of the impurity electrons can also be caused by the random potential at varying impurity sites, as in the theory of Anderson localization.

Clasically, a particle moving in the potential V(x) shown in Figure 1.9 will be delocalized -- that is, it can move through the entire x-space -- when it has an energy greater than E_0. The mobility edge between localization and delocalization occurs at the particle energy $E = E_0$. If the particle has an energy $E_1 < E_0$ it will be localized over the region $x_1 < x < x_2$, or over the region $x_3 < x < x_4$. When quantum mechanical considerations are included, the situation becomes more complicated. For example, tunneling can lead to particle delocalization even for $E < E_0$. An example of this type of delocalization is Bloch states in a perfect crystal. The random potential can also lead to particle localization for energies greater than E_0. For example, any particle in a one-dimensional random potential will be localized regardless of the degree of disorder.

Anderson [1958] proposed the following model of electron localization. Suppose that the impurities are located on sites of a regular lattice but have randomly distributed energy levels. In other words, we consider a system of periodically arranged potential wells of varying depth as shown in Figure 1.10. The energy of an electron at site j

relative to the center of the interval W is denoted by E_j. We suppose that the energy distribution is uniform over an interval W, leading to the distribution function

$$P(E) = 1/W \qquad |E| < W/2,$$
$$P(E) = 0 \qquad |E| > W/2.$$

The Hamiltonian of this system contains two terms [Shklovskii and Efros, 1984],

$$H = \sum_j E_j a_j^\dagger a_j + \sum_{j,m\neq 0} I(m) a_j^\dagger a_{j+m} \, . \tag{1.23}$$

The first term represents the sum of electron energies on isolated sites and the second represents the energy overlap integrals betweeen different sites. I(m) is called the energy overlap integral, and contains a factor $\exp(-c|\mathbf{x}_j-\mathbf{x}_{j+m}|/\zeta)$ where c is a numerical coefficient. $\mathbf{x}_j$ is the location of site j, and ζ is the characteristic size of the electron wavefunction. Clearly, except for neighboring sites I(m) will be extremely small.

In order to formulate the question of whether or not an electron state is localized, a mathematical definition of localization is required. Anderson used the following criterion. Suppose that at time t = 0 the electron has a finite probability of being located at site i in a system with infinitely large dimensions. In other words, $|\psi(\mathbf{x}_i,t=0)|^2$ is finite where ψ is the electron wavefunction. The electron state is said to be localized if in the limit $t \rightarrow \infty$, the electron remains in approximately the same region of space so that $|\psi(\mathbf{x}_i,t=\infty)|^2$ is finite. If the electron state is not localized the initial wave packet spreads out over the system with time, leading to $|\psi(\mathbf{x}_i,t=\infty)|^2 = 0$.

The Anderson model does not have an exact solution, but has been studied extensively both theoretically and numerically. The critical parameter in the Anderson model is the dimensionless ratio W/I where I is the energy overlap integral between neighboring sites. Anderson's result is that for sufficiently large values of W/I, all impurity states are localized. As W/I decreases it reaches a critical value $(W/I)_c$ for which states at E = 0 begin to be delocalized. Further decrease in W/I causes the delocalization to spread through the energy band as shown in Figure 1.11.

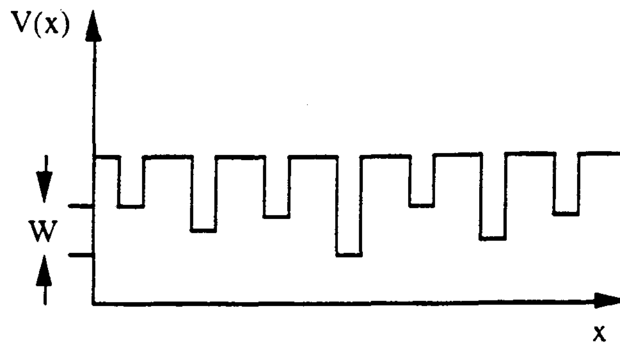

Fig. 1.10 Potential wells in the Anderson model, adapted from Shklovskii and Efros [1984].

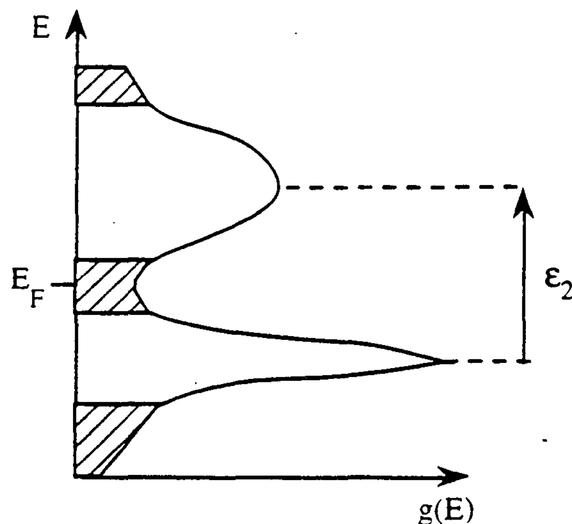

Fig.1.11 Model of the density of states in the impurity band. The shaded areas indicate regions over which the electron states are localized. When the density of states increases above a critical value, the nearest neighbor energy overlap integral I correspondingly increases and the dimensionless ratio W/I in the Anderson model decreases below the critical value for electron delocalization.

For a sufficiently large values of I correponding to an impurity concentration N_c, states at the Fermi level will become delocalized. This transition from extended to localized states at the Fermi level is known as the metal-insulator transition (MIT), and occurs at the impurity concentration

$$N_c = (1/4a)^3 \tag{1.24}$$

where a is the localization radius of an isolated impurity as discussed in Section 1.3. Equation 1.24 has been experimentally verified in a wide variety of materials [Edwards and Sienko, 1978].

Chapter 2

Theory of non-Ohmic impurity conduction in doped semiconductors

In this chapter we review the theoretical and experimental studies of non-Ohmic impurity conduction in doped semiconductors. Non-Ohmic conduction can be considered under three headings [Mott, 1971]:

(1) Bulk non-Ohmic conduction, independent of the conditions at the electrodes;
(2) Contact effects, such as space-charge limited currents, depending on the conditions at the electrodes;
(3) Hot electron effects due to heating of the charge carriers.

The subject of this thesis is primarily non-Ohmic impurity conduction of the first type. However, we will also discuss contact effects and hot electron effects at some length in order to distinguish between the three types of behavior.

2.1 Bulk non-Ohmic impurity conduction

Bulk non-Ohmic impurity conduction in doped semiconductors may be further divided into two subcategories:

(1.1) Impurity charge carriers excited into extended states in the conduction band (ε_1 conduction);
(1.2) Impurity charge carriers making transitions between states in the impurity band (ε_2 conduction and hopping conduction).

For impurity conduction of the first type, the non-Ohmic conductivity is well understood and is described by the Poole-Frenkel effect [Frenkel, 1938; Hartke; 1968]. For sufficiently large electric fields impact ionization breakdown will occur [Reggiani and Mitin, 1989; Parisi, 1991]. Non-Ohmic impurity conduction of the second type is more complex and remains poorly understood. For the remainder of this thesis we use non-Ohmic impurity conduction to refer to the second category. We will describe the many contradictions that exist between different theories of non-Ohmic impurity conduction and

between theory and experiment. The existing theories, developed for nearest neighbor hopping and Mott variable range hopping, assume a lightly doped semiconductor for which a constant localization radius can be assumed throughout the impurity band. No theory has yet been developed which includes the effects of electron-electron interactions, the variation of localization throughout the impurity band, and the influence of an applied electric field on the impurity wavefunctions. These considerations become important as the impurity concentration nears the critical concentration for a metal-insulator transition. As we will show, studies of the influence of an applied electric field on the impurity band conduction provide an important probe of the structure of the impurity band.

We provide a detailed summary of the theoretical and experimental studies that have been done on non-Ohmic impurity band conduction. This is the first thorough review of the field of non-Ohmic impurity conduction. We show that the dependence of the non-Ohmic conductivity on the applied electric field, the temperature, and the impurity concentration has not yet been well-established for low and moderate electric fields.

2.1.1 Poole Frenkel effect

The Poole-Frenkel effect [Frenkel, 1938; Hartke; 1968] refers to the electric-field induced increase in the concentration of conduction band electrons due to the reduction in the ionization energy of a donor electron under an applied electric field as shown in Figure 2.1. The potential energy of an electron at a distance x from an impurity site in the direction of an applied electric field F is

$$V(x) = -\frac{e^2}{\kappa|x|} - eFx , \tag{2.1}$$

where κ is the dielectric constant of the bulk semiconductor. This function has its maximum when $e^2/\kappa x_{max}^2 = eF$. The potential energy at a distance x_{max} from the impurity

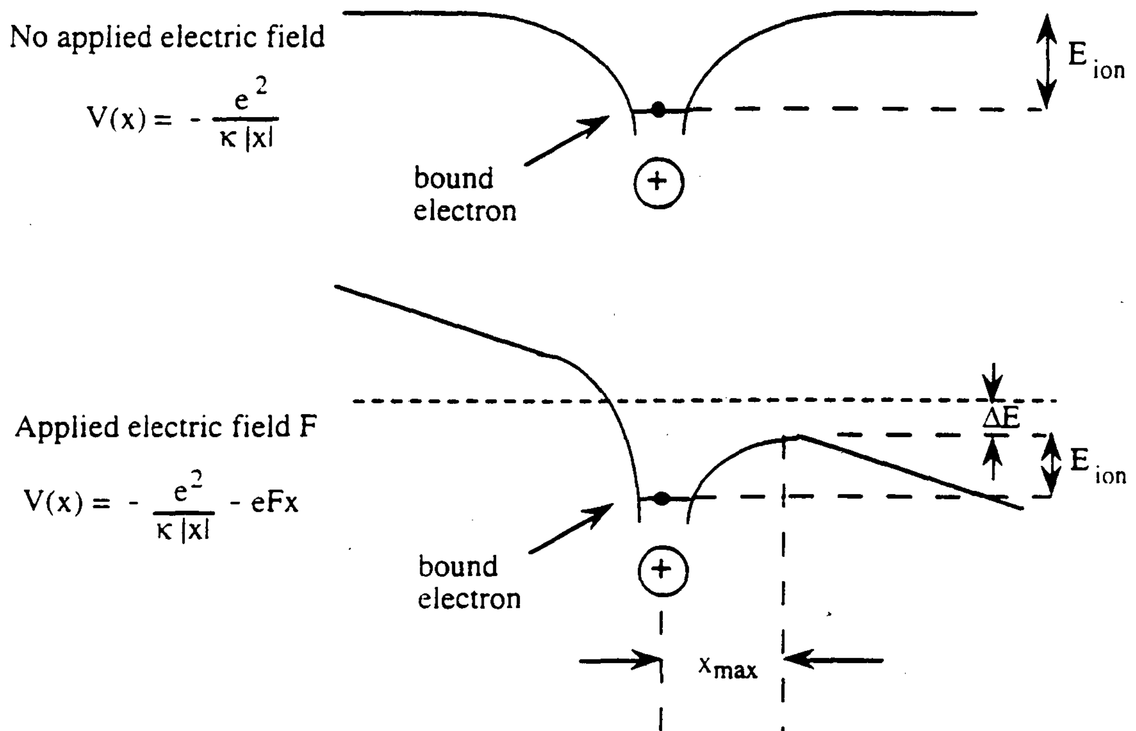

Fig. 2.1 Potential energy of an electron (black dot) in the field of a positively charged donor (top curve) and in the field of a positively charged donor with an applied electric field F (bottom curve). Under an applied electric field the ionization energy E_{ion} is reduced by $\Delta E = 2e^{3/2}F^{1/2}/\kappa^{1/2}$.

site is $V = -2e^{3/2}F^{1/2}/\kappa^{1/2}$. Therefore the energy required to ionize an electron is lowered by $\Delta E = 2e^{3/2}F^{1/2}/\kappa^{1/2}$ and the ε_1 conductivity increases with electric field as

$$\sigma_1(F) = \sigma_{01} \exp\left(-\frac{(\varepsilon_1 - \beta F^{1/2})}{kT}\right), \qquad (2.2)$$

where $\beta = 2e^{3/2}/\kappa^{1/2}$.

2.1.2 Impact ionization breakdown

For sufficiently high electric fields, an impurity electron excited into the conduction band can accelerate under an applied field up to the ionization energy of an occupied impurity site. When this occurs the electron can excite other impurities into the conduction

band through scattering processes, and the number of ionized impurities increases dramatically. This process is known as impact ionization breakdown [Parisi, 1991]. The impurity conductivity can rise by several orders of magnitude just above the critical electric field F_B for which breakdown occurs. F_B increases linearly with impurity concentration N because as the number of dopants increases, so does the rate at which conduction electrons lose energy due to scattering. Therefore a conduction electron requires a correspondingly larger electric field in order to gain sufficient energy to ionize other impurity electrons. The breakdown field is insensitive to the lattice temperature at low temperatures because the dominant scattering mechanism is impurity scattering rather than phonon scattering. At sufficiently high temperatures all the impurity carriers are thermally ionized into the conduction band and no breakdown occurs.

We believe that impact ionization processes are negligible for all of the data discussed in this thesis. Impact ionization requires activation into extended states so that the charge carriers can accelerate under an applied electric field. The non-Ohmic impurity conduction studied in this work is by charge carriers tunneling between localized states in the impurity band rather than by charge carriers excited into extended states in the conduction band. Charge carriers in hopping conduction cannot accelerate freely under an applied electric field and no impact ionization is expected to occur.

Even if we were studying the non-Ohmic behavior of electrons excited into the conduction band, impact ionization processes would be insignificant for the range of electric field strengths studied in this work. For example, breakdown in lightly doped Ge:Ga with $N = 1\times10^{13}$ cm^{-3} occurs at an electric field $F_B \approx 2.7$ V/cm [Parisi, 1991]. Since all of the samples studied in this work have impurity concentrations greater than 10^{15} cm^{-3}, F_B is expected to be at least several hundred V/cm for conduction band electrons. This is an order of magnitude larger than the maximum electric field $F_{max} \approx 16$ V/cm studied in this work.

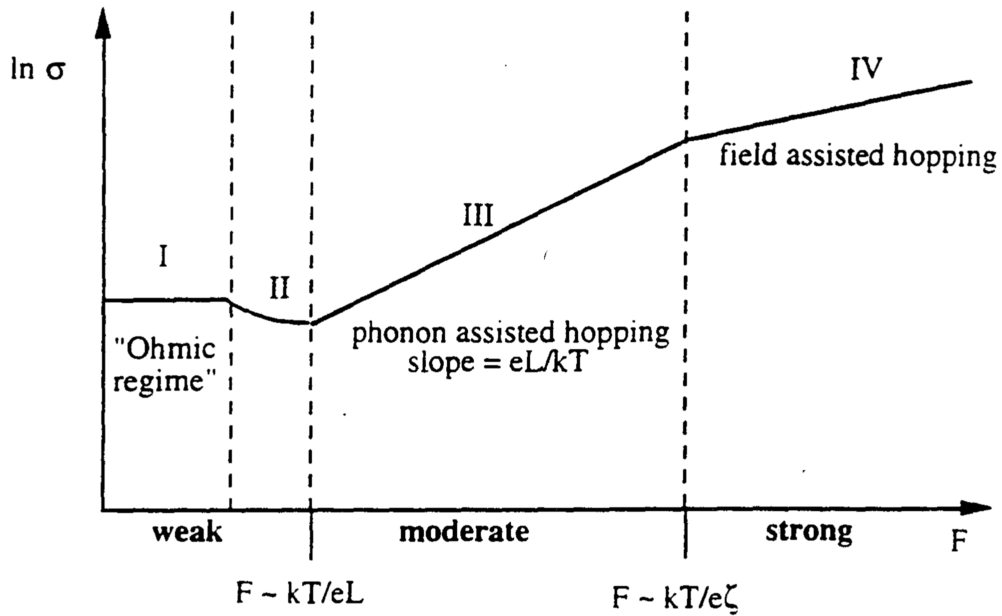

Fig. 2.2 Weak, moderate, and strong field regimes predicted by most theories of hopping conduction in an applied electric field F.

2.1.3 Non-Ohmic conduction in the impurity band

We now turn our attention to the main subject of this thesis, the characterization of impurity conduction in an applied electric field. The existing theoretical studies assume a lightly doped semiconductor for which the dominant conduction mechanism is hopping between impurity states with a constant localization radius ζ. It is useful to define a characteristic length parameter L which is related to the optimum hop length R. L is typically many times larger than ζ. As shown in Figure 2.2, theoretical studies of non-Ohmic impurity conduction distinguish between conduction in weak fields ($F < kT/eL$), moderate fields ($kT/eL < F < kT/e\zeta$), and strong fields ($F > kT/e\zeta$). We will discuss each of these regimes in turn.

As we will show, there are many contradictions between the existing theoretical and experimental studies of non-Ohmic impurity conduction in weak and moderate fields. In particular, the dependence of L on temperature and impurity concentration remains poorly understood. In Chapter 3 we show that the standard fitting function used to analyze the

moderate field data can give misleading results. In Chapter 4 we show that some of the experimental discrepancies can be attributed to sample stress.

2.1.3.1 Impurity conduction in weak electric fields

The dependence of the nearest neighbor hopping conductivity of a lightly doped semiconductor on a weak electric field was first derived by Hill [1971]. A concise derivation of Hill's result can be found in Mott and Davis [1979]. They assume that for weak electric fields the percolation path is unaffected. This is equivalent to the assumption that the hopping electrons move isotropically through the crystal and are as likely to hop against the applied field as in the direction of the field. The hopping probabilities in the direction of the applied field and against the field Γ^+ and Γ^- are given by

$$\Gamma^{\pm} = \nu_{ph} \exp\left[-\frac{2R}{\zeta} - \frac{W \pm eRF}{kT} \right], \tag{2.3}$$

where ν_{ph} is a factor depending on the phonon spectrum and depends weakly on temperature. As discussed in Chapter 1, R is the optimum hop length and W is the typical energy barrier encountered by hopping electrons. The hopping current density j is defined as $j = NeR(\Gamma^+ - \Gamma^-)$, where N is the concentration of hopping electrons. At temperature T, $N = 2g(E_F)kT$ where $g(E_F)$ is the density of states at the Fermi level. Thus j is given by

$$j = 2eRkTg(E_F)\nu_{ph} \exp\left[-\frac{2R}{\zeta} - \frac{W}{kT} \right] \sinh\left(\frac{eRF}{kT} \right). \tag{2.4}$$

The conductivity is then

$$\sigma = \frac{j}{F} = 2e^2R^2g(E_F)\nu_{ph} \exp\left[-\frac{2R}{\zeta} - \frac{W}{kT} \right] \frac{\sinh\left(\frac{eRF}{kT} \right)}{\left(\frac{eRF}{kT} \right)}. \tag{2.5}$$

In the limit $F \rightarrow 0$, $\sinh(x)/x \rightarrow 1$ and σ can be written in the familiar form

$$\sigma = \sigma_0 \exp\left[-\frac{2R}{\zeta} - \frac{W}{kT} \right]. \tag{2.6}$$

In the limit $eRF/kT << 1$, we can use the approximation

$$\frac{\sinh\left(\frac{eRF}{kT}\right)}{\left(\frac{eRF}{kT}\right)} \approx 1 + \frac{1}{6}\left(\frac{eRF}{kT}\right)^2 . \tag{2.7}$$

Thus according to Hill's model, in very weak electric fields the conductivity will increase with field and temperature as $\Delta\sigma \sim F^2/T^2$.

Apsley and Hughes [1974] have also proposed a theoretical model for isotropic hopping conduction in weak electric fields. Using the formalism of averaging in four-space for which three dimensions are spatial and the fourth dimension corresponds to energy, they find that for n = 1/4 variable range hopping

$$\sigma(F) = \sigma(F{=}0)\exp\left[\frac{AF^2}{T^{9/4}}\right] \tag{2.8}$$

where A is a numerical factor related to the impurity localization radius ζ and the impurity concentration N. For sufficiently small values of F, the conductivity will increase with field and temperature as $\Delta\sigma \sim F^2/T^{9/4}$. Therefore in the low field limit, both Hill's model and the model of Apsley and Hughes predict that $\Delta\sigma \sim F^2$.

Several articles on non-Ohmic impurity conduction state that in weak fields the conductivity is nearly independent of the applied field, without presenting a specific form for the low field dependence of the conductivity. In weak fields the hopping conductivity is expected to be isotropic, so that the additional energy eER gained by electrons hopping against the applied field is balanced by the energy -eER lost by electrons hopping in the direction of the field. This is the so-called "ohmic regime" indicated in Figure 2.2 at field strengths $F < F_c = kT/eL$ and discussed in the theoretical models of Shklovskii [1976], Pollak and Riess [1976], and van der Meer *et al.* [1982]. The length parameter L must be determined from the moderate field dependence of σ, for which theoretical models predict $\sigma(F,T) = \sigma(0,T)\exp[eFL/kT]$ as described in Section 2.1.3.2.

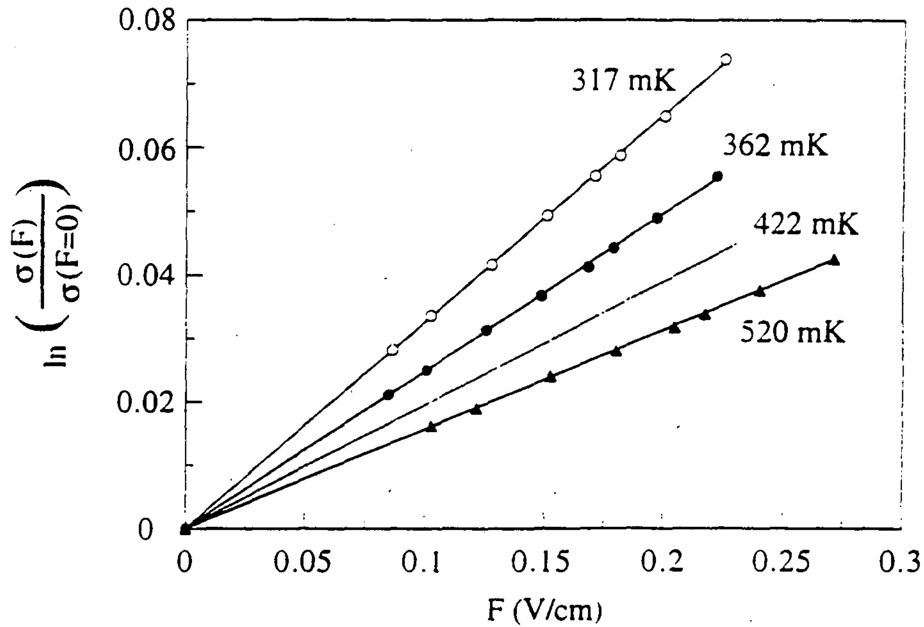

Fig. 2.3 Electric field dependence of the conductivity of neutron transmutation doped Ge:Ga with a net impurity concentration $N = 3.3\times10^{16}$ cm^{-3} measured at temperatures between 317 mK and 520 mK.

Experimental results on the electric field dependence of the conductivity in the weak field regime disagree with each other and with theoretical predictions. The published data of many authors [Aladashvili *et al.*, 1989; Grannan *et al.*, 1992; Kenny *et al.*, 1989; Redfield, 1975; Timchenko *et al.*, 1981; Timchenko *et al.*, 1989] can be described by the theoretical expression for the moderate field dependence of the conductivity at electric fields many times lower than kT/eL. Figure 2.3 shows the electric field dependence of the conductivity of neutron transmutation doped Ge:Ga with a net impurity concentration $N = 3.3\times10^{16}$ cm^{-3} measured by Grannan *et al.* [1992]. In the limit $F \rightarrow 0$ the conductivity is very well described by $n = 1/2$ variable range hopping. For the measured values of $L \sim 1000$ Å - 1500 Å, theory predicts that the Ohmic regime should extend to $F_c \sim 2$ V/cm. Instead we observe a linear dependence of ln σ on the applied field at field strengths below 0.1 V/cm. Similar results were observed in a second Ge:Ga sample with $N = 2.6\times10^{16}$

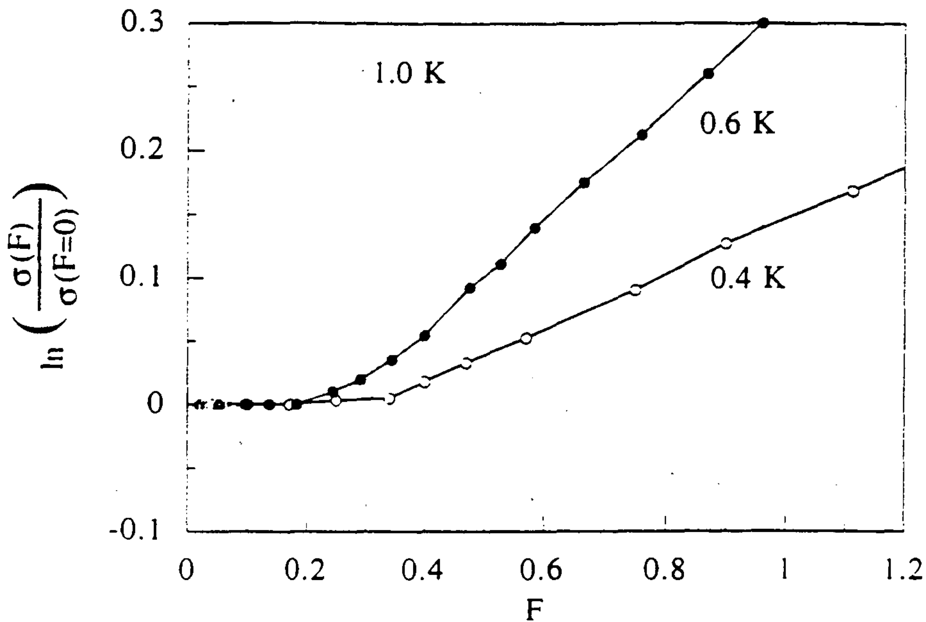

Fig. 2.4 Electric field dependence of the conductivity of a germanium bicrystal with a tilt angle $\theta \approx 8.5$, adapted from the published data of Zavaritskaya *et al.* [1985]. The electric field F for the 0.4 K curve (open circles) is in units of 10^{-2} V/cm; F for the 0.6 K curve (solid circles) is in units of 10^{-1} V/cm; F for the 1.0 K curve (open triangles) is in units of V/cm.

cm^{-3}. Therefore for these samples, F_c is significantly smaller than predicted by theoretical models and is smaller than the lowest field strength in our measurement. The linear dependence of ln σ on F extends to values of the conductivity $\sigma(F) \approx 1.01\sigma_{ohm}$ where σ_{ohm} is the value of the conductivity in the limit $F \rightarrow 0$. This result contradicts the results of a computer simulation by Levin and Shklovskii [1984], in which the linear dependence of ln σ on F begins at $\sigma(F) \approx 1.3\sigma_{ohm}$.

Evidence for an Ohmic regime can be found in the experimental study of Zavaritskaya *et al.* [1985]. They have measured the non-Ohmic behavior of a germanium bicrystal with a tilt angle $\theta \approx 8.5°$ over the temperature range 0.05 K < T < 1 K. As in the study by Grannan *et al.*, the conductivity in the limit $F \rightarrow 0$ is very well described by n = 1/2 variable range hopping. Figure 2.4 is adapted from their published data and shows the

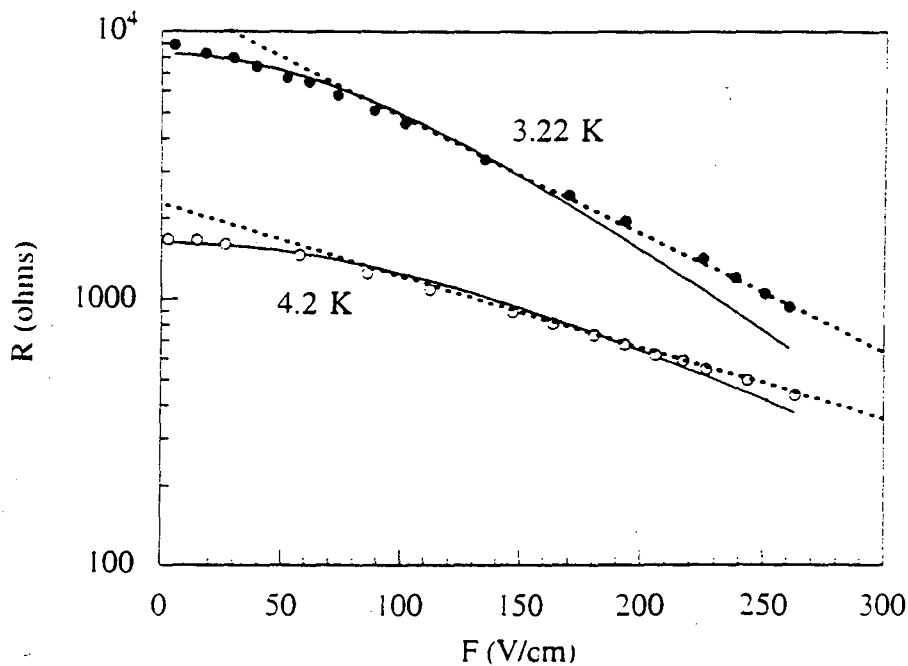

Fig. 2.5 Electric field dependence of the resistance of 100 nm layers of ion implanted Si:As, adapted from the published data of Gang *et al.* [1989]. The data over the entire range of F are fit to the function $R \propto (eFL/kT)/\sinh(eFL/kT)$ (solid line). At field strengths $F > 120$ V/cm the data are better described by an exponential dependence of the resistance on applied field (dashed line).

observed field dependence of the conductivity. $\sigma(F)$ is not well described by the theoretical models of Hill and Pollak and Reiss. However, Zavaritskaya *et al.* observe a clear distinction between Ohmic behavior at fields less than a critical field F_c and moderate field behavior at $F > F_c$.

Zavaritskaya *et al.* do not analyze their data to determine the length parameter L at each temperature. Using the values of L determined from the slope of $\ln \sigma$ vs. F at values $F > F_c$, we find that their observed values of F_c are ten to twenty times smaller than the value $F_c = kT/eL$ predicted by theory. The length parameter L has a temperature dependence $L = (4820 \pm 270)T^{-3}$ Å where the power exponent of the temperature, -3, is determined to within 2%.

The theoretical prediction of Hill that the weak field conductivity has a dependence $\sigma(F) \propto \sinh(eFL/kT)/(eFL/kT)$ has been observed in the experimental studies of Gang *et al.* [1989], Nair and Mitra [1977], and Zhang [1992]. Figure 2.5 shows the measured electric field dependence of the resistance of 100 nm layers of ion implanted Si:As, adapted from the published data of Gang *et al.* As in the studies of Grannan *et al.* and Zavaritskaya *et al.*, the conduction mechanism in the limit $F \rightarrow 0$ is $n = 1/2$ variable range hopping. Although Gang *et al.* do not analyze the weak field dependence of their data, we find that the data can be well described by Hill's prediction $R \propto (eFL/kT)/\sinh(eFL/kT)$ at fields below ~ 150 V/cm. At field strengths $F > 120$ V/cm the data are better described by the moderate field exponential dependence of the resistance on the applied field, as shown by the dashed line.

To our knowledge the prediction of Apsley and Hughes that the hopping conductivity in weak electric fields has a dependence $\ln [\sigma(F)/\sigma(F=0)] \propto F^2$ has not been observed experimentally.

2.1.3.2 Negative differential conductance

Aladashvili *et al.* [1989] have developed a model for non-Ohmic hopping conduction in the temperature range of saturation of the hopping conductivity. Over this temperature range the concentration of hopping electrons is a constant equal to the net impurity concentration. They find that in lightly doped semiconductors with very low compensation, the conductivity will decrease with increasing field before increasing exponentially with the field. This effect, known as negative differential conductance, has also been theoretically studied by Bottger and Bryksin [1979, 1980] for saturated hopping with a strong electron-phonon coupling. Negative differential conductance arises as follows: the resistance across a doped semiconductor can be modelled by a random resistor network between impurity sites. The most probable path that a hopping electron will follow is the path of minimum resistance. Under a small applied electric field the electron

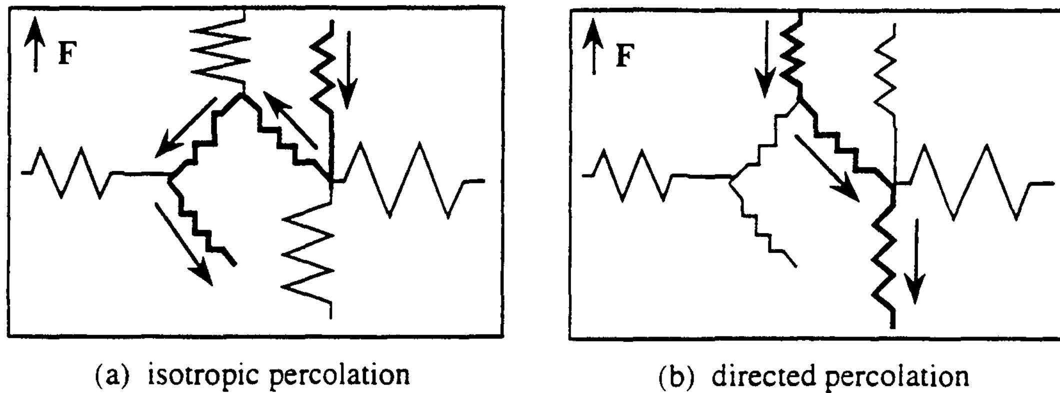

(a) isotropic percolation (b) directed percolation

Fig.2.6 The resistance across a doped semiconductor can be modelled by a random resistor network between impurity sites. The most probable path that a hopping electron will follow is the path of minimum resistance. Under a small applied electric field (a), the electron will hop isotropically. As the field is increased (b), the path of minimum resistance changes and the electron will hop along a path directed against the applied field.

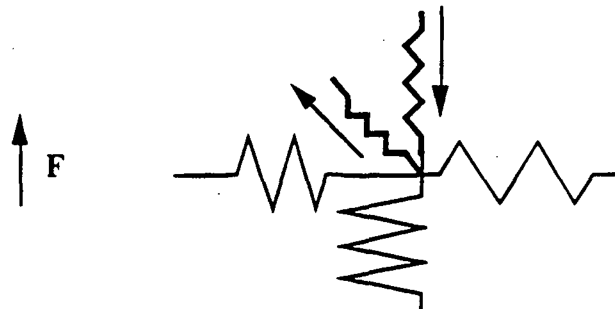

Fig. 2.7 The random resistor network has "dead ends" from which the probability of escaping is exponentially less than the probability of entering. For modest electric fields the hopping electron can only exit the dead end by the energetically unfavorable process of hopping in the direction of the applied field.

will hop isotropically, but as the field increases the path of minimum resistance changes and the electron will hop along a path directed primarily against the applied field. Therefore the conductivity undergoes a continuous transition from "isotropic" to "directed" percolation as shown in Figure 2.6. For saturated hopping conductivity in a semiconductor with very low compensation, during this transition a significant number of the hopping

electrons become captured by dead ends in the random resistor network as shown in Figure 2.7. When an electron leaves a dead end, it spends some time in a new dead end and so on. This phenomenon leads to a drop in the conductivity as the electric field increases because the trapped electrons do not contribute to the conductivity. As the electric field increases further, the bottlenecks in the random resistor network disappear and the conductivity rises exponentially with F. Negative differential conductance has been confirmed experimentally by Aladashvili *et al.* [1989], Aleshin and Shlimak [1987], Yakimov [1993], and Zabrodskii and Shlimak [1977].

2.1.3.3 Impurity conduction in moderate electric fields

In moderate fields $kT/eL < F < kT/e\zeta$ the conductivity is by directed percolation. Hill [1971] and Pollak and Reiss [1976] predict a conductivity of the form

$$\sigma(F,T) = \sigma(0,T)\exp(eFL/kT). \qquad (2.9)$$

where L is a length parameter related to the optimum hop length $R = (\zeta/2)(T_o/T)^n \sim T^{-n}$. The factor $\exp(eFL/kT)$ can be thought of as a Boltzmann factor and eFL can be thought of as the average energy gained by a hopping electron under an applied electric field. According to Hill, L = CR where C = 0.75. However, Pollak and Reiss find that C = 0.17. They predict a weaker dependence on field because their theoretical model includes the effect of correlations between neighboring pairs of resistances via the energy of the common site. Since $L \propto R$ in both theoretical models, L is predicted to vary with temperature as T^{-n}.

By considering the difference between "hard" and "soft" resistances in the percolation path, Shklovskii [1976] predicted a different moderate field behavior

$$j(F,T) = \sigma(T)\, F_c \exp\left(\frac{eFL}{kT}\right)^{\frac{1}{1+\nu}} . \qquad (2.10)$$

$$\sigma(F,T) \propto \exp\left(\frac{eFL}{kT}\right)^{\frac{1}{1+\nu}} . \qquad (2.11)$$

where $\nu \approx 0.9$ is the critical exponent of the correlation radius L of the critical hopping conduction subnetwork. Shklovskii's result arises from his consideration of the exponential scatter in the resistances $R_{ij} \sim \exp(\zeta_{ij})$ in the random resistor network which can be used to model the doped semiconductor. The quantities $\zeta_{ij} \gg 1$ are governed by the separations and energies of the impurity states. According to this model, in the limit $F \rightarrow 0$ the conductivity is dominated by resistances with values close to the percolation threshold $\zeta_c \equiv (T_0/T)^n$. These key resistances are relatively far apart and are linked by highly conducting chains of smaller resistances, creating an effective hopping conduction subnetwork. The drop in the electrochemical potential, related to the current, is governed by the voltage drop across the distances between the key resistances in the subnetwork. This length $L = R\zeta_c^{\nu}$ is much larger than the average hop length R and has a temperature dependence $L \sim T^{-(n+n\nu)}$.

In a later study by Levin and Shklovskii [1984], the field dependence of the conductivity was described by Equation 2.9 with $L = \alpha R\zeta_c$, where $\alpha \approx 10^{-2}$. This model may be distinguished from the theoretical models of Hill and Pollak and Reiss because the length parameter L is predicted to vary with temperature as T^{-2n} rather than as T^{-n}. We can therefore discriminate between various theories of non-Ohmic impurity conduction in moderate fields by measuring the temperature dependence of L.

We note that the prediction of Apsley and Hughes that the electrical conductivity varies with field as $\ln[\sigma(F)/\sigma(F{=}0)] \propto F^2/T^{2+n}$ is usually discussed as a prediction for moderate field behavior [Talamantes *et al.*, 1989]. However, due to their assumption of isotropic percolation their theory properly belongs to the weak field regime.

Although the models discussed above were developed for the case of $n = 1/4$ variable range hopping, corresponding to a constant density of states near the Fermi level, it has been suggested that the derivations of Equations 2.9, 2.10, and 2.11 should not depend on n [Aleshin and Shlimak, 1987]. Equation 2.9 has been experimentally observed for both $n = 1/4$ conduction and for $n = 1/2$ conduction, supporting this claim.

The exponential dependence of the conductivity on applied electric field has been observed in a large number of materials including amorphous $Ge_{1-x}Cu_x$ films [Aleshin and Shlimak, 1987], Ge bicrystals with a tilt angle $\theta \approx 8.5°$ [Zavaritskaya *et al.*, 1985], Ge:Ga [Grannan *et al.*, 1992; Kenny *et al.*, 1989], n-type ZnSe crystals [Timchenko *et al.*, 1981, 1989], n-Si:P [Ionov *et al.*, 1987; Rosenbaum *et al.*, 1980], n-Si and p-Si [Aladashvili *et al.*, 1989], n-GaAs [Redfield, 1975], and Si:As thin films [Gang *et al.*, 1989]. However, the dependence of L on temperature and impurity concentration has not been carefully studied and remains poorly understood.

The temperature dependence of L can be described as a power law $L \sim T^{-x}$ as discussed above. The following temperature exponents have been observed for $n = 1/2$ variable range hopping with a field dependence of the conductivity described by Equation 2.9. Aleshin and Shlimak [1987] observe the values $x = 0.8$ and $x = 1.3$. Kenny *et al.* [1989] find that $x > 0.5$. Ionov et al. observe a value $x = 0.9 \pm 0.2$. Grannan *et al.* [1992] observe the values $x = 0.99 \pm 0.03$ and $x = 1.01 \pm 0.04$. These experiments tend to support the theoretical model of Levin and Shklovskii [1984], which predicts that $x = 1$ for $n = 1/2$ VRH. However, the dependences $x = -3$ [Zavaritskaya *et al.*, 1985], $x = 0.5$ [Timchenko *et al.*, 1989], and $x = 0$ [Rosenbaum *et al.*, 1980] have also been observed. In a study of the non-Ohmic behavior of ZnSe crystals, Timchenko *et al.* [1981] observe the value $x = 0.5$ when $F > 20$ V/cm and $x = 0.8$ when $F < 20$ V/cm.

The dependence of L on the net impurity concentration is also controversial. Some authors [Grannan *et al.*, 1992; Timchenko *et al.*, 1981; Aleshin and Shlimak, 1987] find that L decreases as N increases. This is expected because as the impurity concentration increases, the average separation between impurity sites decreases. However, others observe that L increases with increasing N [Kenny *et al.*, 1989; Zabrodskii and Shlimak, 1977]. In the study of Aladashvili *et al.* [1989], the length parameter L was found to be nearly independent of impurity concentration over the range 3×10^{17} cm^{-3} $\leq N \leq 23 \times 10^{17}$ cm^{-3}. Gang *et al.* [1989] also observe that L is a weak function of N. Finally, Timchenko

et al. [1989] observe widely different values of L as a function of impurity concentration, but the dependence L(N) seems to be completely random and does not monotonically increase or decrease.

In Chapters 3 and 4, we will discuss possible explanations for the conflicting observations of the dependence of L on temperature and impurity concentration.

2.1.3.4 Impurity conduction in strong electric fields

In strong electric fields $F > kT/e\zeta$, theoretical models predict that the conduction becomes "activationless," meaning that the electrons participating in hops acquire the energy necessary for executing a hop not from thermal activation but from the electric field. In this case the conductivity is independent of temperature and increases with increasing electric field as

$$\sigma(F) \sim \exp(-F_o/F)^N, \tag{2.12}$$

where the power exponent N is equal to the power exponent n for the ohmic conductivity. Equation 2.12 was first derived by Shklovskii [1973] for the case of n = 1/4 variable range hopping and was derived by Rentzsch *et al.* [1979] for an arbitrary value of n.

Following Rentzsche *et al.*, we derive Equation 2.12 using an analysis similar to that used in Chapter 1 to determine the exponent n for variable range hopping in the limit $F \to 0$. Assuming that the density of states near the Fermi level varies with energy as $g(E) = N_0|E|^x$, then variable range hopping takes place over a concentration of impurity states

$$N \sim 2\int_0^{|E|} \varepsilon^x \, d\varepsilon = \frac{2}{x+1} E^{x+1} . \tag{2.13}$$

The average hopping distance can be estimated by

$$R \approx N^{-1/3} \sim E^{-(x+1)/3} . \tag{2.14}$$

Since the hopping electrons gain energy from the electric field F rather than by thermal activation, $E \approx eFR$. The hopping distance can therefore be rewritten as

$$R \sim F^{-(x+1)/(x+4)} . \quad (2.15)$$

Since the current $j \sim \exp(-R/\zeta)$ we find that

$$j \sim \exp\left[-\left(\frac{F_o}{F}\right)\right]^{(x+1)/(x+4)} . \quad (2.16)$$

Therefore the strong field exponent N is equal to the hopping exponent $n = (x+1)/(x+4)$.

Activationless hopping conductivity has been observed experimentally, with most authors finding that n = N over a wide range of temperatures in a variety of materials. In a study of hopping between deep levels in Ge:Zn, Aleinikov *et al.* found that N = 1/4 when n = 1/4. The relation N = 1/2 when n = 1/2 has been observed in amorphous Si<Mn> by Dvurechenskii et al. [1988], in n-GaAs by Tremblay *et al.* [1989], and in Ge bicrystals with a tilt angle $\theta \approx 8.5^\circ$ by Zavaritskaya *et al.* [1985]. Rentzsch *et al.* [1979] studied the high field dependence of the conductivity of ZnSe films and found that for n = 0.6 - 0.8, N = 0.6 - 0.8.

In two-dimensional films with a constant density of states near the Fermi level, the conductivity is described by n = 1/3 VRH. Thus n = 1/3 VRH in two dimensions is analogous to n = 1/4 VRH in three dimensions. The relation n = N was also confirmed by Faran and Ovadyahu [1988], who studied the strong field behavior of polycrystalline In_2O_{3-x} films and observed that when n = 1/4, N = 1/4 and when n = 1/3, N = 1/3. In a later study, Shahar and Ovadyahu [1990] examined the strong field behavior of polycrystalline In_2O_{3-x} films as a function of film thickness. They found that under an applied field the I-V curves showed an inflection point between the field dependence exponent N = 1/3 and N = 1/4, which they attribute to a dimensional crossover induced by the electric field.

An anomalous strong field behavior N = 1/4 when n = 1/2 was observed by Aleshin and Shlimak [1987] in a study of amorphous $Ge_{1-x}Cu_x$ films. van der Heijden *et al.* [1992] also observed the relation N = 1/4 when $n \geq 1/2$ in ion-implanted Si:As. In both

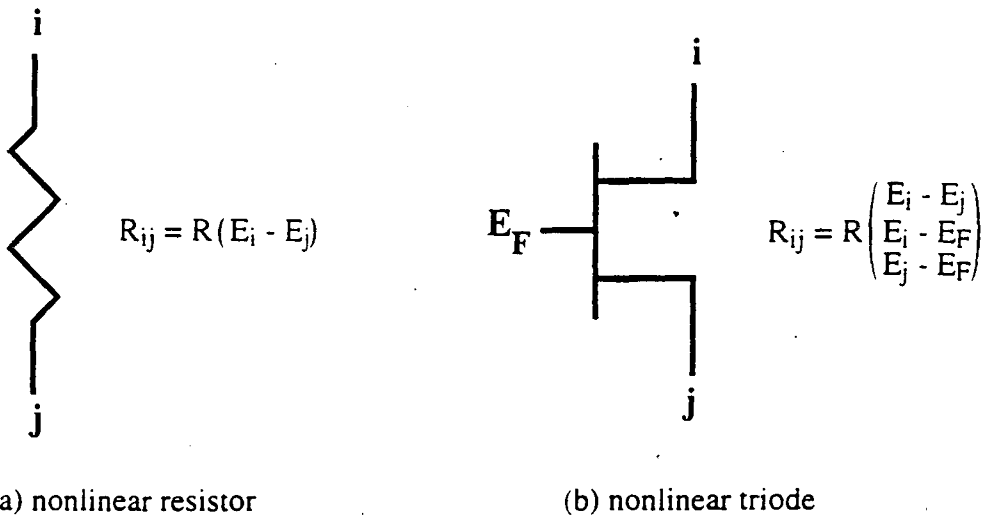

Fig. 2.8 As the impurity concentration increases, the doped semiconductor is modelled by a network of nonlinear triodes rather than by a network of nonlinear resistors.

studies, the impurity concentration was near the critical concentration for a metal-insulator transition. The observed field dependences are in conflict with the theoretical model and imply that a strong electric field is not equivalent to a high temperature as N approaches N_c.

2.1.3.5 Non-ohmic impurity conduction in moderately and heavily doped semiconductors

The theories of non-Ohmic impurity conduction described above assume a lightly doped semiconductor and neglect Coulomb interactions between impurities. As the impurity concentration increases and approaches the critical concentration for a metal insulator transition, a constant localization radius can no longer be assumed throughout the impurity band. The doped semiconductor must be then modelled by a network of nonlinear triodes rather than a network of nonlinear resistors [Bottger and Bryksin, 1985] as shown in Figure 2.8. In other works, the transition rate between impurity sites i and j depends not only on the energy difference $E_i - E_j$, but also on the quantities E_i and E_j relative to the Fermi level E_F. As N approaches N_c the effects of electron-electron interactions, the

variation of localization throughout the impurity band, and the influence of the applied electric field on the impurity wavefunctions may become important.

The few experimental studies of non-Ohmic behavior in moderate electric fields in moderately and heavily doped semiconductors [Gang *et al.*, 1989; Matveev and Lonchakov, 1993; Rosenbaum *et al.*, 1980] typically analyzed the data according to Equation 2.9 which is derived for a lightly doped semiconductor, rather than used the data to test whether this expression remains valid. It is plausible that at impurity concentrations such that carriers are no longer localized at individual impurities, a different field dependence should apply because Anderson localization cannot be assumed throughout the impurity band and L may no longer be well-defined. Non-Ohmic conductivity studies at higher impurity concentrations can conceivably provide an exciting probe of impurity localization, the position of the mobility edge in the impurity band, and the metal-insulator transition. In Chapter 3 we explore the weak and moderate electric field dependence of σ as N approaches N_c.

2.1.3.6 Summary of non-Ohmic impurity conduction in doped semiconductors

In summary, for sufficiently low electric fields $E < kT/eL$ the hopping conductivity in a lightly doped semiconductor is predicted to be nearly independent of the applied field. In moderate electric fields, $kT/eL < E < kT/e\zeta$ where $\zeta \approx 39$ Å for an isolated As impurity in Ge, the theoretical models predict a conductivity of the form $\sigma(F,T) = \sigma(0,T)\times\exp(eFL/kT)$ where the factor eEL may be thought of as the energy gain due to the electric field. Experimental studies of lightly doped semiconductors show that this form of $\sigma(F,T)$ describes the moderate field data very well and can be used to study the temperature dependence of the length parameter L. For nearest neighbor hopping conduction L is constant, thus σ varies with E and T as $ln\,[\sigma(F,T)/\sigma(0,T)] \propto F\times T^{-1}$. For VRH conduction with an exponent n, $L \propto T^{-n}$ according to the models of Hill [1971] and Pollak and Reiss

Reference	Regime	A(T)	x
Apsley and Hughes [1974]	weak fields	C_1/T^{2+n}	2
Hill [1971]	moderate fields	C_2/T^{1+n}	1
Pollak and Reiss [1976]	moderate fields	C_3/T^{1+n}	1
Shklovskii [1976]	moderate fields	$C_4/T^{1+n+\nu n}$	$1/(1+\nu)$
Levin and Shklovskii [1984]	moderate fields	C_5/T^{1+2n}	1
Shklovskii [1973]	strong fields	C_6	-n
Rentzsch *et al.* [1979]	strong fields	C_6	-n
Frenkel [1938]	Poole-Frenkel	C_7/T	1/2

Table 2.1 Theoretical predictions for the electric field dependence of the conductivity at various electric field strengths. The parameters A and x are defined in Equation 2.17. C_1 -C_7 are numerical constants. The parameter n is the temperature exponent of the variable range hopping conductivity and is typically 1/4 (constant density of states at the Fermi level) or 1/2 (parabolic density of states at the Fermi level). The parameter $\nu \approx 0.9$ is the critical exponent of the correlation radius L of the critical hopping conduction subnetwork and is defined in Section 2.1.3.3.

[1976], and $L \propto T^{-2n}$ according to the model of Levin and Shklovskii [1984]. The dependence of L on temperature and impurity concentration has not yet been established experimentally. In very high electric fields the transport becomes field-assisted rather than phonon-assisted: this activationless regime has been studied experimentally and agrees well with the theory. As yet no separate model for non-Ohmic phonon-assisted impurity conduction at higher doping concentrations has been developed.

We can define a generic fitting for the non-Ohmic impurity conductivity [Bottger and Bryksin, 1985,

$$\sigma(F,T) = \sigma(0,T) \exp\left[AF^x \right] . \qquad (2.17)$$

When ln σ is plotted as a function of F, A is a measure of the slope and x is a measure of the curvature. Table 2.1 summarizes the various theories of non-Ohmic impurity conduction using Equation 2.17.

2.2 Contact effects

Contact resistances between different materials arise from contact barriers, which in turn arise from space charges. Space charges are always present at interfaces between materials of different conductivity. This may be seen from Poisson's relationship, since the bulk electric fields differ and a space charge must reside wherever the field changes. In that sense, there can be no such thing as an "Ohmic contact," even between two different metals. In practice, the resistive consequence arising from such interfaces can be very small.

Contact barriers can arise in two different ways: (a) through differences in the thermionic work functions of the two contacting materials, and (b) through the action of surface states. When a metal and a semiconductor are brought into contact, a barrier arises known as the "Schottky barrier." The books of Henisch [1984] and Rhoderick [1978] are useful general references on semiconductor contacts and metal-semiconductor contacts from which we have drawn the following discussion of Schottky barriers and Ohmic contacts.

2.2.1 The Schottky barrier

We begin with some preliminary definitions. The work function φ_m of a metal is the amount of energy required to raise an electron from the Fermi level to a state of rest outside the surface of the metal. As with a metal, the work function φ_s of a semiconductor is the difference in energy between the Fermi level and the energy of an electron at rest outside the surface. Another important surface parameter of a semiconductor is the electron affinity χ_s. This is the difference in energy between an electron at the bottom of the conduction band and an electron at rest outside the surface. If the bands are flat (i.e. there is no electric field inside the semiconductor), χ_s and φ_s are related by

$$\varphi_s = \chi_s + \xi \tag{2.18}$$

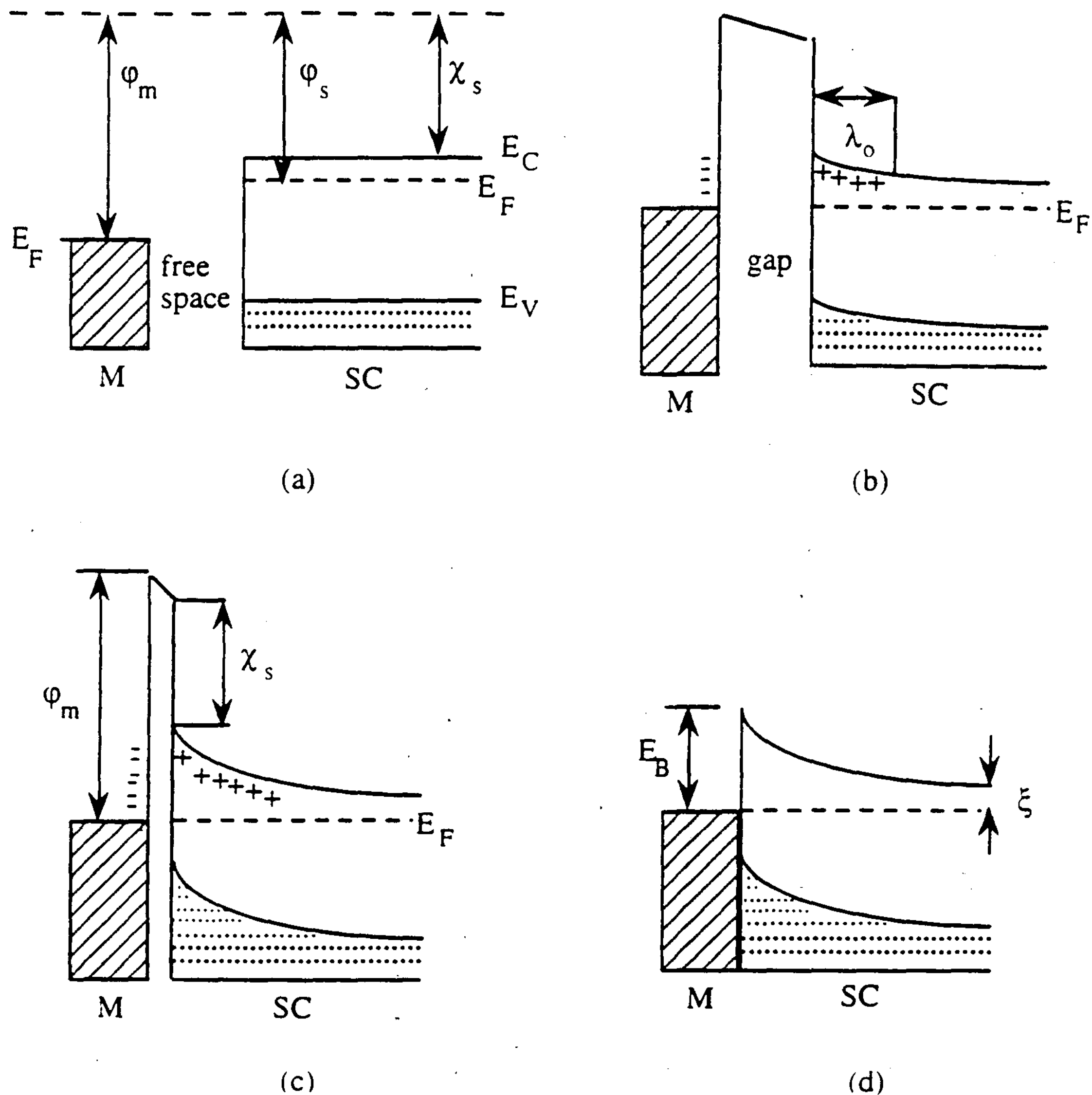

Fig. 2.9 Formation of a Schottky barrier between a metal and a semiconductor (a) not yet in contact; (b) separated by a gap with an electrical contact so that the Fermi levels are in coincidence; (c) separated by a narrow gap; and (d) in perfect contact. The plus signs denote positively charged donor ions; the minus signs denote electron charge accumulation at the surface of the metal. Other symbols are defined in Section 2.2.1.

where ξ is the energy difference between the Fermi level and the bottom of the conduction band.

To see how a barrier is formed when a metal and a semiconductor are brought into contact, we perform the following thought experiment. Suppose that the metal and semiconductor are both electrically neutral and are separated from each other. The energy band diagram is shown in Figure 2.9(a) for an n-type semiconductor with a work function less than that of the metal. The assumption that $\varphi_s < \varphi_m$ is usually true; when $\varphi_s > \varphi_m$ for an n-type semiconductor the contact is known as an Ohmic contact (see Section 2.2.2) and the Schottky barrier does not form.

If the metal and semiconductor are connected electrically by a wire, electrons pass from the semiconductor into the metal until electronic equilibrium is established and the Fermi levels of the two materials come into coincidence as shown in Figure 2.9(b). Relative to the Fermi level in the semiconductor, the Fermi level in the metal must rise by an amount equal to the difference between the two work functions on thermodynamic grounds. The energies of electrons at rest outside the surfaces of the two solids are no longer the same, and there is an electric field in the gap between the two materials. There must be a negative charge on the surface of the metal balanced by a positive charge in the semiconductor. The charge on the surface of the metal consists simply of extra conduction electrons contained within the Thomas-Fermi screening distance ($\approx$ 0.5 Å). Since the semiconductor is n-type, the positive charge will be provided by conduction electrons receding from the surface leaving uncompensated positive donor ions in a region depleted of electrons. Because the donor concentration N_D is many orders of magnitude less than the electron concentration in a metal, the uncompensated donors are distributed over a region with screening length λ_0 known as the depletion layer and the bands in the semiconductor are bent upwards.

When the two surfaces are allowed to approach each other as shown in Figure 2.9(c) the capacitance of the system increases at constant voltage. Accordingly, an increasing negative charge is built up on the surface of the metal and an opposite positive charge continues to build up on the surface of the semiconductor until the two materials are

finally brought into contact as shown in Figure 2.9(d). The final barrier height E_B relative to the Fermi level is given by

$$E_B = \varphi_m - \chi_s. \tag{2.19}$$

Electrical conduction across the Shottky barrier can occur by thermionic emission, thermionic-field emission, and field emission (tunneling). At sufficiently high temperatures virtually all of the electrons have enough thermal energy to go over the top of the barrier; this process is known as thermionic emission over the barrier. At lower temperatures, electrons can penetrate the barrier by a combination of quantum mechanical tunneling through the barrier and thermal excitation over the barrier; this intermediate regime is known as thermionic-field emission. At very low temperatures the dominant electron current arises from the tunneling of electrons with energies close to the Fermi energy. This process is known as field emission.

It is useful to define a characteristic energy parameter E_{oo} (using the nomenclature of Padovani and Stratton [1966]) which plays an important role in tunneling theory and is defined as

$$E_{oo} = \frac{h}{4\pi}\left[\frac{N_D}{m^*\varepsilon}\right]^{1/2}, \tag{2.20}$$

where N_D is the donor concentration, m^* is the effective mass of electrons in the semiconductor, and ε is the dielectric constant in the semiconductor. The dominant mechanism for electron conduction across the Schottky barrier has been discussed by Yu [1970]. Yu finds that the contact resistance R_c is determined predominantly by the factors

$\exp(E_B/E_{oo})$	for field emission ($E_{oo}/kT \gg 1$)
$\exp\{E_B/E_{oo} \coth(E_{oo}/kT)\}$	for thermionic field emission ($E_{oo}/kT \sim 1$)
$\exp(E_B/kT)$	for thermionic emission ($E_{oo}/kT \ll 1$).

For lightly doped materials and/or at high temperatures the dominant conduction process is thermionic emission. Therefore R_c is independent of the donor concentration and varies

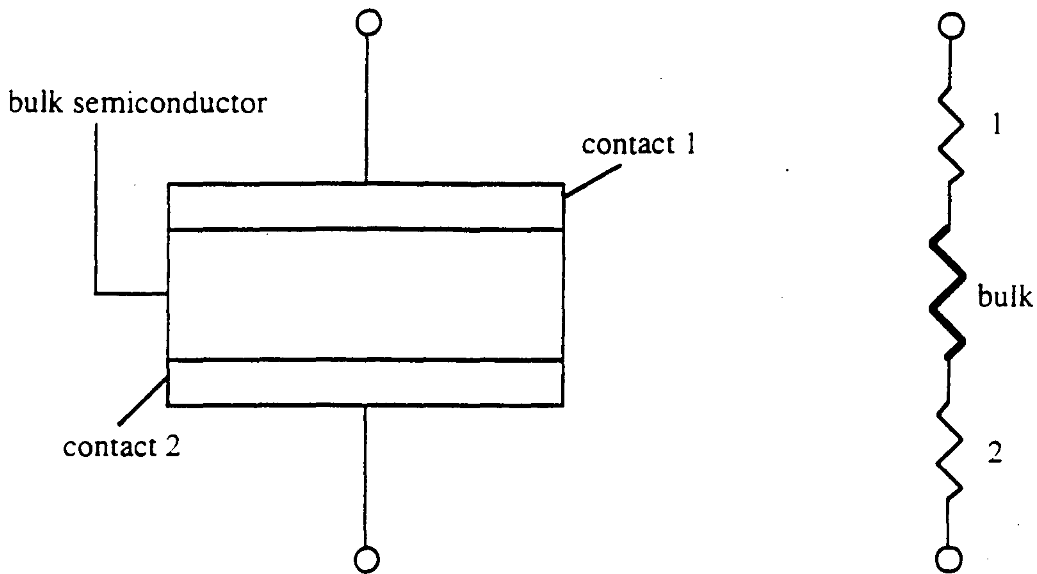

Fig. 2.10 An Ohmic contact to a semiconductor is one for which the current-voltage characteristic is determined by the resistivity of the semiconductor, rather than by the characteristics of the contact. The contact resistances should be very small compared to the resistance of the bulk semiconductor.

exponentially with the inverse temperature. For heavily doped materials and/or at low temperatures, the dominant conduction process is field emission. In this case ln R_c is proportional to $N_D^{-1/2}$ and R_c is independent of temperature.

We have considered the case of a metal-n-type-semiconductor contact for which the work function of the metal is greater than the work function of the semiconductor. We have shown that the resulting energy contour corresponds to a Schottky barrier. If instead the work function of the metal is smaller than that of the n-type semiconductor, the conduction and valence bands bend down at the interface. An electron accumulation layer forms in the semiconductor over a distance λ_0 from the contact interface. This accumulation layer is distinguished from the depletion layer discussed for the Schottky barrier because it serves as an electron reservoir.

2.2.2 Ohmic contacts

Semiconducting samples and devices require low resistance contacts to which electrical connections can be made. Low resistance contacts on semiconductors are usually (somewhat misleadingly) referred to as "Ohmic contacts." An Ohmic contact to a semiconductor is one for which the current-voltage characteristic is determined by the resistivity of the semiconductor, rather than by the characteristics of the contact. It is not essential that the current-voltage characteristic of the contact itself is linear, provided that its resistance is very small compared to the resistance of the semiconductor as shown in Figure 2.10. In principle, such contacts can be made by using a metal with a work function less than the work function of an n-type semiconductor or greater than the work function of a p-type semiconductor because the accumulation layer will serve as a charge carrier reservoir. In practice, however, there are very few metal-semiconductor combinations which satisfy this condition.

The vast majority of Ohmic contacts are formed by placing a thin layer of very heavily doped semiconductor between the metal and semiconductor regions as shown in Figure 2.11. The boundary layer is doped with extra donors (n+) for an n-type semiconductor or with extra acceptors (p+) when dealing with a p-type material, and simulates an accumulation layer. The depletion region is then so thin that field emission takes place and the contact has a very low resistance. A number of recipes for producing this type of Ohmic contact are given by Schwartz [1969].

2.2.3 Contact resistance for the samples studied in this work

We assume throughout this thesis that the samples studied in this work do not have any significant contact resistance compared to the resistance of the bulk semiconductor. The following theoretical and experimental arguments lead us to believe that the contact resistances to our samples are negligible.

(1) Values of the characteristic energy parameter E_{00} as a function of N_D for various semiconductors are listed in Rhoderick [1978]. For Ge with a donor concentration

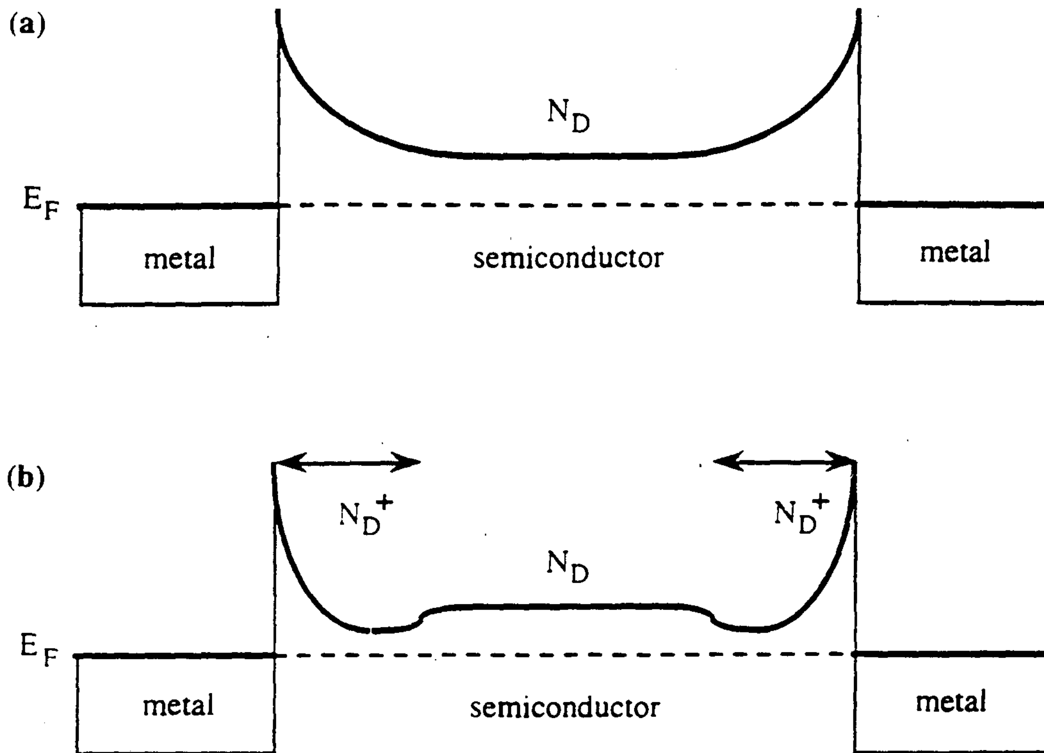

Fig. 2.11 Formation of a low resistance contact by additional doping. (a) Metal-semiconductor-metal device with two Schottky barriers; (b) the same with an additional boundary layer of heavily doped n-type semiconductor material between the metal-semiconductor contacts. The additional doping thins the depletion layer and simulates an accumulation layer which serves as a free carrier reservoir.

of 4×10^{16} cm^{-3}, typical of samples studied in this work, $E_{00} \approx 2.5$ meV. Even if our samples did not have a thin layer of very heavily doped semiconductor between the metal-sample contact, at temperatures $T \ll 30$ K for which $E_{00}/kT \gg 1$ field emission would dominate the contact resistance. The samples studied in this work have been doubly ion-implanted to produce very low resistance metal/n+/n and metal/p+/p contacts. The contacting procedure is described in Section 3.2.3. These contacts are very heavily doped with cross-sectional impurity concentrations of ~ 5×10^{14} cm^{-2} over regions of ~ 2000 Å. Thus in the contact region the net impurity concentration is > 10^{21} cm^{-3} and the energy parameter E_{00} will be correspondingly small [Rhoderick, 1978]. For the samples

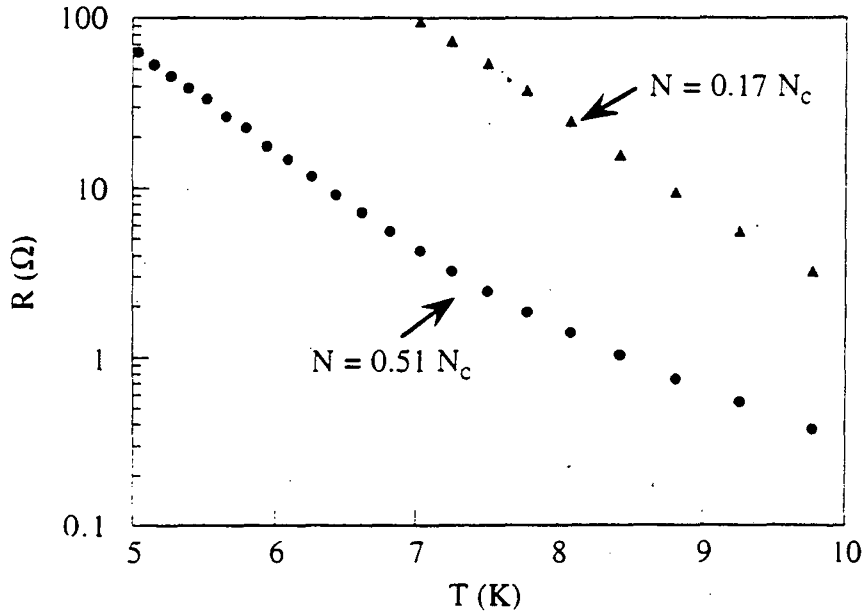

Fig.2.12 Measured temperature dependence of the resistance of the two $^{74}Ge:As$ samples studied in this work at $T > 5$ K. As described in the text, the smallest measured sample resistance can be used to place an upper limit on the contact resistance R_c when R_c is determined by field emission across the contact barrier.

studied in this work we expect field emission (tunneling) to dominate the contact resistance when $T < 300$ K. All measurements of the non-Ohmic behavior of the samples discussed in this thesis were made at $T < 1.8$ K.

Since field emission produces a temperature-independent resistance, for the samples studied in this work the contact resistance R_c is a constant at small electric fields. The temperature dependence of the sample resistance R_s is therefore given by

$$R_s(T) = R_c + R_b(T), \tag{2.21}$$

where R_b is the bulk resistance. The measured sample resistance R_s at any temperature below 300 K can be used to place an upper bound on the contact resistance.

At temperatures between 4 K and 10 K, the samples studied in this work have measured resistances < 10 Ω as shown in Figure 2.12. We conclude that $R_c < 10\ \Omega$. Since measurements of the non-Ohmic conduction properties require sample resistances $R_s > 1\ \mathrm{M}\Omega$ in order to avoid sample heating, the contact resistance is at least five orders of magnitude smaller than the studied resistances. From the above theoretical argument, we conclude that contact resistances are completely negligible in this work.

(2) In addition, we performed a four-probe measurement of the sample resistance for a ^{70}Ge:Ga sample with $N = 0.5\ N_c$ using the sample geometry shown in Figure 2.13(a). This geometry allows a direct measurement of R_c. However, we were unable to determine R_c because it was less than our 1% measurement error over the measured temperature range $0.6\ \mathrm{K} < T < 1.6\ \mathrm{K}$ corresponding to a range in resistance $10\ \mathrm{k}\Omega < R < 10\ \mathrm{M}\Omega$. Making the assumption that the contact resistance is determined by field emission (tunneling) across the contact barrier and is temperature independent, we conclude that $R_c < 100\ \Omega$. Thus the experimentally determined contact resistance is at least four orders of magnitude smaller than the sample resistances in our study of non-Ohmic impurity conduction.

All of the data presented in this thesis were measured using the sample geometry shown in Figure 2.13(b). This geometry provides a uniform electric field across the sample but does not allow a measurement of the contact resistance. Since the contacting technique is identical for the two geometries shown in Figure 2.13, we believe that the contact resistances of the samples studied in this work are negligible.

(3) Under an applied electric field F, the resistance change is given by $\Delta R_s = R_s(F=0) - R_s(F)$. For typical values of F studied in this work, ΔR_s is between 100 kΩ and 100 MΩ. The maximum resistance drop across the contacts is $\Delta R_c < 10\ \Omega$ by argument (1) and $\Delta R_c < 100\ \Omega$ by argument (2). Therefore, the effect of F on the contact resistance must be completely negligible compared to the effect of F on the bulk resistance.

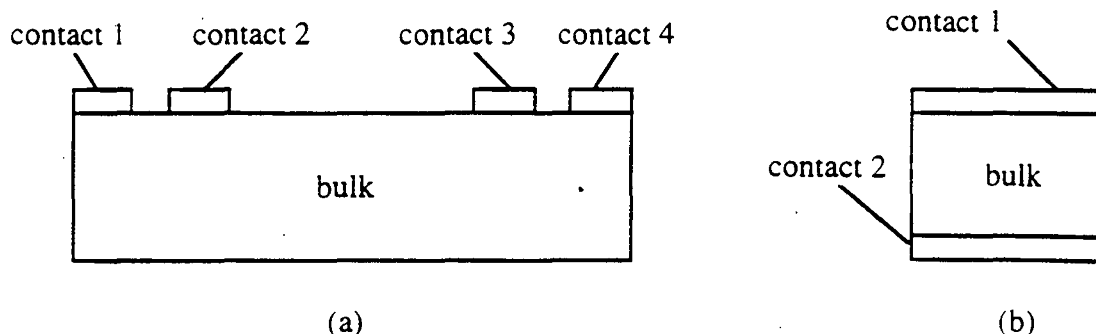

Fig.2.13 Diagram (a) shows the sample geometry used to perform a four-probe measurement of the contact resistance. Diagram (b) shows the sample geometry used for studies of non-Ohmic impurity conduction. The second geometry allows a uniform electric field to be applied across the sample.

2.3 Hot electron effects

The resistance R of a doped semiconductor decreases with increasing electric field strength as discussed in Section 2.1. R also decreases with increasing electron temperature. Under certain conditions, an electric field applied across a conducting material can raise the electron temperature significantly above the phonon temperature. It can therefore be difficult to distinguish between non-Ohmic effects and "hot electron" effects. We first review the general theory of hot electron effects. We then investigate the consequences for non-Ohmic conductivity in metals and doped semiconductors. To our knowledge this is the first detailed discussion of the implications of hot electron effects for conduction in doped semiconductors.

2.3.1 Definition of the hot electron regime

We can regard a conducting material as a thermodynamic system which is composed of two subsystems, the electron and the phonon, which are coupled by the electron-phonon interaction [Wellstood *et al.*, 1988]. If we suppose that the conducting material is connected to a thermal reservoir, the phonon subsystem itself can further

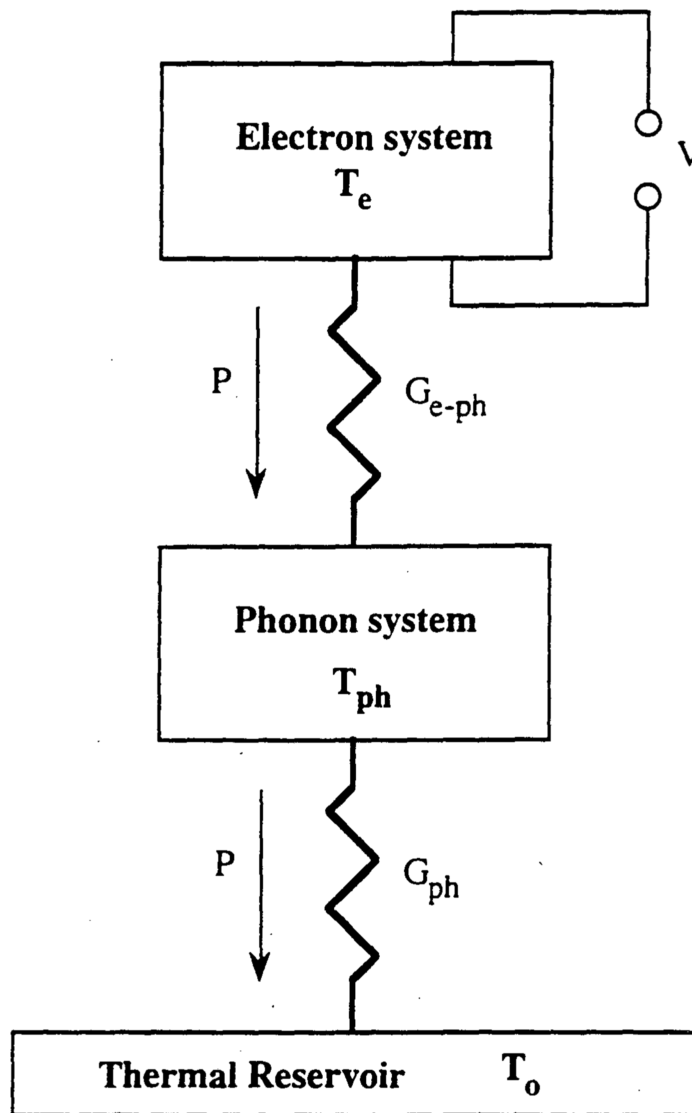

Fig. 2.14 Thermal model for the theory of hot electron behavior. Electrical power P = IV is applied to an electron system, which is coupled to a phonon system through a thermal conductance $G_{e\text{-}ph}$. The phonons are connected to a thermal reservoir at temperature T_0 by a thermal conductance G_{ph}.

subdivided into two parts: phonons in the conducting material and phonons in the thermal reservoir (see Figure 2.14). When an electric field F is applied across a conducting material with free charge carriers, the velocity distribution of the carriers is modified leading to an increase of their mean energy above the thermal equilibrium value. This condition is usually called the "hot electron regime" because a Boltzmann-like distribution

function with a characteristic electron temperature T_e can be introduced to describe the increase of the carrier mean energy:

$$f(E) = \exp\left[\frac{E - E_F}{kT_e}\right], \tag{2.22}$$

where E is the electron energy relative to the Fermi energy E_F.

When power $P = IV$ is dissipated in the electron system, its temperature T_e rises above that of the phonon system T_{ph}, which in turn is higher than the thermal reservoir temperature T_o. The power balance equation requires that

$$P = IV = G_{e\text{-}ph}\,(T_e - T_{ph}) = G_{ph}\,(T_{ph} - T_o), \tag{2.23}$$

where $G_{e\text{-}ph}$ is the average thermal conductivity between the electron system and the phonon system, and G_{ph} is the average thermal conductivity between the phonon system and the thermal reservoir.

2.3.2 Hot electron effects in metals

At room temperature, the thermal resistance between the electrons and the phonons in a metal is extremely small, so that even when a large power is dissipated in the metal only an immeasurably small temperature difference is generated. For example, a power dissipation of 50 W in a 1 mm^3 volume of Cu at 300 K would produce an electron-phonon temperature difference of approximately 50 nK [Wellstood et al., 1994]. However, at temperatures below a few hundred millikelvin the thermal resistance between the electrons and phonons is greatly increased, and it is possible to drive the electrons far out of thermal equilibrium with the phonons [Roukes *et al.*, 1985]. The theory of the hot electron effect in metals has been summarized by Wellstood *et al.* [1994].

We present a simple derivation for the electron temperature in a metal. We obtain the same expression that is found with a more detailed derivation to within a small

numerical factor. We assume that the electronic heat capacity per unit volume, C_e, scales linearly with temperature as

$$C_e = \gamma T_e. \tag{2.24}$$

The constant, γ, is a characteristic of the metal [Kittel, 1986] and is given by

$$\gamma = \pi^2 D(E_F) k^2 / 3\Omega, \tag{2.25}$$

where $D(E_F)$ is the density of states at the Fermi level and Ω is the volume of the metal. We also assume that the electron-phonon scattering rate τ^{-1} scales with temperature [Ghantmaker, 1974] as

$$\tau^{-1} = \alpha^* T_e^3. \tag{2.26}$$

The constant α^* is a thermally averaged electron-phonon scattering rate given by

$$\alpha^* = \frac{48\xi(3)\pi^3 k_B^3}{\mu (h v_s)^4 v_F} \left(\frac{2E_F}{3} \right)^2, \tag{2.27}$$

where $\xi(n)$ is the Riemann zeta function, μ is the mass density per unit volume of the metal, v_s is the velocity of sound, v_F is the Fermi velocity, and E_F is the Fermi energy. Ghantmaker and Gasparov [1973] have confirmed the T^3 dependence of the electron-phonon scattering rate in pure samples of Cu and Ag using the radio frequency size effect.

Using the above expressions for C_e and τ^{-1} we find that the thermal conductance between the electron-phonon systems is

$$G_{el\text{-}ph} \approx \frac{\Omega C_e}{\tau} = \Omega \gamma \alpha^* T_e^4 . \tag{2.28}$$

We can then obtain the following simple expression for the net rate at which an electron gas in a metal transfers energy to the phonons:

$$P = \int G_{el\text{-}ph}\, dT \approx \frac{\Omega \gamma \alpha^*}{5} \left(T_e^5 - T_{ph}^5 \right) . \tag{2.29}$$

This simple derivation gives the same result for P that is obtained by the more detailed derivation of Wellstood et al. [1994] to within a constant factor of about 2.5.

Arai [1983] demonstrated theoretically that an electron gas achieves a well-defined temperature T_e when it is electrically heated and that this temperature can be determined by measuring the Nyquist voltage noise e_n:

$$e_n = \sqrt{4kT_eR} \, . \tag{2.30}$$

Experimentally, hot electron effects in metals have been established by measuring white voltage noise levels in thin films at millikelvin temperatures and comparing the value T_e deduced from the noise level with the value T_{ph} measured independently [Roukes *et al.*, 1985; Wellstood *et al.*, 1989]. The excess noise in thin metal films at dilution refrigerator temperatures is of practical interest, because hot electron effects can substantially limit the sensitivity that can be achieved by thin film dc Superconducting Quantum Interference Devices (SQUIDS) [Wellstood *et al.*, 1994].

Under an applied electric field, the conductivity $\sigma(T)$ of a metal can be written as $\sigma(T_e)$ where T_e is a function of F. However, because the conductivity of a typical metal is an extremely weak function of temperature, hot electron effects in most metallic conductors do not lead to significant non-Ohmic behavior. An exception to this statement is electron conduction in doped semiconductors on the metallic side of the metal-insulator transition. The field dependent conductivity of a disordered metal [Anderson *et al.*, 1979; McMillan, 1981; Osofsky *et al.*, 1988] can be described by a hot electron model as

$$\begin{aligned} \sigma(F) &= \sigma(T) + AF^{1/3} \, , \\ \sigma(T) &= \sigma_0 + \sigma_1 T^{1/2} \, , \end{aligned} \tag{2.31}$$

where A, σ_0, and σ_1 are material-dependent constants.

2.3.3 Hot electron effects in semiconductors

2.3.3.1 Hot electron effects and ε_1 impurity conduction

Hot electron effects arising from free carriers in the conduction band are well known in semiconductors (for a review, see Sze [1981]). In doped semiconductors, free carrier impurity conduction occurs when electrons are thermally excited from localized

impurity states to the conduction band (ε_1 conduction). Because the carrier concentration is much smaller than in a metal, each electron receives proportionately much more energy for a given input power and the electron temperature is correspondingly increased. In other words, the small number of charge carriers leads to a small thermal conduction between the electron-phonon system.

The conductivity as a function of electric field F can be written as

$$\sigma(F) = n(F) \cdot e \cdot \mu(F), \tag{2.32}$$

where n(F) is the free carrier concentration as a function of electric field, $\mu(F) = v_d(F)/F$ is the carrier mobility, and $v_d(F)$ is the free carrier drift velocity. The effect of an electric field on the ε_1 conductivity is therefore two-fold. First, n(F) increases with increasing electric field due to the reduction in the impurity potential caused by F. This is the Poole-Frenkel effect as discussed in Section 2.1.1. Secondly, the mean free carrier velocity $v_d(F)$ is determined by a Boltzmann-like distribution function with a characteristic temperature T_e rather than T_{ph}.

2.3.3.2 Hot electron effects and hopping conduction

One of the unstated assumptions made in deriving the electric field dependence of the hopping conductivity is that the electron-phonon coupling is sufficiently strong that we need not distinguish between T_{ph}, the phonon temperature, and T_e, the electron temperature. At very low temperatures ($T < 50$ mK) this assumption may no longer be valid and some groups [Wang *et al.*,] claim to have seen a hot electron effect for hopping conduction in doped semiconductors similar to that seen in metals and in semiconductors for conduction by free electrons in the conduction band. It is not obvious how to define an electron temperature for localized electron states, since electron-electron interactions are weak and each hop between localized states requires the absorption or emission of a phonon. In contrast, free electrons have a strong electron-electron interaction and can accelerate under an applied electric field until emitting or scattering phonons.

Because of these difficulties, as yet no theory of a hot electron effect for hopping conduction between localized states near the Fermi level exists. However, Shklovskii et al. [1990] have studied the properties of the intermediate conduction regime between hopping conduction and band conduction for an amorphous semiconductor. This intermediate regime corresponds to hopping in the conduction band tail.

Transport properties of amorphous semiconductors, as opposed to doped semiconductors, are dominated by the disorder-induced density of localized states in the gap between the conduction and valence bands. The standard assumption about the density of states is that it decays exponentially with energy (where energy is measured from the band edge into the gap, i.e., deeper states have higher energies),

$$g(E) = \frac{N}{\varepsilon_0} \exp\left(- \frac{E}{\varepsilon_0}\right) , \tag{2.33}$$

where N is the total concentration of states in the tail and ε_0 is a characteristic decay energy much smaller than the Fermi energy E_F. Under these assumptions, Shklovskii *et al.* [1990] find that at $T = 0$ a strong electric field F creates a Boltzmann-like distribution function with an effective electron temperature $T_e = eFa/2k_B$ where a is the localization radius. Marianer and Shklovskii [1992] studied the same problem numerically for $T > 0$ and found a Boltzmann distribution function with an effective electron temperature described phenomenologically by

$$T_e^2(T,F) = T^2 + (0.67eFa/k_B)^2. \tag{2.34}$$

As shown in Figure 2.15, the exponential growth of the density of states plays an important role in the field dependence of the electron temperature because as the electric field increases a much higher density of shallower localized states is available for the electrons to hop into.

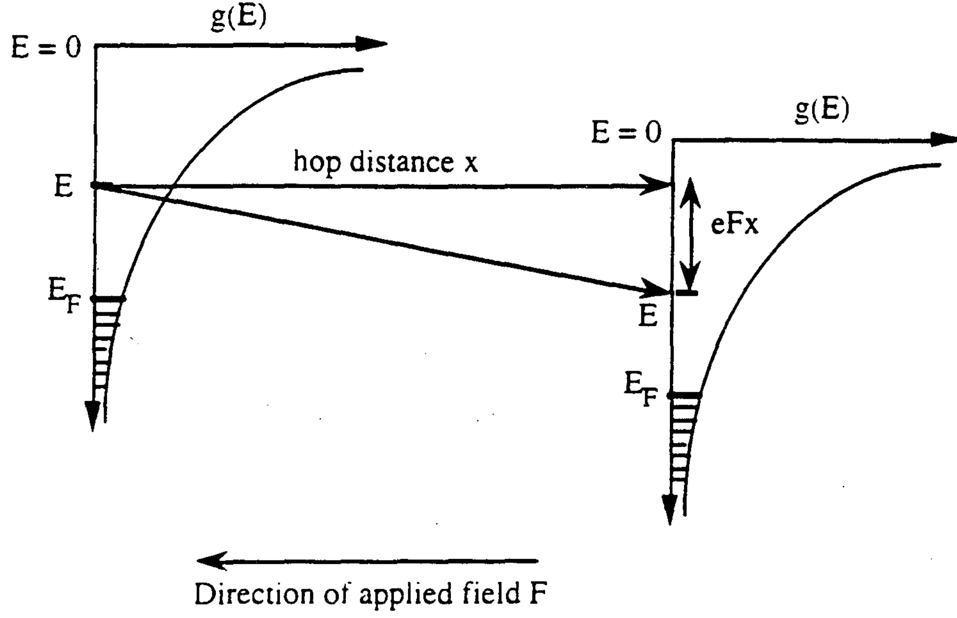

Fig. 2.15 Electron hop against the electric field for an amorphous semiconductor with an exponential dropoff of localized electron states in the conduction band tail. Due to the inclination of the conduction band a higher concentration of shallower localized states is available for the electron. The filled area below E_F represents the occupied states in the mobility gap. (Figure adapted from Marianer and Shklovskii [1992].)

In the limit of small electric fields $eFa/k_B \ll T$, the numerical result of Marianer and Shklovskii can be written as $T_e \approx T(1 + BF^2/T^2)$ where $B = 0.67ea/2k_B$. Therefore the hopping conductivity as a function of electric field is

$$\sigma(F,T_e) = \sigma_o \exp\left[-\left(\frac{T_o}{T_e}\right)^n\right] \approx \sigma_o \exp\left(-\left(\frac{T_o}{T}\right)^n\left[1 - n\,\frac{B^2F^2}{T^2}\right]\right). \tag{2.35}$$

For small fields the conductivity will increase with electric field and temperature as $\ln \sigma(F,T)/\ln \sigma(F=0,T) \propto F^2/T^{2+n}$. As discussed in Section 2.1.3.1, this is the same functional dependence that Apsley and Hughes [1974] derived for n = 1/4 VRH in the weak field limit. In the limit of large electric fields $eFa/k_B \gg T$, Equation 2.35 can be written as $T_e \approx 0.67eFa/k_B$. In this limit the hopping conductivity varies with F as

$$\sigma(F,T_e) = \sigma_o \exp\left[-\left(\frac{k_BT_o}{0.67eFa}\right)^n\right] \approx \sigma_o \exp\left(-\left(\frac{F_o}{F}\right)^n\right). \tag{2.36}$$

Thus the numerical result for hot electron hopping in the conduction band tail of an amorphous semiconductor has exactly the same functional form as the theoretical result for high field non-Ohmic impurity conduction in doped semiconductors (Section 2.1.3.4).

Despite this correspondence at high electric fields, the result of Marianer and Shklovskii has an uncertain relevance for hopping conduction in doped semiconductors in small and moderate electric fields. The density of states near the Fermi level in a doped semiconductor is assumed to be constant (Mott VRH) or parabolic (Shklovskii VRH), which may lead to significantly different behavior than is found for an amorphous semiconductor with an exponentially decaying density of states at the Fermi level.

By analogy with the hot electron effect in metals, we can estimate the magnitude of a hot electron effect for hopping conduction in doped semiconductors using Equation 2.28,

$$G_{el\text{-}ph} \approx \frac{\Omega C_e}{\tau}, \tag{2.28}$$

where C_e is the electronic heat capacity per unit volume, Ω is the volume, and τ is the electron-phonon scattering rate. Unfortunately, the dependence of C_e on temperature in doped semiconductors is not yet well understood. For a lightly doped semiconductor with a Coulomb gap in the density of states, the conductivity at very low temperatures is described by the Shklovskii variable range hopping formula $\sigma(T) = \sigma_0 \exp[-(T_o/T)^{1/2}]$ and the specific heat is predicted to vary with temperature as [Shklovskii and Efros, 1984]

$$C_e \propto \frac{T}{\left[\ln\left(\frac{\Delta}{T}\right)\right]^{1/2}}, \tag{2.37}$$

where Δ is the width of the Coulomb gap. Thus C_e has a sublinear dependence on T as $T \to 0$. In a study of the specific heat of uncompensated Si:P below the metal insulator transition, Lakner and Lohneysen [1989] found that above 1.5 K the samples were well described by $C_e = \gamma T + \beta T^3$. Below 1 K, strong deviations from this behavior were observed with an upturn of C_e towards a sublinear dependence. At the lowest temperatures

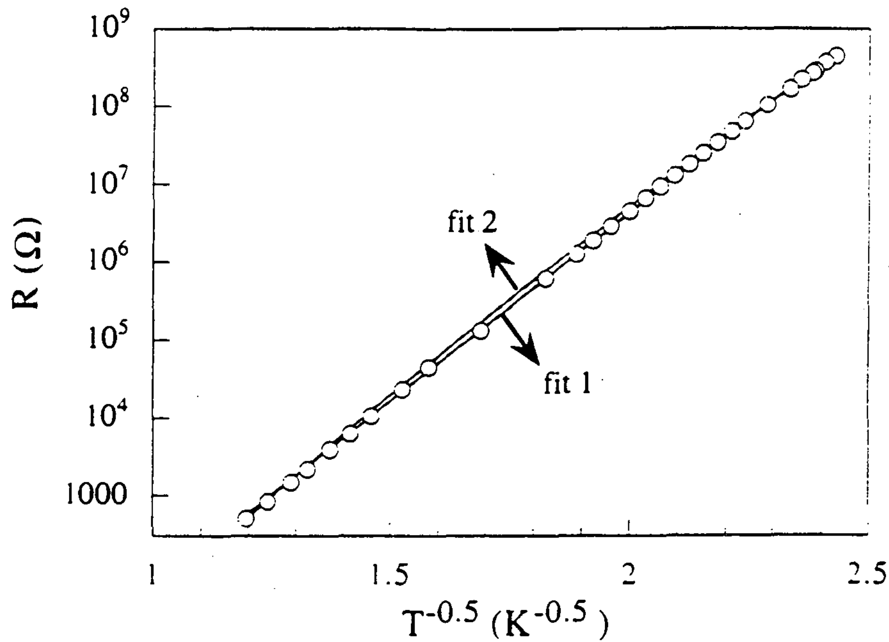

Fig. 2.16 Temperature dependence of the resistance of ^{70}Ge-1.65. The two fits are described in the text.

C_e varied as T^{α} where α was equal to 0.2 for the more heavily doped samples and decreased below zero with decreasing impurity concentration. Some indications of such a behavior were also found by Paalanen *et al.* [1988]. The sublinear temperature dependence of C_e is attributed to exchange interactions between localized electrons.

The temperature dependence of the electron-phonon scattering rate τ^{-1} is not well understood in doped semiconductors at low temperatures. As discussed in Chapter 1, the temperature dependence of τ^{-1} is equivalent to the temperature dependence of σ_0, where $\sigma = \sigma_0 \exp[-(T_0/T)]^n$. Most theories of hopping conduction assume that σ_0 is temperature independent. However, in Figure 2.16 we show the resistance as a function of temperature of one of the samples studied in this work in the n = 1/2 variable range hopping regime. The sample is described in Chapter 3 and is labelled ^{70}Ge:Ga-1.65. We have fit the R(T) curve to two equations. For the first fit, we make the standard assumption that R_0 is

temperature independent: $R(T) = R_0 \exp[-(T_0/T)]^{1/2}$. Using Fit 1, we find that $R = 8.92\times10^{-4} \exp(11.16/\sqrt{T})$ (Ω) with a linear correlation coefficient $\Re = 0.99923$. For the second fit, we make the non-standard assumption that R_0 varies as T^{-3} (equivalent to the assumption that σ_0 varies as T^3): $R(T) = AT^{-3} \exp[-(T_0/T)]^{1/2}$. To our surprise, we found that using Fit 2 the resistance can be very well described by $R = 1.63\times10^{-2}\, T^{-3} \exp(7.714/\sqrt{T})$ (Ω) with a linear correlation coefficient $\Re = 0.99988$. This second fit describes the data as well or better than the standard fitting equation. We find similar results from the other samples described in this work. Therefore, we conclude that the electron-phonon scattering time in doped semiconductors cannot be determined from the conductivity curves in this experiment.

If we assume that the electron-phonon scattering rate τ^{-1} scales with temperature as T^3 in doped semiconductors as well as in metals then we find that

$$P = g_{el\text{-}ph}\left(T_e^{\alpha+1} - T_{ph}^{\alpha+1}\right), \qquad (2.38)$$

where $\alpha < 4$ due to the sublinear dependence of C_e on T at low temperatures. If we instead assume that the electron-phonon scattering rate is temperature-independent, equivalent to the assumption that σ_0 is independent of temperature, then we find that $\alpha < 1$.

2.3.3.3 Discrepancies in the existing hopping conduction data which are analyzed using a hot electron model

Some unexplained questions about the existing data which utilize a hot electron theory for low temperature non-Ohmic impurity conduction in doped semiconductors are as follows.

(1) The values observed for α are ≥ 4 when the data are parametrized by Equation 2.38 [Mack *et al.*, 1983; Wennberg *et al.*, 1986; Wang *et al.*, 1990], contradicting our expectation that α should be < 4 as discussed above. Wang *et al.* studied two samples with an identical geometry and identical impurity concentrations and found the surprising result

that α differed and was best fit by $\alpha = 4.5$ and $\alpha = 5$, rather than having a single value. As we will show in Chapter 4, the different values of α can most likely be explained by sample stress.

(2) The thermal conductance deduced from assuming a hot electron model in planar Ge thermometers does not scale with sample size [Mack *et al.*, 1983]. According to Demoulin *et al.* [1993], the deduced electron-phonon coupling does not depend on impurity concentration N. This is a very unexpected result because $G_{el\text{-}ph}$ should be proportional to C_e which is proportional to the density of states at the Fermi level, which in turn depends strongly on N.

(3) The existing experiments [Wang *et al.*, 1990; van der Heijden *et al.*, 1992; Zammit *et al.*, 1990; Dumoulin *et al.*, 1993] which postulate a hot electron effect have been analyzed using Equation 2.38 and state that the data are not well described by Equation 2.9 for the moderate electric field dependence of the conductivity. To our knowledge, except for the study of van der Heijden *et al.* [1991] no attempt has been made to compare hot electron effects and the theoretical expression Equation 2.12 for the strong electric field dependence of the conductivity. van der Heijden *et al.* found that their data for the field dependence of ion-implanted Si:As could be equally well described both by an electric-field-assisted hopping model (Equation 2.12) and by a heating model (Equation 2.38) for larger values of the electric field. We propose the following argument to explain this result. If we replace the phonon temperature T in the variable range hopping formula with an electron temperature $T_e = T + eFL/k$, we obtain the following formula for the hopping conductivity:

$$R(T_e) = R_0 \exp\left[\frac{T_0}{T + \frac{eFL}{k}}\right]^n . \tag{2.39}$$

This expression is physically plausible because the average energy gained by an electron in applied field should be proportional to eFL, which is equivalent to a temperature increase

eFL/k. In the weak field limit $eFL/kT << 1$, Equation 2.39 reduces to the familiar exponential dependence of the resistance on applied field:

$$R(T_e) = R_o \exp\left[\left(\frac{T_o}{T}\right)^n - \frac{neFL}{kT}\left(\frac{T_o}{T}\right)^n \right] . \qquad (2.40)$$

In the strong field limit $eFL/kT >> 1$ Equation 2.39 reduces to the temperature independent expression

$$R(T_e) = R_o \exp\left[\frac{kT_o}{eFL} \right]^n = R_o \exp\left[\frac{F_o}{F} \right]^n , \qquad (2.41)$$

which is identical in form to Equation 2.12 for the activationless hopping conduction in a strong electric field. If this argument is correct, "hot electron effects" in doped semiconductor are effectively accounted for by existing theories of non-Ohmic impurity conduction.

(4) Anomalous time constants which have been seen are taken for evidence for a thermal coupling time between the electron and phonon systems. However, long system time constants which depend on both temperature and bias level may also be found in the traditional electric field dependent hopping model through the transition rates W_{ij}, as discussed in Chapter 1.

(5) The thermal conductivity G_{el-ph} between the electron and phonon systems has been deduced from current-voltage curves, a method which will give misleading results if both non-Ohmic effects and hot electron effects are present. The electron heat capacity has been deduced from the system time constants using $C_e = G_{el-ph}\tau_{el-ph}$. The values of C_e deduced from nominally identical samples differ by factors of more than ten [Wang *et al.*, 1990].

The above problems indicate that the hot electron model as applied to non-Ohmic impurity conduction needs to be modified. Existing theoretical predictions for hopping conduction in a strong electric field effectively account for an increase in the electron temperature $T_e = T + eFL/k$.

Chapter 3

Experimental studies of non-Ohmic impurity conduction in neutron transmutation doped Germanium

3.1 Overview

In this chapter we describe three experimental studies of non-Ohmic impurity conduction in neutron transmutation doped Ge. These experiments were designed to answer some of the questions raised in Chapter 2 about the behavior of the non-Ohmic conduction in weak and moderate electric fields over a range of impurity concentrations. In Figure 3.1 we indicate the regions probed by the three experiments on a phase space diagram of the electric field dependence of the conductivity for various impurity concentrations and electric field strengths. The first experimental study is of lightly and moderately doped p-type Ge:Ga samples with a compensation $K \approx 0.32$. As we will show, the conductivity in the low-field limit is very well described by the Shklovskii theory of variable range hopping. Experiment 1 probes the region of the phase space over which the conductivity is predicted to vary with electric field as $\sigma \sim \exp(eFL/kT)$. We attempt to answer the following questions raised in Chapter 2: What is the weak field dependence of the conductivity? How well are the data described by $\sigma \sim \exp(eFL/kT)$ in moderate fields? What is the dependence of L on impurity concentration and temperature?

The second experiment is of moderately and heavily doped p-type ^{70}Ge:Ga samples with a compensation $K < 0.01$. The conductivity in the low-field limit is very well described by the Shklovskii theory of variable range hopping. In Experiment 2, we study the change in the field dependence of the conductivity as N nears the critical concentration for a metal-insulator transition.

The third experiment is of moderately doped n-type ^{74}Ge:As with a compensation $K < 0.01$. The conductivity in the low-field limit is in a transition regime between ε_2 conduction and Mott variable range hopping conduction. Experiment 3 probes the

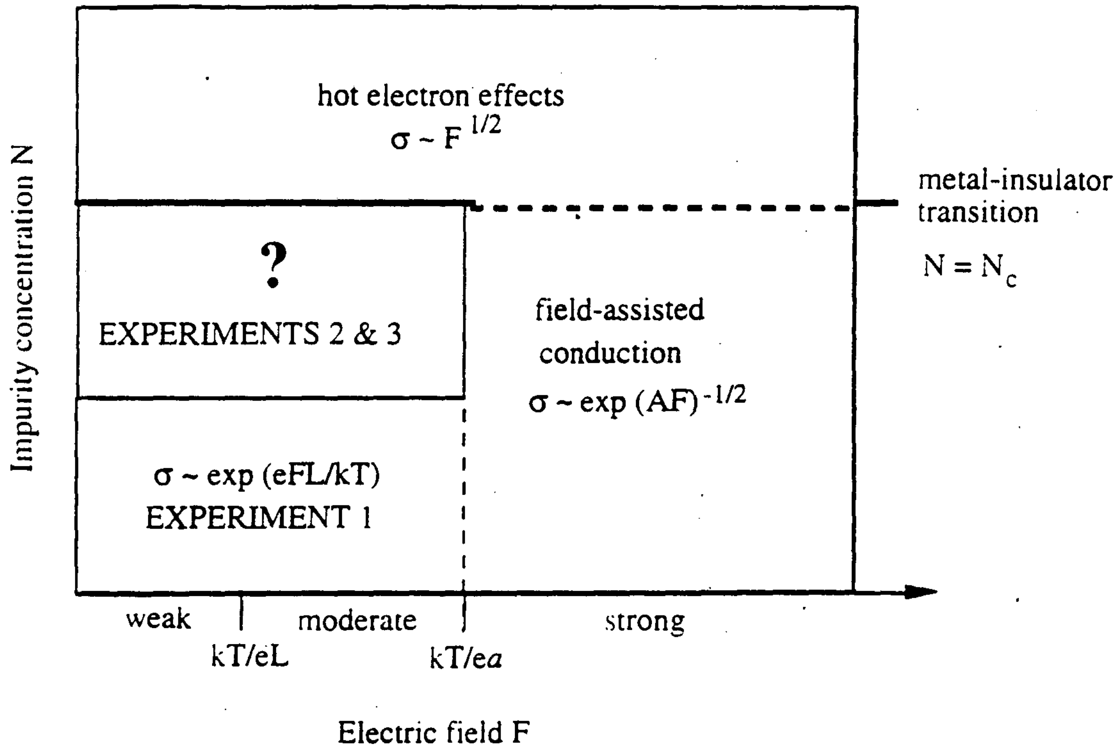

Fig. 3.1 Phase space diagram of the electric field dependence of the conductivity for various impurity concentrations and electric field strengths. The question mark indicates a region of the phase space for which no theory of non-Ohmic behavior has been developed.

electric field dependence of the conductivity for donor electrons excited into extended states in the impurity band rather than donor electrons hopping between localized states.

We will first describe the experimental procedure, and then discuss the results of each experiment in detail.

3.2 Experimental procedure

Our study of non-Ohmic impurity conduction in doped Ge semiconductors requires well-characterized, randomly doped Ge samples. In addition, the electrical contacts to the samples must have a negligible resistance compared to the resistance of the bulk. In this section we discuss how these sample requirements are satisfied, followed by a description of our measurement technique.

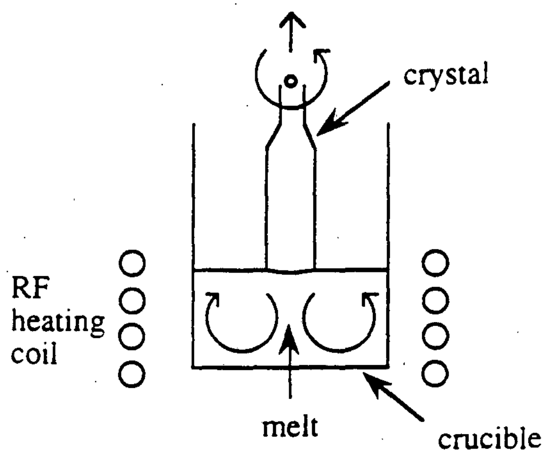

Fig. 3.2 In the melt doping process, the doped crystal is slowly pulled out of the melt from an initial seed.

3.2.1 Semiconductor doping

Semiconductor doping is the process of introducing desired impurities into an ultra-pure semiconductor sample. Bulk semiconductors can be doped during crystal growth by adding dopants to the melt. In germanium melt doping the dopants are added to the germanium melt in the form of a piece of heavily doped germanium called the "master dopant alloy," and a crystal is then slowly pulled from the melt as shown in Figure 3.2. Impurity striations -- local fluctuations in the impurity concentration on the order of a few percent -- occur in all melt-doped crystals because of temperature gradients in the melt which lead to melt convection and fluctuations in the crystal growth rate. The growth rate fluctuations lead to periodic changes in the effective segregation coefficient and to dopant striations. At temperatures below 2 K, local impurity variation can lead to resistivity fluctuations of more than an order of magnitude.

The experiments discussed in this thesis require samples with extremely uniform, random dopant distributions and precisely known net-carrier concentrations and compensation ratios. These properties are achieved by the method of neutron

Fraction	Isotope	Reaction	σ_c	$t_{1/2}$	dopant type
20.5%	$^{70}Ge_{32}$	$^{71}Ge_{32} \rightarrow {}^{71}Ga_{31} + K$	3.25	11.2 days	acceptor
27.4%	$^{72}Ge_{32}$	$^{73}Ge_{32}$ stable	1.0		
7.8%	$^{73}Ge_{32}$	$^{74}Ge_{32}$ stable	15.0		
36.5%	$^{74}Ge_{32}$	$^{75}Ge_{32} \rightarrow {}^{75}As_{33} + \beta^-$	0.52	82.8 min	donor
7.8%	$^{76}Ge_{32}$	$^{77}Ge_{32} \rightarrow {}^{77}As_{33} + \beta^- \rightarrow {}^{77}Se_{34} + \beta^-$	0.16	11.3 hrs	deep donor

Table 3.1 Reactions following neutron capture which take place in natural germanium to produce dopant isotopes.

transmutation doping [Haller *et al.*, 1984; Haller *et al.*, 1985; Haller, 1994] which allows an unrivaled doping uniformity and control over doping parameters.

3.2.2 Neutron transmutation doping

Neutron transmutation doping, also referred to as NTD, takes place when semiconductor crystals are irradiated with thermal neutrons at a nuclear reactor. Because neutrons are electrically neutral, they readily penetrate the semiconductor and are captured by the semiconductor nuclei at a rate R per unit volume given by

$$R = N_T \sigma_c \phi \tag{3.1}$$

where N_T is the number of target nuclei per unit volume and ϕ is the thermal neutron flux. Each isotope of the semiconductor material has a characteristic capture cross section σ_c which is a measure of the probability of interaction between the nucleus and the neutron. σ_c increases with decreasing neutron energy as

$$\sigma_c \propto E^{-1/2}. \tag{3.2}$$

After neutron capture the nucleus is in an excited state and decays with a characteristic half-life until it reaches a stable isotopic state. The reactions following neutron capture which occur in germanium to produce dopant isotopes are listed in Table 3.1. The gamma ray

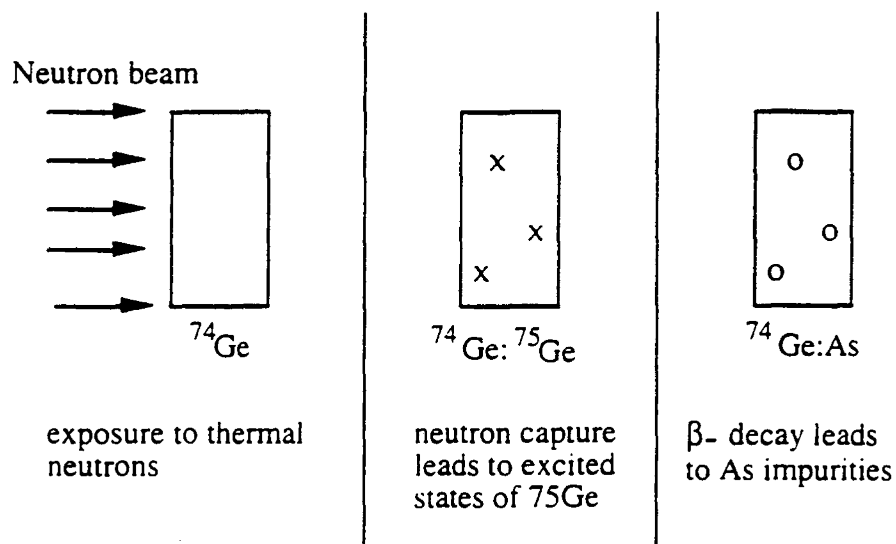

Fig. 3.3 Illustration of the neutron transmutation doping process for the germanium isotope ^{74}Ge.

spectrum has been measured to determine which isotopes have been produced. Figure 3.3 shows the neutron transmutation doping process for the germanium isotope ^{74}Ge.

The NTD process produces a precisely randomly doped semiconductor sample for several reasons. First, the extent of the neutron field produced by a nuclear reactor is many orders of magnitude larger than the typical semiconductor sample and hence the neutron flux across the semiconductor may be regarded as constant. Secondly, the small capture cross sections of the semiconductor isotopes minimize "self-shadowing" so that the neutron flux through the semiconductor may be regarded as constant. Finally, the various semiconductor isotopes are located at perfectly random positions throughout the crystal.

The compensation ratio K for NTD Ge with a natural isotopic composition is

$$K_{NTD\ Ge} = N_D/N_A = \{[As] + 2[Se]\}/[Ga] = 0.322 \qquad (3.3)$$

Selenium is counted twice because it is a doubly charged donor and can compensate two acceptors.

Although neutron transmutation doping of natural germanium produces samples with a fixed compensation ratio, the NTD process can also be used to produce samples with a controlled compensation by controlling the isotopic composition of the pure Ge crystal [Itoh et al., 1993-A; Itoh et al., 1993-B; Itoh, 1994]. For example, neutron transmutation doping of a high-purity single crystal of ^{74}Ge produces the n-type material ^{74}Ge:As with a compensation $K < 0.01$, while neutron transmutation doping of a high-purity single crystal of ^{70}Ge produces the p-type material ^{70}Ge:Ga with a compensation $K < 0.01$. Mixtures of ^{74}Ge:As and ^{70}Ge:Ga can result in doped crystals with both a precisely controlled impurity concentration and compensation.

3.2.3 Sample preparation

The basic steps in preparing NTD germanium for conductivity measurements are as follows. Ultra-pure germanium crystals are first neutron transmutation doped to the desired impurity concentrations, typically 10^{15} cm^{-3} to 10^{17} cm^{-3}. Doping accuracy can be controlled to better than 1% by controlling the exposure time and the thermal neutron flux ϕ. Approximately a year after thermal neutron irradiation, many times the longest half-life in NTD Ge (11.2 days for the decay ^{71}Ge $\rightarrow$ ^{71}Ga), the crystals are thermally annealed in dry argon gas to heal radiation damage caused by fast neutrons. A slow annealing at temperatures of ~ 400 °C is performed for the less heavily doped samples and a rapid annealing at temperatures of up to ~ 700 °C is performed for the more heavily doped samples. After annealing, the crystals are cut into small ~ 300 μm thick wafers which are then etched in a 3:1 HNO_3:HF solution for approximately 1 minute to remove surface damage. The etch is quenched with methanol. The surfaces appear shiny and damage free.

In order to produce ohmic metal/n+/n or metal/p+/p contacts to the doped Ge samples as discussed in Section 2.2.2, the samples are doubly ion implanted on both sides of the wafer with phosphorus ions (n-type Ge) or boron ions (p-type Ge). The double ion implantion produces a metallic region in the Ge approximately 2000 Å deep. The top 500

Å of Ge is removed by etching the samples for ~ 30 s in a 5% NaOCl solution in order to reach the depth of maximum P or B concentration. A 200 Å layer of Pd and a 4000 Å layer of Au are then argon sputtered onto the wafers. The Pd is used as a sticking layer because the Au will not otherwise wet the surface. The samples are then annealed at 250 °C in dry argon gas for an hour. The annealing helps to activate the implanted phosphorus or boron ions and also relieves stress in the samples caused by the metallization process.

The wafers are finally cut into chips ~ 300 μm per side, which are etched in a 9:1 HNO_3:HF solution for 40 seconds and quenched in methanol. Etching should leave the chips shiny and damage-free, removing any surface electronic states which could otherwise provide a parallel conduction path across the chip and contribute to the electronic conduction at low temperatures. After etching, the cross sectional area of the chips shrinks from ~ $(300\ \mu m)^2$ to ~ $(275\ \mu m)^2$. The gold plating is not affected by the etching solution and the sample thickness remains ~ 300 μm.

The last step in sample preparation is to attach 25 μm diameter Au wires to the metal contacts by wedge bonding. Au was chosen for the wire material because it has a high thermal conductivity κ relative to other metals and we wanted to minimize the electrical self-heating of the chips. The wire diameter 25 μm was chosen because it is a convenient size to work with and because for larger wire diameters the thermal boundary resistance (Kapitza resistance) will dominate the thermal resistance of the wire. The Au wires were connected to the Au contact pads by the wedge bonding technique because, unlike other bonding techniques which use materials such as silver epoxy or indium solder, Au wedge bonding does not significantly stress the samples. It is important that the samples be

Measurement circuit:

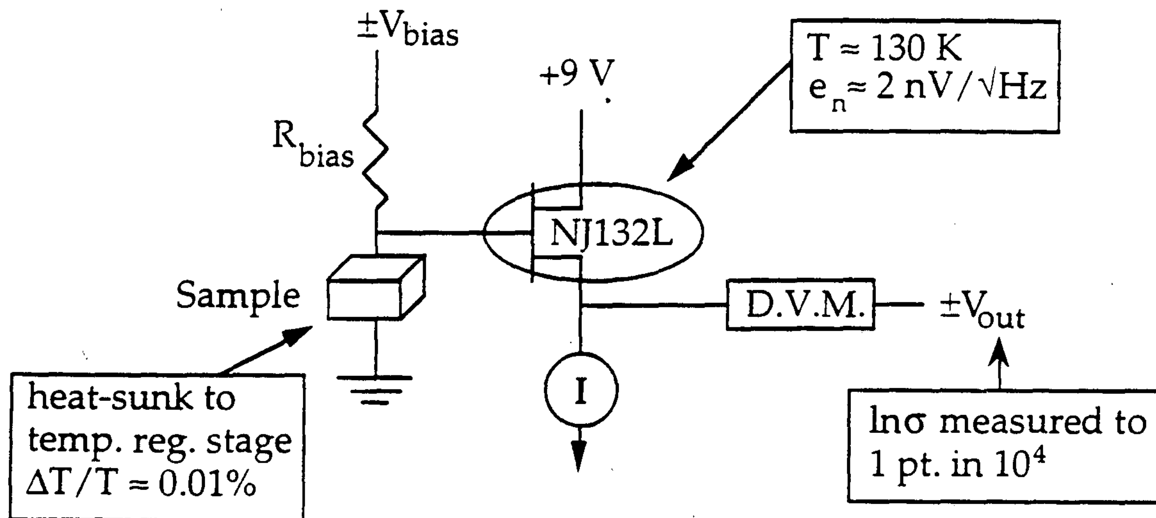

unstressed because stress can significantly affect their non-Ohmic conduction properties as discussed in Chapter 4.

3.2.4 Measurement technique

The samples were thermally attached through the wire leads to a temperature regulated stage with $\Delta T/T \sim 0.1\%$. The stage was cooled with an adiabatic demagnetization refrigerator for temperatures below 0.3 K and with a ^{3}He refrigerator for temperatures above 0.3 K. Electrical resistances were measured to an accuracy of a few parts in 10^4 using a dc bias voltage switched between +V and -V (to eliminate the effects of thermal emfs) applied across the series combination of a load resistor at 1.5 K and the sample. The voltage drop across each sample was measured through a junction field-effect transistor operating in source follower mode.

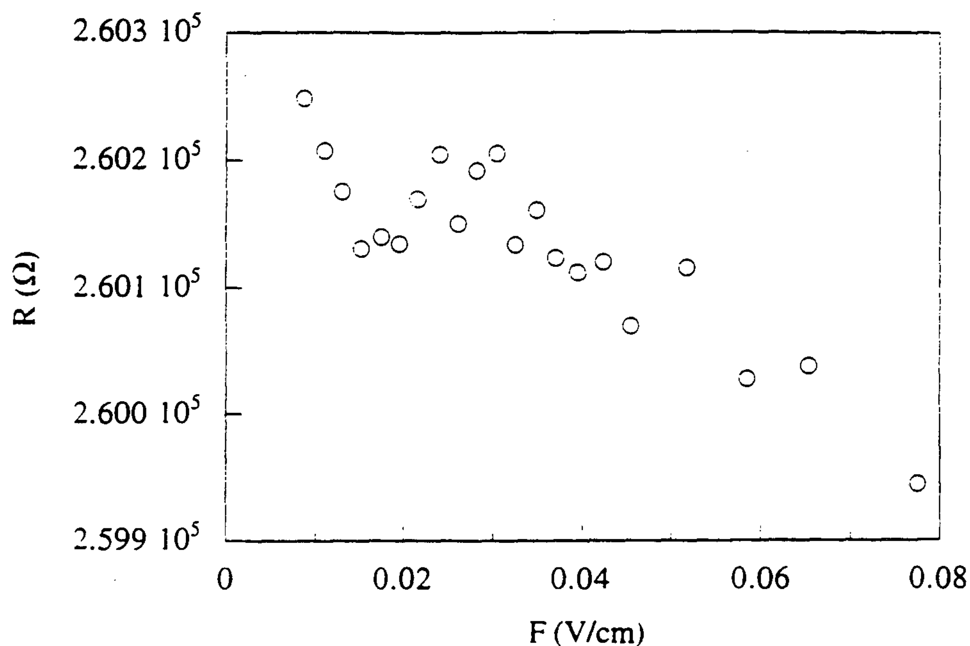

Fig. 3.5 Measured low field resistance at 1.2 K of a ^{70}Ge:Ga sample from Experiment 2 with an impurity concentration $N \approx 0.16\ N_c$. The relative error in the resistance measurement is on the order of a part in 10^4. The overall slope is due to the dependence of the resistance on the applied field.

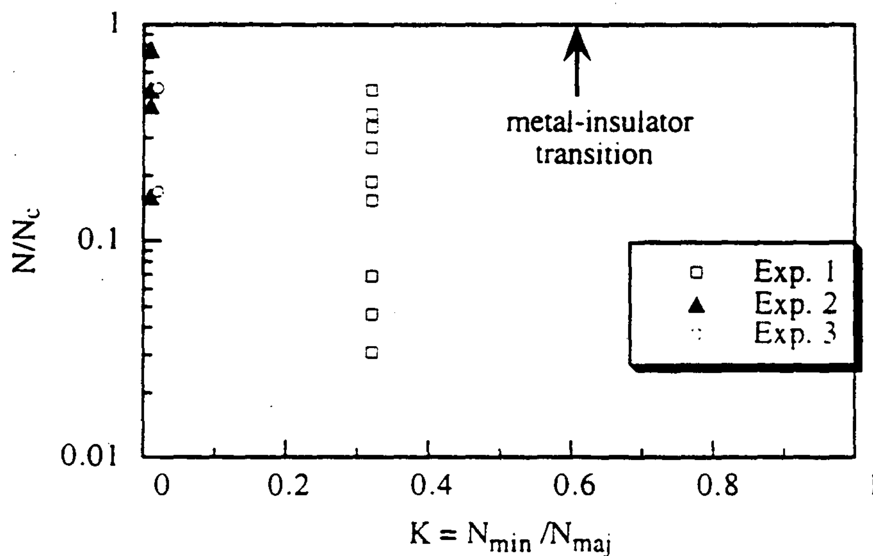

Fig. 3.6 Phase space diagram showing the impurity concentrations and compensations of the ^{nat}Ge:Ga samples studied in Experiment 1 (open squares), the ^{70}Ge:Ga samples studied in Experiment 2 (solid triangles), and the ^{74}Ge:As samples studied in Experiment 3 (open circles).

3.3 Experimental results

The three studies of non-Ohmic impurity conduction discussed in this work cover a range of impurity concentrations and compensations, as shown in Figure 3.6. In Experiment 1, we study nine ^{nat}Ge:Ga samples with a compensation of 0.32 covering a range of impurity concentrations $0.03 < N/N_c < 0.50$. We have assumed that the critical concentration N_c for a metal-insulator transition in ^{nat}Ge:Ga is $N_c \sim 1\times10^{17}$ cm^{-3}, as discussed in Section 3.3.1. In Experiment 2, we study four ^{70}Ge:Ga samples with very low compension $K < 0.01$ covering a range of impurity concentrations $0.16 < N/N_c < 0.77$. We have used the value $N_c = 1.89\times10^{17}$ cm^{-3} measured in ^{70}Ge:Ga by Itoh *et al.* [1994]. Finally, in Experiment 3 we study two ^{74}Ge:As samples with very low compension $K < 0.01$ with impurity concentrations $0.17N_c$ and $0.51N_c$. We have assumed the value $N_c = 3.5 \times 10^{17}$ cm^{-3} [Edwards and Sienko, 1978].

As we will show, the non-Ohmic hopping conductivity for the lightly doped samples in Experiment 1 can be collapsed onto a single universal curve. As the impurity concentration nears N_c, we find the counter-intuitive result that the non-Ohmic conductivity of the samples in Experiments 1 and 2 begins to depend more strongly on the applied field in the weak field regime than in the moderate field regime. This result has not been previously reported and is not predicted by any existing theory. In Experiment 3, we find that when the conduction mechanism is intermediate between ε_2 conduction and hopping conduction, the non-Ohmic conductivity is extremely well described by $ln\,[\sigma(F)/\sigma(0)] \propto F^{1.5}$. These results, though surprising, do not conflict with previous theories which assume a lightly doped semiconductor.

3.3.1 Experiment 1

NTD ^{nat}Ge:Ga is produced by Eugene Haller and his group for a range of doping concentrations labeled NTD 1 through NTD 25. The numbers 1 through 25 indicate chronological order (the order in which each material was developed) rather than increasing

Sample	N (10^{16} cm^{-3})	N/N_c	σ_0 (Ω cm)$^{-1}$	T_0 (K)
NTD 2	0.307	0.031	0.0074	122
NTD 3	0.461	0.046	0.01	126
NTD 4	0.692	0.069	0.4	104
NTD 5	1.54	0.15	2	87.0
NTD 10	1.89	0.19	4.5	77.2
NTD 14	2.70	0.27	5.3	49.1
NTD 11	3.38	0.34	1.0	39.6
NTD 6	3.85	0.39	16.7	36.6
NTD 17	4.99	0.50	5.6	21.2

Table 3.2 Parameters describing the NTD ^{nat}Ge:Ga samples studied in this work. N is the net impurity concentration. The parameters σ_0 and T_0 are defined in Equation 3.4. We have assumed that the critical concentration N_c is approximately 1×10^{17} cm^{-3} as discussed in the text.

or decreasing doping density. Table 3.2 lists the basic parameters of the NTD ^{nat}Ge:Ga samples studied in this work. The dependence of the conductivity on temperature in the weak field limit is shown in Figure 3.7. The $\sigma(T)$ curves are extremely well described by the equation for variable range hopping with a Coulomb gap in the density of states (see Section 1.5.2.1),

$$\sigma(T) = \sigma_0 \exp(-T_0/T)^{1/2}. \tag{3.4}$$

The dependence of T_0 on impurity concentration has not been theoretically or experimentally established for doped semiconductors with an intermediate value of the compensation. In the limit $K \ll 1$, T_0 is predicted to vary with impurity concentration as

$$T_0 = T_0^* \,(1 - N/N_c)^\beta \tag{3.5}$$

where T_0^* and β are constants [Shklovskii and Efros, 1984]. Theories of the metal-insulator transition, confirmed by experimental studies, predict that $1 \le \beta \le 2$. However, when we use Equation 3.5 to fit the measured dependence $T_0(N)$ in ^{nat}Ge:Ga with K = 0.32, we find that the best fit values are $T_0^* = 137$ K, $N_c = (1.26\pm.05)\times10^{17}$ cm^{-3}, and $\beta = 3.8\pm2$ as plotted in Figure 3.8. This result is surprising for two reasons: the best fit

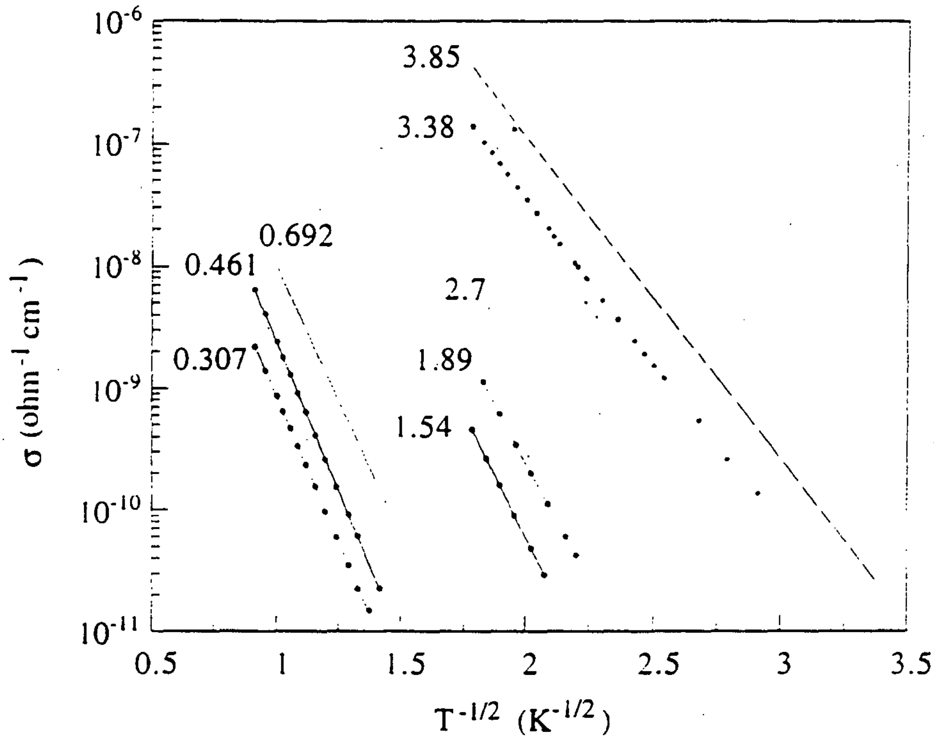

Fig. 3.7 Measured temperature dependence of the conductivity of the NTD ^{nat}Ge:Ga samples studied in Experiment 1. The impurity concentration of each sample is labelled next to each curve in units of 10^{16} cm^{-3}.

value of N_c is smaller in compensated Ge:Ga than the value $N_c = 1.89\times10^{17}$ cm^{-3} measured in uncompensated Ge:Ga although theory predicts it must be larger [Shklovskii and Efros, 1984], and the best fit value of β is significantly larger than predicted by theories for uncompensated semiconductors. If we require that $\beta = 2$, we find that N_c is $(0.79\pm.03)\times10^{17}$ cm^{-3}. Visual inspection of Figure 3.8 shows that T_0 intercepts zero at a critical concentration $N_c \sim 1\times10^{17}$ cm^{-3}. Therefore in this work we assume the value $N_c \sim 1\times10^{17}$ cm^{-3}.

We measured the electric field dependence of the resistance of the samples over a range of temperature limited at higher temperatures by the need to avoid Joule heating and at lower temperatures by measurement technology (we were unable to measure resistances

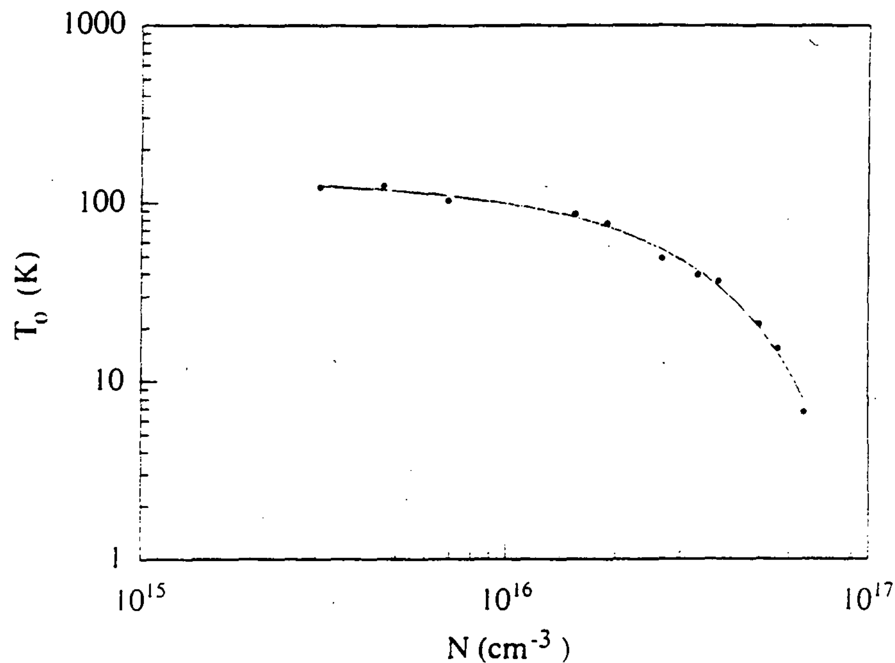

Fig. 3.8 Measured dependence of the variable range hopping parameter T_0 on impurity concentration N for the NTD $^{nat}Ge:Ga$ samples studied in Experiment 1.

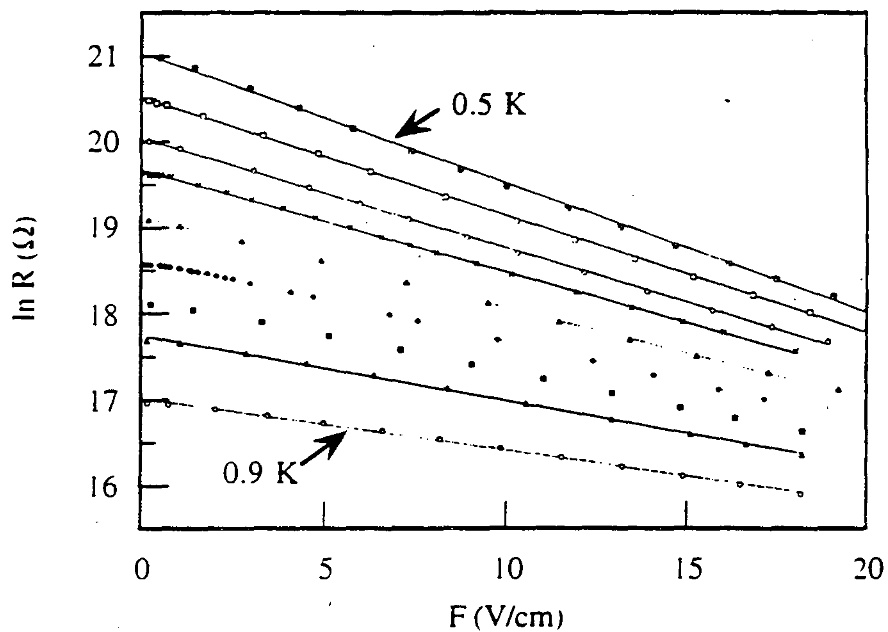

Fig. 3.9 Electric field dependence of the resistance of a lightly doped $^{nat}Ge:Ga$ sample with an impurity concentration $N \approx 0.046N_C$. Curves were measured at temperatures between 0.5 K and 0.9 K, with successive curves separated by 0.05 K.

$> 2\ G\Omega$). The range of field strengths measured in each sample was determined by similar considerations. Figure 3.9 shows the measured electric field dependence of the resistance of a lightly doped ^{nat}Ge:Ga sample with an impurity concentration $N \approx 0.046N_c$. The data were measured over a range in resistance $10\ M\Omega < R < 1\ G\Omega$, corresponding to a range in temperature $0.5\ K < T < 0.9\ K$. Similar data sets were measured for the other eight samples. At each temperature the data were fit to the theoretical prediction for non-Ohmic hopping conduction in a moderate electric field (Equation 2.9),

$$\ln R(F) = \ln R(F{=}0) - eFL/kT. \tag{3.6}$$

as described in Section 2.1.3.3.

The natural log of the resistance appears to be very well described by a linear dependence on electric field at each temperature, confirming the validity of Equation 3.6. Figure 3.10 confirms that a linear dependence provides a much better fit than the weak field predictions for the electric field dependence of the resistance of Hill [1971] or Apsley and Hughes [1974]. The three fitting functions shown in Figure 3.10 are: Fit 1, the theoretical prediction for moderate field behavior $\sigma(F) \propto \exp(AF)$ (Equation 3.6); Fit 2, Hill's prediction $\sigma(F) \propto \sinh(AF)/(AF)$ (Equation 2.5); and Fit 3, Apsley and Hughes' prediction $\sigma(F) \propto \exp(AF^2)$ (Equation 2.8). However, we will show that the use of Equation 3.6 to fit the data in Figure 3.9 can give misleading results for the dependence of L on temperature and impurity concentration. We then propose a new method of plotting the electric field dependence of the resistance. We show that the data from the six most lightly doped samples, covering a range in impurity concentration $0.031 < N/N_c < 0.27$ and a range in temperature $0.15\ K < T < 1.0\ K$, can be collapsed onto a single curve.

3.3.1.1 Motivation for a new method of analyzing the non-Ohmic impurity conductivity

We can use Equation 3.6 to determine a length parameter L for each curve in Figure 3.9. Figure 3.11 shows the values of L determined for $F < 10$ V/cm and $F > 10$ V/cm.

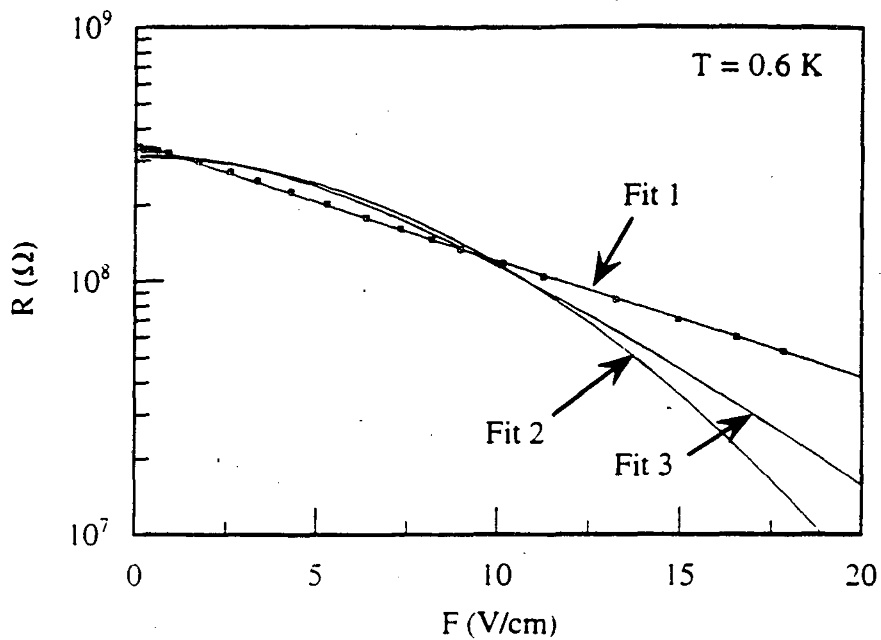

Fig. 3.10 Electric field dependence of the resistance of $^{nat}Ge:Ga$ with an impurity concentration $N \approx 0.046N_C$. The three fits are described in the text.

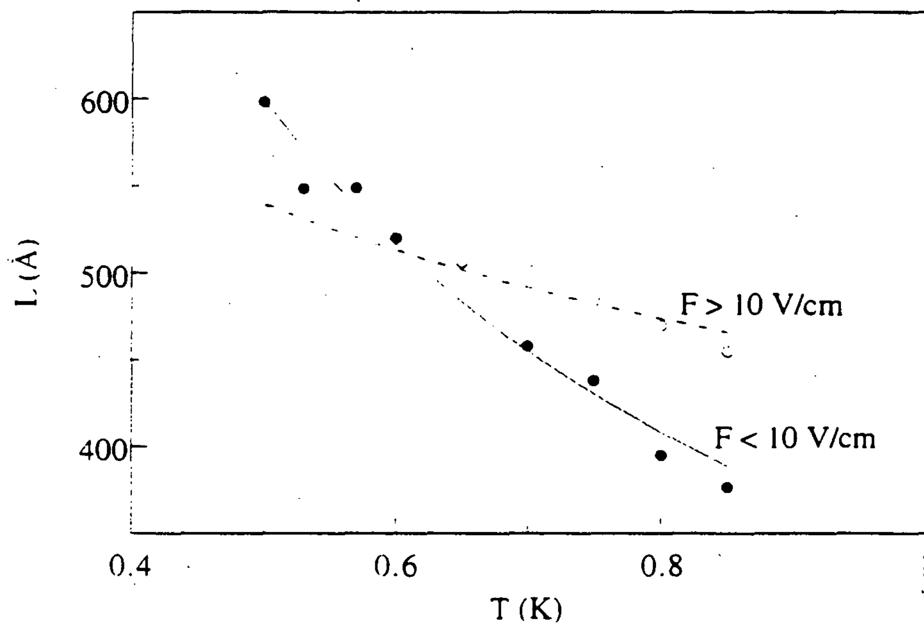

Fig. 3.11 Dependence of the hop length parameter L on temperature measured for F < 10 V/cm (solid circles) and F > 10 V/cm (open circles).

We find the surprising result that although the data appear to be well described by a single linear fit over the entire range of field strengths, L has a varying dependence on electric field and temperature. We can parametrize the temperature dependence of L by

$$L = L_0 T^{-x} \tag{3.7}$$

as discussed in Section 2.1.3.3. We observe the values $L_0 = 446 \pm 8$ Å and $x = 0.28 \pm 0.04$ when we fit the data for $F > 10$ V/cm. However, we find that $L_0 = 341 \pm 10$ Å and $x = 0.81 \pm 0.06$ when we fit the data for $F < 10$ V/cm. Timchenko *et al.* [1989] also observed different values of x depending on the range of field strengths. In a study of the non-Ohmic behavior of ZnSe crystals, they found $x = 0.5$ when $F > 20$ V/cm and $x = 0.8$ when $F < 20$ V/cm. The dependence of x on field strength can help to explain the many conflicting results in the published literature with $0 < x < 1.3$ for $n = 1/2$ VRH.

The fact that the measured value of L depends on the range of field strengths used at each temperature also affects the observed dependence of L on impurity concentration. As discussed in Section 2.1.3.3, different authors have found that L increases with N, decreases with N, or has a random dependence on N. This can be explained by the following example. Suppose that L is measured for 0 V/cm < F < 10 V/cm in one sample and for 10 V/cm < F < 20 V/cm in a second sample. We also suppose that L has no dependence on impurity concentration. If the data are similar to the data in Figure 3.11, then when the field dependence is measured at T = 0.8 K the length parameter L will appear larger for the second sample. However, when the field dependence is measured at T = 0.5 K then L will appear smaller for the second sample.

Therefore any conclusions drawn about the dependence of L on impurity concentration can be misleading unless the dependence of L on field strength is also taken into account. This is shown graphically in Figure 3.12. We have plotted the measured length parameter L as a function of temperature for three lightly doped ^{nat}Ge:Ga samples. At each temperature L was determined using the entire range of field strengths, but no effort was made to ensure that a consistent range of F was used for the different samples.

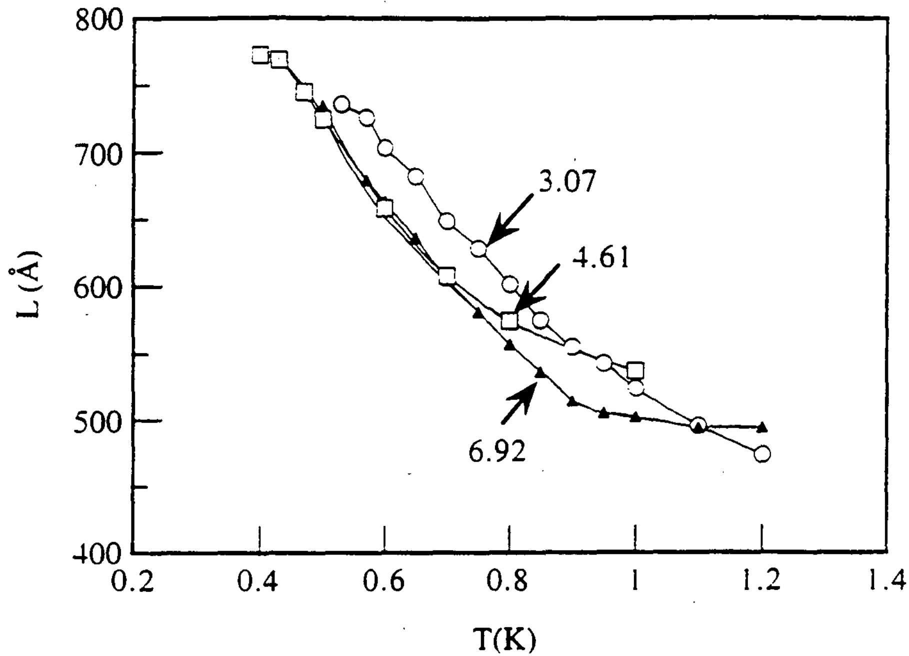

Fig. 3.12 Measured dependence of the hop length parameter L on temperature for three lightly doped ^{nat}Ge:Ga samples. The impurity concentrations are indicated next to each curve in units of 10^{15} cm^{-3}.

If we consider the data at T > 1 K, we find that the most lightly doped sample has a smaller value of L than the more heavily doped samples. The opposite conclusion will be drawn if we consider the data at T < 0.8 K.

3.3.1.2 Universal curve describing the field dependence of the conductivity in lightly doped ^{nat}Ge:Ga

In order to account for an electric field dependence of the length parameter L, rather than plotting ln σ as a function of F we examine the derivative of ln σ. Using Equations 3.6 and 3.7 we can write

$$\ln \sigma(F) = \ln \sigma(F{=}0) + \frac{eFL_0}{kT^{1+x}} . \tag{3.8}$$

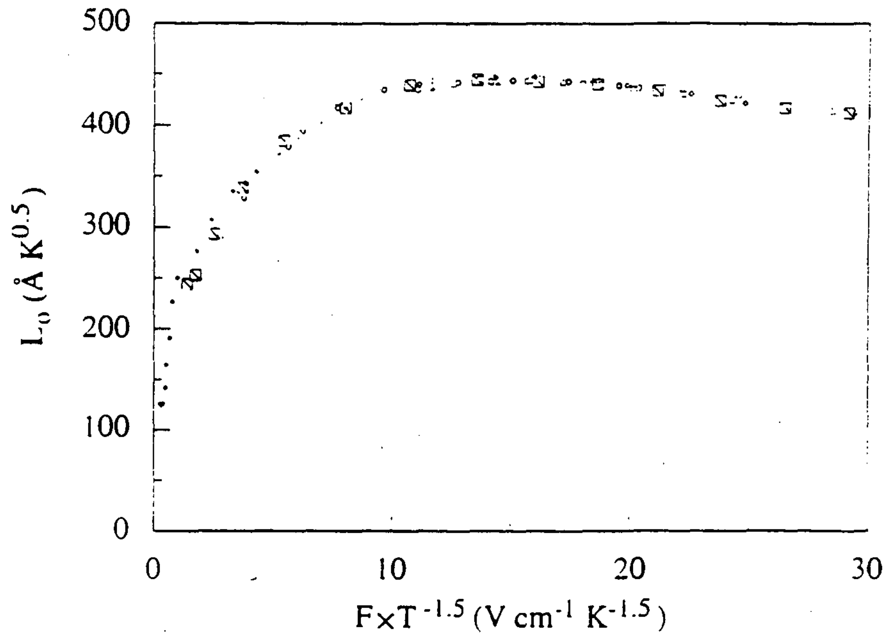

Fig. 3.13 Electric field dependence of the conductivity of six $^{nat}Ge:Ga$ samples, plotted using a new method. We have taken the derivative of ln σ with respect to F×$T^{-1.5}$ at each data point and used Equation 3.9 to determine the parameter L_0. The data collapse onto a single curve covering an order of magnitude in temperature, an order of magnitude in impurity concentration, and three orders of magnitude in conductivity for each sample.

After differentiating ln σ with respect to F/T^{1+x} we find that

$$\frac{d(\ln \sigma)}{d\left(F/T^{1+x}\right)} = \frac{eL_0}{k} . \qquad (3.9)$$

L_0 is therefore a length parameter determined by taking the slope at each value of the field, and provides more information than the length parameter L which is determined by fitting the entire data set to a straight line. According to the theories of Hill [1971] and Pollak and Reiss [1976], the value of x in Equation 3.9 is 0.5 for n = 1/2 variable range hopping. Using the measured electric field dependence of the conductivity of the six $^{nat}Ge:Ga$ samples with impurity concentrations between 0.031 N_c and 0.27 N_c, we have taken the

derivative of ln σ with respect to $F \times T^{-1.5}$ at each point and used Equation 3.9 to determine the parameter L_0. The data collapse onto a single universal curve as shown in Figure 3.13. This curve contains data from samples with impurity concentrations ranging between 0.031 N_c and 0.27 N_c measured at temperatures between 0.15 K and 1.0 K. Remarkably, we have been able to condense more than fifty measured curves for the electric field dependence of the conductivity covering almost an order of magnitude in impurity concentration, almost an order of magnitude in temperature, and three orders of magnitude in conductivity onto a single curve.

The following conclusions can be drawn from the shape of this curve.

(1) Although the conductivity is well described by Equation 2.9 for non-Ohmic impurity conduction in a moderate electric field, the parameter $L = L_0 / T^{0.5}$ where L_0 is a constant should be replaced by the field dependent length parameter $L = L_0(F) / T^{0.5}$.

(2) The parameter x in Equation 3.7 is equal to 0.5.

(3) The hop length is independent of impurity concentration. This may be due to two competing effects: the average separation between sites decreases as the impurity concentration leading to a smaller value of L, and the overlap between wavefunctions increases leading to a larger value of L. These two effects appear to balance each other so that the net effect of increasing the impurity concentration is to leave L unchanged.

(4) The data show an immediate onset of non-Ohmic impurity conduction in weak electric fields. In other words, there is no region for which $L_0 = 0$. The data for field strengths $F \times T^{-1.5} < 10$ $Vcm^{-1}K^{-1.5}$ cannot be described by the weak field models of Hill [1971] or Apsley and Hughes [1974].

(5) The data for field strengths $F \times T^{-1.5} > 10$ $Vcm^{-1}K^{-1.5}$ are well described by Equation 2.9 using $L_0 = 450Å \times K^{0.5}$. However, L_0 decreases weakly with increasing field strength for values of $F \times T^{-1.5}$ greater than 20 $Vcm^{-1}K^{-1.5}$. When $F \times T^{-1.5} = 60$ $Vcm^{-1}K^{-1.5}$, $L_0 = 350Å \times K^{0.5}$.

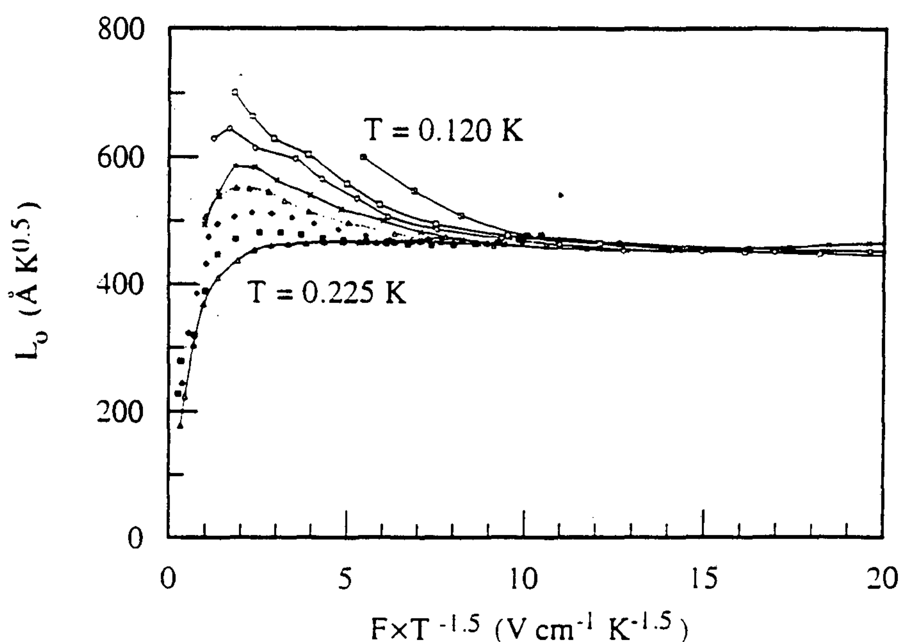

Fig. 3.14 Measured dependence of the parameter L_o on $F\times T^{-1.5}$ in $^{nat}Ge:Ga$ with an impurity concentration $N = 0.34N_c$. The data were measured over the temperature range $0.12\ K \leq T \leq 0.225\ K$. As the impurity concentration nears N_c, the data are no longer described by the universal curve shown in Figure 3.13.

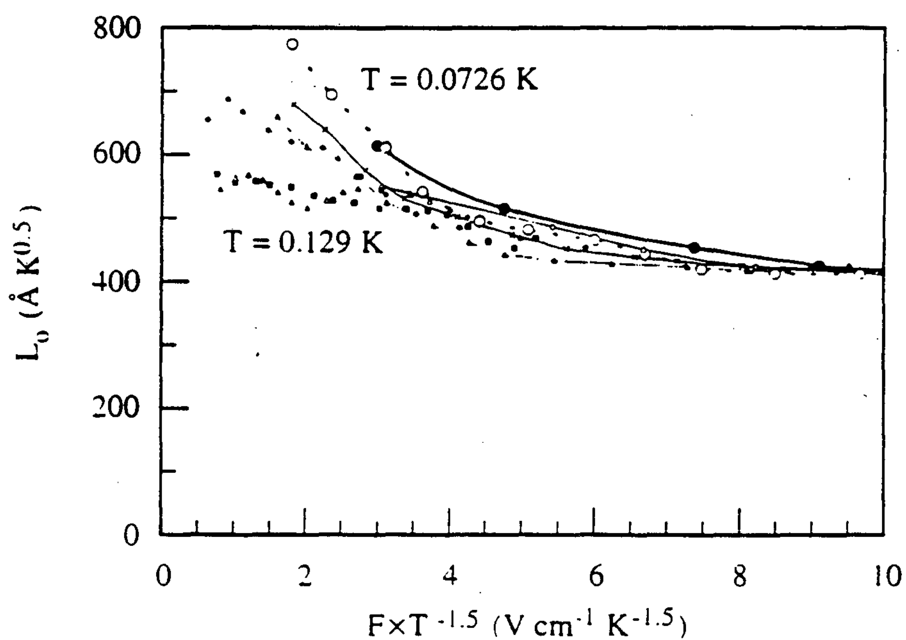

Fig. 3.15 Measured dependence of the parameter L_o on $F\times T^{-1.5}$ in $^{nat}Ge:Ga$ with an impurity concentration $N = 0.50N_c$. The data were measured over the temperature range $0.073\ K \leq T \leq 0.129\ K$.

Sample	N (10^{16} cm^{-3})	N/N$_c$	σ_0 (Ω cm)$^{-1}$	T$_0$ (K)
70Ge-3.3	3.02	0.16	2.94	365
70Ge-2.98	8.00	0.42	135	248
70Ge-1.90	9.36	0.50	526	201
70Ge-1.65	14.5	0.77	1670	100

Table 3.3 Parameters describing the NTD ^{70}Ge:Ga samples studied in this work. N is the net impurity concentration. The parameters σ_0 and T_0 are defined in Equation 3.4. The critical concentration N_c is 1.89×10^{17} cm^{-3}.

As the impurity concentration increases above $0.27N_c$ and nears the critical concentration for a metal-insulator transition, the non-Ohmic impurity conductivity can no longer be collapsed onto a single curve. Figures 3.14 and 3.15 show the measured dependence of L_0 on $F\times T^{-1.5}$ for the impurity concentrations $N = 0.34\ N_c$ and $0.50\ N_c$. L_0 is a measure of the strength of the non-Ohmic behavior. As the impurity concentration increases, we observe the surprising result that L_0 does not decrease in weak electric fields. The data do not show an Ohmic regime ($L_0 = 0$) or a weaker field dependence of the conductivity in small fields. Instead the conductivity begins to depend more strongly on the applied field in weak electric fields. This result is not predicted by any theory of non-Ohmic impurity conduction. We note that for field strength > 10 V cm^{-1} K$^{-1.5}$, the parameter L_0 approaches the value 450 ÅK$^{0.5}$ that it has for the more lightly doped samples. We will present a possible explanation for this surprising behavior after describing similar results from Experiment 2.

3.3.2 Experiment 2

We have also measured the electric field dependence of the conductivity of four uncompensated ^{70}Ge:Ga samples with impurity concentrations between $0.16N_c$ and $0.77N_c$. As in Experiment 1, the conductivity in the weak field limit is extremely well

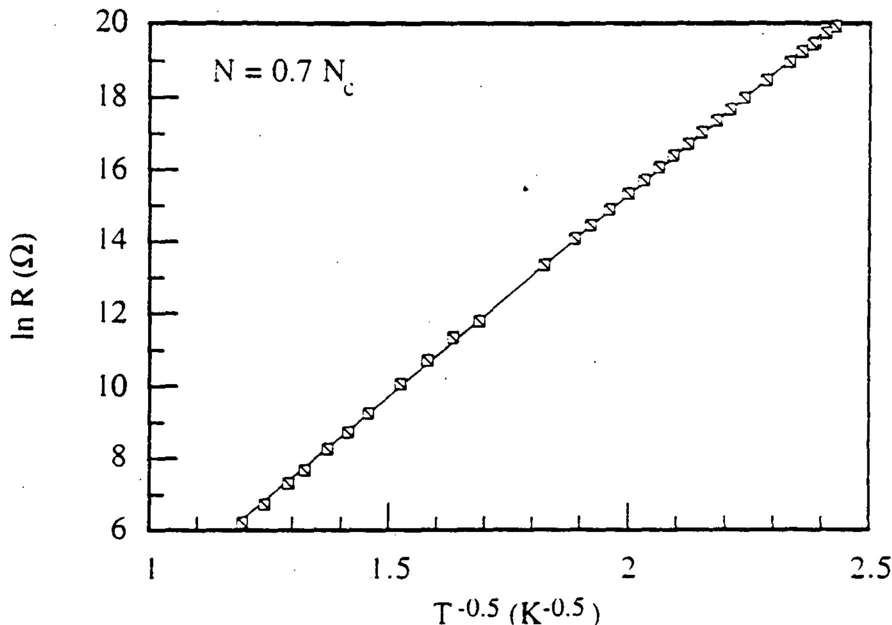

Fig. 3.16 Temperature dependence of the resistance of a ^{70}Ge:Ga sample. The data are extremely well described by Equation 3.4 over more than six orders of magnitude in resistance.

described by Equation 3.4 for n = 1/2 variable range hopping. A typical measurement of the temperature dependence of the resistance is shown in Figure 3.16. The resistance can be described by Equation 3.4 over more than six orders of magnitude in resistance. The parameters describing the NTD ^{70}Ge:Ga samples are summarized in Table 3.3.

Figures 3.17, 3.18, 3.19, and 3.20 show the measured electric field dependence of the resistance of the four ^{70}Ge:Ga samples. The impurity concentrations are indicated in the top right corner of each figure. The data have been plotted in the same fashion as the data in Experiment 1. We have computed the derivative of ln σ with respect to $F\times T^{-1.5}$ at each data point and used Equation 3.9 to determine the parameter L_0. We then plot L_0 as a function of $F\times T^{-1.5}$. We again observe that L_0 depends strongly on F, and that as the impurity concentration increases the conductivity begins to depend more strongly on the applied field in weak electric fields. The non-Ohmic behavior of the most lightly doped

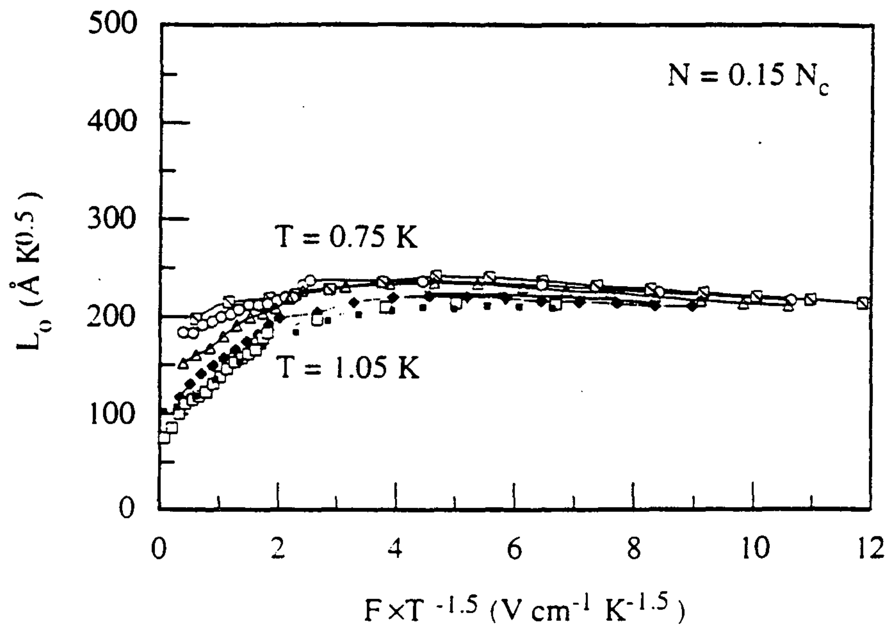

Fig. 3.17 Electric field dependence of the conductivity of ^{70}Ge:Ga with an impurity concentration $N = 0.15N_C$.

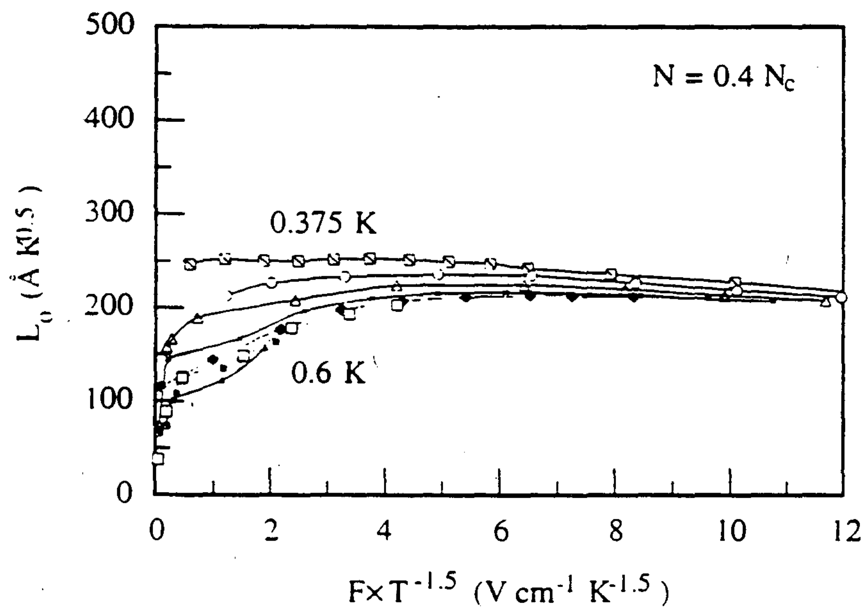

Fig. 3.18 Electric field dependence of the conductivity of ^{70}Ge:Ga with an impurity concentration $N = 0.40N_C$.

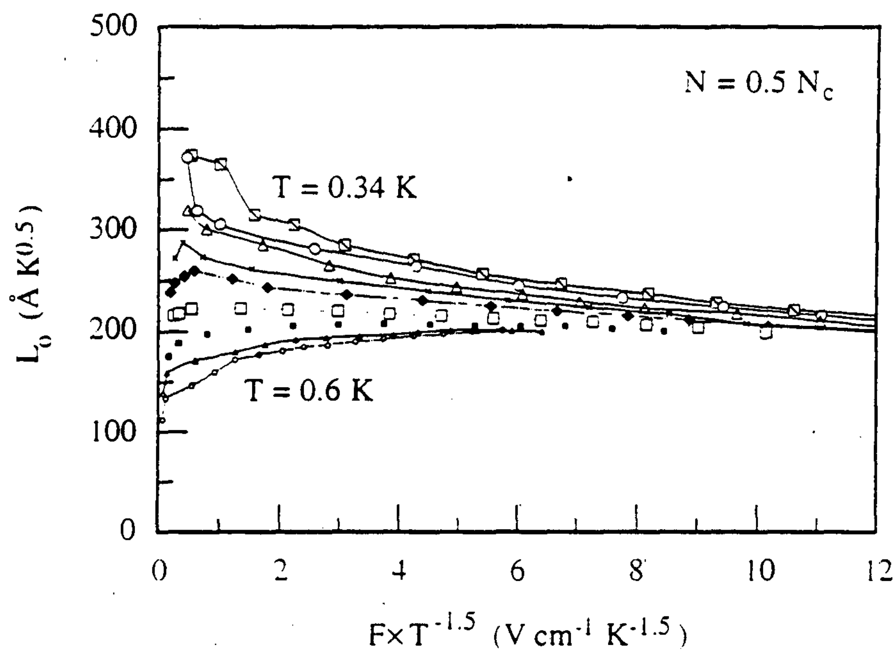

Fig. 3.19 Electric field dependence of the conductivity of $^{70}Ge:Ga$ with an impurity concentration $N = 0.50N_c$.

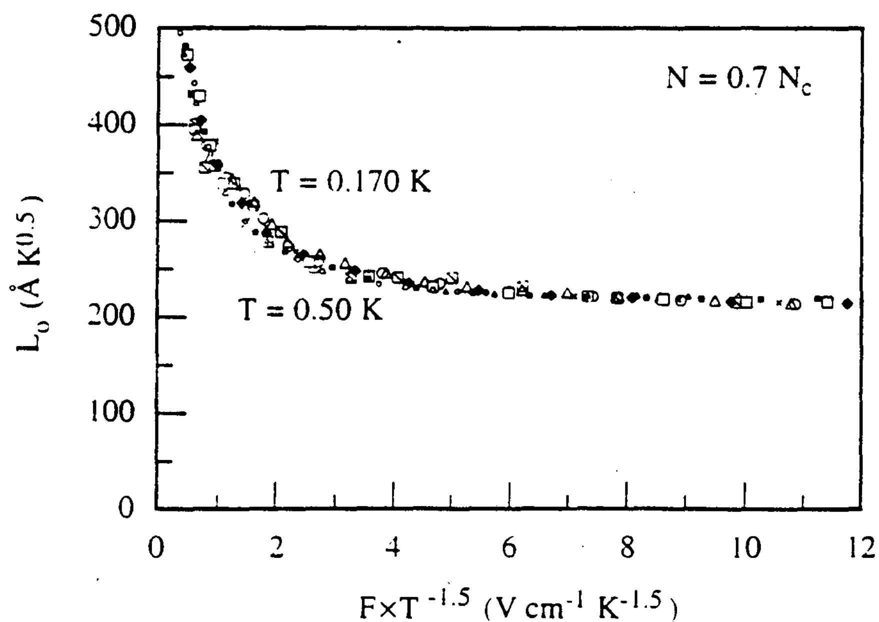

Fig. 3.20 Electric field dependence of the conductivity of $^{70}Ge:Ga$ with an impurity concentration $N = 0.77N_c$.

sample with an impurity concentration $N = 0.14\ N_c$ can be collapsed onto a curve similar in shape to the universal curve observed in Experiment 1.

We note that the parameter L_o is approximately 225 Å×K$^{0.5}$ for all four samples when F×T$^{-1.5}$ is greater than 8 Vcm^{-1}K$^{-1.5}$. This result is similar to that of Experiment 1, for which L_o is approximately 450 Å×K$^{0.5}$ when F×T$^{-1.5}$ is greater than 10 Vcm^{-1}K$^{-1.5}$.

The non-Ohmic impurity conduction in the most heavily doped sample with an impurity concentration $N = 0.77\ N_c$ can be described by a single curve which is inverted in shape from the universal curve observed in lightly doped ^{nat}Ge:Ga. The data in this curve were measured over a range of temperature $0.17\ K < T < 0.50\ K$ and a range of resistance $10\ k\Omega < R < 1\ G\Omega$. The dependence of the conductivity on electric field is proportional to L_o and is more than twice as strong in weak fields as in moderate fields for this sample.

Although no theory has been developed for non-Ohmic impurity conduction in moderately and heavily doped semiconductors, we propose a possible explanation for this unexpected behavior based on the effect of an electric field on the impurity wavefunctions.

3.3.3 Effect of an electric field on the impurity wavefunctions

3.3.3.1 Wannier-Stark localization in a regular crystal lattice

Before describing the effect of an applied field on an electron state in a disordered lattice, we review the case of a regular crystal lattice in order to distinguish between the two behaviors. The dynamics of an electron in a regular crystal lattice subjected to a uniform, static electric field is one of the classic topics in solid state physics [Holthaus et al., 1995]. Wannier [1960] proposed that at very low temperatures, a conduction electron moving in an ideal lattice free from scattering by impurities, imperfections, and lattice vibrations will become localized under the application of an electric field F. An infinite set of localized eigenstates equally spaced in energy will be created, known as the Wannier-Stark ladder. The separation between the energy levels is $\Delta E = eFa$, where a is the lattice spacing. An electron at a given energy level becomes localized over a radius ξ defined by

$$\xi = W/eF, \tag{3.10}$$

where W is the width of the original energy band. This localization mechanism is much weaker than the disorder-driven Anderson localization which occurs in disordered systems.

3.3.3.2 Disordered systems

Although theoretical models of non-Ohmic impurity conduction neglect the effect of an applied electric field on the impurity wavefunctions, an electric field may strongly influence the electron localization in disordered systems. The theory of Anderson localization in an electric field has been a controversial issue for many years. The model which has been studied is that of electrons propagating in a random potential. When an electric field is applied, the electrons gain kinetic energy by accelerating against the direction of the field.

According to Altshuler *et al.* [1981], a static electric field should not directly affect the electron wavefunction because it preserves time reversal symmetry. However, Altshuler neglected the decrease in scattering probability with increasing electron energy. Bryksin *et al.* [1994] found that for a one-dimensional disordered system, power-law localization emerges at small but finite electric fields. At some critical value of the field a mobility edge appears, above which the electrons are delocalized. Another study by Kirkpatrick [1986] concluded that all two- and three- dimensional electronic states are delocalized in a finite electric field. Jayannavar [1989] also found a field-induced delocalization in three-dimensional disordered systems with a mobility edge which shifts further into the localized regime with increasing electric field.

The above studies do not apply to all localized impurity states found in doped semiconductors, because strongly localized impurity electrons are not free to gain kinetic energy under an applied electric field. We propose a model for the effect of an electric field

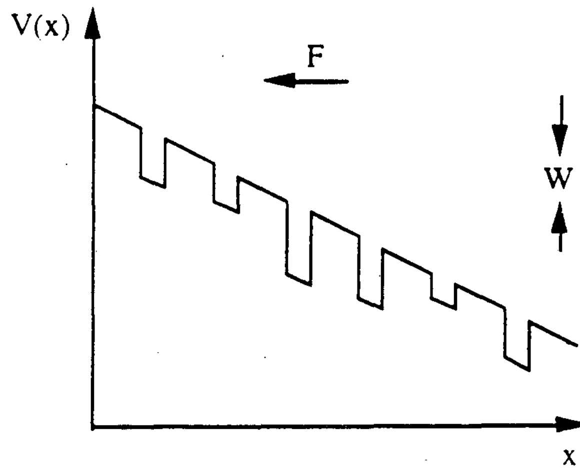

Fig. 3.21 Anderson localization in an applied electric field.

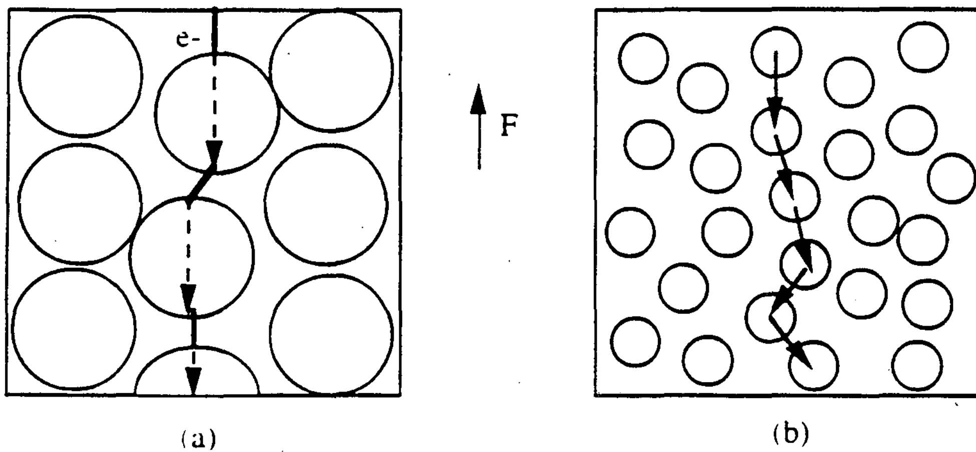

Fig. 3.22 Proposed model for the effect of an electric field on the impurity wavefunctions. (a) $F = 0$; (b) $F > 0$.

on the impurity wavefunctions which we apply to the anomalous non-Ohmic impurity conduction observed in ^{nat}Ge:Ga and ^{70}Ge:Ga as N approaches N_c. Instead of the field-induced delocalization found for electrons moving in a random potential, we propose a field-induced localization of extended impurity states.

3.3.3.3 Proposed model of Anderson localization in an electric field

Whereas Wannier-Stark localization arises from a static electric field applied across a perfect crystal lattice, Anderson localization is the result of random disorder in the energy levels of sites on a regularly spaced lattice as discussed in Section 1.6. We consider a static electric field F applied across a lattice with randomly disordered energy levels with a spread in energy given by W. The effect of F is to locally increase W over a region x by an amount eFx as shown in Figure 3.21. Anderson's result is that impurity states will be localized for sufficiently large values of W/I where I is the energy overlap integral between neighboring sites. Therefore, we propose that the effect of F on the impurity wavefunctions is to increase W and thus to induce localization.

Figure 3.22 shows the effect of an electric field on the impurity wavefunctions in this model. As the field increases, the localization radius of the impurity wavefunctions decreases and hopping electrons can no longer move as freely under an applied electric field. In other words, when F is small the hopping electrons can accelerate and gain energy from the field over the distance of their localization radius. However, as F increases the electrons become strongly localized and gain less energy from the field. The center-to-center distance between hops decreases as F increases, leading to a decrease in the parameter L_0.

3.3.4 Experiment 3

Our final study of non-Ohmic impurity conduction in doped semiconductors was performed on two uncompensated ^{74}Ge:As samples with impurity concentrations $N_1 = 0.17N_c$ and $N_2 = 0.51N_c$, where $N_c \approx 3.5 \times 10^{17}$ cm^{-3} is the critical concentration for a metal insulator transition in Ge:As. The temperature dependence of the conductivity in the weak field limit is shown in Figure 3.23. Because the conductivity was not described by the well-understood n=1/2 variable range hopping mechanism as in Experiment 1 and 2, we performed a careful analysis of the $\sigma(T)$ for temperatures 1.15 K < T < 10.4 K in Sample 1 and for temperatures 0.5 K < T < 10.4 K in Sample 2. These temperature ranges

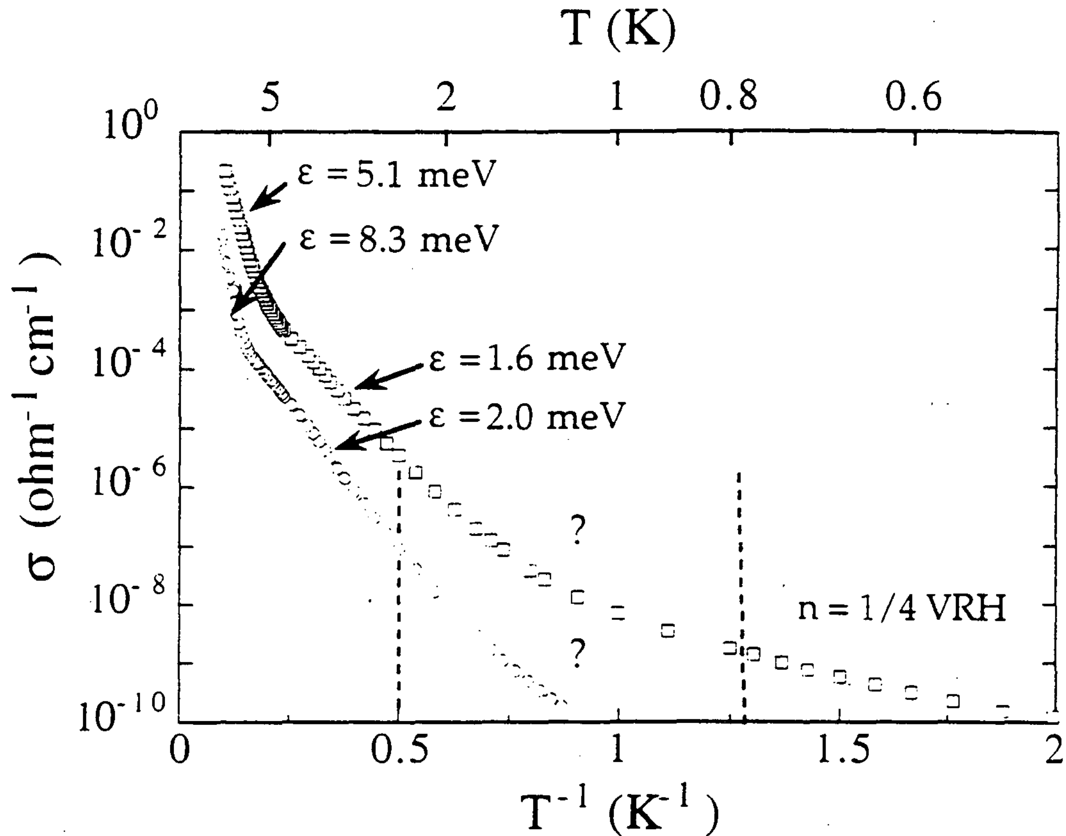

Fig. 3.23 Measured temperature dependence of the conductivity as a function of temperature of two ^{74}Ge:As samples for an electric field strength F ~ 0.05 V/cm indicating the various conduction regimes discussed in the text. In the regions marked with a question mark, the conductivity is in transition between ε_2 conduction and n = 1/4 VRH conduction. The structure of the impurity band is not well understood over this region.

correspond to a range in conductivity of approximately $10^{-10}\ \Omega^{-1}\text{cm}^{-1} < \Omega < 10^{-1}\ \Omega^{-1}\text{cm}^{-1}$. We determined the best fit to $\sigma(T) \propto \exp[-(\Delta/kT)^n]$ over several temperature ranges in each sample in order to identify the various conduction regimes. The results of this analysis are summarized in Table 3.4. At higher temperatures the dominant conduction mechanism in both samples is ε_1 activated conduction. At temperatures T < 4 K the activation energies of both samples were characteristic of ε_2 conduction. At the lowest temperatures studied in Sample 2, T < 0.73 K, we found that Mott n = 1/4 VRH conduction predominated. These

Sample	T(K)	n	DCM	Δ (meV)	σ_0 ($\Omega^{-1}cm^{-1}$)
1	2.5 - 3.9	1.03 ± 0.06	ε_2 (n = 1)	2.02 ± 0.02	0.0101
1	8.1 - 10.4	0.98 ± 0.1	ε_1 (n = 1)	8.25 ± 0.06	183
2	0.5 - 0.73	0.26 ± 0.1	VRH (n = 1/4)	$(1.63 \pm 0.1)\times10^4$	6.09
2	2.5 - 3.7	0.97 ± 0.07	ε_2 (n = 1)	1.65 ± 0.02	0.0436
2	6.1 - 9.8	0.98 ± 0.07	ε_1 (n = 1)	5.15 ± 0.03	94.4

Table 3.4 Measured conductivity parameters of the two 74Ge:As samples studied in Experiment 3. The best fit parameters are for the function $\sigma(T) = \sigma_0\times\exp[-(\Delta/kT)^n]$ over temperature ranges where a dominant conduction mechanism (DCM) can be identified. Over the temperature ranges not represented here, the conductivity is in transition and cannot be described by constant values of n and Δ.

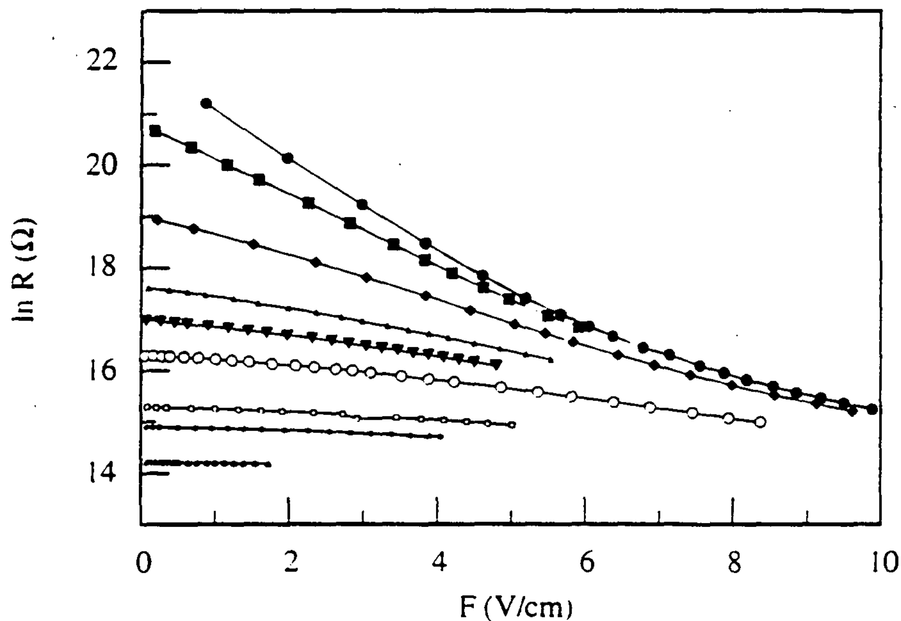

Fig. 3.24 Measured electric field dependence of the resistance of ^{74}Ge:As Sample 2. The curves were measured at the following temperatures, from top to bottom: 0.5 K, 0.6 K, 0.8 K, 1.0 K, 1.1 K, 1.2 K, 1.36 K, 1.4 K, and 1.5 K.

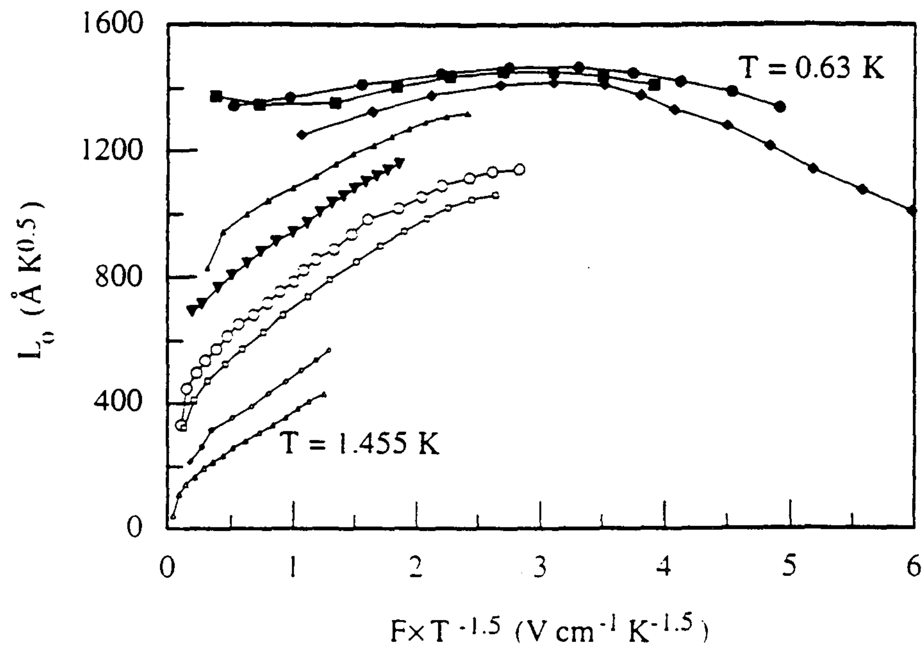

Fig. 3.25 Data from Fig. 3.24 replotted in a different form. The results for the ^{74}Ge:As samples are different from those for the samples in Experiments 1 and 2.

results are in extremely good agreement with the recent experimental results of Gershenzon *et al.* [1991] for moderately doped p-type and n-type Si with very low compensation.

The electric field dependence of the conductivity of Sample 2 is shown in Figure 3.24. The field dependence of Sample 2 was measured over the temperature range 0.5 K < T < 1.5 K. Similar curves were measured in Sample 1. We have taken the derivative of ln σ with respect to $F \times T^{-1.5}$ at each data point and used Equation 3.9 to determine the parameter L_0. Figure 3.25 shows the data from Figure 3.24 replotted in the form L_0 as a function of $F \times T^{-1.5}$. The non-Ohmic conductivity behaves quite differently than the non-Ohmic conductivity in Experiments 1 and 2. At temperatures below 0.73 K the data are described by a single curve, but at higher temperatures the electric field dependence is weaker and varies strongly with temperature.

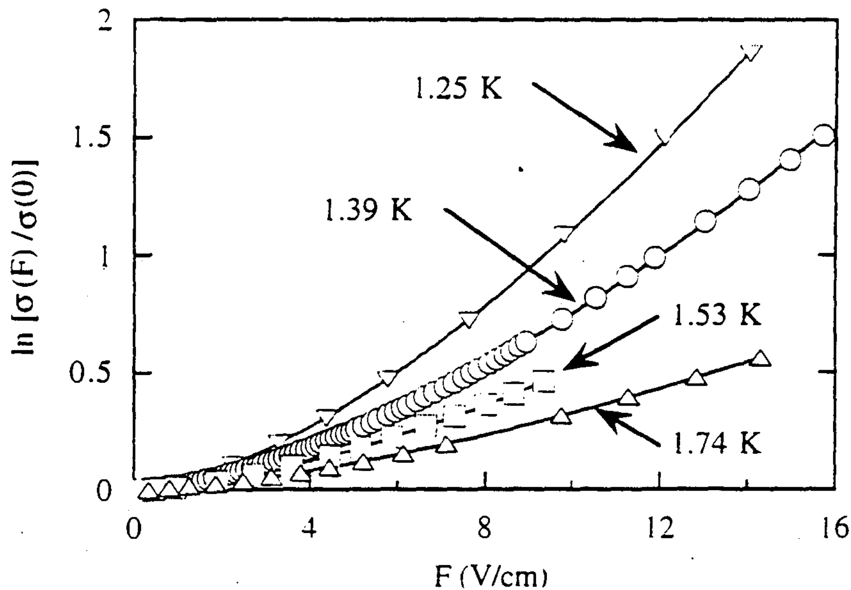

Fig. 3.26 Measured electric field dependence of the conductivity for ^{74}Ge:As Sample 1 at various temperatures between 1.25 K and 1.74 K.

Because the electric field dependence of the conductivity was not well described by either the theory of non-Ohmic hopping conduction in moderate fields discussed in Section 2.1.3.3 or by the universal curve observed in Experiments 1 and 2, we searched for a new fitting function for the data. At each temperature we fit $\sigma(F,T)$ using the following general function typical of phonon-assisted non-Ohmic impurity transport described in Section 2.1.3.6:

$$\sigma(F,T) = \sigma(0,T) \times \exp(AF^x), \qquad (3.11)$$

where $\sigma(0,T)$, A, and x are fitting parameters. We describe the results of using Equation 3.11 to fit the field dependence of the conductivity in Samples 1 and 2.

3.3.4.1 ^{74}Ge:As, Sample 1: $N = 0.17\ N_c$

We measured $\sigma(F,T)$ in Sample 1 for field strengths 2 Vcm^{-1} < F < 16 Vcm^{-1} and temperatures 1.15 K < T < 1.74 K as shown in Figure 3.26. Over this temperature range

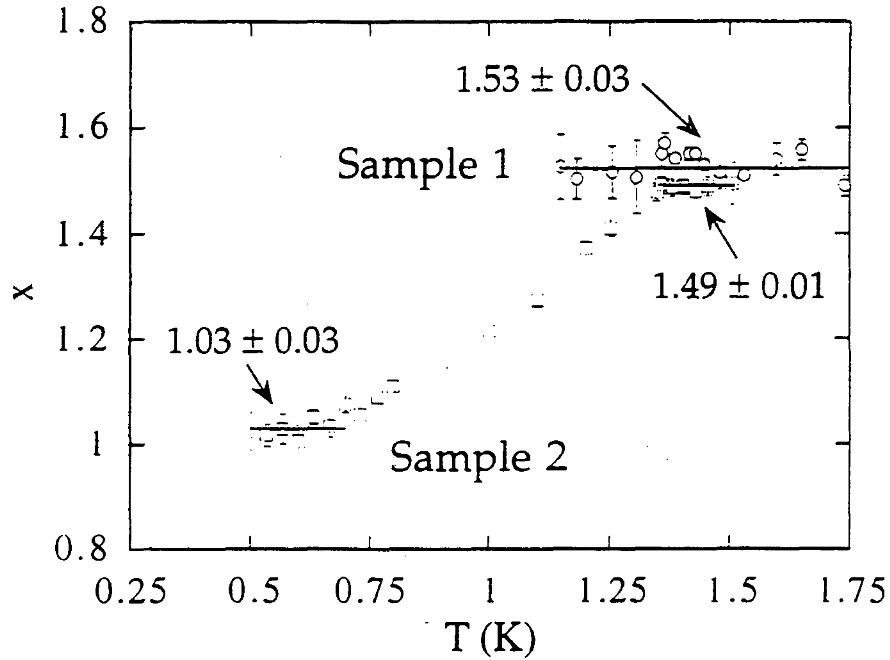

Fig. 3.27 Temperature dependence of the parameter x from Equation 3.11. (1) Sample 1, denoted by circles; (2) Sample 2, denoted by squares. Error bars of $\pm 2\sigma$ have been included for each data point.

the conduction mechanism was intermediate between ε_2 conduction and variable range hopping conduction. The average best fit exponent x to Equation 3.11 over this temperature range was 1.53 ± 0.03. The measured values of x at each temperature are plotted in Figure 3.27.

The exponent $x \approx 1.5$ has not been previously reported. However, it provides an extraordinarily good fit to the data. Figure 3.28 shows the field dependence of $\ln \sigma$ measured in Sample 1 at 1.39 K plotted as a function of $F^{1.5}$. The data are extremely well fit by a straight line. In Figure 3.29 the data from Figure 3.28 have been differentiated to obtain the dependence of the parameter x on electric field. The data are fit by the exponent $x = 1.5$ over the entire range of fields.

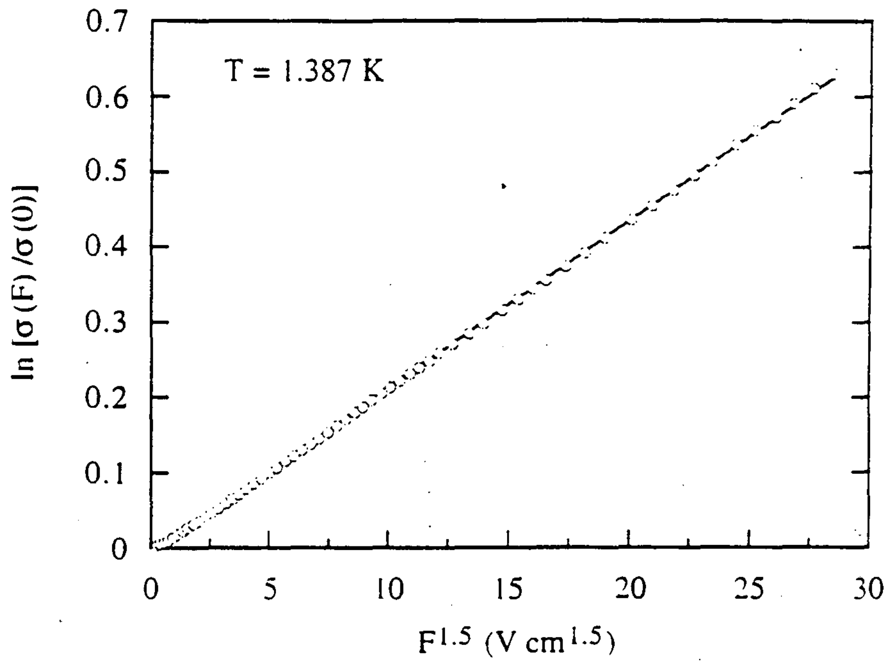

Fig. 3.28 Measured dependence of ln σ on $F^{1.5}$. The data are extremely well described by a straight line over the entire range of electric fields.

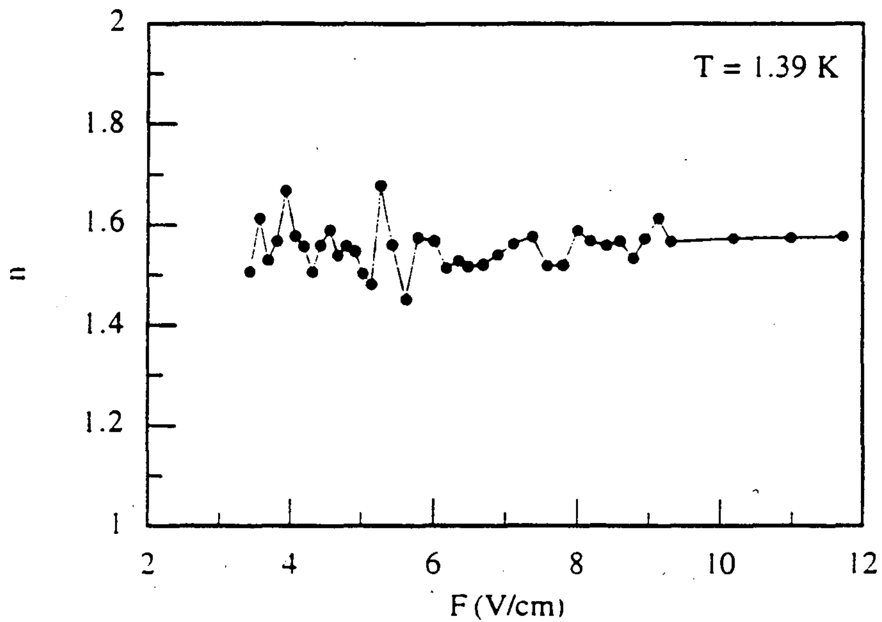

Fig. 3.29 Exponent x from Equation 3.11 as a function of electric field. The data are described by $x \approx 1.54$ over the entire range of fields.

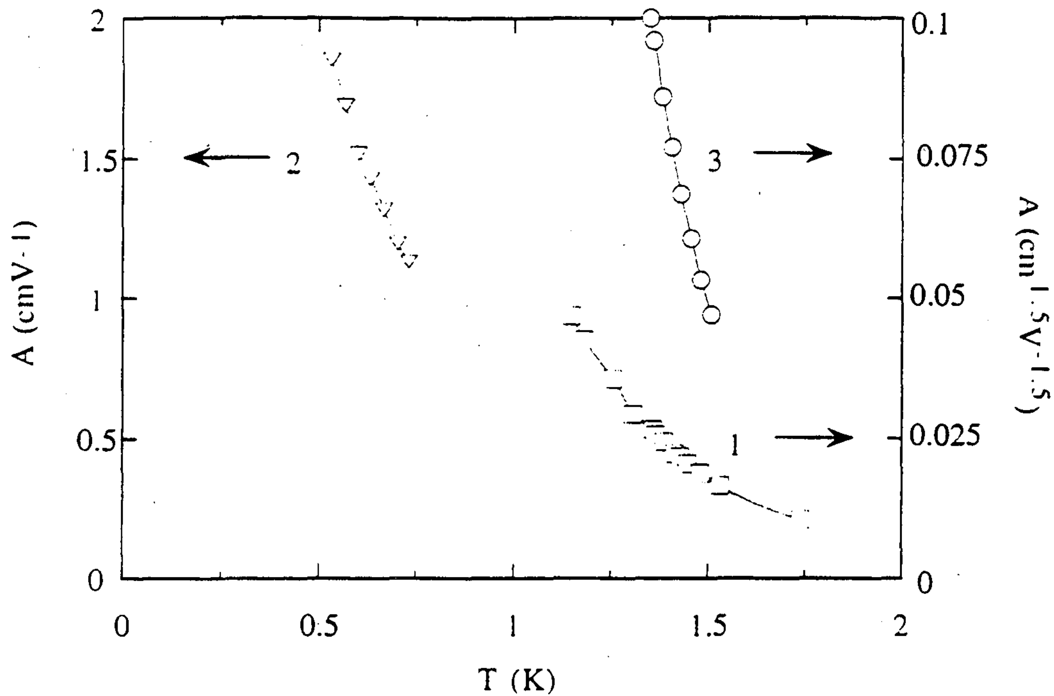

Fig. 3.30 Temperature dependence of the parameter A from Equation 1. The error in each value of A is estimated to be ~ 1%. (1) Sample 1, x = 1.5; (2) Sample 2, x = 1; (3) Sample 2, x = 1.5.

We determined the temperature dependence of the non-Ohmic impurity conduction in Sample 1 by setting x = 1.5 in Equation 3.11 and fitting the data to $\sigma(F,T) = \sigma(0,T)\times\exp(AF^{1.5})$ at each temperature. We found that A(T) was extremely well described by the power law dependence $A(T) = CT^{-3.66 \pm 0.09}$ with C = 0.080 $(cm/V)^{3/2}$. The temperature dependence of A is plotted in Figure 3.30, Curve 1. This temperature dependence is much stronger than seen in any previous study of non-Ohmic impurity conduction.

3.3.4.2 ^{74}Ge:As, Sample 2: N = 0.51 N_c

We used the same procedure to determine the best fit values of x and A in Sample 2. At the lowest temperatures measured, 0.5 K < T < 0.73 K, the conductivity in the weak

field limit was described by $n = 1/4$ variable range hopping conduction. Over this temperature range the average best fit exponent x to Equation 3.11 was 1.03 ± 0.03. Thus when the conductivity proceeds by variable range hopping, the non-Ohmic behavior is very well described by the standard theory for moderate electric fields, $\sigma(F) \propto \exp(eFL/kT)$. The measured values of x at each temperature are plotted in Figure 3.27 as Curve 2.

We determined the temperature dependence of the non-Ohmic impurity conduction in Sample 2 by setting $x = 1.0$ in Equation 3.11 and fitting the data to $\sigma(F,T) = \sigma(0,T)\times\exp(AF)$ at each temperature. The temperature dependence of A is plotted in Figure 3.30 as Curve 2. We found that $A(T) = CT^{-1.56 \pm 0.06}$ with $C = 0.69$ cm/V. The theoretical model of Levin and Shklovskii [1984] discussed in Section 2.1.3.3 predicts a field dependence $\sigma(F,T) = \sigma(0,T)\exp(CFT^{-1.5})$, where C is of order unity in units of cm/V. Our measurements for temperatures $0.5 \text{ K} < T < 0.73 \text{ K}$ are therefore in complete agreement with this prediction within the limits of our error. Due to our inability to measure resistances greater than 2 GΩ, we were unable to determine whether Sample 1 also showed a transition to $n = 1/4$ VRH with a different electric field dependence of the conductivity at temperatures less than 1.15 K.

As the temperature of Sample 2 was increased from 0.75 K to 1.5 K, the conduction mechanism was in transition between $n = 1/4$ variable range hopping conduction and ε_2 conduction. Over the temperature range $0.73 \text{ K} < T < 1.35 \text{ K}$, the best fit exponent x to Equation 3.11 increased monotonically from 1.06 to 1.48. Over the temperature range $1.35 \text{ K} < T < 1.5 \text{ K}$, the average value of x was 1.49 ± 0.01 as shown in Figure 3.27, Curve 2. Within a small margin of error this is identical to the value of $x = 1.5$ observed in Sample 1.

We determined the temperature dependence of the non-Ohmic impurity conduction in Sample 2 over the temperature range $1.35 \text{ K} < T < 1.5 \text{ K}$ by setting $x = 1.5$ in Equation 3.11 and fitting the data to $\sigma(F,T) = \sigma(0,T)\times\exp(AF^{1.5})$ at each temperature. The temperature dependence of A is plotted in Figure 3.30, Curve 3. We found that A(T) =

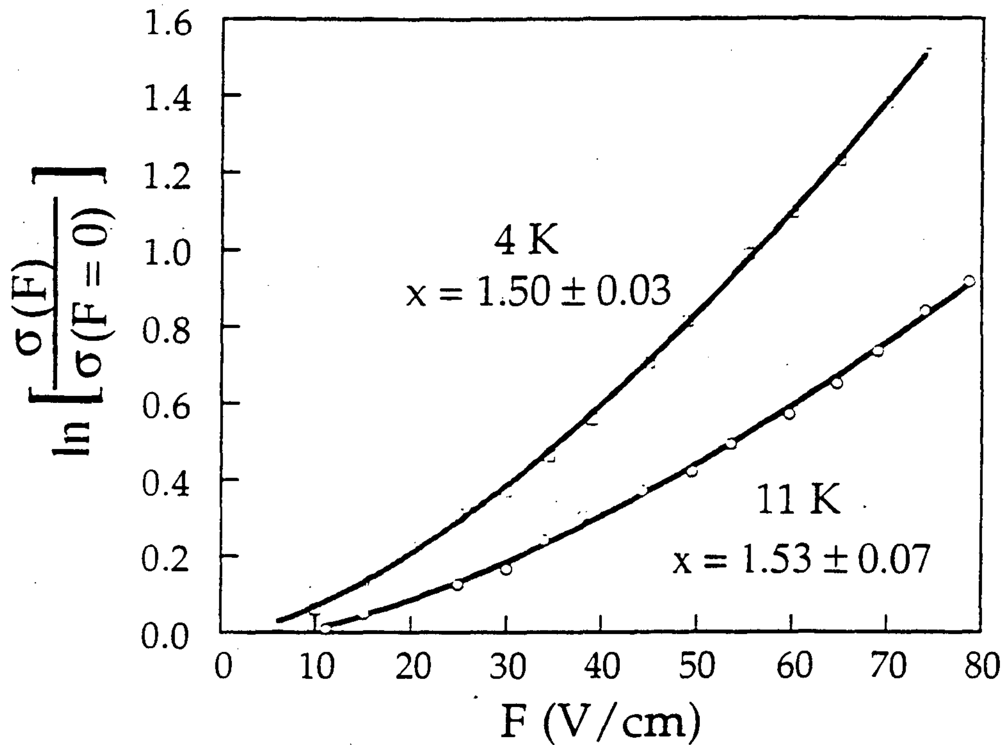

Fig. 3.31 Field dependence of the conductivity of Ge:Sb with an impurity concentration $N \approx 0.67N_c$ adapted from the published data of Matveev *et al.* [1993]. The data are very well described by the exponent x = 1.5 in Equation 3.11.

$CT^{-6.81 \pm 0.14}$ with C = 0.78 $(cm/V)^{3/2}$ (Figure 4. Curve 3). A(T) could also be described by the exponential temperature dependence A(T) = C × exp(-4.78T) where C = 63.7 $(cm/V)^{3/2}$. This exceptionally strong temperature dependence is much stronger than seen in any previous study of non-Ohmic impurity conduction and is stronger than observed in Sample 1.

Although the field dependence $\sigma(F) \propto \exp(AF^{3/2})$ has not been previously reported in the literature. Matveev *et al.* [1993] did recently measure the non-Ohmic hopping conductivity in a Ge:Sb sample doped with an impurity concentration $0.67N_c \approx 1 \times 10^{17}$ cm^{-3}. Thus their sample is more heavily doped relative to the MIT than Sample 2 in our

study. The dominant conduction mechanism in the ohmic limit was determined to be activation into extended states in the impurity band with a constant activation energy 0.4 meV over the temperature range $2.5 \text{ K} < T < 12 \text{ K}$. Their study was unusual because they were examining the non-Ohmic dependence of the activated conduction into extended states rather than variable range hopping conduction between localized states.

Matveev *et al.* measured $\sigma(F)$ at $T = 4.2$ K and $T = 11$ K for $5 \text{ Vcm}^{-1} < F < 120 \text{ Vcm}^{-1}$, and assumed the exponent $x = 1$ in Equation 3.11. However, when we determined the best fit value of x using their published data we found that $x = 1.50 \pm 0.03$ at 4.2 K and $x = 1.53 \pm 0.07$ at 11 K. This is in complete agreement with the value $x = 1.49 \pm 0.01$ that we find in Sample 2 for $1.35 \text{ K} < T < 1.50 \text{ K}$ within the limits set by experimental error. When we assumed the fitting function $\sigma(F,T) \propto \exp(AF^{3/2})$, we found that the data of Matveev *et al.* was well described by $A = 5.46 \times 10^{-3} \text{ (cm/V)}^{3/2}$ at $T = 4.2$ K and $A = 3.11 \times 10^{-3} \text{ (cm/V)}^{3/2}$ at $T = 11$ K. These values indicate a significantly weaker temperature dependence $A(T)$ than that observed by us in Sample 2.

Although no theory has been developed for non-Ohmic impurity conduction when the conduction mechanism is not hopping between localized states, our model of electric field-induced localization of impurity sites (Section 3.3.3.3) suggests a possible explanation for the observed dependence $\sigma(F,T) \propto \exp(AF^{3/2})$. We propose that $AF^{3/2} = eFL/kT$. In other words, we assume that the field dependence of the conductivity has an activated form, where eFL is the activation energy. With this assumption we find that the length parameter L has an electric field dependence

$$L = (AkT/e)\sqrt{F}. \tag{3.12}$$

Figure 3.32 shows the dependence of L on electric field at 1.4 K for the 74Ge:As samples, determined using Equation 3.12.

From the temperature dependence of the conductivity in the weak field limit, we know that when we observe the field dependence $\sigma(F,T) \propto \exp(AF^{3/2})$ the conductivity is in transition between variable range hopping and ε_2 conduction. Since the impurity states

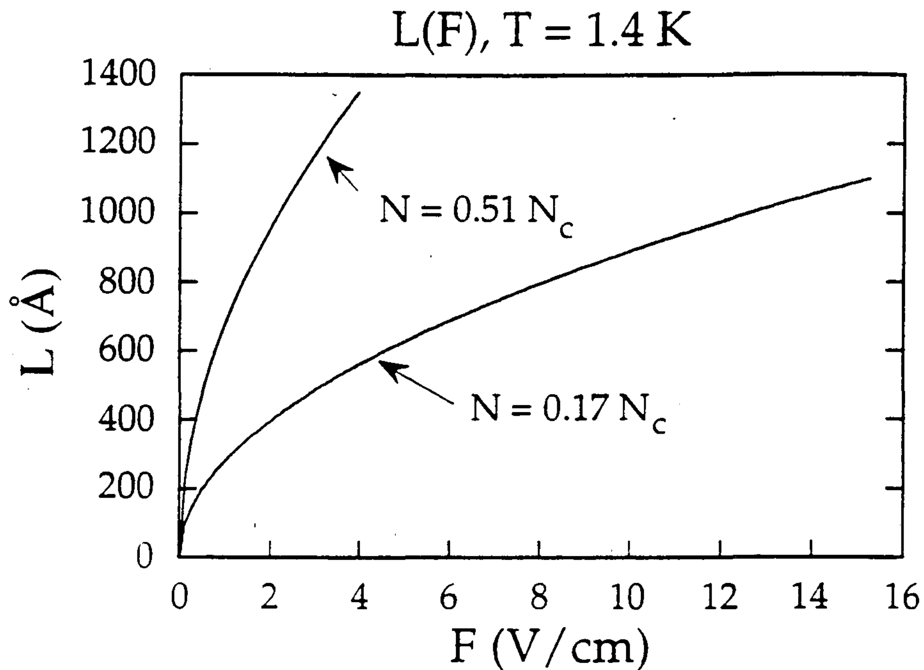

Fig. 3.32 Dependence of the length parameter L on electric field when the conduction is described by $\sigma(F,T) \propto \exp(AF^{3/2})$, calculated using Equation 3.12.

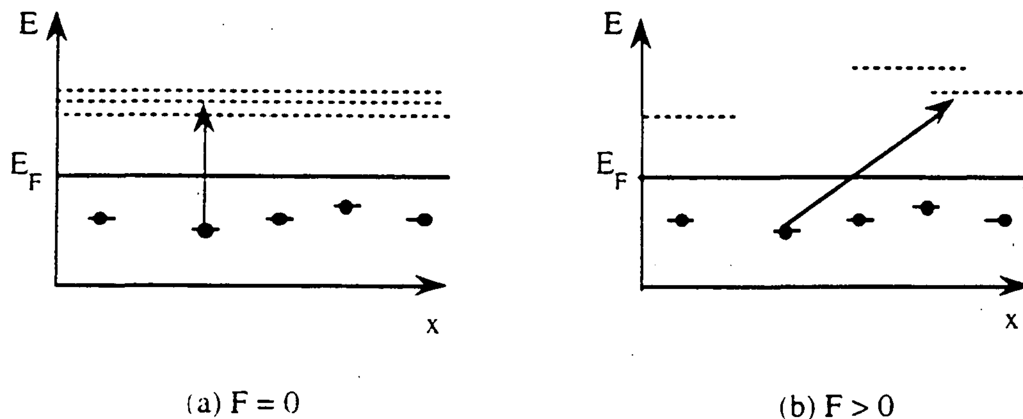

Fig. 3.33 Proposed model for the effect of an electric field on non-Ohmic impurity conduction into extended states in the impurity band. When F = 0, the average hop distance is 0 because electrons can make direct transitions in energy. However, due to electric field-induced localization of the extended states, under an applied field the electrons must hop some distance L which is proportional to $\sqrt{F}$.

are localized for variable range hopping and extended for ε_2 conduction, we can assume that in the transition region the impurity states are either weakly localized or extended on the verge of becoming localized. If our model of electric field-induced localization of the impurity wavefunctions is correct, then the weakly localized states or marginally extended states will shrink under the application of an electric field as shown in Figure 3.33. In the Anderson model the spread in energy W over a distance ζ is $W \sim eF\zeta$. Therefore $\zeta \sim 1/F$. In variable range hopping conduction with Coulomb interactions between impurities, the hop length R is proportional to $(e^2/\kappa\zeta)^{1/2}$. Since $\zeta \sim 1/F$, we find that $R \sim F^{1/2}$ and hence that $eFL \propto eFR \propto F^{3/2}$. From this argument we obtain the observed field dependence $\sigma \propto \exp(AF)^{3/2}$.

In conclusion, we found that σ varied with applied electric field F and temperature T as $ln\ [\sigma(F,T)/\sigma(0,T)] \propto F^{1.5}\times T^{-3.7}$ in Sample 1 and as $ln\ [\sigma(E,T)/\sigma(0,T)] \propto F^{1.5}\times T^{-6.8}$ in Sample 2. This well-defined new field dependence and the very strong temperature dependence are quite different from the well-known behavior of lightly doped semiconductors. These results, though surprising, do not conflict with previous theories which assume hopping between localized impurity states in a lightly doped semiconductor. Further study of this new, well-defined non-Ohmic behavior in moderately doped semiconductors may help to increase our understanding of the impurity band structure, the dependence of the impurity localization on an applied electric field, and the metal-insulator transition.

Chapter 4

Effect of stress on non-Ohmic impurity conduction

In this chapter we review the effects of stress on the impurity states in doped semiconductors. We present qualitative results on the effects of stress on non-Ohmic impurity conduction in neutron transmutation doped germanium. We show that stress can either enhance or suppress the magnitude and temperature dependence of the hopping length parameter L, depending on the orientation of the applied stress relative to the measurement axis.

4.1 Effect of stress on impurity states

Shallow donors and acceptors in doped semiconductors are hydrogen-like centers whose energies and wavefunctions are determined by the dielectric constant κ and the effective mass tensor m^* of the semiconductor host material, as described in Chapter 1. The hopping probability P_{ij} between an occupied impurity site (i) and a neighboring unoccupied impurity site (j) separated by a distance r_{ij} is proportional to the overlap integral between the impurity wavefunctions ψ_i and ψ_j:

$$P_{ij} \propto \exp\left(\frac{-2r_{ij}}{\zeta}\right). \tag{4.1}$$

Here ζ is the radius of the impurity wavefunction envelope. Under uniaxial stress, the impurity wavefunction becomes anisotropic. Rather than having a circular exponential dropoff with a single radius ζ, the impurity wavefunction envelope has an elliptical exponential dropoff with two radii ζ_1 and ζ_2. Figure 4.1 shows the elliptical surfaces of constant wavefunction about randomly located donors in a semiconductor crystal. A uniaxial stress is assumed to be applied along the z-axis. The wavefunction falls off more rapidly in the direction of stress. Therefore the hopping probability in the x and y directions is greater than the hopping probability in the z direction. This means that in

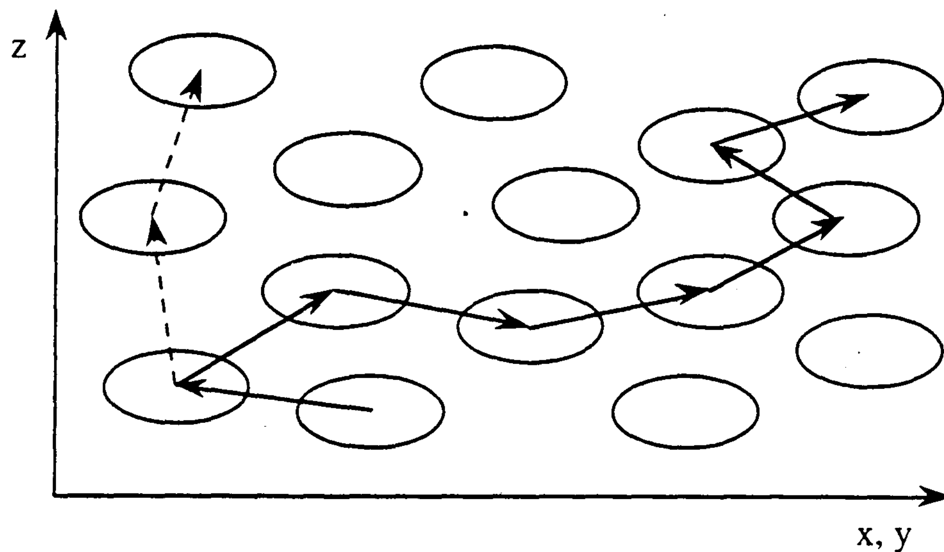

Fig. 4.1 The ellipses represent surfaces of constant wavefunction amplitude constructed about randomly located impurity sites. The z-axis points in the direction of compression; in this direction the wave function falls off faster. The arrows indicate electron hopping paths, which determine the resistances along the z- and x-y-axes. The dashed line shows a "head-on" path along the z-axis which corresponds to a much higher resistance.

order to move along the z-axis, an electron will most likely "tack" at an angle θ to the z-axis. The degree of tacking increases with increasing stress. In sections 4.1.1 and 4.1.2, we explain the origin of the elliptical dropoff of the impurity wavefunction with uniaxial stress in germanium. A general review of the effects of deformation on impurity states in doped semiconductors can be found in the textbook by Bir and Pikus [1974].

4.1.1 Effect of uniaxial stress on acceptor ground state in p-type germanium

The effects of uniaxial stress on impurity conduction in p-type Ge were first studied by Pollak [1965]. Pollak measured the nearest neighbor hopping resistivity ρ of p-type Ge as a function of uniaxial stress χ applied along the <100> direction. The function $\rho(\chi)$ was found to be non-monotonic; that is, as χ increased, ρ first increased by a factor of 2-5 and

then decreased by several orders of magnitude. The extent of the increase and decrease were found to depend on the temperature T and the impurity concentration N. Pollak's results were confirmed by subsequent measurements in p-type Si [Staunton and Pollak, 1967].

These results can be explained by examining the effect of stress on the valence band structure. Germanium and silicon crystallize in the diamond structure with the top of the valence band at the Γ point of the Brillouin zone. The valence band states near $k = 0$ are six-fold degenerate in the absence of the spin-orbit interaction. When spin-orbit coupling is taken into account, the valence band splits into two bands, which are four-fold and two-fold degenerate. The four-fold degenerate band consists of the heavy hole and light hole mass bands which are degenerate at Γ. The two-fold degenerate band is shifted down by the amount Δ, which is the energy of the spin-orbit interaction. In germanium, $\Delta = 0.29$ eV which is much larger than the binding energies $E_b \sim .01$ eV of shallow acceptors in Ge. The influence of the split-off band on the acceptor states can therefore be neglected.

When compressional stress is applied along the {111} axis it lifts the degeneracy of the valence band at Γ and splits the acceptor ground state. Chroboczek [1980] carried out the first detailed study of the behavior of acceptor wave functions at intermediate stress. Subsequent calculations [Chroboczek et al., 1981; Buczko and Chroboczek, 1984] account for the observed behavior of $\rho(\chi)$. The initial increase in ρ by a factor of 2-5 which occurs under the application of uniaxial stress can be attributed to the decrease in wavefunction overlap caused by the shrinkage of the acceptor wavefunctions in the direction of the applied stress. The strong decrease in ρ which occurs for larger values of stress is a result of the χ-induced decrease in the acceptor binding energies.

4.1.2 Effect of uniaxial stress on donor ground state in n-type germanium

In germanium there are four conduction band valleys corresponding to the minima in the {111} and equivalent directions. When a uniaxial stress is applied along the {111}

direction, the energy of the valley with its ellipsoidal axis along {111} is lowered while the other three valleys are shifted to higher energies. If we denote the band minimum of the *i*th valley by T_i, then

$$T_1 = -3T; T_2 = T_3 = T_4 = T, \tag{4.2}$$

where T is an energy shift proportional to the stress [Kamimura and Aoki. 1989]. At pressures of order 10^9 dyne/cm^2 this splitting becomes so large that the electron ground state of the donor atoms are no longer associated with all four valley ellipsoids as they are in the absence of pressure, but with one ellipsoid only [Shklovskii and Efros, 1984].

In contrast to unstressed germanium, where the electrical conductivity is a scalar quantity, germanium stressed along the {111} axis loses its cubic symmetry and becomes a uniaxial crystal [Shklovskii and Efros. 1984]. In this case the resistivity tensor has two independent components, ρ_{zz} and $\rho_{xx} = \rho_{yy}$. As in the case of p-type Ge, under the application of stress ρ_{zz} initially increases due to the decrease in wavefunction overlap along the z-direction.

4.2 Effect of stress on non-Ohmic hopping conduction

For the measurements described in Chapter 3, we took great care to ensure that the samples were unstressed by using Au wedge-bonded contacts to the samples. However, the effects of stress are generally ignored in the published literature on non-Ohmic impurity conduction. For example, Wang *et al.* [1991] studied two samples with an identical geometry and identical impurity concentrations. The samples differed in that one was glued to a substrate and the other was unstressed. Although the non-Ohmic impurity conduction differed significantly in the two samples, stress was not mentioned as a contributing factor.

We intentionally stressed several samples using silver epoxy, 907 epoxy, and immersion in a bead of GE varnish. We present the following qualitative argument to

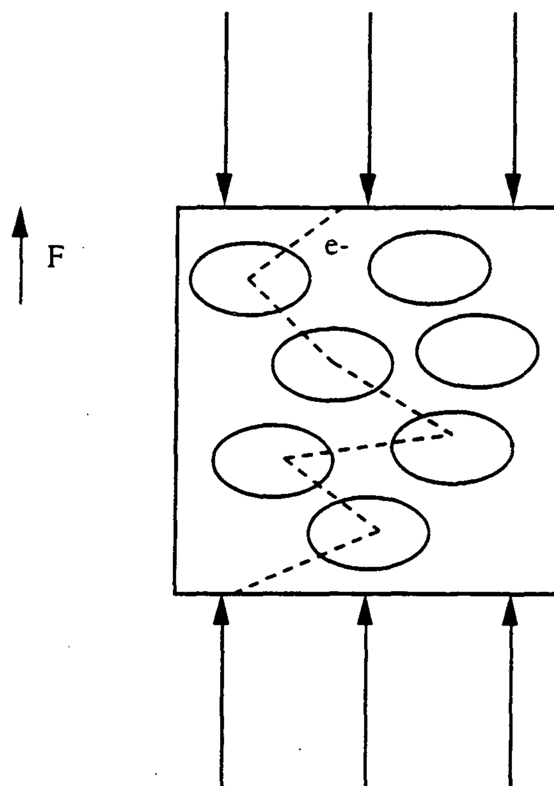

Fig. 4.2 The effect of stress in the direction parallel to the applied field is to shrink the wavefunctions in the direction of the field, reducing the magnitude of the field dependence of the conductivity. An example of this type of stress is a wire contact made to the sample with silver epoxy.

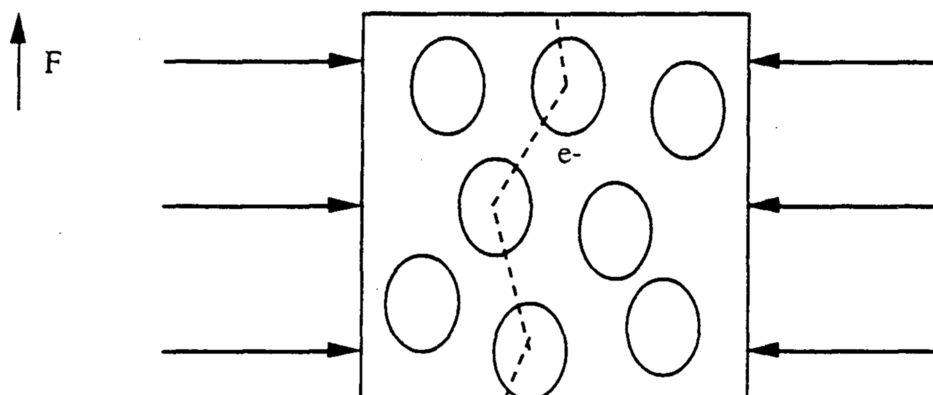

Fig. 4.3 The effect of stress in a direction perpendicular to the applied field is to enhance the hopping conductivity in the direction of the field, increasing the magnitude of the field dependence of the conductivity. An example of this type of stress is a 907 epoxy glue bond between the side of the sample and a substrate.

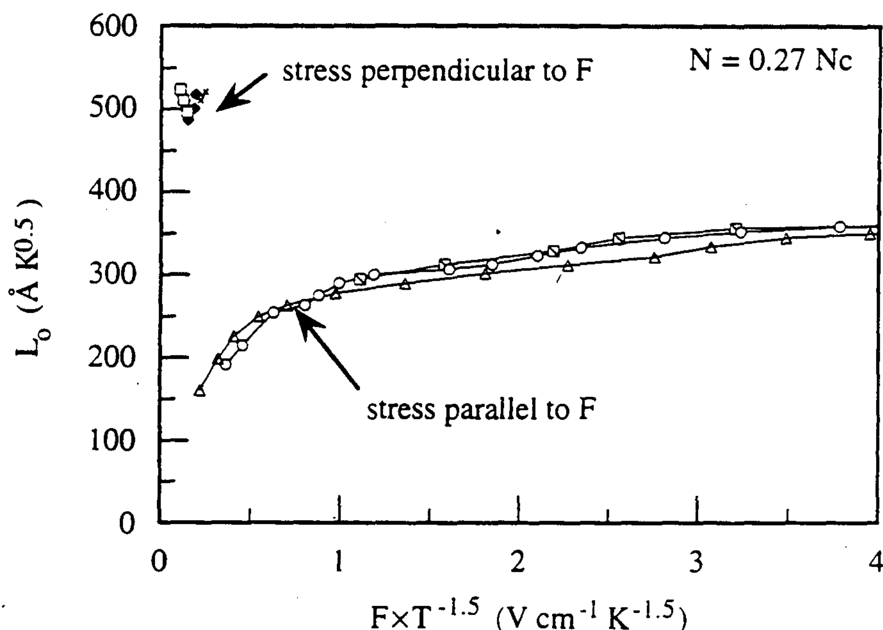

Fig. 4.4 The effect of stress in the direction parallel to the applied field is to reduce the dependence of the conductivity on the applied field, while the effect of stress in a direction perpendicular to the field is to enhance the dependence of σ on F.

explain the observed dependence of the non-Ohmic conductivity of our samples on stress. As shown in Figure 4.2, the effect of stress in the direction parallel to the applied field is to shrink the wavefunctions in the direction of the field. Therefore stress parallel to F should reduce the magnitude of the field dependence of the conductivity. An example of this type of stress is a wire contact made to a sample with silver epoxy. As shown in Figure 4.3, the effect of stress in the direction perpendicular to the applied field is to enhance the hopping conductivity in the direction of the field. Therefore stress perpendicular to F will increase the magnitude of the field dependence of the conductivity. An example of this type of stress is a 907 epoxy glue bond between the side of the sample and a substrate.

Figure 4.4 shows the measured field conductivity parameter L_o as a function of $F\times T^{-1.5}$ for two nominally identical samples. As expected, the sample with a 907 epoxy bond causing stress in a direction perpendicular to F has a greatly enhanced conductivity relative to the sample with a silver epoxy bond causing stress in the direction parallel to F.

Chapter 5

Numerical optimization of bolometric infrared detectors including optical loading, amplifier noise, and electrical nonlinearities*

One of the most important applications of doped Ge semiconductors is their use as temperature sensitive resistors for bolometric detectors. In this chapter we present numerical methods for the global optimization of bolometric infrared detectors which use current-biased semiconducting thermistors. We extend the analysis of Griffin and Holland to explicitly include both the electric field dependence of the thermistor resistance and amplifier noise. These methods allow the user to design and evaluate an optimized bolometer once such parameters as the optical loading, the heat sink temperature, and the materials for the thermal link and the thermistor have been chosen. Measured parameters which describe the electrical nonlinearities in neutron transmutation doped germanium are presented. The consequences for bolometer optimization of including these effects are illustrated.

5.1 Introduction

Typical applications for bolometric detectors include infrared astronomy and laboratory infrared spectroscopy. The optical loading differs by many orders of magnitude in these applications. Thus, the optimization of infrared bolometer performance is a matter of great practical importance. One frequently used figure of merit is the optical noise equivalent power (NEP), defined as the incident signal power required to obtain an output signal equal to the rms noise in a 1 Hz bandwidth. The ratio of the output voltage to the input power is called the voltage responsivity S. The theory of bolometer responsivity,

---

*The numerical optimization program is made available at http://physics7.berkeley.edu/bolometer.html.

noise, and optimization has been discussed by several authors [Low, 1961; Mather, 1984-A; Moseley *et al.*, 1984] and has recently been reviewed by Richards [1994]. Mather has given a complete analysis which includes the effect of electrical nonlinearities in the thermistor material on bolometer responsivity [1982] and nonequilibrium effects on thermal noise [1984-B]. The responsivity and NEP of a bolometric detector are degraded by electrical nonlinearities as well as by optical loading, thermal noise, Johnson noise in the thermistor, and noise in the read-out electronics.

In this chapter we extend the discussion by Griffin and Holland [1988] of the effects of radiant power loading on bolometer performance to explicitly include the effects of amplifier noise and electrical nonlinearities. We assume throughout that the bolometer uses a current-biased semiconducting thermistor and is operated in the dc limit. Due to the increased complexity of the equations describing the bolometer responsivity and NEP, as well as the large number of parameters required to describe the system, a numerical solution is required.

We have developed a numerical optimization routine to be used as a tool for bolometer design. The user must first select an optical system (including detector area) which maximizes the signal power and minimizes the background optical power Q on the bolometer. Once this has been done, the goal is to design a bolometer whose inherent noise is less than or close to the background photon noise. Decisions must also be made about the heat sink temperature T_0 which may be practically achieved, the thermistor material, and the material for the thermal link. Depending on the type of bolometer chosen, the required speed of response can influence these choices. Our program can then be used to determine the global optimum values for the thermistor resistance R, the thermal conductance G linking the bolometer to the heat sink, and the ratio ϕ of the bolometer temperature T to the heat sink temperature T_0. This determination of the optimum value for ϕ is equivalent to a determination of the optimum bias current I.

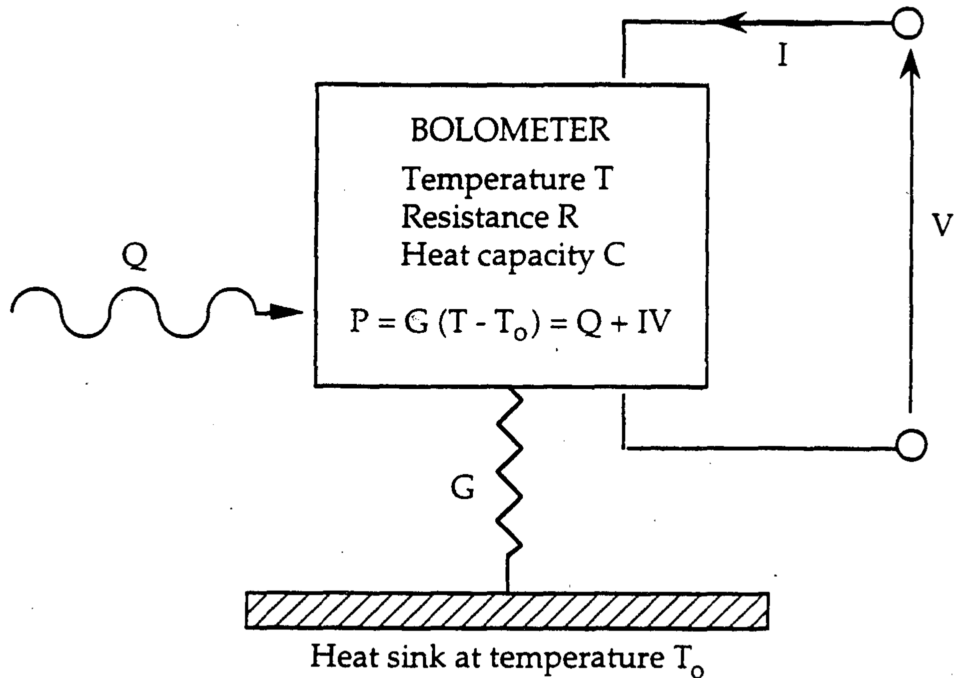

Fig. 5.1 Schematic illustration of bolometer operation.

As we will show, our program can be easily used to compare the effect of using different thermistor materials, heat sink temperatures, or materials for the thermal link on the performance of a bolometric detector. It can also be used to optimize a bolometer for an application which requires a specific time constant. We first review the theory of bolometer responsivity and NEP, and then describe the numerical optimization routine and discuss the implications for bolometer design.

5.2 Bolometer Model

The principle of operation of a bolometric detector is illustrated in Figure 5.1. We consider a bolometric detector consisting of a radiation absorber attached to a temperature sensitive resistor at temperature T coupled to a heat sink at temperature T_0 by a thermal conductance G. The thermistor is current biased with a constant current I which generates the measured voltage V. Any change in optical loading Q gives rise to a change in the

thermistor resistance R and consequently in V. We assume that the thermistor resistance R varies with applied voltage and temperature as:

$$R(V,T) = R_0 \exp\left[\left(\frac{\Delta}{T}\right)^n - \frac{eVL}{dkT}\right]. \tag{5.1}$$

As we discussed in Chapters 1 and 2, this is a generic fitting function which describes a large number of semiconducting materials at low temperatures for which the dominant conduction mechanism is hopping between localized sites [Hill, 1971; Pollak and Riess, 1976]. The exponential variation of thermistor resistance with applied voltage has been observed in a number of materials including Ge:Ga [Grannan *et al.*, 1992], n-GaAs [Redfield, 1975], Si:As [Gang *et al.*, 1989], and Si:P [Rosenbaum *et al.*, 1980] and over a range of temperatures $0.05 \text{ K} < T < 10 \text{ K}$. The parameter R_0 in Equation 5.1 is equal to $\rho_0 d/A$ where ρ_0 depends on the thermistor material and impurity concentration, d is the distance between contact electrodes, and A is the cross-sectional area. The parameter Δ also depends on the thermistor material and impurity concentration. The parameter n is observed to be 1 when the dominant conduction mechanism is nearest neighbor hopping and is typically observed to be 1/4 or 1/2 when variable range hopping conduction dominates [Shklovskii and Efros, 1984]. L is related to the average hopping distance between impurity sites. The temperature dependence of L can be described by two parameters L_0 and m,

$$L(T) = \frac{L_0}{T^m}. \tag{5.2}$$

The temperature exponent m is typically observed to be 0, 1/4, 1/2, or 1 depending on the material and the dominant conduction mechanism. Thus a typical thermistor material can be fully characterized by the above six parameters R_0, Δ, n, d, L_0, and m. In order to simplify the expressions for responsivity and NEP we also define a parameter B which is equal to eL_0/k_B, where e and k_B are the electronic charge and Boltzmann's constant. As shown in Chapter 3, the widely used neutron transmutation doped Ge thermistors produced by Haller [Haller *et al.*, 1985; Haller *et al.*, 1994] are well described by $n = 1/2$, $L_0 = 450$

ÅK$^{0.5}$, and m = 1/2 over a range of impurity concentrations 3×10^{15} cm^{-3} < N < 5.6×10^{16} cm^{-3}.

Following Mather [1984-A], we assume that the differential thermal conductance G_d has a power law dependence on temperature and can be written as

$$G_d = G_o T^\beta = G_o T_o^\beta \phi^\beta, \tag{5.3}$$

where $\phi = T/T_o$. The power exponent β ranges between 1 for a metallic thermal link to the bolometer and 3 for an insulating or superconducting thermal link (see Appendix in Richards, 1994). This form for G_d differs from the form assumed by Griffin and Holland. They assume that the thermal conductivity integral $\int G_d\,dT$ can be expressed as a power law, leading to a non-power law dependence of G_d. Our expressions for the power balance equation for the bolometer, the bolometer responsivity, and the bolometer NEP therefore differ slightly from those derived in Griffin and Holland. Under steady state conditions, the power balance equation for the bolometer is

$$I^2R + Q = \int_{T_o}^{T} G_d(t)\,dt = \frac{G_o T_o^{\beta+1}(\phi^{\beta+1} - 1)}{(\beta + 1)}. \tag{5.4}$$

The power balance equation can be solved for the bias current I,

$$I = \frac{\sqrt{\dfrac{G_o T_o^{\beta+1}}{(\beta+1)}(\phi^{\beta+1} - 1) - Q}}{\sqrt{R}}. \tag{5.5}$$

We can therefore rewrite the thermistor resistance as

$$R = R_o \cdot \exp\left[\left(\frac{\Delta}{\phi T_o}\right)^n\right] \cdot \exp\left[\frac{-B\sqrt{R}\sqrt{\dfrac{G_o T_o^{\beta+1}}{(\beta+1)}(\phi^{\beta+1} - 1) - Q}}{(\phi T_o)^{m+1}}\right]. \tag{5.6}$$

After computing the derivative $\partial R/\partial T$, keeping in mind that we assume a constant bias current I, we find that the temperature coefficient of resistance of the thermistor material α can be written as

$$\alpha = \frac{1}{R}\frac{\partial R}{\partial T} = \frac{\dfrac{-n\Delta^{n}}{(\phi T_o)^{n+1}} + \dfrac{(m+1)B\sqrt{R}\sqrt{\dfrac{G_oT_o^{\beta+1}}{(\beta+1)}(\phi^{\beta+1}-1)-Q}}{(\phi T_o)^{m+2}}}{1+\dfrac{B\sqrt{R}\sqrt{\dfrac{G_oT_o^{\beta+1}}{(\beta+1)}(\phi^{\beta+1}-1)-Q}}{(\phi T_o)^{m+1}}}. \tag{5.7}$$

We note that this definition of α is not universal. Some authors [Mather, 1984-A] use the dimensionless parameter $\alpha = -(T/R)(dR/dT)$. When electrical nonlinearities are neglected, $B = 0$ and α is given by the first term in the numerator. When electrical nonlinearities are included, $B > 0$ and the absolute value of α is decreased. Mather [1984-B] neglects the second term in the denominator; however this term must be included for a current-biased thermistor [Silver *et al.*, 1989].

5.3 Bolometer Responsivity and NEP

The bolometer responsivity S is defined as the change in thermistor voltage produced by a change in optical loading,

$$S = \frac{\partial V}{\partial Q} = \frac{I\cdot\left(\dfrac{\partial R}{\partial T}\right)}{\left(\dfrac{\partial Q}{\partial T}\right)}. \tag{5.8}$$

Using $Q = G_oT_o^{\beta+1}(\phi^{\beta+1} - 1)(\beta+1)^{-1} - I^2R$, we can write

$$S = \frac{\alpha IR}{G_d - \alpha I^2R}. \tag{5.9}$$

After substituting for I, we find that S can be expressed as

$$S = \frac{\alpha\sqrt{R}\sqrt{\dfrac{G_oT_o^{\beta+1}}{(\beta+1)}(\phi^{\beta+1}-1)-Q}}{G_oT_o^{\beta}\phi^{\beta}-\alpha\left(\dfrac{G_oT_o^{\beta+1}}{(\beta+1)}(\phi^{\beta+1}-1)-Q\right)} \quad (5.10)$$

This expression for the responsivity is valid regardless of the form assumed for R(V,T). The decrease in responsivity due to electrical nonlinearities in the thermistor material comes about entirely from the decreased magnitude of α.

The current-biased bolometer is subject to many sources of noise including thermal noise due to the flow of heat from the bolometer to the heat sink, Johnson noise in the thermistor, amplifier noise from the readout electronics, and photon noise from the incident radiation. When referred to the detector input, these noise sources contribute to the noise equivalent power as NEP_T, NEP_J, NEP_A, and NEP_{ph}, respectively. The photon noise contribution NEP_{ph} is assumed to be minimized by careful optical design. Throughout this discussion we use NEP to refer only to the bolometer NEP without including the photon noise contribution,

$$NEP^2 = NEP_P^2 + NEP_J^2 + NEP_A^2 \; . \quad (5.11)$$

The three terms can be minimized by an appropriate choice of R_o, G_o, and ϕ. The separate contributions to the bolometer noise can be summarized as follows:

$$NEP_T{}^2 = 4kT_o{}^{\beta+2}G_o \cdot \left(\frac{\beta+1}{2\beta+3}\right) \cdot \left(\frac{\phi^{2\beta+3}-1}{\phi^{B+1}-1}\right) \quad (5.12)$$

$$NEP_J{}^2 = \frac{4kT_o\phi R}{S^2} \quad (5.13)$$

$$NEP_A{}^2 = \frac{e_n{}^2 + i_n{}^2R^2}{S^2} \quad (5.14)$$

where e_n and i_n are the amplifier voltage noise and current noise, respectively. The thermal noise contribution to the NEP accounts for the fact that there is a temperature gradient between the bolometer and the heat sink:

$$NEP_T^2 = 4k_B G_d(T)\cdot \frac{\int_{T_o}^{T} [t\cdot\kappa(t)]^2\, dt}{\kappa(T)\int_{T_o}^{T} \kappa(t)\, dt} \tag{5.15}$$

where κ is the thermal conductivity of the thermal link material.

For purposes of comparison it is useful to compute the absorbed power photon noise NEP_{ph} in the shot noise limit [Richards, 1994],

$$NEP_{ph}^2 = \frac{2}{\eta^2}\int P_\nu h\nu d\nu \approx 2h\nu Q. \tag{5.16}$$

In the above expression P_ν represents the power absorbed in the detector at optical frequency ν, h is Planck's constant, and η is the bolometer absorptivity.

For a sufficiently large responsivity S the thermal noise contribution NEP_T will always dominate the bolometer noise. Values of S larger than needed to meet this condition are not generally useful. For smaller values of S, the bolometer resistance must be carefully selected in order to avoid excessive amplifier noise and to minimize degradation of the bolometer performance from electrical nonlinearities as discussed below.

5.4 Numerical Optimization Program

We have developed a program which allows the user to select one of two distinct optimization routines to minimize the NEP of an infrared bolometer. Two distinct routines were used both as a consistency check and to allow easy generalization of this program to include other types of thermistor materials. As expected, both routines converge to the same optimum values for R_o, G_o, and ϕ. There is no significant difference in the computer

time required to run either routine; both find the minimum NEP within seconds on a SPARC-II workstation. The first optimization routine uses a variable metric method called the Davidon-Fletcher-Powell (DFP) algorithm [Press *et al.*, 1990] to minimize the NEP. The DFP algorithm requires derivative calculations to locate the optimum values of R_o, G_o, and ϕ. The second optimization routine uses the downhill simplex method [Press *et al.*, 1990] which requires only function evaluations, not derivatives. The downhill simplex method is thus simpler to use than the DFP algorithm but somewhat less efficient.

The optimization routine asks the user to enter each of the quantities R_o, G_o, and ϕ either as a variable to be optimized or as a user-specified parameter. When the goal is to optimize the performance of a bolometer that has already been built, R_o and G_o must be specified and the only adjustable parameter is ϕ. When the thermistor geometry can be varied by adjustment of the dimensional ratio d/A the parameter $R_o = \rho_o d/A$ can be treated as a variable; otherwise R_o must be specified. The optimization program also requires the user to specify the following eleven parameters in a file: the thermistor parameters ρ_o, Δ, n, d, L_o, and m, the exponent β which gives the temperature dependence of the thermal conductance, the optical loading Q, the base temperature T_o, the amplifier voltage noise e_n, and the amplifier current noise i_n. The routine proceeds by selecting values for R_o, G_o, and ϕ and finding the value of R which satisfies Equation 5.6. A separate equation-solving routine is used at this step since no analytic solution for Equation 5.6 exists. The program then calculates α, S, and NEP and adjusts R_o, G_o, and ϕ in the direction of minimization of the NEP until each parameter is stable to three digits.

In addition to using two distinct optimization routines, we performed an additional consistency check by comparing the results of our optimization routine with those of Griffin and Holland [1988]. As discussed above, Griffin and Holland assume that that the thermal conductivity integral $\int G_d \, dT$, rather than the differential thermal conductivity G_d, can be expressed as a power law. When our program is modified to account for this assumption, we find that when we set $L_o = 0$, $m = 0$, $e_n = 0$, and $i_n = 0$ (equivalent to the

assumption of no electrical nonlinearities or amplifier noise) and use the specified parameters for their 100 mK bolometer, our program generates the same minimum NEP and is completely consistent with their results.

Although we have assumed a specific form for R(V,T), the program can be adjusted in a straightforward manner to include thermistors with other temperature and voltage dependences. This can be accomplished by appropriately modifying the temperature coefficient of resistance α of the thermistor and by using the downhill simplex method so that no partial derivatives are required.

5.5 Implications for bolometer design

When electrical nonlinearities are included, the temperature coefficient of resistance α of the thermistor can be written as:

$$\alpha = \frac{\alpha^* + x\sqrt{R}\sqrt{G_o - z}}{1 + y\sqrt{R}\sqrt{G_o - z}}, \tag{5.17}$$

where $\alpha^* = -n\Delta^n/(\phi T_o)^{n+1}$ and x, y, and z depend on L_o, m, ϕ, T_o, and Q. If electrical nonlinearities are neglected ($L_o = 0$, $m = 0$), $\alpha = \alpha^*$ which depends only on the thermometric material, the bolometer temperature, and the heat sink temperature. In this case, α is independent of R, and S varies as $\sqrt{R}$. Thus NEP_T and NEP_J are independent of R, and NEP_A is minimized at the optimum thermistor resistance $R_{opt} = e_n/i_n$. Since α^* is negative and $xR^{1/2}(G_o-z)^{1/2}$ and $yR^{1/2}(G_o-z)^{1/2}$ are positive, the absolute value of α and hence the bolometer responsivity S are reduced when electrical nonlinearities are included. The primary effect on bolometer design of including electrical nonlinearities is that the optimum values of the thermistor resistance and the thermal conductance parameter G_o are smaller when electrical nonlinearities are neglected. This occurs because large values of R and G_o cause a significant reduction in α through the terms $xR^{1/2}(G_o-z)^{1/2}$ and $yR^{1/2}(G_o-z)^{1/2}$. We note that bolometers with higher background optical loading Q have a

correspondingly larger value of G_o. Thus more heavily loaded bolometers have more reduction in sensitivity due to electrical nonlinearities.

We will now illustrate the use of our numerical optimization program as a tool for bolometer design using the parameters of a conventional composite bolometer used for the Millimeter Wave Anisotropy Experiment (MAX) [Tanaka *et al.*, 1995; Clapp *et al.*, 1994; Devlin *et al.*, 1994]. MAX is a balloon-born millimeter wave instrument which has successfully measured anisotropy in the cosmic microwave background on half degree angular scales. The background optical loading Q comes from the residual atmosphere and the ambient 200 K optics. The MAX bolometers are coupled to a heat sink with $T_o = 85$ mK, which is cooled with an adiabatic demagnetization refrigerator. In order to show significant effects of electrical nonlinearities the example we have chosen is a bolometer with a relatively large optical loading. We will discuss the selection of a thermistor material, selection of the material for the thermal link, and the effect of including electrical nonlinearities for bolometer optimization. The results of this discussion can be readily generalized to include other bolometer applications. In all of the following examples we characterize the amplifier noise with $e_n = 3$ nV/√Hz and $i_n = 10^{-16}$ A/√Hz. Unless otherwise specified, we have assumed a thermal link with $\beta = 2$ (typical of a number of commonly used materials including silicon nitride membranes and graphite fibers), a background optical power $Q = 40$ pW, and a heat sink temperature $T_o = 85$ mK.

The MAX bolometers use neutron transmutation doped germanium (NTD Ge) produced by Haller [Haller *et al.*, 1985; Haller *et al.*, 1994] as the thermistor material. Neutron transmutation doping provides an extremely homogeneously and randomly doped thermistor with a precisely controlled impurity concentration. In order to reduce their heat capacity the thermistors are cut into small 240 μm cubes. Therefore, in the discussion that follows R_o is considered to be a user-specified parameter equal to $\rho_o d/A$ where $d/A = (240\ \mu m)^{-1}$ rather than an optimized parameter.

Material	N (10^{16} cm^{-3})	ρ_o (Ω cm)	Δ (K)	n	m	L_o (Å K^m)
NTD-6	3.85	0.28	36.0	0.5	0.5	450
NTD-17	4.99	0.18	21.2	0.5	0.5	450
NTD-19	5.63	0.13	16.0	0.5	0.5	450

Table 5.1 Impurity concentration N and measured thermistor parameters for three neutron transmutation doped germanium materials.

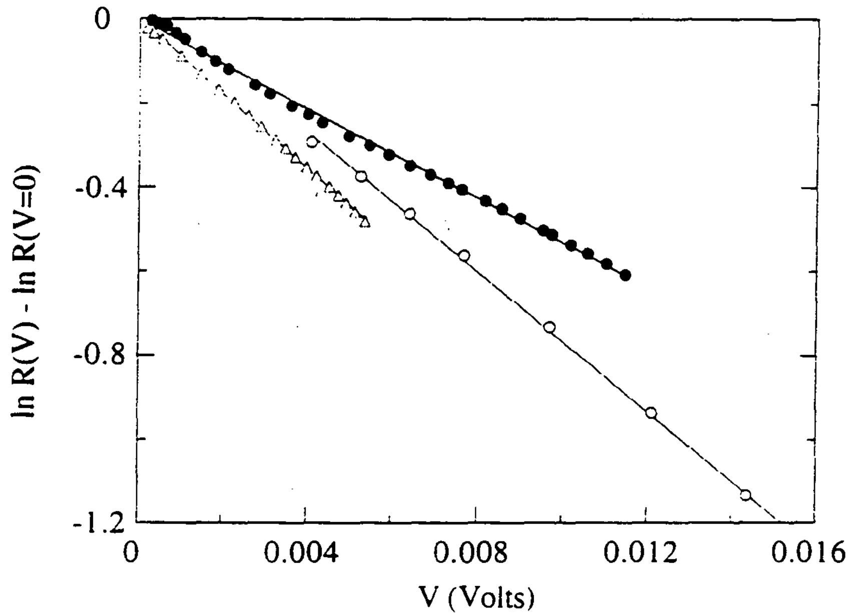

Fig. 5.2 Measurements of the electrical nonlinearities in neutron transmutation doped germanium. The curves are very well fit by a straight line, in agreement with Equation 5.1. Similar curves have been measured for a wide range of temperatures, from which we deduce a length parameter $L = 450/T^{0.5}$ Å for all three samples. The curves represent NTD-19 at T = 96 mK (open triangles), NTD-6 at T = 101 mK (open circles), and NTD-17 at T = 113 mK (closed circles).

In this work we do not discuss the optimization of the thermistor dimensions. In practice, the thermistor dimensions are selected by balancing the following considerations. In order to minimize the heat capacity all thermistor dimensions should be made as small as possible. In order to minimize the bolometer NEP when the effects of electrical nonlinearities are negligible, the ratio d/A should be that which produces a thermistor resistance $R_o = \rho_o d/A = e_n/i_n$. In order to minimize microphonic noise and heating, the thermistor resistance should typically be less than 10 MΩ, which produces an upper limit on the ratio d/A. When electrical nonlinearities are important, the optimum distance between the contact electrodes d is large in order to minimize the electric field across the thermistor. When electrical nonlinearities are neglected the bolometer NEP is independent of d and depends only on the ratio d/A. Finally, fabrication considerations place practical limits on the thermistor dimensions that can be achieved.

For a heat sink temperature of 85 mK, we will examine the minimum NEP that can be achieved from three different thermistor materials known as NTD-6, NTD-17, and NTD-19. The impurity concentrations and measured thermistor parameters for each material are listed in Table 5.1. Figure 5.2 shows the measured linear dependence of the log of the thermistor resistance on applied voltage [24]. The influence of Joule heating on the thermistor resistance is negligible for the three curves. All three materials are very well described by Equation 5.1 with the thermistor parameters $L_o = 450$ Å$K^{0.5}$ and $m = 0.5$.

Figure 5.3 shows the optimized bolometer NEP as a function of heat sink temperature T_o for NTD-19, NTD-17, and NTD-6 including electrical nonlinearities. As the temperature is lowered, the NEP for each thermistor makes a transition from being amplifier voltage noise limited at small thermistor resistances to being amplifier current noise limited at large thermistor resistances. We note that at 120 mK NTD-6 provides the same NEP of 6×10^{-17} W/$\sqrt{\text{Hz}}$ that NTD-17 provides at 82 mK and NTD-19 provides at 60 mK. The explanation is that thermistor materials which provide an appropriate thermistor resistance at lower temperatures have to be more heavily doped in order to prevent charge

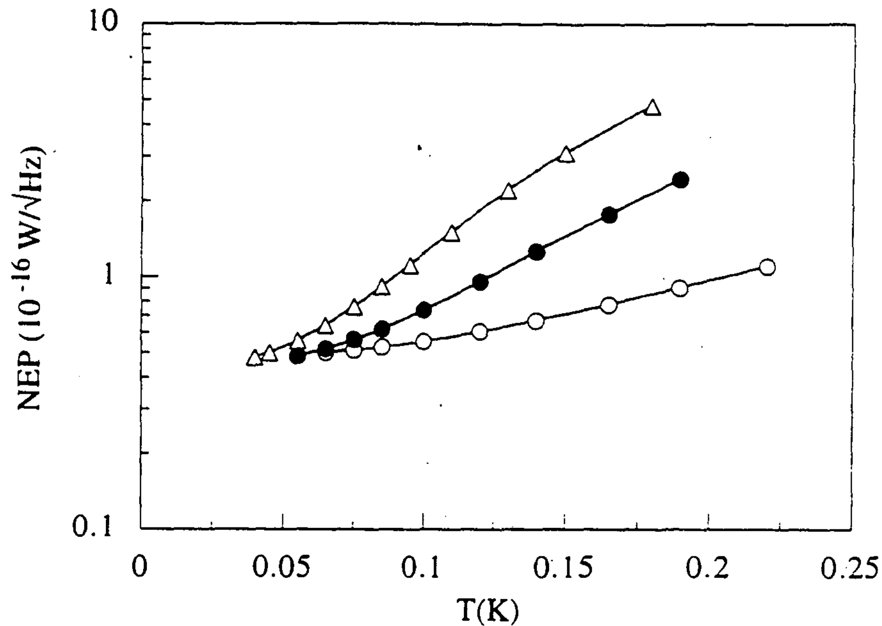

Fig. 5.3 Optimized NEP as a function of heat sink temperature T_0 for NTD-19 (open triangles), NTD-17 (closed circles), and NTD-6 (open circles). We assume that Q = 40 pW, $\beta = 2$, $e_n = 3$ nV/√Hz, $i_n = 10^{-16}$ A/√Hz, and that the thermistors are 240 μm cubes. For each value of T_0, we determine the values of G_0 and ϕ which lead to a minimum value of NEP.

carriers from freezing out. A heavily doped material such as NTD-19 will have a smaller value of Δ and thus a smaller responsivity than a more lightly doped material such as NTD-6 at the same temperature. Practical considerations, however, limit the use of more lightly doped materials. Microphonic noise, which is not explicitly included in the optimization, may be large for the optimized NTD-6 bolometer which has a resistance of 10 MΩ.

Time constant and materials considerations can also reduce the operating temperature chosen for a given application. The optimization program assumes that an arbitrarily small value of G_0 can be selected at each heat sink temperature to produce the minimum NEP. However, there may be limits to the range of values of G_0 which can be

Material	R	G_o	ϕ	NEP	NEP_T	NEP_J	$NEP_{A,e}$	$NEP_{A,i}$
NTD-19	0.616	1.76	1.35	9.19	4.04	4.73	7.17	0.15
	(0.958)	(2.41)	(1.29)	(7.59)	(4.31)	(4.19)	(5.22)	(0.17)
NTD-17	1.99	0.917	1.55	6.24	3.80	4.33	3.41	0.23
	(4.00)	(1.31)	(1.43)	(5.16)	(3.92)	(3.57)	(2.06)	(0.28)
NTD-6	10.0	0.254	2.19	5.29	4.05	4.28	1.27	0.42
	(67)	(0.557)	(1.75)	(4.25)	(3.79)	(3.06)	(0.39)	(0.88)

Table 5.2 Optimized parameters G_o and ϕ for NTD-19, NTD-17, and NTD-6 for a heat sink temperature of 85 mK and parameters given in Section V. For each material, underneath the values obtained by a theory including electrical nonlinearities we have indicated with a parenthesis the values obtained by a theory which neglects electrical nonlinearities. R is given in units of MΩ, G_o in units of 10^{-7} W/K^3, and all NEP's in units of 10^{-17} W/√Hz. $NEP_{A,e}$ and $NEP_{A,i}$ indicate contributions to the bolometer NEP from voltage noise and current noise in the readout electronics.

realistically achieved leading to significantly higher noise. Throughout this thesis we have assumed that the bolometer is operated in the dc limit. This assumption is equivalent to the requirement that the bolometer response time τ_e given by

$$\tau_e = C/G_e = C/(G - I^2R\alpha), \tag{5.18}$$

is fast compared to the characteristic frequencies being studied. Here C is the bolometer heat capacity and G_e is the effective thermal conductance to the bolometer [Richards, 1994]. The optimization routine can easily be used to study the performance which can be achieved for a given τ_e. The user must compute the heat capacity of the bolometer at the estimated operating temperature $T \sim 1.5T_o$ and determine the resulting minimum value of G which will provide a sufficiently fast response from Equation 5.18. The parameter G_o must then be specified by the user rather than optimized. This procedure can then be successively iterated for the new estimated operating temperature.

After optimizing over the parameters G_o and ϕ for each material, we find that NTD-19, NTD-17, and NTD-6 have a minimum NEP at T_o = 85 mK of 9.2×10^{-17}, 6.2×10^{-17},

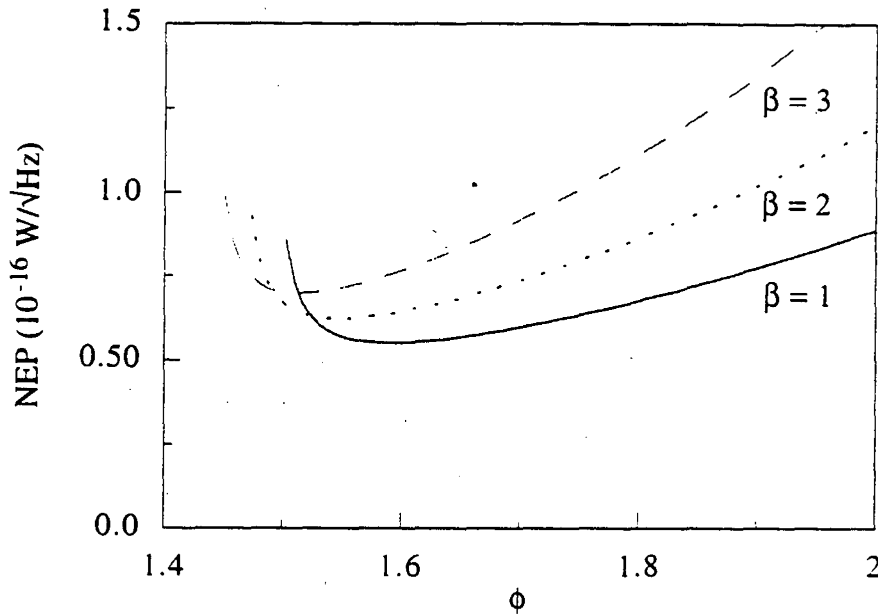

Fig. 5.4 Variation of NEP with ϕ for a thermal link material with $\beta = 1$ (solid line), $\beta = 2$ (small dashed line), and $\beta = 3$ (large dashed line). For each value of β, G_0 was fixed at the globally optimum value. The heat sink temperature, optical loading, and other parameters are listed in Appendix B as the configuration file "NTD17".

and 5.3×10^{-17} W/√Hz, respectively. These values of the NEP are 21, 21, and 25% higher than predicted by a theory which neglects electrical nonlinearities. Table 5.2 summarizes the various contributions to the NEP for the above cases and also lists the optimized values of G_0 and ϕ along with the corresponding thermistor resistance R.

In addition to the quantities listed in Table 5.2, our numerical optimization program calculates the detector responsivity S, the bias current I which will produce the optimum ϕ, and the average thermal conductance G. When R_0 is an optimized rather than a user-specified parameter, the program will calculate the thermistor cross-sectional area which leads to a minimum NEP. The program can also be used to generate tables listing either S, NEP, or I as a function of G_0 or ϕ.

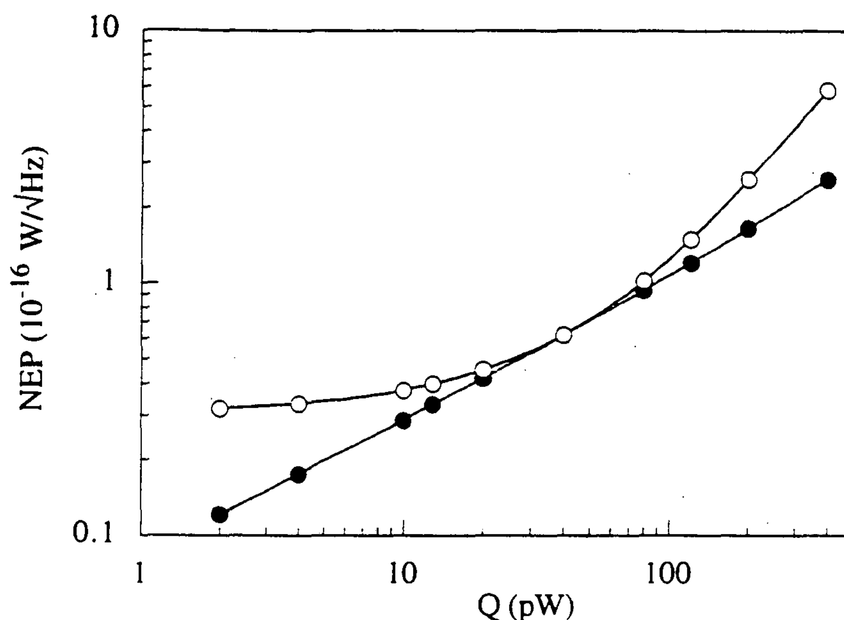

Fig. 5.5 Variation of bolometer NEP with the background optical power Q. The two curves represent the minimum NEP that can be achieved when G_o and ϕ are optimized at each point (closed circles) and when G_o is fixed at the value which produces the minimum NEP for Q = 40 pW (open circles). The heat sink temperature and other bolometer parameters are listed in Appendix B as the configuration file "NTD17".

We now demonstrate the use of this program in selecting a thermal link material for an 85 mK bolometer made with NTD-17 including electrical nonlinearities. As discussed in Section II, materials used for the thermal link can be differentiated by their temperature exponent of the thermal conductance, β, which typically falls between 1 and 3. Figure 5.4 shows the variation of NEP with ϕ for $\beta = 1$, $\beta = 2$, and $\beta = 3$. For each value of β, G_o was fixed at the globally optimum value. The minimum bolometer NEPs that can be achieved with $\beta = 1$, $\beta = 2$, and $\beta = 3$ are 5.5×10^{-17}, 6.2×10^{-17}, and 7.0×10^{-17} W/√Hz. Thus if a metallic rather than an insulating thermal link material is used, the NEP can be decreased by 21%. A further benefit from using $\beta = 1$ rather than $\beta = 3$ is that if the thermistor is overbiased by as little as 15% ($\phi = 1.15\times\phi_{opt}$), the NEP will be increased by 27% for $\beta = 1$ but by 41% for $\beta = 3$.

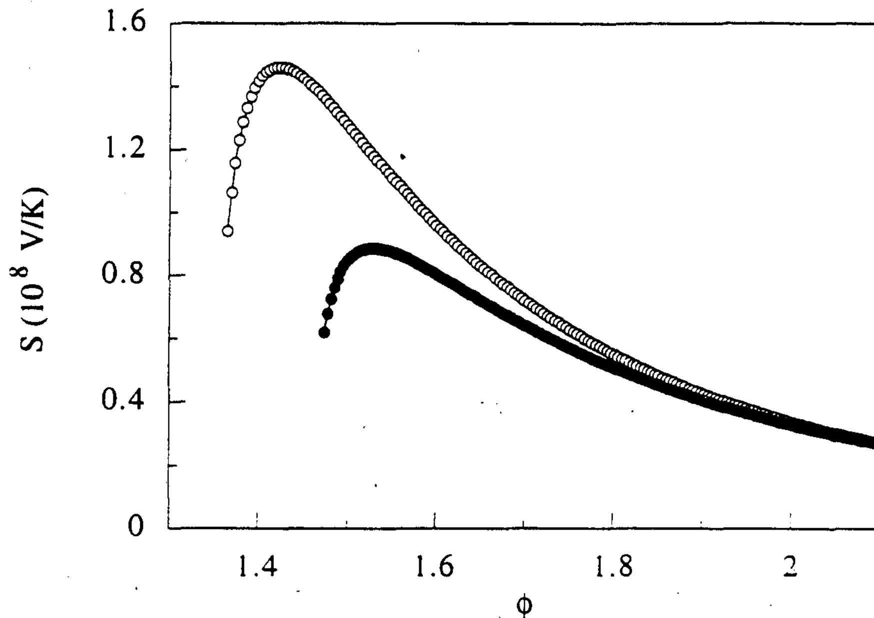

Fig. 5.6 Variation of responsivity S with the bias parameter ϕ. The heat sink temperature, optical loading, and other parameters are listed in Appendix B as the configuration file "NTD17". The two curves were calculated assuming no electrical nonlinearities (open circles) and using the measured values $L_0 = 450$ Å$\cdot$K$^{0.5}$ and $m = 0.5$ (solid circles). For each curve, G_0 was fixed at the globally optimum value.

One serious concern of bolometer designers is that the background optical power Q may not be known with certainty when the material for the thermal link is selected. Figure 5.5 illustrates the consequences of underestimating or overestimating Q for a fixed value of G_0, assuming a bolometer with $\beta = 2$ and the thermistor material NTD-17 including electrical nonlinearities. The two curves represent the minimum NEP that can be achieved when G_0 and ϕ are optimized at each point (closed circles) and when G_0 is fixed at the value which produces the minimum NEP for Q = 40 pW (open circles). When G_0 is optimized for Q = 40 pW, the minimum NEP is within 25% of its globally minimum value over the range 13 pW < Q < 120 pW. Thus when the background optical power is within a factor of three of its estimated value, the minimum bolometer NEP is not strongly affected

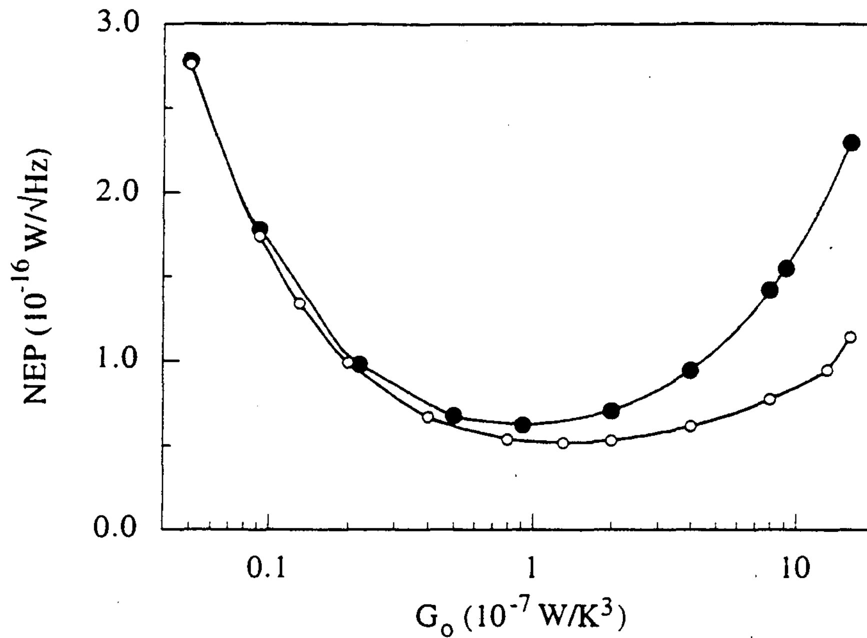

Fig. 5.7 Variation of NEP with thermal conductance parameter G_0. At each value of G_0, the NEP was calculated for the corresponding optimum value of the bias parameter ϕ. The heat sink temperature, optical loading, and other parameters are the same as in Figure 5.6. The two curves were calculated assuming no electrical nonlinearities (open circles) and using the measured values $L_0 = 450$ Å$\cdot K^{0.5}$ and $m = 0.5$ (solid circles).

as long as the bias parameter ϕ can be adjusted. However, when Q is an order of magnitude smaller (larger) than its estimated value of 40 pW and G_0 is fixed at the value which produces the minimum NEP for Q = 40 pW, the NEP increases by 164% (127%) above its globally minimum value. When both G_0 and ϕ are optimized at each value of Q, the globally minimum NEP is well described by $NEP_{min}(Q) = (6.95 \pm .05) \times Q^{0.6}\ 10^{-18}$ W/$\sqrt{\text{Hz}}$ over the range 2 pW < Q < 400 pW.

As a final example, we will discuss the effect of including electrical nonlinearities on the optimization of a relatively high background MAX bolometer with Q = 40 pW, assuming $\beta = 2$ and the thermistor material NTD-17. Figure 5.6 shows the variation of responsivity S with bias parameter ϕ. When electrical nonlinearities are included (solid

circles), the responsivity that can be achieved at the optimum value of ϕ is 39% smaller than calculated when these effects are neglected (open circles). For each curve, G_0 was fixed at the globally optimum value listed in Table 5.2. The responsivity S is equal to zero at the value ϕ_{min} which satisfies Equation 5.5 with $I = 0$.

Figure 5.7 shows the variation of the bolometer NEP with the thermal conductance parameter G_0 when electrical nonlinearities are included (solid circles) and neglected (open circles). At each value of G_0, the NEP is calculated for the corresponding optimum value of ϕ (not shown). For small values of G_0, the NEP is very nearly the same for the two cases. However, at higher G_0, the much stronger reduction in responsivity with increasing G_0 when electrical nonlinearities are included leads to a strong increase in NEP with G_0. For example, when G_0 is an order of magnitude above its globally optimum value the NEP increases by 150% when electrical nonlinearities are included, and only by 83% when they are neglected. Thus the advice given by Griffin and Holland that "G_0 can be made considerably greater than the theoretical optimum value resulting in a faster speed of response for the detector with very little decrease in sensitivity" is no longer valid when electrical nonlinearities are included.

5.6 Conclusion

In conclusion, we have demonstrated the use of our numerical optimization routine as a valuable tool for bolometer design. Specifically, we have investigated the effects of using different thermistor materials, materials for the thermal link, and including electrical nonlinearities on the design of a relatively high background bolometer used in the Millimeter Anisotropy Experiment. We found the general result that when electrical nonlinearities are included, the bolometer resistance and the thermal conductance between the bolometer and the heat sink should be made smaller than if these effects were not present. The program can be easily used to investigate the influence of many other

parameters including the heat sink temperature, thermistor size, noise in the readout electronics, and a time constant requirement on thermistor design.

Chapter 6

Collection of athermal phonons into doped Ge thermistors using quasiparticle trapping

In this chapter, we describe a novel application of doped Ge thermistors used as calorimeters in a low temperature particle detector. This detector, the Superconducting Large Area Phonon Sensor (SLAPS), uses a quasiparticle trapping mechanism to funnel athermal phonon energy from an 80 mg Ge absorber into a 1.6 mg doped Ge thermistor via a superconducting Al film. We report on pulse height spectra obtained at 320 mK by scanning a ^{241}Am alpha source along the device, and show that up to 20% of the energy deposited in the Ge absorber by a 5.5 MeV alpha particle interaction can be collected into a thermistor with fifty times less volume via quasiparticle trapping. We show that the pulse shapes obtained with this device can be used to determine the position of an alpha particle interaction in the Ge absorber for interaction distances of up to 6 mm from a quasiparticle trap. To our knowledge, this is the first low temperature calorimetric particle detector which allows a determination of the particle interaction distance.

6.1 Introduction

Small thermometers operating at cryogenic temperatures have been used to detect small amounts of energy deposited in a target material by single particle interactions [Booth and Salmon, 1992]. Such detectors are potentially useful for broad-band X-ray spectroscopy, the search for dark matter candidates, and in the determination of neutrino properties, as they provide high energy resolution, the ability to detect low energy nuclear recoils, and flexibility in the choice of target materials. However, these thermometers are typically poorly coupled to high energy phonons in the target which, before they thermalize, carry information about the location and nature of the initial event. One way to greatly increase the sensitivity of such a thermometer to athermal phonons is to couple it to

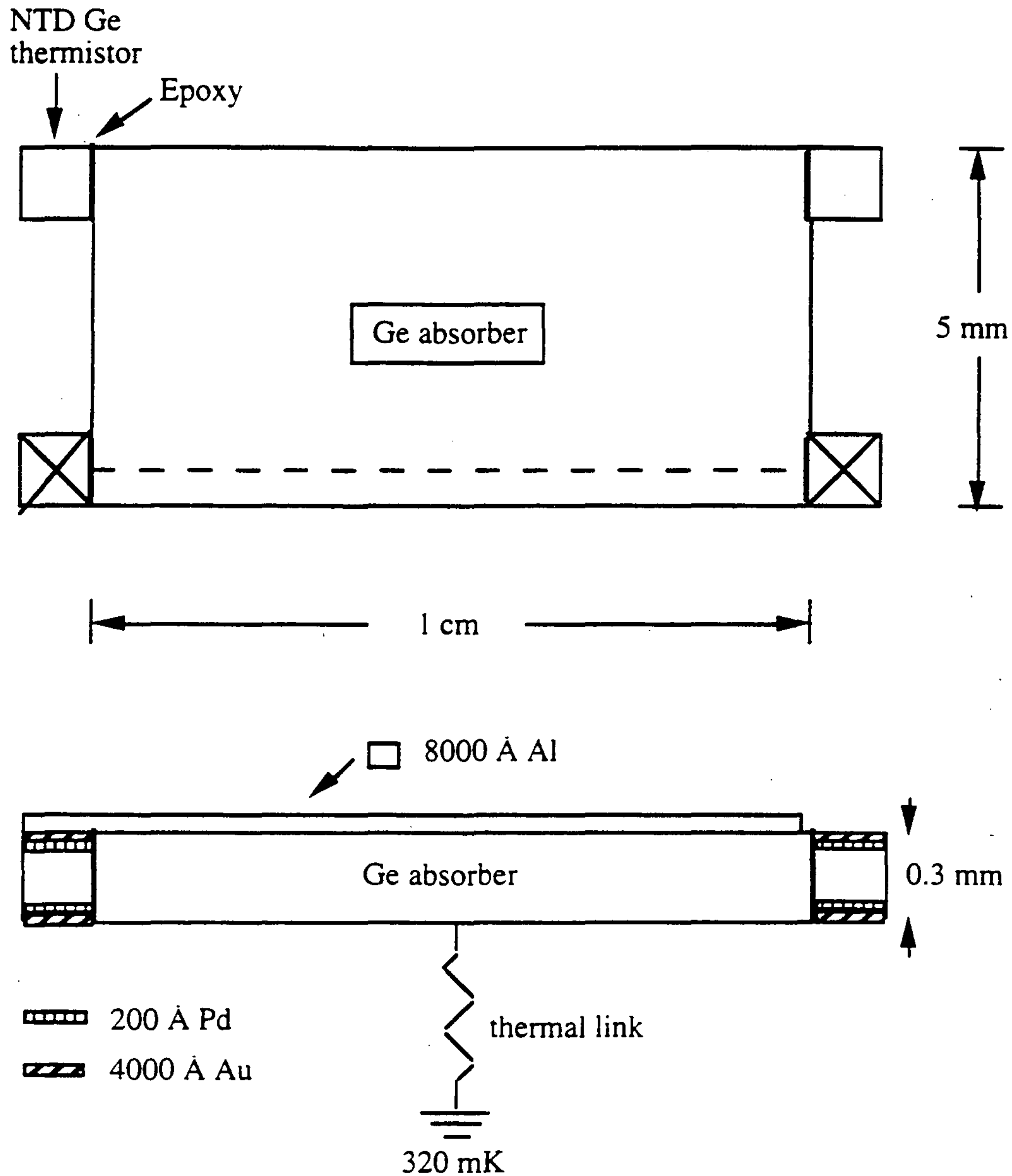

Fig. 6.1 Schematic diagram of the SLAPS device showing top and side views (not to scale). The two thermistors studied in this experiment are each denoted by X, and the axis scanned by the ^{241}Am source is indicated by the dashed line.

the target via a thin film superconductor. The superconducting film readily absorbs athermal phonons, which create quasiparticles that quickly diffuse through the film and can be concentrated through the quasiparticle trapping mechanism (see Section II).

Quasiparticle trapping is a recently developed technique which has been used to significantly improve the performance of particle detectors that measure the quasiparticle current through superconducting tunnel junctions (STJs). Such detectors have been of two types, with quasiparticles diffusing into the trapping region of the junction from a thin strip of superconducting film [Kraus *et al.*, 1989] deposited on top of an absorber (quasiparticle diffusion over distances of ~ 0.5 mm), and directly from superconductors used as the absorber material [Booth, 1987; Goldie *et al.*, 1990; Mears *et al.*, 1993]. However, to our knowledge the quasiparticle trapping technique has never been used in conjunction with a calorimetric detector or to study quasiparticle diffusion in thin films over distances of ~ 1 cm.

To study the feasibility of using quasiparticle trapping to collect athermal phonons over distances of up to 10 mm, we have built the Superconducting Large Area Phonon Sensor (SLAPS). As shown in Figure 6.1, the SLAPS device consists of four symmetrically-located doped Ge thermistors (1 $mm^2 \times 300\ \mu m$) attached with epoxy to the edge of a Ge absorber (10 mm $\times$ 5mm $\times$ 300 μm). The Ge absorber was thermally heat-sunk to a 320 mK temperature- regulated stage through a thin layer of vacuum grease. Electrical contacts were made on opposing faces of each thermistor by boron implantation followed by thermal annealing and evaporation of 200 Å of Pd and 4000 Å of Au. An 8000 Å thick Al film was sputtered onto the top surface of the composite device, covering the Ge substrate and three of the four thermistors. These three thermistors were used to study the quasiparticle trapping mechanism, while the fourth uncovered thermistor is sensitive only to thermal phonons and was used for comparison and device calibration.

6.2 Principles of Operation

When an incident particle interacts in the Ge substrate, it produces high energy phonons which propagate to the surface of the crystal. Phonons which strike the superconducting Al film and have energies greater than the Al gap energy $E_g = 2\Delta \approx 350$

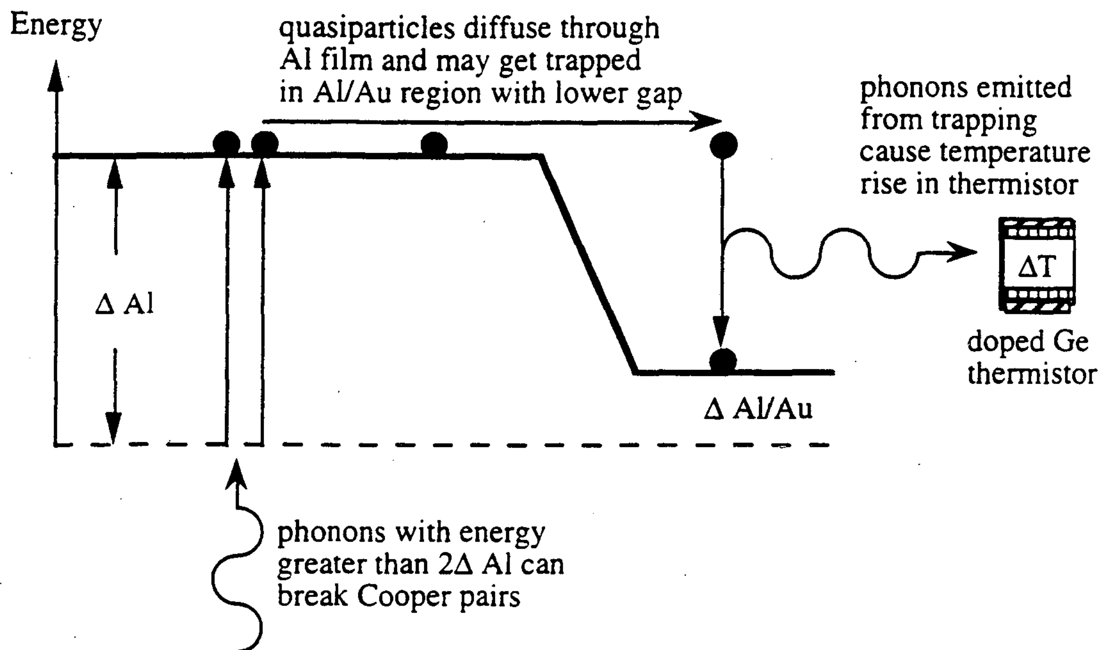

Fig. 6.2 The SLAPS device funnels athermal phonon energy from a large volume Ge absorber into a small volume doped Ge thermistor by employing a quasiparticle trapping mechanism.

μeV can break Cooper pairs, creating quasiparticles which diffuse through the Al film as shown in Figure 6.2. If the quasiparticles have a sufficiently long mean free path and lifetime, they will diffuse to the ends of the detector where the thermistors are attached. Due to the proximity effect the Al/Au/thermistor region has an energy gap several times smaller than the gap in the Al/Ge region. Quasiparticles moving into the smaller gap region scatter to lower energies by phonon emission and are then "trapped" because they have insufficient energy to return to the Al film. This process of phonon emission heats the attached thermistor and produces a voltage pulse as the thermistor resistance drops.

6.3 NTD Ge Thermistors

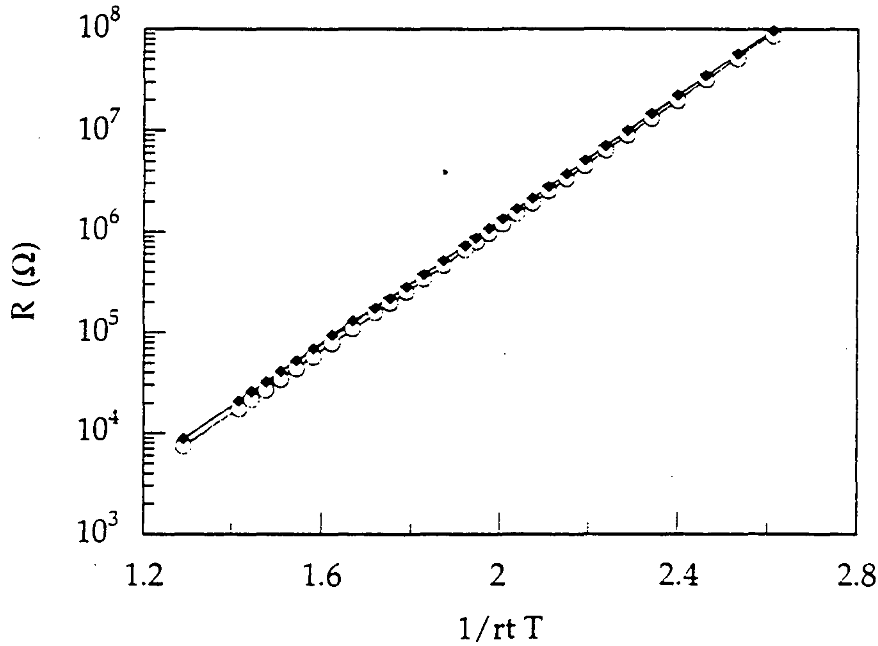

Fig. 6.3 Temperature dependence of the resistance of the thermistor with an Al/Au qp trap (open circles) and the thermistor without a qp trap (solid diamonds).

The thermistor material used in the SLAPS device is neutron transmutation doped (NTD) germanium [Haller *et al.*, 1985; Beeman and Haller, 1994; Haller *et al.*, 1994] with a net impurity concentration of 2.6×10^{16} cm^{-3}. The neutron transmutation process is described in detail in Chapter 3. This material is known as NTD-14 and was chosen for its low noise and high electrical responsivity at ^{3}He temperatures. As described in Chapter 1, low temperature electrical conduction in NTD Ge proceeds by variable range hopping [Shklovskii and Efros, 1984] in which holes tunnel between impurity sites rather than enter the valence band. The electrical resistivity varies extremely rapidly with temperature, and is well described by $\rho = \rho_0 \exp(T_0/T)^{1/2}$. NTD-14 is well described by $\rho_0 \approx 0.26$ Ω-cm and $T_0 \approx 51$ K. The temperature dependence of the resistances of the two thermistors studied in this work are plotted in Figure 6.3. At 360 mK the thermistor resistance R is approximately 120 kΩ and the voltage noise $e_n = \sqrt{4kTR}$ is 1.4 nV/$\sqrt{\text{Hz}}$. Since this is less

than the 7 nV/√Hz noise of our read-out electronics, our experimental results are not thermistor noise limited.

The maximum voltage drop across a thermistor after an energy input E is approximately $\Delta V = I(dR/dT)E/C_{th}$ where C_{th} is the heat capacity of the thermistor and I is the bias current [Mather, 1982]. Since the thermistor is connected to the surrounding environment at base temperature T_b by a link of thermal conductance G_{th}, over time the signal will decay with time constant $\tau_{th} \approx C_{th}/G_{th}$:

$$\Delta V(t) = I \cdot \frac{dR}{dT} \cdot \frac{E}{C_{th}} \exp\left(\frac{-t}{\tau_{th}}\right) .$$

For the thermistors in this experiment, biased to 360 mK above a base temperature of 320 mK, the optimum bias current I is 0.5 μA, C_{th} is approximately 7×10^{-11} J/K (see Section VI), dR/dT is approximately -2×10^{6} Ω/K, and $\Delta V/E \approx -2.3\times10^{-9}$ V/eV. Thus when a thermistor absorbs a 60 keV γ-ray its initial temperature rise is ~ 140 μK and the voltage drop is ~ 140 μV.

6.4 Aluminum Film Properties

The criteria we used to select aluminum as the superconducting film material on the SLAPS device were: (1) we required a high purity film with minimal defects in order to minimize quasiparticle energy losses through processes other than phonon scattering, (2) the lifetime for nonequilibrium quasiparticles created in the film, τ_{qp}, had to be long so that quasiparticles could diffuse over large distances, and (3) T_c had to be several times greater than the operating temperature (320 mK) for a small population of thermally excited quasiparticles in the film. Aluminum, with a measured T_c of 1.24 K in our 8000 Å Al film, is a material which has been well studied and is known to have a long quasiparticle lifetime[11,12]. Furthermore, techniques exist for making very high quality Al films with long electron mean free paths.

Sample	Thickness (Å)	$\Re$	λ (Å)	Method	Deposition Rate (Å/s)
DH1	2250	6.50	968.5	sputtered	2
DH2	2275	5.53	824	"	134
DH3	1700	5.19	773	"	114
DH4	2115	3.61	538	"	11
DH5	2030	3.63	541	"	7
DH6	2000	2.72	405	"	2
DH7	2000	2.73	407	"	2
DH8	2055	8.22	1225	"	2
DH9	950	7.10	1058	"	2
DH10	2290	12.0	1790	"	222
DH11	1390	9.41	1402	"	200
Balzers	2500	4.19	624	"	?
Grython	**8000**	**42**	**6258**	**"**	**?**
SL1	14000	9.40	1400	"	4
SL2	9724	9.9	1475	"	4
SL3	2167	4.7	700	"	4
SL4	2197	4.5	671	"	15
SL5	**11400**	**28.8**	**4291**	**e-beam**	**572**
SL6	11000	19.2	2861	"	548
SL7	2800	18.1	2697	"	560
SL8	2700	12.3	1833	"	532
SFU	2000	5.35	797	"	?

Table 6.1 Low temperature mean free path deduced from the residual resistance ratio for a number of aluminum films with different deposition conditions. The two samples with the longest mean free paths are indicated in boldface.

Before building the SLAPS device, we produced the series of Al films listed in Table 6.1 using a variety of deposition conditions in order to determine the conditions which lead to a large mean free path λ. The Al film in the SLAPS device must have a large mean free path at low temperatures so that the quasiparticles can travel over large distances and become trapped in the thermistor before recombining. λ was determined by measuring the residual resistance ratio $\Re = R_{300}/R_{4.2}$ between 300 K and 4.2 K. $\Re$ can be related to the low temperature mean free path in aluminum using the equation $\lambda_{4.2} = v_F \cdot \tau_{4.2} = m^* \cdot v_F/(n \cdot e^2 \cdot \rho_{4.2}) = \Re \cdot m^* \cdot v_F/(n \cdot e^2 \cdot \rho_{300})$, where n is the concentration, m^* the effective mass, e the charge, and v_F the Fermi velocity of the conduction electrons in aluminum. The low temperature mean free path is therefore $\lambda \approx (149\ \text{Å}) \times \Re$, using the values $\rho_{300} =$

$2.74 \times 10^{-6}\ \Omega\cdot$cm, $m^*/n\cdot e^2 = 1.965 \times 10^{-6}\ \Omega\cdot$cm$\cdot$s, and $v_F = 2.74 \times 10^{-6}$ cm/s [Kittel, 1986].

The Al film with the longest mean free path listed in Table 6.1 was produced in a UHV deposition chamber called "Grython" by dc-magnetron sputtering. Using the same chamber, we sputtered an 8000 Å film onto the SLAPS device and onto a reference substrate. The reference substrate had a residual resistance ratio $\Re$ of 27. As the temperature was lowered below 4.2 K, $\Re$ remained constant indicating that λ had reached its maximum value. Therefore, we believe that the mean free path λ of the Al film used in the SLAPS device is $\approx$ 4000 Å. The quasiparticle diffusion length L in three dimensions [Reif, 1965] is related to λ by $L = (2v_F\lambda\tau_{qp}/3)^{1/2}$, where v_F is the Fermi velocity. As discussed in Section VI, we assume that the quasiparticle lifetime τ_{qp} has the same order of magnitude as our signal risetimes (40 μs). Using this formula to obtain a rough estimate of the diffusion length L in our thin film, with $v_F = 2\times10^8$ cm/s, $\lambda = 4000$ Å, and $\tau_{qp} \sim 40$ μs we find:

$$L \sim \sqrt{\frac{2}{3} v_F \lambda \tau_{qp}} \sim 5 \text{ mm}.$$

6.5 Experimental Procedure

To study the quasiparticle trapping mechanism and quasiparticle diffusion length, we mounted the SLAPS detector on a temperature-regulated stage thermally linked to a ^{3}He refrigerator. Electrical contacts were made to each thermistor by attaching two copper wires 5 mm long and 25 μm in diameter to the metallized thermistor contacts with a small amount of conductive epoxy. Resistances were measured using a dc bias voltage applied across the series combination of a 10 MΩ metal-film resistor at 1.6 K and the thermistor. The voltage drop across the thermistor was read through a cooled junction field-effect transistor (JFET) operating in source follower mode. We measured the resistance vs. temperature curves of the thermistors, shown in Figure 6.3, and measured the

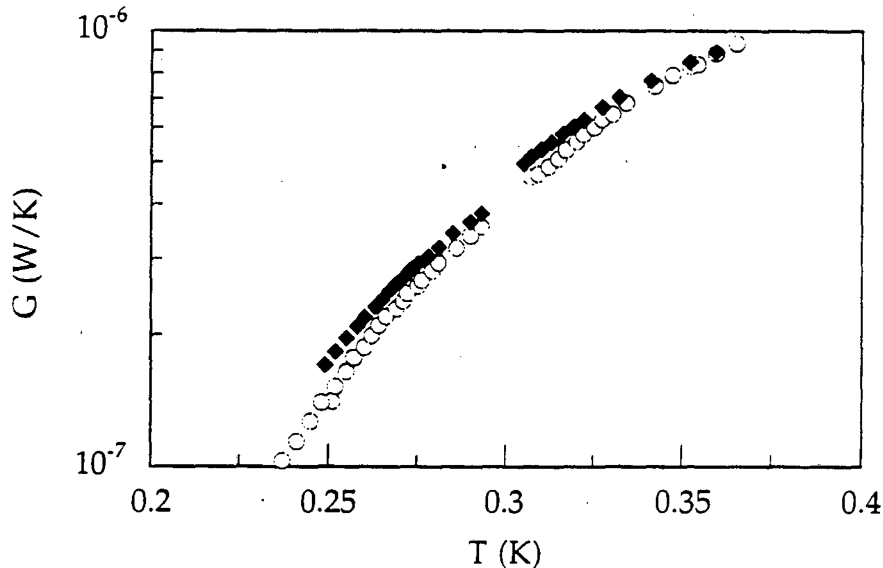

Fig. 6.4 Temperature dependence of the thermal conductivity of the epoxy bond connecting the germanium absorber to the thermistor with an Al/Au qp trap (open circles) and the thermistor without a qp trap (solid diamonds).

thermal conductivities G_{th} and time constants τ_{th} of the epoxy bonds linking the thermistors to the germanium substrate at 220 mK < T < 370 mK. The temperature dependence of G_{th} for the two thermistors is plotted in Figure 6.4. We saw no significant difference between the values of G_{th} and τ_{th} measured in the thermistor covered with an 8000 Å Al film compared to the values measured in the thermistor with no Al film. We therefore conclude that the Al film does not significantly contribute to the thermal link between the thermistor with a quasiparticle trap and the Ge absorber.

After characterizing the thermistors we installed a lead-collimated 0.7 μC ^{241}Am alpha source (spot size ≈ 1mm) above the SLAPS device. An alpha particle striking the device deposits 0.4% of its energy (22 keV) into the 8000 Å Al film and travels an additional 20 μm into the 300 μm thick Ge substrate, depositing the remainder of its energy

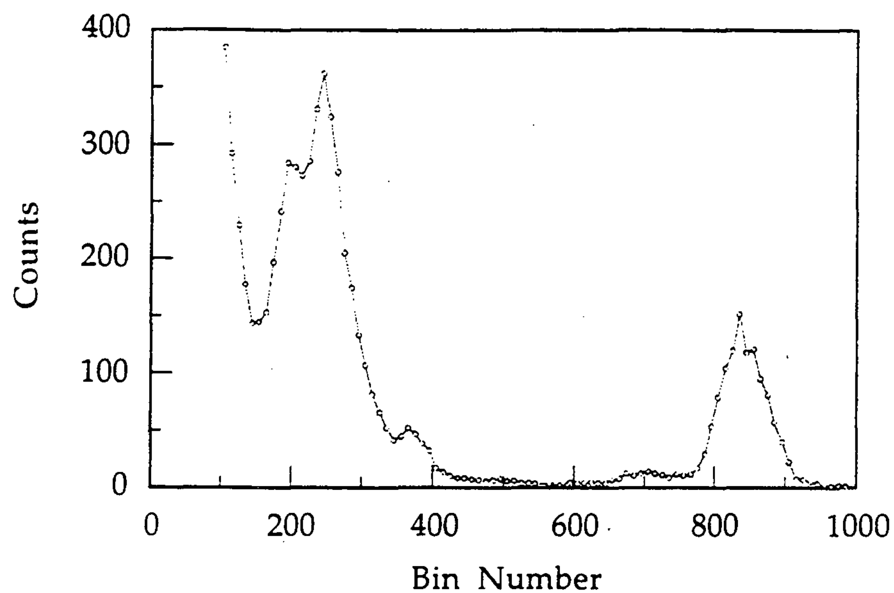

Fig. 6.5 Pulse height spectrum of γ-rays produced by the ^{241}Am source obtained with the thermistor without an Al/Au quasiparticle trap. The spectrum clearly shows γ-ray energy peaks at bins 195, 245, 365, and 835.

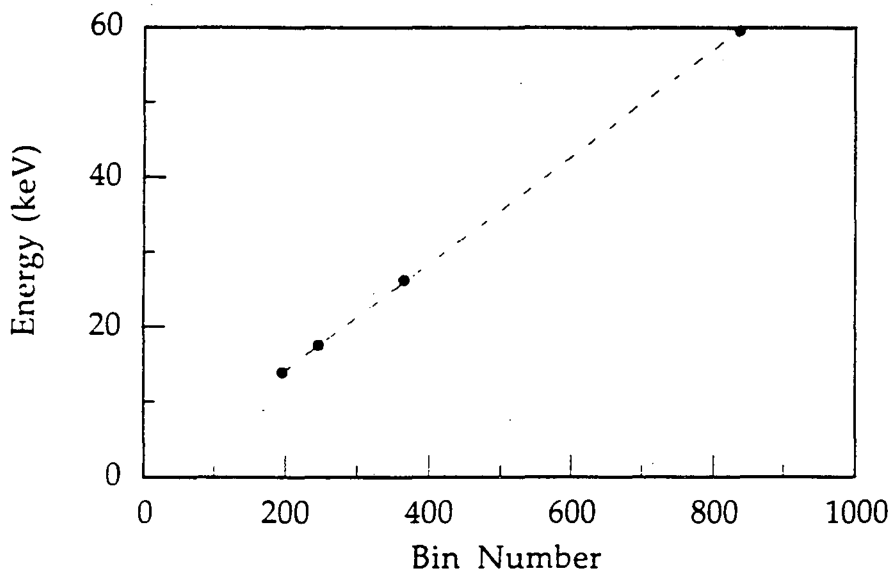

Fig. 6.6 Linearity of the thermistor response determined from the pulse height spectrum shown in Figure 6.5.

in the form of athermal phonons which travel through the Ge substrate. We scanned the device with the alpha source along a line parallel to the 1 cm long axis and centered on two NTD Ge thermistors, one with an Al/Au trap and one without. Successive source positions were separated by 1/2 mm, thus we were able to study the pulse height spectrum observed in the two thermistors for 20 different source positions.

In addition to emitting alpha particles at the nearly identical energies 5.443 MeV (12.8%) and 5.486 MeV (85.2%), the ^{241}Am source emits a number of gamma-rays which were used to calibrate the detector. The five primary gamma-rays emitted by the ^{241}Am have energies of 13.93 keV (13.0%), 17.61 keV (20.2%), 21.00 keV (5.2%), 26.34 keV (2.4%), and 59.54 keV (35.7%). Figure 6.5 shows the pulse height spectrum observed in the thermistor without an Al/Au trap for the ^{241}Am source located directly above the thermistor. The energy peaks at bins 195, 245, 365, and 835 correspond to the 13.93, 17.61, 26.34, and 59.54 keV γ-rays produced by the ^{241}Am source. A thin 250 μm sheet of copper shimstock was inserted between the source and the thermistor in order to remove the high energy alpha particles while allowing most of the gamma-rays to strike the thermistor. The linearity of the thermistor response determined from the pulse height spectrum of Figure 6.5 is shown in Figure 6.6. The thermistor response is extremely linear (dashed line), and is best fit by the equation E (keV) = 0.0713 ± 0.0002 * Bin Number.

6.6 System Time Constants

The voltage pulses observed in each thermistor are characterized by four major time constants: the response time of the readout electronics τ_{el}, the characteristic time for quasiparticles to deposit athermal phonon energy into the thermistor τ_{ath}, the time constant τ_{th} of the thermal link connecting the thermistor to the Ge substrate, and the time constant τ_{Ge} of the thermal link between the Ge substrate and the 320 mK stage. The magnitudes of these time constants are related to each other by $\tau_{el} \ll \tau_{ath} < \tau_{th} < \tau_{Ge}$. This is the optimum

ordering for the following reasons: τ_{el} should be at least an order of magnitude smaller than the other system time constants so that the JFET output voltage can rapidly track voltage changes across the thermistor. The quasiparticle sensing time τ_{ath} must be shorter than the thermistor time constant τ_{th} in order for the additional phonon signal produced in the thermistor by quasiparticle trapping to produce a significant temperature rise before the thermistor reaches thermal equilibrium with the germanium absorber. (This requirement significantly constrains the design of future devices utilizing a quasiparticle trapping mechanism). Similarly τ_{th} should be several times shorter than τ_{Ge} so that the thermistor can respond to temperature changes in the absorber before the system returns to equilibrium.

We have measured these time constants in the SLAPS device by exponentially fitting the rise and fall times of the various pulses observed at different ^{241}Am source positions (see Section VII) and find that $\tau_{el} \approx 4.2$ μs, $\tau_{ath} \approx 40$ μs, $\tau_{th} \approx 90$ μs, and $\tau_{Ge} \approx 300$ μs. The value for τ_{el} is consistent with a thermistor resistance of 120 kΩ and a capacitance of 35 pF from the JFET input to ground, and agrees with the value $\tau_{el} \sim 4$ μs we measured by biasing the thermistors with an ac square wave. The characteristic time τ_{ath} for athermal phonon sensing in the thermistor is a complicated function of the athermal phonon lifetime in the Ge substrate, the quasiparticle lifetime in the Al film, the trapping time for quasiparticles in the Al/Au/thermistor region, and the relaxation time for the hot electrons in the Au film. We have calculated that these characteristic times are considerably faster than our electronic response time of 4.2 μs except for the quasiparticle lifetime in the Al film, which we calculated to be ~ 25 μs at T = 320 mK using the theoretical approximation of Kaplan [1976] assuming a superconductor with impurities and a near-equilibrium distribution of phonons and quasiparticles. It is also close to the quasiparticle lifetime $\tau_{qp} \sim 35$ μs measured by Gray [1971] in a much thinner (300 Å) Al film at the same value of $\Delta/kT \approx 6.4$. We conclude that τ_{ath} is primarily determined by the quasiparticle lifetime τ_{qp} and by the spread in diffusion times to the trap. The thermistor time constant

τ_{th} agrees with the value of 90 ± 10 μs measured electrically, and combined with our measurement of $G_{th} = (8 \pm 1)\times10^{-7}$ W/K gives a total thermistor heat capacity C_{th} of 7×10^{-11} J/K.

6.7 Pulse height spectra

Two types of signals were observed in each thermistor when the ^{241}Am source was positioned over the germanium absorber, each signal having a characteristic pulse shape and height: (1) 60 keV γ-rays directly striking the thermistor, and (2) 5.5 MeV alpha particles depositing energy into the Ge substrate at a distance from the thermistor edge ranging from 0 mm to 10 mm. The γ-ray event rate was approximately 1 sec^{-1} and the alpha particle event rate was approximately 2 sec^{-1}. The γ-ray pulses were observed at all positions of the ^{241}Am source because the lead collimator was designed to stop stray alpha particles while not fully attenuating the γ-rays. The γ-ray peak in each pulse height spectrum was used to calibrate the thermistor signal produced by alpha particles interacting in the germanium absorber and to determine the thermistor energy resolution (6 keV FWHM for a 60 keV energy input at 360 mK). For all source positions, the γ-ray pulses had an electronics limited rise time of about 4.2 μs and a decay time constant of 90 μs equal to τ_{th}. As expected, we observed no significant difference in the pulse height and shape produced by γ-rays striking either thermistor.

The height and shape of the voltage pulses produced by 5.5 MeV alpha particles depositing energy in the germanium absorber showed a strong position dependence in the thermistor with an Al/Au quasiparticle trap and were nearly position independent in the thermistor with no aluminum film. For all source positions further than 5 mm from the thermistor edge the pulse height spectra of the two thermistors were essentially identical: in both thermistors the 5.5 MeV peak center had a pulse height 2.2 times greater than the pulse height of the 60 keV (direct hit in the thermistor) peak center. Assuming that the germanium heat capacity per unit volume is comparable to that of the doped germanium

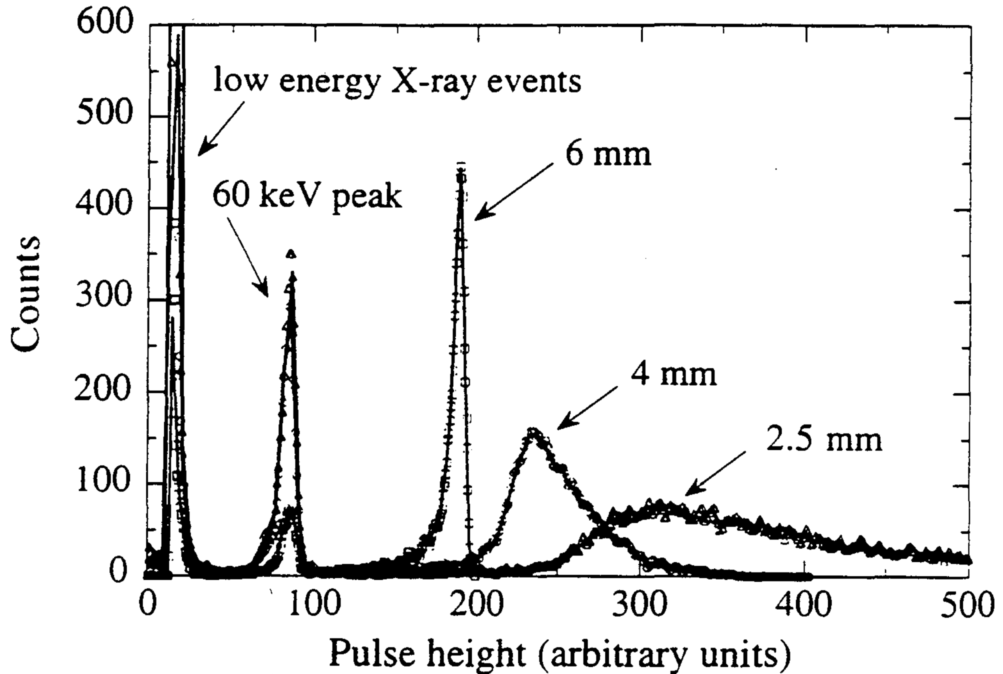

Fig. 6.7 Superimposed pulse height spectra obtained with quasiparticle trapping thermistor for collimated alpha source located at 6 mm, 4 mm, and 2.5 mm from the thermistor edge.

thermistors, we expect a pulse height ratio of around two because an alpha particle interacting in the Ge absorber deposits ninety times more energy in a volume fifty times greater than that of a 60 keV γ-ray interacting in a thermistor. These pulses from alpha particles absorbed far from the thermistor showed an exponential rise with time constant τ_{th} of 90 μs in both thermistors as the thermistors reached equilibrium with the Ge absorber, and then an exponential decay with time constant τ_{Ge} of 300 μs.

As the ^{241}Am source position was moved to the thermistor edge, the thermistor with no aluminum film showed a small increase in pulse height above the 60 keV peak from 2.2 to 2.65 (see Figure 6.7). We attribute this 20% rise in energy detected in the thermistor to a small number of athermal phonons absorbed in the epoxy joint heating the thermistor above

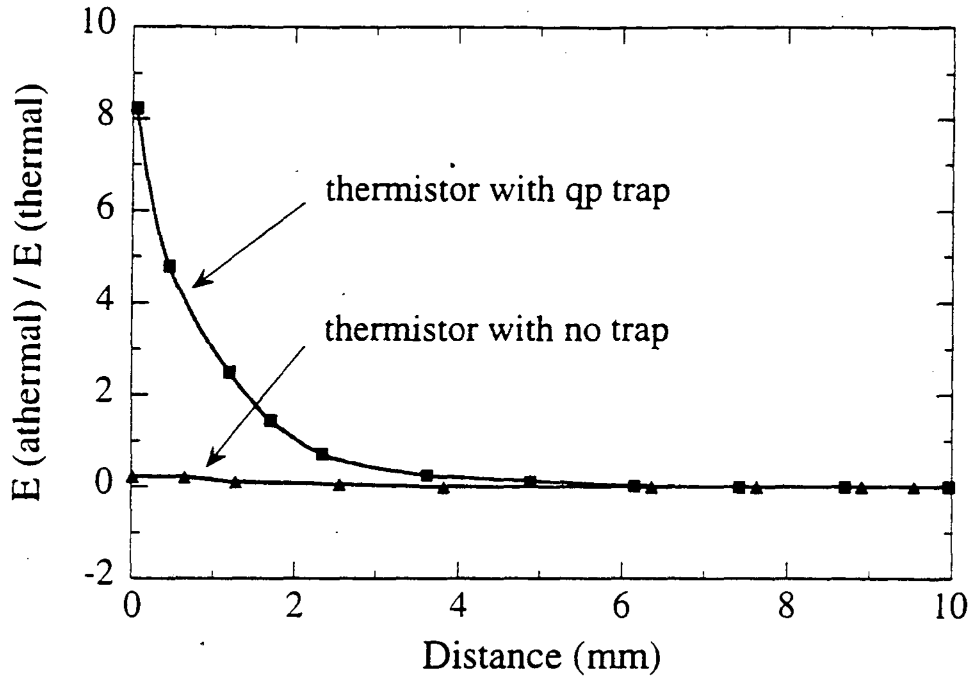

Fig. 6.8 Ratio of athermal to thermal phonon energy detected in each thermistor for various alpha source positions (measured relative to the respective thermistor edges).

the equilibrium temperature of the Ge absorber. The time constants of the thermal rise and fall of the thermistor with no aluminum film were the same for all source positions to within the accuracy of our fit.

In contrast, the thermistor with an Al/Au quasiparticle trap began to show an increase in mean pulse height over the 60 keV peak at a source distance of 5 mm (see Figure 6.7), indicating athermal phonon collection into the thermistor. As the ^{241}Am source was moved to the thermistor edge the mean pulse height of the 5.5 MeV peak rose dramatically to a value 20 times greater than the 60 keV peak, corresponding to a total energy input into the thermistor of 1.2 MeV. In other words, the use of a quasiparticle trapping mechanism allowed us to collect 20% of the energy deposited initially in the 80 mg Ge absorber into the 1.6 mg thermistor. At a source distance of 5 mm the athermal phonon

energy deposited in the thermistor by quasiparticle trapping, determined by the mean pulse height, was 14% of the energy deposited by thermal phonons; at 2 mm the same ratio was 100%, and at the thermistor edge this ratio was 820% (see Figure 6.8). We note that the nonlinearity of the quasiparticle trapping efficiency vs. source distance produced increasingly non-Gaussian peaks in the pulse height spectra as the alpha source was moved toward the thermistor edge, as shown in Figure 6.7. The peak maximum, or mode, was therefore not equal to the mean pulse height.

As the ^{241}Am source was moved toward the thermistor with an Al/Au quasiparticle trap both the rise and fall times of the thermal pulse decreased, which is another indication that quasiparticle trapping into the Al/Au/thermistor region was dominating the energy input. At the thermistor edge the signal rise time τ_{ath} was 40 μs. The initial decay time of this signal was 90 μs (τ_{th}), reflecting that the thermistor had heated significantly above the Ge absorber temperature. A second time constant of 300 μs (τ_{Ge}) was needed to fit the tail of this signal, indicating that the thermistor-absorber system had reached equilibrium. Thus as the alpha source was moved toward the thermistor edge, the signal rise time decreased from 90 μs to 40 μs and the signal decay time decreased from a single time constant of 300 μs to two decay time constants of 90 μs and 300 μs.

An additional study of the SLAPS device was performed two years after the original experiment discussed above. Due to improvements in our computer software and our understanding of the device performance, we were able to carefully measure the dependence of the signal rise time on alpha source position. Due to degradation over time of the epoxy bond linking the thermistors to the Ge absorber, the performance of the SLAPS device was superior to the performance discussed above. The weaker thermal link between the thermistor with a qp trap and the Ge absorber meant that athermal energy was collected into the thermistor by qp trapping over longer time periods. As shown in Figure 6.9, the signal rise time gives position information for interaction distances of more than 6 mm from the quasiparticle trap. The signal rise time increases by more than a factor of 13

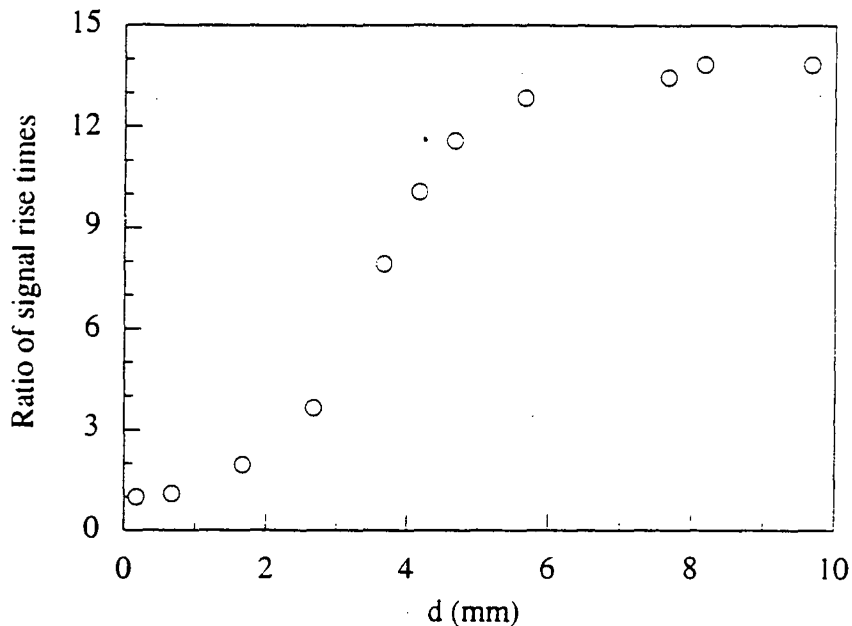

Fig. 6.9 Ratio of the signal rise time for an alpha particle interaction at distance d from the thermistor with a qp trap to the pulse rise time for an alpha particle interaction at a distance of 0 mm from the qp trap. The strong position dependence of the signal rise time is not observed in the thermistor without a qp trap.

when the alpha particle interaction in the Ge absorber occurs at a distance of 6 mm from the qp trap compared to a distance of 0 mm from the qp trap. We note that the position sensitivity of the SLAPS device is related to but not equal to the quasiparticle diffusion length. Athermal phonons produced by an interaction in the Ge will excite quasiparticles throughout the Al film, with the highest quasiparticle density just above the interaction position. Thus the range of interaction distances for which the thermistor signal is enhanced by quasiparticle trapping is a function of device geometry, athermal phonon lifetime, and the spread of quasiparticle diffusion times into the trap.

6.8 Conclusion

In conclusion, we have demonstrated with the SLAPS device that the quasiparticle trapping mechanism can be used to dramatically increase the sensitivity of a calorimetric detector to athermal phonons. The performance of this device could be improved by optimizing the film thickness and the ratio of film volume to trap volume, by using a superconducting film with a larger value of $v_F \cdot \lambda \cdot \tau_{qp}$, and by operating at lower temperatures to reduce the quasiparticle energy loss from inelastic phonon scattering. Rather than relying on a random diffusion process to send quasiparticles into the trapping region a film could be devised with a decreasing energy gap gradient around the traps, thereby more efficiently funneling quasiparticles into the trapping regions. Finally, the position and energy resolution could be improved by separating the quasiparticle traps by distances on the order of the diffusion length and comparing pulse heights observed in neighboring traps to obtain curves of constant energy and position [Kraus, 1989].

Chapter 7
Far infrared transmittance of $Sc_2@C_{84}$ and $Er_2@C_{82}$

One of the most important applications of doped Ge semiconductors is their use as temperature sensitive resistors for calorimetric and bolometric detectors, as described in Chapter 5. In Chapter 6 we described a novel low temperature particle detector which uses doped Ge thermistors as calorimeters. In this chapter, we describe an experiment which uses a doped Ge thermistor as part of a conventional low temperature bolometer for far infrared studies of novel materials. We have measured the far infrared transmittance of $Sc_2@C_{84}$ and $Er_2@C_{82}$ at 1.5 K between 30 cm^{-1} and 200 cm^{-1}. Both materials are observed to have a large primary absorption feature centered at 95 cm^{-1} with a width of approximately 50 cm^{-1}, as well as a number of secondary absorption features which are different in the two materials. This is the first study of the far infrared properties of metallofullerenes and may help in the determination of the structural and electronic properties of these materials.

7.1 Introduction

The recently discovered encapsulation of a metal atom or atoms inside fullerene cages [Kroto *et al.*, 1985; Johnson *et al.*, 1992; Bethune *et al.*, 1993] has excited considerable interest because these materials may have novel properties and applications. However, due to the extreme difficulty in producing purified samples in quantities greater than a few hundred micrograms, characterization of these metallofullerenes has been hampered. Many theoretical questions remain concerning the formation, structure, and electronic properties of these materials [Bethune *et al.*, 1993].

Theoretical calculations [Laasonen *et al.*, 1992; Joslin *et al.*, 1993; Nagase *et al.*, 1993; van Cleef *et al.*, 1993; Kobayashi *et al.*, 1995] of the minimum energy configurations for $La@C_{82}$, $La_2@C_{80}$, $Li@C_{60}$, and $Na@C_{60}$ have predicted that a metal

atom encapsulated in a fullerene cage typically donates electrons to the cage and assumes a noncentral position. Charge transfer has been confirmed by ESR studies in several materials [Shinohara *et al.*, 1992; Bandow *et al.*, 1993] and by XPS measurements [Weaver *et al.*, 1992]. In a theoretical investigation of the properties of $Sc_2@C_{84}$, Nagase and Kobayashi [1994] calculated that each Sc atom donates two electrons to the C_{84} cage, and that these four extra electrons are distributed almost uniformly on the cage surface. The two Sc atoms are strongly bound at opposite ends of the C_{84} cage with a separation of ~4 Å. This distance is considerably larger than the Sc-Sc separation in the Sc dimer, 2.7 Å [Harris and Jones, 1979], and hence the atoms are expected to interact independently with the cage. The Sc bonding to the fullerene cage was found to be primarily electrostatic and due to polarization.

Movements of the charged metal atom or atoms trapped inside the cage are expected to have large dipole derivatives and produce very strong far infrared transitions, yielding spectra which are extremely sensitive to the size of the cage, the mass and charge of the encapsulated metal atom or atoms, and the potential inside the cage [van Cleef *et al.*, 1993]. Thus, a measurement of the far infrared properties of these species may provide an excellent diagnostic of the properties of endohedral carbon cage molecules.

In this chapter we demonstrate two experimental techniques for studying the far infrared transmittance of metallofullerenes which are optimized for the study of very small sample quantities. The first technique involves placing the metallofullerene sample in the middle of a 1.2 mm thick parafilm pellet, which is then cooled to 1.5 K and studied using Fourier transform spectroscopy between 30 cm^{-1} and 340 cm^{-1}. Using this technique, we have measured the transmittance spectrum of $Sc_2@C_{84}$ and are able to observe absorption features at the level of one and a half percent. This method allows complete sample recovery. The second technique we have developed is to sublime the metallofullerene sample onto a 1 mm z-cut crystal quartz substrate, which is then cooled to approximately 1.5 K and studied using Fourier transform spectroscopy between 20 cm^{-1} and 200 cm^{-1}.

Using this technique we have measured the transmittance spectrum of $Er_2@C_{82}$ and are able to observe absorption features at the level of one percent. These two techniques are useful for studying the far infrared transmittance of any material available in powder form. The parafilm technique is easier and allows the transmittance to be measured at higher frequencies; however, the sublimation technique should be used when a uniform film is required.

7.2 Sample preparation

The $Sc_2@C_{84}$ and $Er_2@C_{82}$ samples studied in this work were produced by arc-vaporization in helium of cored carbon electrodes packed with a mixture of graphite and metal or metal-oxide [Beyers *et al.*, 1994]. Production efficiency was increased by reversing the arc polarity and "back-burning" the carbide-rich cathode deposit. Fullerene molecules were extracted from the carbon soot with CS_2, and the separation of $Sc_2@C_{84}$ and $Er_2@C_{82}$ was accomplished using two-stage high performance liquid chromatography (HPLC) [Stevenson *et al.*, 1994-A; Stevenson *et al.*, 1994-B]. Following HPLC, the samples were analyzed using laser desorption/laser ionization mass spectroscopy [Meijer *et al.*, 1990] and were found to consist of at least 98% of the desired metallofullerene species.

In order to measure the far infrared transmittance of $Sc_2@C_{84}$, we placed the material in the middle of a parafilm pellet as outlined below. We first deposited approximately 500 μg of $Sc_2@C_{84}$ dissolved in CS_2 into an 0.3 cm diameter indent on a 120 mm thick parafilm substrate and allowed the solvent to slowly evaporate. This was done in a nitrogen atmosphere to avoid condensation of water onto the substrate. This created a $Sc_2@C_{84}$ disk which measured 0.3 cm in diameter and 40 ± 10 μm in thickness. We then baked the sample in a 60 °C oven for 1/2 hr. to remove any residual solvent. The parafilm substrate was surrounded by additional parafilm layers and gently compressed between two glass microscope slides. The composite structure was heated to just above the parafilm melting temperature (< 100 °C) on a hot plate to produce a solid 1.2 mm thick

parafilm pellet. We used the same technique to create a parafilm pellet containing a C_{60} disk measuring 0.3 cm in diameter and 200 ± 20 μm in thickness which we used to confirm the reliability of the measurement technique. In addition we produced three pure parafilm pellets to use as references.

To prepare the $Er_2@C_{82}$ sample, we heated approximately 700 μg of the material to 500 °C in a vacuum and sublimed it onto a 1 mm thick z-cut crystal quartz substrate to form a disk approximately 0.4 cm in diameter and 40 ± 10 μm in thickness. For comparison, we used the same technique to evaporate a C_{60} disk of the same dimensions onto another crystal quartz substrate. In addition we used two crystal quartz substrates as references. All crystal quartz substrates were cut from neighboring spots on a large piece of z-cut crystal quartz in order to minimize the differences in thickness and hence the ratio of their Fabry-Perot interference fringes. The crystal quartz and parafilm substrates were chosen to be 1 mm thick and 1.2 mm thick, respectively, so that the separation between Fabry-Perot fringes was less than 3 cm^{-1}.

7.3 Experimental Technique

The far infrared transmittance of the samples at 1.5 K was measured with a composite bolometer in conjunction with a Michelson interferometer, using Fourier Transform Spectroscopy [Miller, 1993]. A schematic of the experiment is shown in Figure 7.1. Infrared radiation produced by a mercury arc lamp and chopped at 43 Hz passes through a light pipe, both warm and cold filters, and a cold sample wheel before entering a 1.5 K bolometer can. The bolometer uses neutron transmutation doped Ge (NTD Ge) as the thermometric material [Haller *et al.*, 1984]. The interferometer was operated in a step-

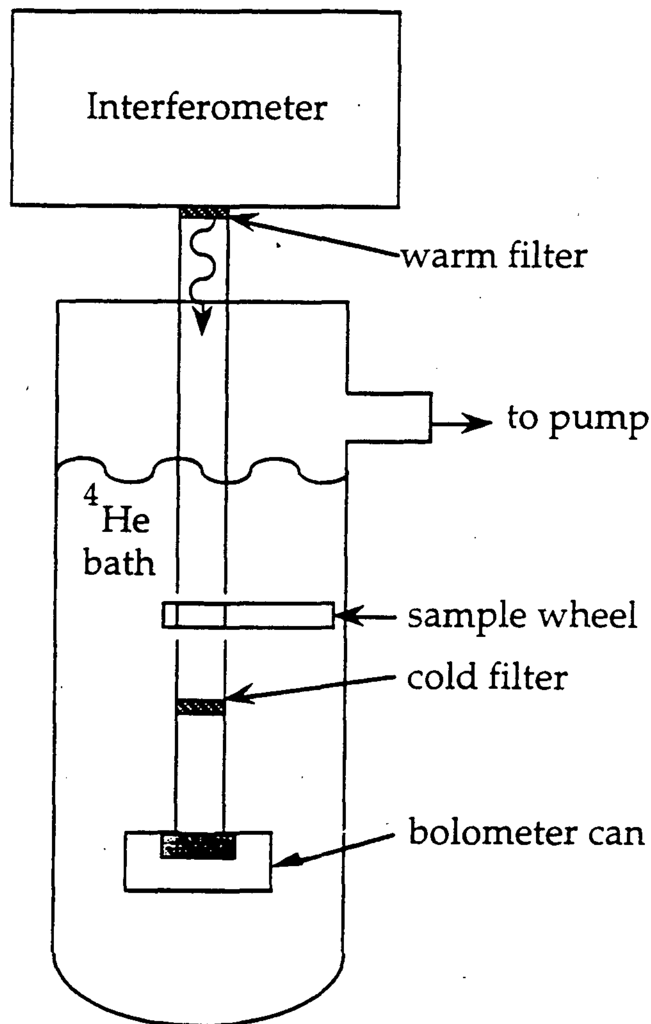

Fig. 7.1 Schematic of the experiment. The Michelson Interferometer is used as a Fourier Transform Spectrometer. Chopped infrared radiation passes through a light pipe, both warm and cold filters, and a sample wheel before entering a 1.5 K bolometer can. The bolometer response is measured as a function of mirror position.

and-integrate mode rather than in a continuous scan mode to improve the noise performance. To measure spectra over an extended frequency region we used several different combinations of beamsplitters and warm filters. The warm filter was selected to remove all radiation at frequencies above the range of study, thus avoiding aliasing effects. The cold 0.001" thick black polyethylene filter was chosen to minimize bolometer loading from unchopped radiation.

The bolometer used in our measurement was not globally optimized (see Chapter 5), because the accuracy of our measurements of the transmittance of $Sc_2@C_{84}$ and $Er_2@C_{82}$ was limited by our ability to match the sample and reference substrates rather than by bolometer noise. The selection of the thermistor resistance was driven by our choice to operate at pumped liquid helium temperatures and by the availability of a laboratory standard, low noise room temperature amplifier. We used the Princeton Applied Research PAR-113 preamplifier with an input voltage noise of 7 $nV/\sqrt{Hz}$ and a current noise of ~ 10^{-15} $A/\sqrt{Hz}$. We chose to use the thermistor material NTD Ge #4, which has an impedance at 1.5 K of approximately 500 kΩ. This impedance corresponds to a voltage noise $e_n \approx 6.3$ $nV/\sqrt{Hz}$, comparable to the noise of the preamplifier. The bolometers were exposed to a maximum background optical loading Q of approximately 1 μW for a 1/8 mil mylar beam-splitter used in combination with a 700 cm^{-1} cutoff lowpass filter [Miller, 1993]. The thermal link between the bolometer and the 1.5 K can was provided by four 12.5 μm diameter brass wires with a combined thermal conductivity $G \approx 5$ μW/K.

We determined the transmittance spectrum of the fullerene samples by computing the ratio of the bolometer response when the fullerene sample and substrate were in the light path to the bolometer response when the bare substrate was in the light path. We also examined the ratio of the bolometer responses when two nominally identical substrates were in the light path. The difference between this ratio and unity determined the degree to which our data were contaminated by systematic noise, drifts, and small differences in substrate thickness or composition. For each position of the sample wheel, we obtained a large number of spectra and averaged them in order to minimize the effects of bolometer noise and slow drifts in the bolometer temperature.

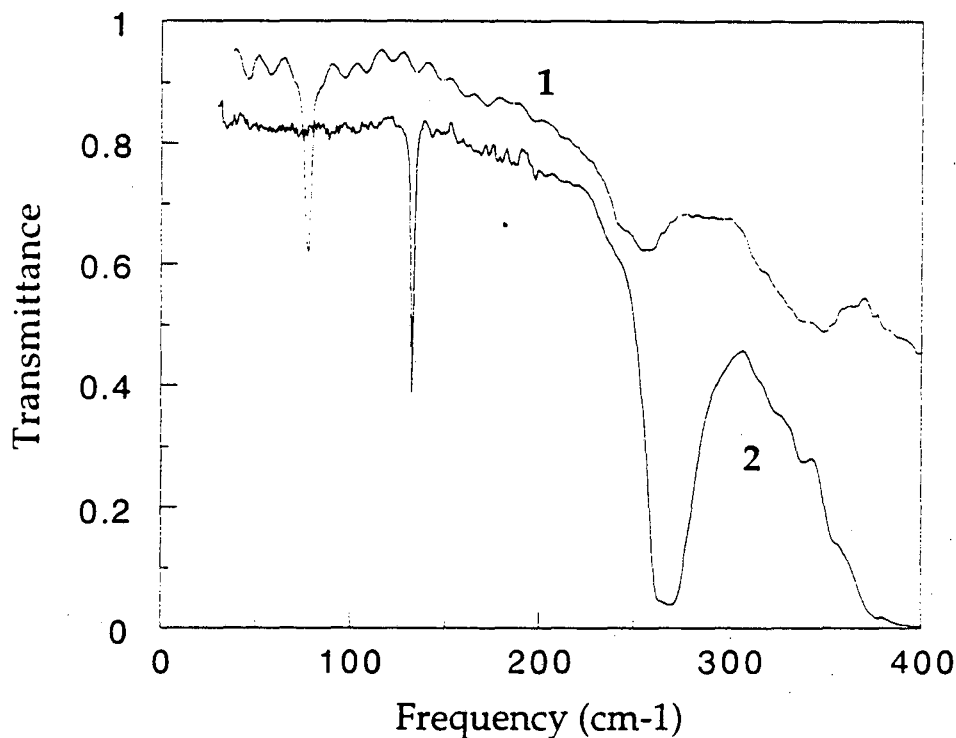

Fig. 7.2 Transmittance at 1.5 K of a 1.2 mm thick parafilm pellet (Curve 1) and a 1 mm thick z-cut crystal quartz substate (Curve 2) between 30 cm^{-1} and 400 cm^{-1}.

7.4 Experimental Results

Due to the very small quantities of sample available, the accuracy of our measurements of the transmittance of $Sc_2@C_{84}$ and $Er_2@C_{82}$ was limited by our ability to match the sample and reference substrates as discussed above. We will first discuss measurements on $Sc_2@C_{84}$ embedded in a 1.2 mm thick parafilm pellet. The transmittance of a reference pellet at 1.5 K is shown in Figure 7.2, Curve 1. Parafilm has a sharp absorption feature at 77 cm^{-1} and two broad absorption features at 255 cm^{-1} and 340 cm^{-1}. In addition, the Fabry Perot interference fringes in the transmittance spectrum of a 1.2 mm thick parafilm pellet are separated by $\Delta f = (2nt)^{-1} \approx 2.7$ cm^{-1} where $n \approx 1.56$. The ratio of the spectra of two parafilm reference pellets is shown in Figure 7.3, Curve 0. This curve

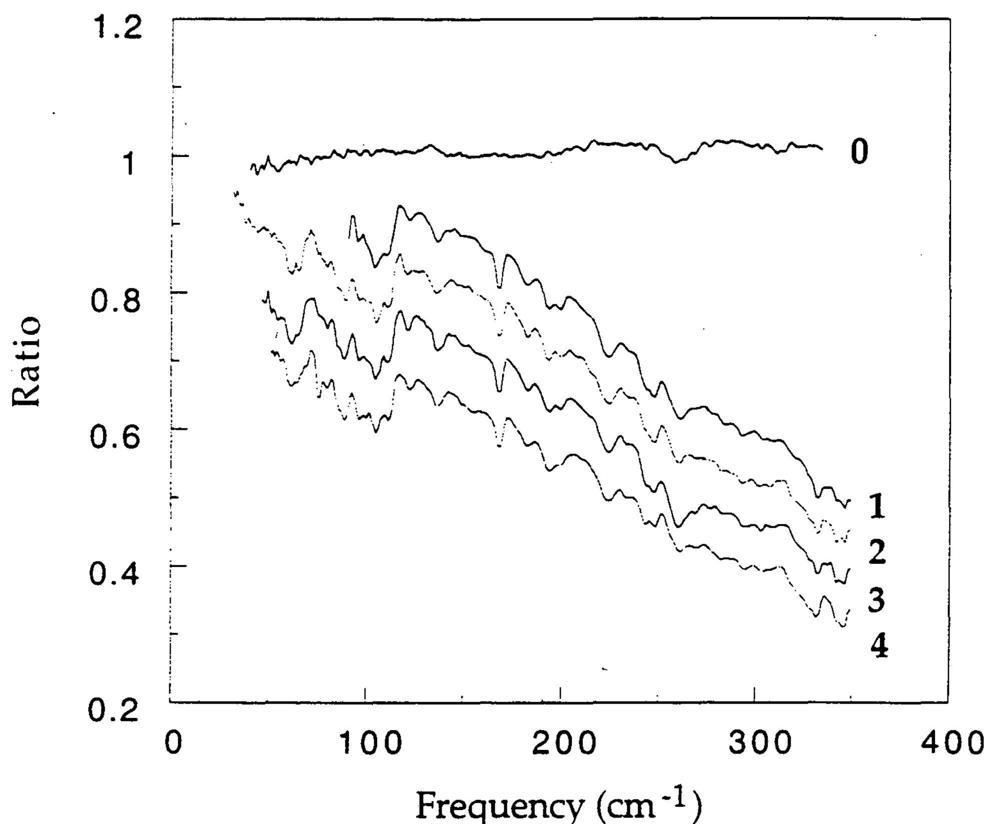

Fig. 7.3 Transmittance of $Sc_2@C_{84}$, determined by taking the ratio of the $Sc_2@C_{84}$-containing parafilm pellet with: parafilm reference #1 (Curve 1); parafilm reference #1 with a different filtering scheme (Curve 2); parafilm reference #2 (Curve 3); and parafilm reference #3 (Curve 4). The curve labelled "0" shows the ratio of parafilm reference #2 to parafilm reference #1. To facilitate comparison, Curves 2, 3, and 4 have been offset from Curve 1 by -0.1, -0.2, and -0.3 respectively.

has a number of features less than 0.01 in height and less than 5 cm^{-1} in width which are due to the differences in the Fabry Perot interference fringes of the two samples. The broad 3% absorption feature at 260 cm^{-1} arises from the broad parafilm absorption feature at 255 cm^{-1}. These features, due to small differences in thickness and composition of the parafilm substrates, are above the noise level of our instrument and fundamentally limit our ability to measure absorption features in $Sc_2@C_{84}$.

The transmittance of $Sc_2@C_{84}$ between 30 cm^{-1} and 350 cm^{-1} is plotted in Figure 7.3, Curves 1 through 4. The four curves were generated by computing the ratio of the $Sc_2@C_{84}$-containing parafilm pellet with: parafilm reference #1 (Curve 1); reference #1, measured with a different filtering scheme (Curve 2); reference #2 (Curve 3); and reference #3 (Curve 4). For comparison purposes Curves 2, 3, and 4 have been offset from Curve 1 by -0.1, -0.2, and -0.3 respectively. The agreement between the four curves is remarkably good, and implies that noise is not important. Curve 4 has a small absorption feature at 77 cm^{-1} not observed in Curves 1, 2, and 3, which we attribute to imperfect ratioing of the 77 cm^{-1} absorption feature in parafilm. Features smaller than 0.015 cannot be distinguished from differences in the Fabry Perot interference fringes between the sample and reference parafilm pellets. In Figure 7.4, Curve 1, we plot the absorption coefficient computed from the average of these transmittance spectra. Table 7.1 summarizes the absorption features observed in $Sc_2@C_{84}$. The most prominent absorption feature we observe is a band centered at approximately 95 cm^{-1}, on top of which are superposed a number of smaller, narrower absorption features.

Our measurements of the transmittance of $Er_2@C_{82}$ were also limited by small differences in thickness and composition between the crystal quartz sample substrate and reference substrate. The transmittance of a 1 mm thick z-cut crystal quartz substrate at 1.5 K is shown in Figure 7.2, Curve 2. Crystal quartz has a sharp absorption feature at 132.5 cm^{-1}. In addition, the Fabry Perot interference fringes in the transmittance spectrum of a 1 mm thick z-cut crystal quartz substrate are separated by $\Delta f = (2nt)^{-1} \approx 2.3$ cm^{-1} where $n \approx 2.2$. The ratio of the spectra of two reference crystal quartz substrates has a number of features less than 0.01 in height and less than 3 cm^{-1} in width which are due to the differences in the Fabry Perot interference fringes of the two samples.

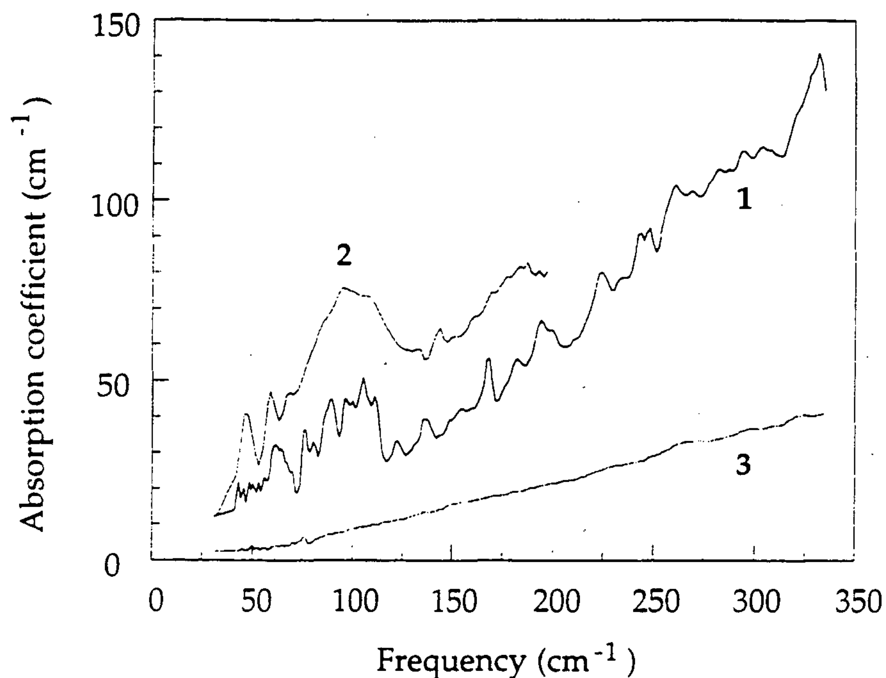

Fig. 7.4 Absorption coefficient as a function of frequency for $Sc_2@C_{84}$ (Curve 1), $Er_2@C_{82}$ (Curve 2), and C_{60} (Curve 3). The $Er_2@C_{82}$ spectrum was measured with a spectral resolution of 2 cm^{-1}. The $Sc_2@C_{84}$ and C_{60} spectra were measured with a spectral resolution of 1 cm^{-1} below 200 cm^{-1} and 1.5 cm^{-1} above 200 cm^{-1}. Due to uncertainty in sample thicknesses, Curves 1, 2, and 3 are determined to within multiplicative errors of 25%, 25%, and 10%, respectively.

We have converted the transmittance spectrum of $Er_2@C_{82}$ into a plot of absorption coefficient as a function of frequency, as shown in Figure 7.4, Curve 2. All features less than 0.01 in the transmittance spectrum are attributed to differences in the Fabry Perot interference fringes between the sample and reference substrates. Table 7.2 summarizes the absorption features observed in $Er_2@C_{82}$, listed in order of increasing frequency. The largest absorption feature we observe is a broad absorption centered at approximately 94 cm^{-1}, similar to the feature observed in $Sc_2@C_{84}$.

Frequency (cm^{-1})	$\Delta\alpha$ (cm^{-1})	Δf (cm^{-1})
62	12	10
76 (pf)	6	3
88	12	10
95	20	40
97	6	8
105	8	7
122	5	8
137	7	10
168	12	10
182	5	8
194	11	14
222	8	12
245	8	10
260 (pf?)	10	20
330 (pf?)	10	10
345 (pf?)	10	10

Table 7.1 Absorption features in $Sc_2@C_{84}$. Columns show the center frequency, height $\Delta\alpha$ relative to the background absorption coefficient, and width Δf. The center frequency is determined to within $\pm$ 2 cm^{-1}; we estimate a 10% error in our determination of $\Delta\alpha$ and Δf. Features which are believed to be due to small differences between the sample parafilm pellet and a reference parafilm pellet are marked by (pf).

Frequency (cm^{-1})	$\Delta\alpha$ (cm^{-1})	Δf (cm^{-1})
45	17	10
59	13	10
69	7	10
94	34	70
144	6	10
177	5	25

Table 7.2 Absorption features in $Er_2@C_{82}$. The center frequency is determined to within $\pm$ 2 cm^{-1}; we estimate a 10% error in our determination of $\Delta\alpha$ and Δf. Columns show the center frequency, height $\Delta\alpha$ relative to the background absorption coefficient, and width Δf.

We re-measured the transmittance spectrum of the sample after approximately 80% of the sample was removed and again observed the same absorption features; however, the absorption was reduced by a factor of approximately five. This confirms that the observed far-infrared absorption features are intrinsic to the Er_2C_{82}.

For comparison purposes, we also measured the transmittance spectrum of a 200 μm thick C_{60} layer embedded in a parafilm pellet and a 40 μm thick C_{60} film sublimed onto a crystal quartz substrate. Both C_{60} samples had been exposed to air. The frequency dependence of the deduced absorption coefficient of the thicker film is shown in Figure 7.4, Curve 3. The spectrum of the 40 μm thick C_{60} film was found to be similar. The absorption coefficient is featureless and increases linearly with frequency between 100 cm^{-1} and 330 cm^{-1}, in agreement with the result of Onari *et al.* [1991]. The small feature at 77 cm^{-1} is an artifact of the 77 cm^{-1} parafilm absorption. Our measured absorption coefficient a at 60 cm^{-1} is 3.9 ± 0.4 cm^{-1} at T = 1.5 K, compared to 4.2 cm^{-1} at T = 4 K measured by FitzGerald and Sievers [1994] in C_{60} which had been exposed to air. Our sample is too thin for us to observe the air-induced impurity bands at 18 cm^{-1}, 27 cm^{-1}, and 59 cm^{-1}. The good agreement between our measured C_{60} absorption and that published in the literature, as well as the fact that we do not observe any significant absorption features between 30 cm^{-1} and 330 cm^{-1}, confirms the reliability of our sample preparation and measurement techniques.

7.5 Discussion and Conclusion

In discussing the vibrational properties of the metallofullerenes we distinguish between internal and external vibrations. The internal motions involve carbon-carbon and metal-carbon bending and stretching vibrations, whereas the external modes involve translational and rotational motions of the entire cage. Theoretical calculations by Negri *et al.* [1992] of the infrared active vibrational modes of an empty C_{84} cage using the quantum chemical force field for pi electrons (CQFF/PI) method predict a lowest energy band at

around 200 cm^{-1}. A similar calculation by Orlandi *et al.* [1993] for an empty C_{82} cage also finds a lowest energy infrared band at around 200 cm^{-1}. In the case of a metallofullerene with a relatively strong metal-cage bonding one expects to measure an experimental spectrum significantly different from these calculations [van Cleef *et al.*, 1993]. In particular one also expects modes to appear below 200 cm^{-1}. Even in the case of a weak metal-cage bonding, the charge transfer to the cage will certainly lead to a significant renormalization of the cage frequencies. The spectra presented here show many reproducible absorption features below 300 cm^{-1}. In view of the above discussion, we propose that many of the observed features are due to modified cage vibrations.

Among the internal modes, the metal-cage vibrations are expected to give the strongest contribution to the far infrared spectrum due to their large dipole derivatives. Without knowledge of the bonding strength between the metal atoms and the cage, it is difficult to predict their vibrational frequencies. Since the Er (atomic weight 167.3) is much heavier than the Sc (atomic weight 44.96), one expects the Er-cage vibrations at lower frequencies than the Sc-cage vibrations for comparable bonding to the cage. However, without more knowledge of the metal-cage interaction we cannot yet assign any of the observed absorption modes.

The most striking feature in the spectra of $Sc_2@C_{84}$ and $Er_2@C_{82}$ is the large absorption at 95 cm^{-1} observed in both materials. The coincidence of the 95 cm^{-1} absorption in both materials suggests that the vibration responsible for this feature should be independent of the large mass difference between Er and Sc. The only modes which are relatively insensitive to this mass difference are the external modes. The frequencies of these modes depend on the intermolecular force constants and either the total masses (translations) or total inertial moments (rotations) of the molecules. If we make the reasonable assumption that the force constants are comparable in both materials, we estimate the difference between the external frequencies of both molecules to be about 10%

for the translational modes and only 2% for the rotational modes. In view of these small differences, we propose that the 95 cm^{-1} absorption feature is due to an external vibration.

Although this is the first experimental study of the far infrared properties of metallofullerenes, Kikuchi *et al.* [1993] have measured the infrared absorption spectra of C_{82} and LaC_{82} above 400 cm^{-1}. They found approximately ten absorption lines between 400 cm^{-1} and 800 cm^{-1} in both samples and some correlation between the LaC_{82} modes and bending motions of the cage. Although some of their absorption features are not clearly distinguishable from the noise, they appear to have typical widths of 10 cm^{-1}, similar to the widths of the absorption features seen in $Sc_2@C_{84}$ and $Er_2@C_{82}$.

Due to the extreme difficulty in producing and purifying metallofullerene samples, we were limited to studying two species of dimetallofullerenes $Sc_2@C_{84}$ and $Er_2@C_{82}$. However, if sample production becomes more efficient, an especially interesting study could be performed on a sequence such as C_{84}, $Sc@C_{84}$, $Sc_2@C_{84}$, and $Sc_3@C_{84}$. As discussed above, the C_{84} cage without inclusions is not expected to show infrared activity below 200 cm^{-1}. If theoretical expectations that the two Sc atoms are essentially noninteracting at opposite ends of the C_{84} cage are correct, $Sc@C_{84}$ and $Sc_2@C_{84}$ would show similar far infrared spectra with the absorption coefficients approximately twice as strong in the dimetallofullerene. $Sc_3@C_{84}$ should show a significantly different transmittance spectrum if the three Sc atoms are enclosed as a trimer which moves relatively freely throughout the C_{84} cage, analogous to the behavior indicated by EPR measurements [van Loosdrecht *et al.*, 1994] for Sc_3C_{82}. A systematic study of a variety of cages and metal inclusions will reveal much about the structure and properties of these fascinating new materials.

Appendix A: JFET noise

The electronic noise in a detector should be negligible compared to more fundamental noise sources such as Johnson noise, thermal noise, and photon noise. We discuss three methods for reducing the noise of readout electronics which use JFETs to amplify a voltage signal. In Section A.1, we describe voltage and current noise measurements of the NJ132L JFET at low frequencies (50 - 400 Hz) as a function of JFET temperature, drain voltage, and current. We find that the noise is minimized for T ~ 130 K, V_d ~ 6 V, and I ~ 0.7 mA. In Section A.2, we describe the fabrication of small, cooled JFET packages which can bolt to a helium cold plate and self-heat to a selected operating temperature. In Section A.3, we present an ultra-low noise voltage preamplifier design for room temperature operation which uses the NJ903L JFET. This preamplifier has a measured gain of 401, a white voltage noise level of 1.2 nV/√Hz, and a voltage noise of less than 3 nV/√Hz at frequencies above 0.5 Hz.

In order to determine the temperature of the cooled JFETs, we used a 1N4448 diode. In Section A.4, we describe how to convert any commercial diode into a calibrated thermometer for use between 77 K and 300 K. Diode thermometers are extremely useful diagnostic tools for a wide variety of cryogenic applications. They are small, inexpensive, simple to use, and can be easily calibrated to an accuracy of a few K within minutes.

A.1 JFET noise minimization: NJ132L JFET

A.1.1 Voltage noise

The voltage noise e_n of a JFET depends on the following controllable parameters: JFET temperature T, drain voltage V_d, and current I through the JFET. The voltage noise does *not* depend uniquely on the power dissipated in the JFET. It also depends on the manufacturing process, the presence of undesired impurities, and the gate width. These variations lead to significant differences in the noise properties of nominally identical

JFETs. The primary JFET property which determines its voltage and current noise is the gate width. Thus, the NJ903L JFET with a 903 μm gate width has a smaller voltage noise, larger current noise, and a larger gate-drain capacitance than the NJ132L JFET which has a 132 μm gate width.

We have measured e_n as a function of T, V_d, and I in the NJ132L dual JFET. In order to measure the voltage noise of a JFET, the noise fluctuations at the gate must be amplified well above the noise level of the measuring device. We accomplished this by using the simple measurement circuit shown in Figure A.1. The JFET sources are connected to a constant-current supply which is designed to be extremely stable against fluctuations or slow drifts in the power supply voltage. The current can be controlled by an appropriate selection of the resistor R_I. The voltage drop across R_I is equal to the sum of the voltage drops across the three 1N4448 diodes minus the base-emitter diode drop of the 2N2222 transistor, and is approximately 3×0.65 V - 0.65 V $\approx$ 1.3 V where 0.65 V is the typical diode voltage drop. Therefore the current through each side of the dual JFET is given by $I \approx 0.65/R_I$. The current through each JFET can be conveniently measured by measuring the voltage drop V_I across the 1 kΩ resistor, using the conversion factor 1 V for every 0.5 mA of current through each JFET.

For a given value of I, the drain voltage $V_D = +V - IR_d$ can be controlled by an appropriate selection of +V and R_d. When the input voltage changes by an amount ΔV_{in}, the voltage at the drain varies by an amount $\Delta V_d = g_m R_d \Delta V_{in}$. The transconductance g_m is defined as

$$g_m = \Delta I_{DS}/\Delta V_{GS}, \tag{A.1}$$

where D refers to the drain, G refers to the gate, and S refers to the source of the JFET. R_d is chosen so that the voltage noise at the drain $g_m R_d e_n$ is several times larger than the input voltage noise of the PAR-113 preamplifier so that e_n can be accurately measured. For typical values $e_n = 2$ nV/√Hz, $g_m = (450\ \Omega)^{-1}$, and a PAR-113 input voltage noise of 7 nV/√Hz, R_d should be above 4.5 kΩ in order to ensure a voltage gain of at least 10.

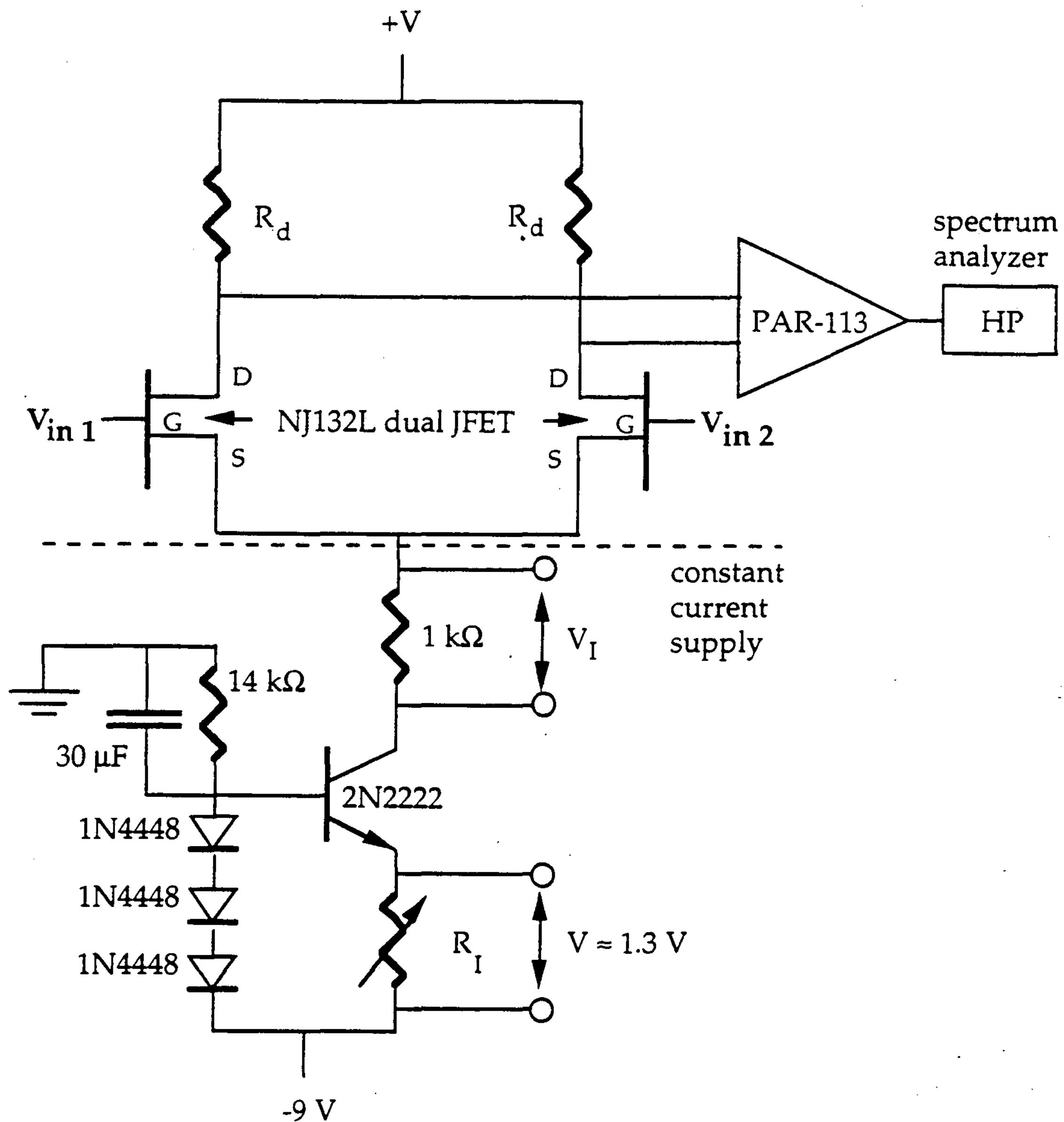

Fig.A.1 Simple voltage noise measurement circuit which allows easy control of JFET current and drain voltage.

In order to measure e_n as a function of temperature, the JFETs were mounted with thick copper wires onto an aluminum stage set off from a 77 K cold plate by nylon screws. The aluminum stage had a calculated time constant of 2.8 minutes, and a measured time constant of ~ 2.5 minutes. Even for the maximum power through each JFET (4 mW), the

JFETS were calculated to be thermally sunk within approximately 2 K. The temperature was measured using a 1N4448 diode mounted on the aluminum stage as described in Section A.4. The stage was heated with a 500 Ω heater.

For each measurement of $e_n(T,V_d,I)$ we applied a small signal into Gate 1, measured the transfer function $g_m R_d$ at Drain 1, and made sure that the transfer function was large enough so that we could ignore corrections for the input noise of the PAR-113. We then measured the shorted input voltage noise of the JFETS using a Hewlett Packard Spectrum Analyzer. We checked the consistency of our noise measurements by comparing the measured voltage noise with the estimated voltage noise of the JFET using the formula [Horowitz and Hill, 1980],

$$e_n = \sqrt{4kT\left(\frac{2}{3g_m}\right)} \left(\frac{V}{\sqrt{Hz}}\right). \tag{A.2}$$

Our measured voltage noise levels confirm the accuracy of our measurement technique. For example, when $R_d = 13$ kΩ we measure a gain of 29.8 and deduce a transconductance $g_m = (436\ \Omega)^{-1}$. Using this value for g_m, we predict a noise level at 300 K of 1.65 nV/√Hz which is nearly identical to our measured noise level of 1.72 nV/√Hz.

Figure A.2 shows the room temperature voltage noise of the NJ132L JFET as a function of drain voltage for a current of 1 mA. The voltage noise has a minimum at $V_d \sim 6$ V and is relatively insensitive to the drain voltage over a broad range $3\text{ V} < V_d < 10\text{ V}$. However, for $V_d < 3$ V both the 1/f noise, as evidenced by the increase in e_n (50 Hz) relative to e_n (400 Hz), and the absolute noise level increase sharply.

In Figure A.3, we plot the voltage noise as a function of current measured using a drain voltage of 7 V. At T = 300 K, e_n (I) has a well-defined minimum value of 2.2 nV/√Hz at I = 0.7 mA. When the temperature is lowered to 130 K, the minimum value of e_n decreases by 35% to 1.45 nV/√Hz at I = 0.7 mA. In contrast to the room temperature voltage noise, e_n (I) at 130 K is nearly independent of current over the range 0.1 mA < I < 1 mA.

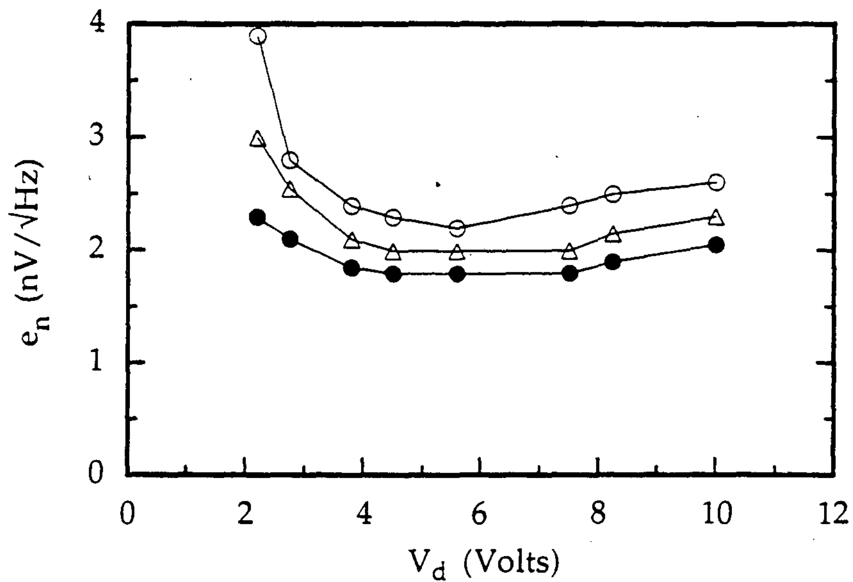

Fig.A.2 Voltage noise of the NJ132L JFET as a function of drain voltage measured at 50 Hz (open circles), 100 Hz (open triangles), and 400 Hz (solid circles). Data were measured at room temperature using a current of 1 mA.

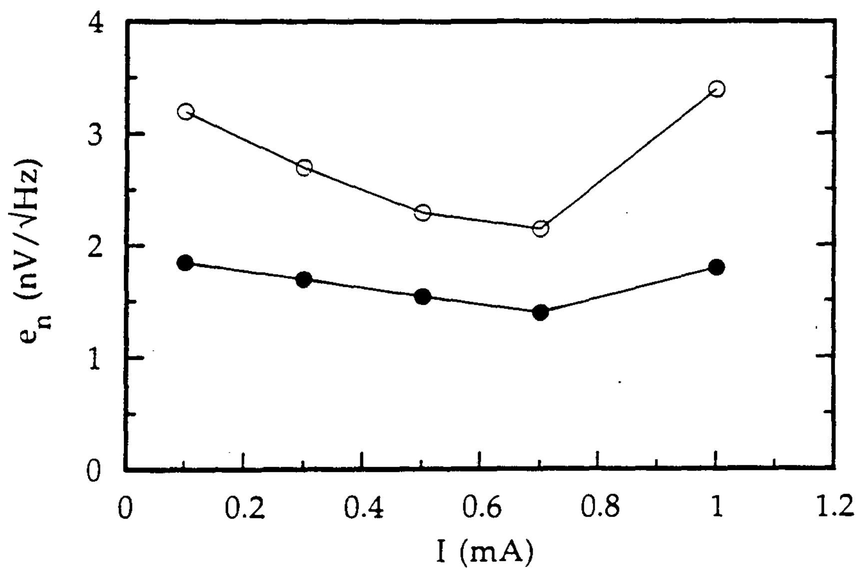

Fig.A.3 Voltage noise of the NJ132L JFET as a function of current measured at 300 K (open circles) and 130 K (solid circles). Data were measured at 100 Hz using a drain voltage of 7 V.

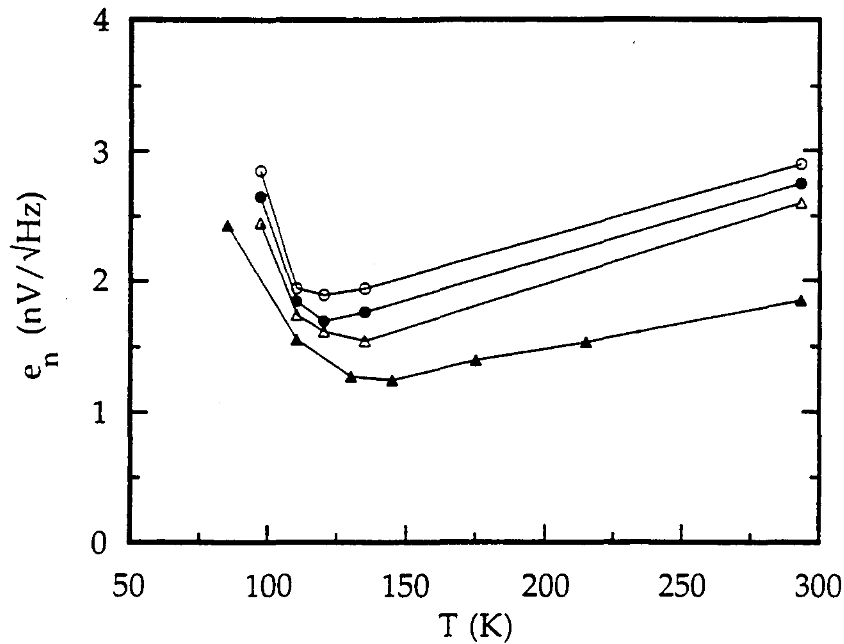

Fig.A.4 Voltage noise of the NJ132L JFET as a function of temperature measured at 50 Hz (open circles), 100 Hz (solid circles), and 400 Hz (open triangles) using a current of 0.3 mA and a drain voltage of 8 V. Data were also measured at 400 Hz (solid triangles) using a current of 0.5 mA and a drain voltage of 2.7 V.

The temperature dependence of the voltage noise is shown in Figure A.4. The minimum value of e_n is found at T ~ 130 K. At temperatures below 100 K, carrier freeze-out leads to a sharp increase in e_n. For temperatures below ~ 80 K, carrier freeze-out in the NJ132L JFET is so severe that the JFET is no longer operable.

A.1.2 Current noise

The JFET current noise i_n can be estimated from the leakage current I_L [Horowitz and Hill, 1980],

$$i_n = \sqrt{2eI_L} \left(\frac{A}{\sqrt{Hz}}\right) \tag{A.3}$$

where e is the electron charge. I_L can be measured using the simple measurement circuit shown in Figure A.5. The JFET gate is connected to ground by a switch. When the

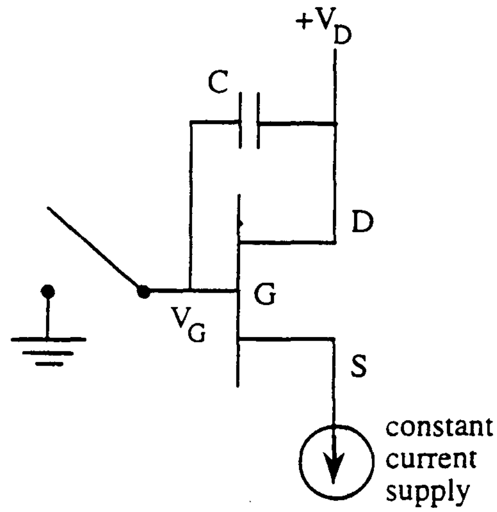

Fig.A.5 Measurement circuit used to determine the leakage current I_L of a JFET. The leakage current is related to the current noise through Equation A.3.

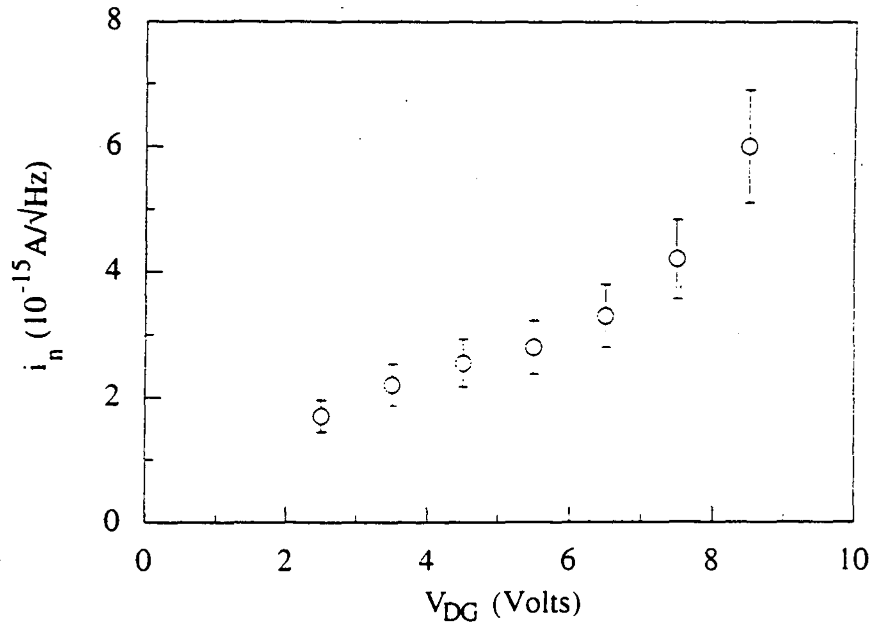

Fig.A.6 Room temperature current noise of the NJ132L JFET as a function of drain-gate voltage.

switch is opened, the voltage difference V_{DG} between the drain and gate voltages can be plotted as a function of time using a chart recorder. The slope at any value of V_{DG} is related to the leakage current by

$$\frac{dV_{DG}}{dt} = \frac{I_L}{C + C_{DG}} . \tag{A.4}$$

The drain-gate capacitance C_{DG} is typically between a few pf and 100 pf. C_{DG} can be experimentally determined by comparing the slopes dV_{DG}/dt obtained with two different values of C, i.e. C = 0 pf and C = 50 pf. If C is sufficiently large, C_{DG} can be neglected in the determination of I_L and hence i_n.

The current noise of the NJ132L JFET at 300 K computed using Equation A.3 is shown as a function of V_{DG} in Figure A.6. The current noise is typically a few 10^{-15} A/√Hz and increases with increasing V_{DG}. For a typical value V_{DG} = 4.5 V, this current noise would have to be applied across a 1 MΩ resistor in order to produce a voltage noise of 2.55 nV/√Hz comparable to the voltage noise of the JFET. For comparison purposes, we note that a 1 MΩ resistor cooled to T = 0.3 K has a Johnson noise equal to $(4kTR)^{0.5}$ = 4 nV/√Hz. When the JFET is cooled below room temperature, its current noise will be significantly reduced and is usually negligible compared to the voltage noise contribution.

A.2 Construction of cooled JFET packages

JFETs are frequently used to read a voltage signal from a low temperature detector mounted in a ^{4}He cryostat. In order to minimize the input capacitance of the amplifier, it is extremely useful to mount the JFET adjacent to the detector in the low temperature environment. Since JFETs will not operate at temperatures below ~ 77 K, the JFET must be contained within a self-heating package which can bolt to the cold plate of the cryostat. The temperature of the JFET is determined by the power balance equation

$$IV_{DS} = \frac{A}{L} \int_{T_{CP}}^{T_{JFET}} \kappa(T)\, dT , \tag{A.5}$$

where IV_{DS} is the power dissipated in the JFET, T_{CP} is the cold plate temperature, T_{JFET} is the JFET operating temperature, and $\kappa(T)$ is the thermal conductivity between the JFET and the cold plate. The cross-sectional area of the thermal link material is A and its length is L. As discussed above, the JFET voltage noise is typically optimized when $T_{JFET} \approx 130$ K. We describe a small JFET package which can bolt onto a cold plate and self-heat to an operating temperature of 130 K with only 1.25 mW of power dissipated in each JFET.

A schematic of the JFET package is shown in Figure A.7. In order to produce a small thermal conductance $G = A\kappa/L$ between the JFET and the cold plate, the JFET is glued with Stycast 2850-FT (or another glue with good low temperature adhesion) to the top of a 1.5 cm long thin-walled fiberglass stalk which is glued at the opposite end to a 6- or an 8-pin header. The thermal conductivity integral of fiberglass $\int \kappa dT$ is ≈ 0.3 W/cm between 1.5 K and 130 K. For a 1.5 cm long fiberglass stalk with a tube diameter of 1.5 mm and a wall thickness of 0.1 mm, 2 mW of power must be dissipated in the dual JFET to produce a temperature difference of 130 K.

An additional thermal link between the JFET and the cold plate is provided by the six 50 μm manganin wires which provide electrical connections between the JFET terminals and the terminals of the 6- or 8-pin header. The thermal conductivity integral of manganin $\int \kappa dT$ is ≈ 11 W/cm between 1.5 K and 130 K. For six wires each 50 μm in diameter and 2.5 cm in length. an additional 0.5 mW of power must be dissipated in the dual JFET to maintain a temperature difference of 130 K. The total power in the JFET is then required to be 2.5 mW, or 1.25 mW per JFET. As shown in Figures A.2 and A.3, for a power dissipation of 1.25 mW the optimum JFET current and drain-source voltage are approximately 0.3 mA and 4.2 V.

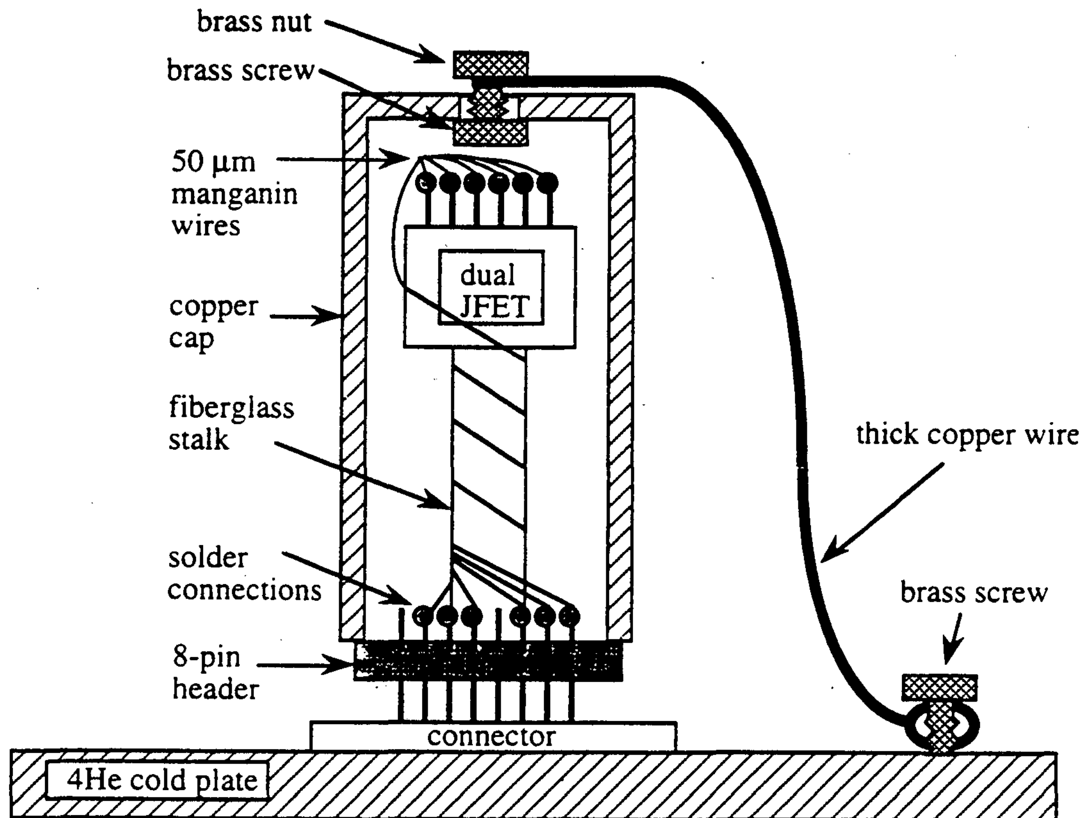

Fig.A.7 Schematic diagram of a small cooled JFET package. The height of the copper cap is ~ 1.25" and the diameter is ~ 0.4".

The manganin wires which connect the JFET terminals to the header are coated with formvar in order to prevent electrical shorts. The insulating coating has been removed from both ends of the wire with a razor blade. The wires are tightly wound around the fiberglass stalk as shown in Figure A.7 in order to prevent microphonics noise. After checking all electrical connections between the JFET and the header, we glue a copper cap onto the header. The purpose of the cap is both to protect the JFET and to prevent 130 K radiation from heating the cooled detectors. The copper cap is thermally heat sunk through a thick copper wire attached to its top. The method we used to attach the copper wire to the cap was to drill a 4x40 screw clearance hole into the top of the cap. We then inserted a 4x40 brass screw into the clearance hole from inside the cap and used a brass nut to clamp the

copper wire (whose ends were formed into appropriately sized loops) between the nut and the cap. The other end of the copper wire was directly bolted onto the cold plate.

Once the cap has been glued onto the JFET package, the electrical connections to the JFET can be tested outside the package using a handheld digital multi-meter (DMM). All JFET wires should be tested for possible shorts to the copper cap. The drain-source resistance R_{DS} should be between 30 Ω and 1 kΩ. For the NJ132L JFET, R_{DS} is ~ 200 Ω. The gate-drain and gate-source resistances should be several MΩ when the gate is positively biased with respect to the drain. When the bias polarity is reversed, R_{GD} and R_{GS} should be larger than the 20 MΩ resistance range of the DMM. The connections between the gate and the drain or source can also be checked by using the DMM in the diode mode. When the gate is positively biased, the room temperature diode drops V_{GD} and V_{GS} are ~ 0.7 V. At 77 K, typical diode drops V_{GD} and V_{GS} are ~ 1.0 V. Thus, the DMM used in the diode mode can provide a measurement of the JFET temperature. The time constant of the thermal link between the JFET and the cold plate can be determined by monitoring $V_{GD}(t)$ or $V_{GS}(t)$ as the JFET package is cooled from room temperature to 77 K. For the JFET package described above, the time constant is 20 - 30 minutes.

A.3 Low noise preamplifier circuit

In Figure A.8 we present an extremely low noise room temperature preamplifier circuit which uses the NJ903L JFET. The gain of this preamplifier is determined by the ratio of the resistors R_A and R_B, and can be derived by the following argument. The feedback from the op-amp works to drive the difference in drain voltages (V_{D2} - V_{D1}) to zero. This quantity is proportional to the difference in gate voltages (V_{G2} - V_{G1}), which is in turn equal to the difference in the source voltages (V_{S2} - V_{S1}). The op-amp can exactly compensate for the voltage difference between the two sources and hence between the two drains by applying an output current I_o across the resistor R_B which produces a voltage drop $I_oR_B = (V_{S1} - V_{S2})$. The output voltage of the preamplifier is

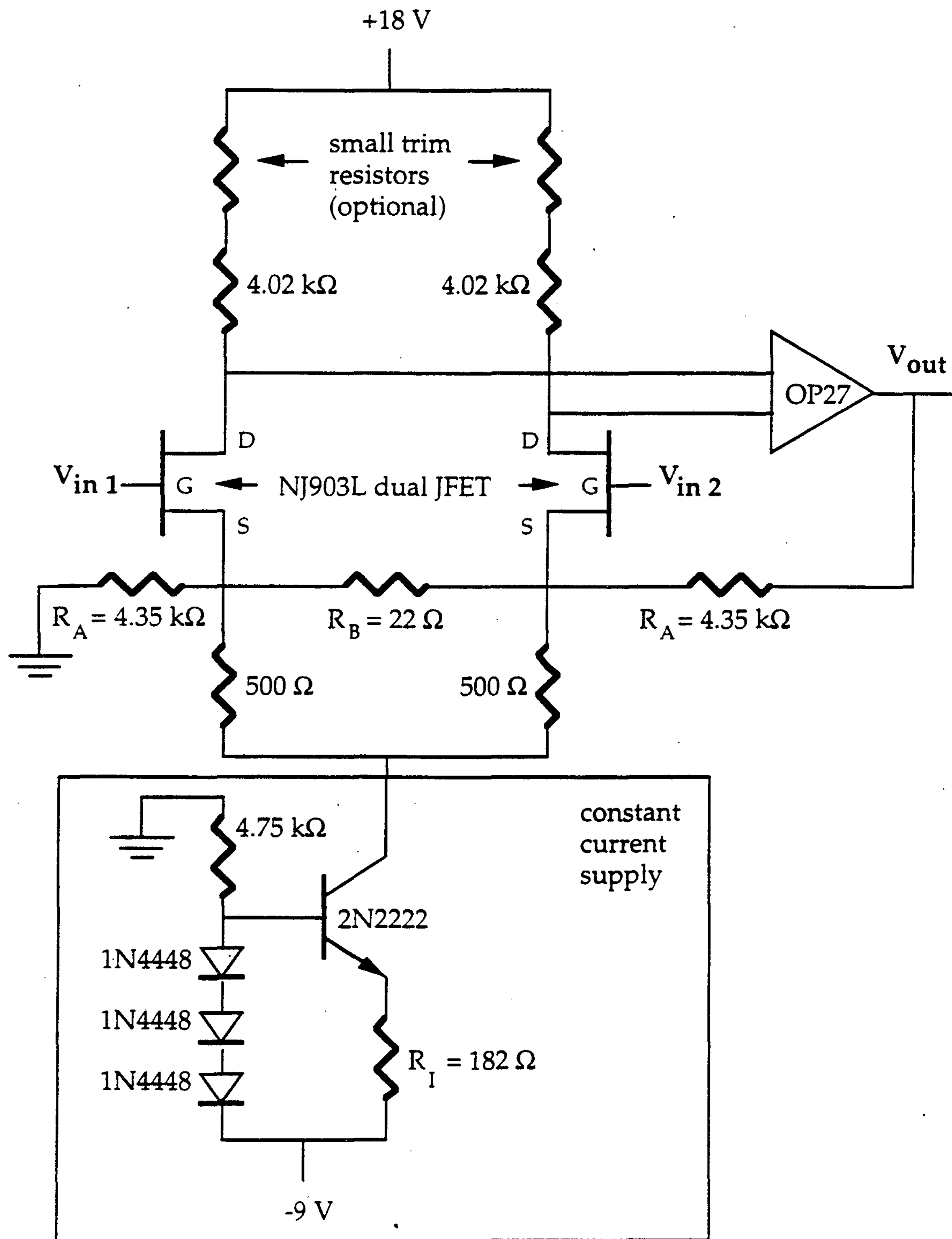

Fig.A.8 Circuit diagram for a low noise voltage preamplifier using the NJ903L JFET.

$$V_{out} = I_o\,(2R_A + R_B) = \frac{(V_{S1} - V_{S2})}{R_B}\,(2R_A + R_B)\,. \tag{A.6}$$

Since $(V_{S1} - V_{S2}) \approx (V_{G1} - V_{G2})$, the gain is

$$\frac{V_{out}}{\Delta V_{in}} \approx \frac{2R_A}{R_B} + 1\,. \tag{A.7}$$

For the values of R_A and R_B given in Figure A.8, the predicted gain is 396 Ω compared to the measured value of 401 Ω.

The value of the resistor R_A is selected so that the current drawn through R_A, $I_A = V_S/R_A$, is small compared to the total current through each JFET, $I \approx 1.3V/2R_I \approx 3.6$ mA. The resistor R_B is selected so that its voltage noise will be comparable to or less than the voltage noise of the NJ903L dual JFET. Due to its large gate width of 903 μm, the NJ903L JFET has an extremely low voltage noise of ~ 0.7 nV/√Hz for an operating current of 3.6 mA. Since a 10 Ω resistor has a room temperature Johnson noise of 0.4 nV/√Hz, the resistor R_B cannot be much larger than 10 Ω before it begins to dominate the voltage noise of the preamplifier circuit. For the selected value R_B = 22 Ω corresponding to a Johnson noise of 0.6 nV/√Hz, we can estimate the total preamplifier voltage noise referred to the input:

$$e_n(\text{input}) = \sqrt{2e_n^2(\text{JFET}) + e_n^2(22\,\Omega)} \approx 1.15\ \text{nV}/\sqrt{\text{Hz}}. \tag{A.8}$$

The estimated voltage noise is in good agreement with the measured white noise level of 1.2 nV/Hz. The frequency dependence of the voltage noise is shown in Figure A.9.

The voltage noise of this circuit remains below 3 nV/√Hz at frequencies down to 0.5 Hz. This exceptionally low noise at low frequencies was achieved by using an unorthodox technique to assemble the preamplifier circuit. We found that when we used solder connections to form electrical contacts, the 1/f knee was always greater than a few Hz and sometimes extended above 20 Hz. We postulate that the excess low frequency noise that we observe when electrical connections are made by soldering is due to damage to the internal contacts of the resistors, JFET, and op-amp caused by the high

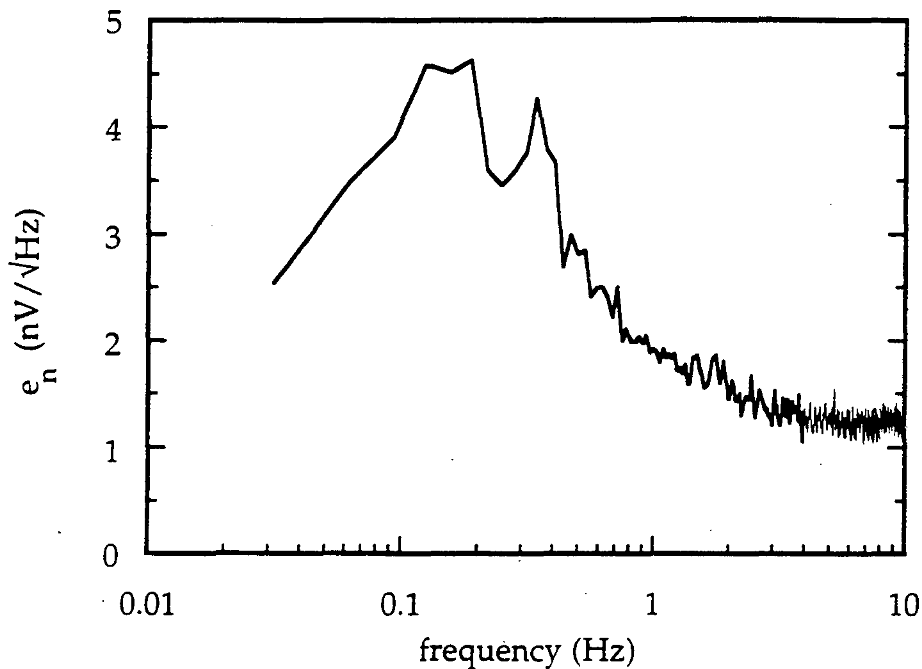

Fig.A.9 Measured voltage noise as a function of frequency of the pre-amplifier shown in Figure A.8.

temperatures. However, we found that when the circuit was assembled in ten minutes on a standard RadioShack breadboard, the 1/f knee was reproducibly near or below 1 Hz and the noise performance shown in Figure A.9 was easily obtained. Because breadboards are rumored to cause excess noise, before insertion into the breadboard all wires were gently scraped with a razor blade and cleaned with a cotton-tipped swab dipped in alcohol in order to remove any oxide layers which could contribute to excess low frequency noise. We found that the noise performance of a preamplifier circuit assembled on a breadboard and inserted into a metal box for shielding purposes was stable over a period of several years. Because this preamplifier circuit has a large gain of ~ 400, the two sides of the dual JFET must be matched in V_{GS} to within a few mV. When this cannot be achieved, small trim

resistors must be added to the circuit as shown in Figure A.8. Because variable trimpots tend to have large 1/f noise, variable trimpots should only be used to determine appropriate values for the trim resistors which can then be permanently mounted into the circuit.

A.4 Calibration of a diode thermometer

The JFET temperature measurements described in Section A.1 and Section A.2 were made using a 1N4448 diode thermometer. Any commercial diode can be used as a calibrated thermometer between 77 K and 300 K with a calibration error of only a few K. The current-voltage relationship of a forward-biased diode at temperatures above ~ 50 K can be approximated by

$$I = I_0 \exp(eV/kT), \tag{A.9}$$

where I_0 depends weakly on temperature.

When a constant current I_B is applied across a diode, the resulting voltage drop can be measured at room temperature ($T \approx 293$ K) and at liquid nitrogen temperature ($T = 77$ K). The 77 K measurement can be performed in minutes by dipping the sample into a contained filled with LN_2. The diode can then be used as a thermometer over the temperature range $77 \text{ K} < T < 300 \text{ K}$ by applying I_B across the diode and measuring the resulting voltage drop V_T. The temperature T can be calculated from V_T using the equation

$$T = 77 + \frac{(293 - 77)}{(V_{293} - V_{77})} (V_T - V_{77}) \tag{A.7}$$

where V_{293} and V_{77} refer to the measured voltage drops at 293 K and 77 K, respectively. In Figure A.10, we plot V_T as a function of temperature for a typical 1N4448 diode between 50 K and 300 K. V_T was measured for a constant current $I_B = 10$ µA across the diode. The data are very well fit by a straight line, justifying the use of Equation A.9 to determine the diode temperature.

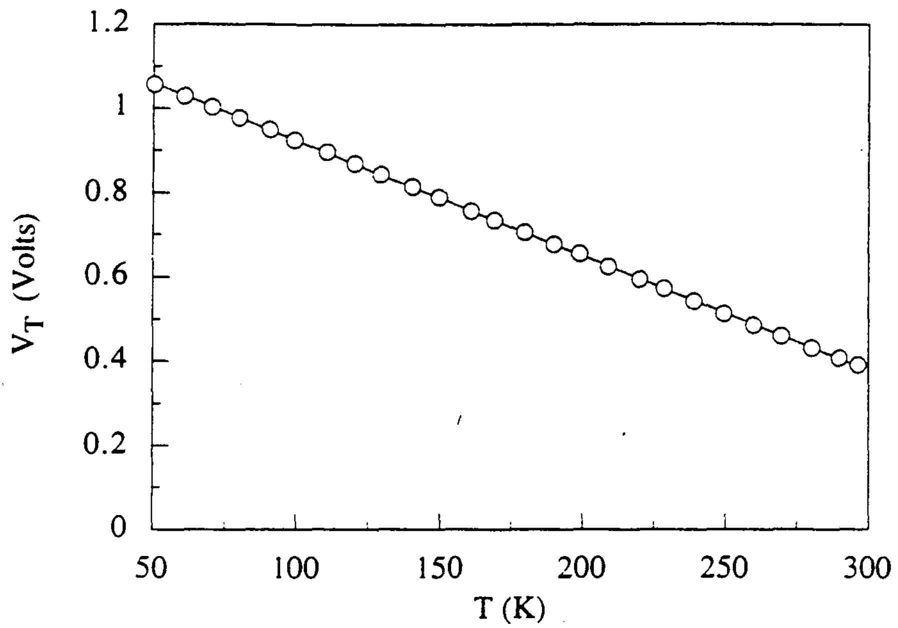

Fig.A.10 Measured temperature dependence of the voltage drop across a 1N4448 diode for a constant bias current I_B = 10 μA. The data are extremely well fit by a straight line.

Appendix B

Details of numerical optimization program

B.1 Instructions for using the numerical optimization program.

As described in Section 5.4, the numerical optimization program we have developed requires the user to specify eleven bolometer parameters in a text file called a "configuration file". The eleven parameters are listed below, along with the prompt given by the computer:

Bolometer Parameter	Prompt
β, the temperature exponent of G	Beta(1<=Beta<=3)
Q, the background optical power	OpticalLoading(nW)
T_o, the heat sink temperature	BaseTemperature(K)
Δ, related to the slope of ln R vs. T^{-n}	Delta(K)
n, the temperature exponent of ln R	n(.25,.5,1.0)
ρ_o, the resistivity parameter	rho(ohm-cm)
d, the distance between electrodes	BolometerThickness(microns)
L_o, defined by $L = L_o/T^m$	A(Angstroms*K^m)
m, the temperature exponent of L	m(0,.25,.5,1)
e_n, the amplifier voltage noise	AmpVoltageNoise(nV/Sqrt(Hz))
i_n, the amplifier current noise	AmpCurrentNoise(1e-16A/Sqrt(Hz))

When electrical nonlinearities are neglected, the user should specify $L_o = 0$ and $m = 0$.

In addition to the bolometer parameters listed above, the following three parameters must either be specified by the user or defined as a variable for optimization:

Bolometer Parameter	Prompt
R_o, the resistance parameter: $R_o = \rho_o d/A$	R_o(ohm)
G_o, thermal conductance parameter in W/K	G_o
ϕ, the ratio of T_{bolo} to T_o	Phi

When the user wishes to optimize one of the above parameters, rather than specifying a numerical value for R_o, G_o, or ϕ the user must specify the letter "o". In addition the user must specify whether the Davidon-Fletcher Powell minimization method ("DFPMIN") or the downhill simplex minimization method ("AMOEBA") is to be used.

The following is an actual configuration file named "NTD17" for an 85 mK bolometer with an optical loading of 40 pW. The bolometer parameters are typical of NTD-17. The chip size is fixed at $(240\ \mu m)^3$. Therefore, $R_o = \rho_o d/A$ is a user-specified parameter equal to 7.5 Ω. The "o" after "G_o" and "Phi" indicates that G_o and ϕ are variables to be optimized.

Configuration file "NTD17"

Beta(1<=Beta<=3)	2.0
OpticalLoading(nW)	0.040
BaseTemperature(K)	0.085
Delta(K)	21.2
n(.25,.5,1.0)	0.5
rho(ohm-cm)	0.18
BolometerThickness(microns)	240
A(Angstroms*K^m)	450
m(0,.25,.5,1)	0.5
AmpVoltageNoise(nV/Sqrt(Hz))	3
AmpCurrentNoise(1e-16A/Sqrt(Hz))	1
R_o(ohm)	7.5
G_o	o
Phi	o
OutputFile	NTD17out
Method	AMOEBA

The user can run the bolometer optimization program for the above configuration file using the command

```
>>bolo NTD17
```

The following is the actual text file "NTD17out" created by running the numerical optimization program with the configuration file "NTD17".

<u>Bolometer Optimization Program output file "NTD17out"</u>

Total NEP (W/sqrt(Hz))	6.235278 e-17
Amplifier voltage noise contribution (W/sqrt(Hz))	3.414448 e-17
Amplifier current noise contribution (W/sqrt(Hz))	2.265353 e-18
Johnson noise contribution (W/sqrt(Hz))	4.325453 e-17
Thermal noise contribution (W/sqrt(Hz))	3.799817 e-17
R_o (ohms)	7.500000 e+00
G_o (W/K^(beta+1))	9.170009 e-08
T/T_o	1.546572 e+00
Responsivity S (V/W)	-8.786194 e+07
Bolometer resistance R (ohms)	1.990383 e+06
Average thermal conductance G (W/K)	1.090630 e-09
Bias current I (amps)	2.315242 e-09
Bolometer thickness (microns)	2.400000 e+02

B.2 Constants and partial derivatives used in the Davidon-Fletcher-Powell algorithm

The numerical optimization program described in Chapter 5 allows the user to select between two distinct optimization routines to minimize the NEP of an infrared bolometer. The first optimization routine uses a variable metric method called the Davidon-Fletcher-Powell (DFP) algorithm [Press *et al.*, 1990] to minimize the NEP. The DFP algorithm requires derivative calculations to locate the optimum values of R_0, G_0, and ϕ. The following are the constants and partial derivatives used in the Davidon-Fletcher-Powell algorithm. Note that when electrical nonlinearities are neglected, $L_0 = 0$ and consequently all terms which are multiplied by B are equal to zero.

B.2.1 Constants

$$B = \frac{eL_o}{dk}$$

$$C_1 = \sqrt{\frac{G_o T_o^{\beta+1}\left(\phi^{\beta+1} - 1\right)}{\beta + 1} - Q}$$

$$C_2 = 1 + \frac{BC_1\sqrt{R}}{2(T_o\phi)^{m+1}}$$

$$C_3 = G_o T_o^{\beta+1}\phi^{\beta}$$

$$C_4 = \frac{B\sqrt{R}\,T_o^{\beta+1}}{(\beta + 1)}\left(\phi^{\beta+1} - 1\right)$$

$$C_5 = \frac{(m + 1)BC_1\sqrt{R}}{(T_o\phi)^{m+2}} - \frac{n\Delta^n}{(T_o\phi)^{n+1}}$$

$$C_6 = 1 + \frac{BC_1\sqrt{R}}{(T_o\phi)^{m+1}}$$

$$C_7 = G_o T_o^{\beta}\phi^{\beta} - \alpha C_1^2$$

$$C_8 = \frac{2i_n^2 R + 4k_B T_o\phi}{S^2}$$

$$C_9 = \frac{-2}{S^3}\left[e_n^2 + i_n^2 R^2 + 4k_B T_o\phi R\right]$$

$$C_{10} = \frac{T_o^{\beta+1}\left(\phi^{\beta+1} - 1\right)}{2C_1(\beta + 1)}$$

B.2.2 Partial derivatives

$$\frac{\partial R}{\partial R_o} = \frac{R}{R_o C_2}$$

$$\frac{\partial \alpha}{\partial R_o} = \frac{\partial R}{\partial R_o}\left[\frac{BC_1}{2(T_o\phi)^{m+1}C_6\sqrt{R}}\left(\frac{(m + 1)}{T_o\phi} - \frac{C_5}{C_6}\right)\right]$$

$$\frac{\partial S}{\partial R_o} = \frac{\partial R}{\partial R_o}\left[\frac{\alpha C_1}{2C_7\sqrt{R}}\right] + \frac{\partial \alpha}{\partial R_o}\left[\frac{C_1\sqrt{R}}{C_7} + \frac{\alpha C_1^3\sqrt{R}}{C_7^2}\right]$$

$$\frac{\partial NEP^2}{\partial R_o} = C_8\frac{\partial R}{\partial R_o} + C_9\frac{\partial S}{\partial R_o}$$

$$\frac{\partial R}{\partial G_o} = \frac{C_4 R}{2(T_o\phi)^{m+1}C_1C_2}$$

$$\frac{\partial \alpha}{\partial G_o} = \frac{1}{(T_o\phi)^{m+2}}\left[\frac{(m+1)C_4}{2C_1C_6} + \frac{(m+1)C_1B}{2\sqrt{R}C_6}\frac{\partial R}{\partial G_o}\right]$$

$$- \frac{C_5}{C_6^2(T_o\phi)^{m+1}}\left[\frac{C_4}{2C_1} + \frac{C_1B}{2\sqrt{R}}\frac{\partial R}{\partial G_o}\right]$$

$$\frac{\partial S}{\partial G_o} = S\left(\frac{C_{10}}{C_1} + \frac{1}{2R}\frac{\partial R}{\partial G_o} + \frac{1}{\alpha}\frac{\partial \alpha}{\partial G_o}\right)$$

$$+ \frac{C_1\alpha\sqrt{R}}{C_7^2}\left[-T_o^{\beta}\phi^{\beta} + C_1^2\frac{\partial \alpha}{\partial G_o} + 2\alpha C_1C_{10}\right]$$

$$\frac{\partial NEP^2}{\partial G_o} = 4k_BT_o^{\beta+2}\frac{(\beta+1)}{(2\beta+3)}\left(\frac{\phi^{2\beta+3}-1}{\phi^{\beta+1}-1}\right) + C_8\frac{\partial R}{\partial G_o} + C_9\frac{\partial S}{\partial G_o}$$

$$\frac{\partial R}{\partial \phi} = \frac{R}{C_2}\left[\frac{-T_o n D^n}{(T_o\phi)^{n+1}} - \frac{B\sqrt{R}C_3}{2C_1(T_o\phi)^{m+1}} + \frac{T_oB\sqrt{R}(m+1)C_1}{(T_o\phi)^{m+2}}\right]$$

$$\frac{\partial \alpha}{\partial \phi} = \frac{(m+1)}{C_6(T_o\phi)^{m+2}}\left[\frac{BC_3\sqrt{R}}{2C_1} + \frac{BC_1}{2\sqrt{R}}\frac{\partial R}{\partial \phi} - \frac{C_1(m+2)B\sqrt{R}}{\phi}\right] + \frac{(n+1)nT_o\Delta^n}{C_6(T_o\phi)^{n+2}}$$

$$- \frac{N}{C_6^2(T_o\phi)^{m+1}}\left[\frac{BC_3\sqrt{R}}{2C_1} + \frac{BC_1}{2\sqrt{R}}\frac{\partial R}{\partial \phi} - \frac{C_1(m+1)B\sqrt{R}}{\phi}\right]$$

$$\frac{\partial S}{\partial \phi} = S\left(\frac{C_3}{2C_1^2} + \frac{1}{2R}\frac{\partial R}{\partial \phi} + \frac{1}{\alpha}\frac{\partial \alpha}{\partial \phi}\right)$$

$$+ \frac{\alpha C_1\sqrt{R}}{C_7^2}\left(-\beta G_oT_o^{\beta}\phi^{\beta-1} + \alpha C_3 + C_1^2\frac{\partial \alpha}{\partial \phi}\right)$$

$$\frac{\partial NEP^2}{\partial \phi} = C_8 \frac{\partial R}{\partial \phi} + C_9 \frac{\partial S}{\partial \phi} + \frac{4k_B T_o R}{S^2}$$

$$+ \frac{4k_B T_o{}^{\beta+2} G_o}{\left(\phi^{\beta+1} - 1\right)} \left(\frac{\beta + 1}{2\beta + 3}\right) \left[(2\beta + 3)\phi^{2\beta+2} - \frac{(\beta + 1)\phi^{\beta}\left(\phi^{2\beta+3} - 1\right)}{\left(\phi^{\beta+1} - 1\right)} \right]$$

References

Aladashvili, D. I., Adamiya, Z. A. and Lavdovskii, K. G. (1990), in Transport, Correlation and Structural Defects, ed. Hellmut Fritsche (World Scientific Publishing Company).

Aladashvili, D. I., Adamiya, Z. A. and Lavdovskii, K. G. (1987), *Sov. Phys. Semicond.*, **21**, 921.

Aladashvili, D. I., Adamiya, Z. A., Lavdovskii, K. G., Levin, E. I. and Shklovskii, B. I. (1989), *Sov. Phys. Semicond.*, **23**, 132.

Aladashvili, D. I., Adamiya, Z. A., Lavdovskii, K. G., Levin, E. I. and Shklovskii, B. I. (1990), *Sov. Phys. Semicond.*, **24**, 143.

Aleinikov, A. B., Botte, V. A., Zarubin, L. I., Kollyukh, A. G. and Malyutenko, V. K. (1983), *Sov. Phys. Solid State*, **25**(11), 116.

Anderson, P. W. (1958), *Phys. Rev.*, **109**, 1492.

Anderson, P. W., Abrahams, E. and Ramakrishnan, T. V. (1979), *Phys. Rev. Lett.*, **43**, 718.

Apsley, N. and Hughes, H. P. (1974), *Phil. Mag.*, **30**, 963.

Apsley, N. and Hughes, H. P. (1975), *Phil. Mag.*, **31**, 1327.

Bandow, S., Shinohara, H., Saito, Y., Ohkohchi, M. and Ando, Y. (1993), *J. Phys. Chem.*, **97**, 6101.

Beeman, J. W. and Haller, E. E. (1994), *Infrared Phys. Technol.*, **35**, 827.

Bethune, D. S., Johnson, R. D., Salem, J. R., deVries, M. S. and Yannoni, C. S. (1993), *Nature*, **366**, 123.

Beyers, R. Kiang, C-H., Johnson, R. D., Salem, J. R., deVries, M. S., Yannoni, C. S., Bethune, D. S., Dorn, H. C., Burbank, P., Harich, K. and Stevenson, S. (1994), *Nature*, **370**, 196.

Bir, G. L. and Pikus, G. F. (1974), Symmetry and Strain-induced Effects in Semiconductors (John Wiley & Sons, New York).

Bleibaum, O., Bottger, H., Bryksin, V. V., and Kleinert, P. (1995), *Phys. Rev. B.*, **52**, 16494.

Booth, N. E. (1987), *Appl. Phys. Lett.*, **50**, 293.

Booth, N. E. and Salmon, G. L., eds. (1992), Low Temperature Detectors for Neutrinos and Dark Matter IV (Editions Frontieres, Gif-Sur-Yvette).

Bottger, H. and Bryksin, V. V. (1979), *phys. stat. sol. (b)*, **96**, 219.

Bottger, H. and Bryksin, V. V. (1980), *Phil. Mag. B*, **42**, 297.

Bottger, H. and Bryksin, V. V. (1985), Hopping Conduction in Solids (Akademie-Verlag, Berlin).

Bryksin, V. V., Schlegel, H. and Kleinert, P. (1994), *Phys. Rev. B*, **49**, 13697.

Buczko, R. and Chroboczek, J. A. (1984), *Phil. Mag. B.*, **50**, 429.

Chaabane, H., Ettlinger, E. and Schoepe, W. (1986), *Z. Phys. B.*, **64**, 19.

Chroboczek, J. A. (1987), in Noncrystalline Semiconductors v. III, ed. M. Pollak (CRC Press, Inc., Boca Raton, Florida).

Chroboczek, J. A., Fritzsche, H., Jiange, C.-L, Pollak, M., and Wild, R. L. (1981), *Phil. Mag. B*, **44**, 685.

Clapp, A. C., Devlin, M. J., Gundersen, J. O., Hagmann, C. A. *et al.* (1994), *Ap. J. Lett.*, **433**, L57.

Crandall, R. S. (1970), *Phys. Rev. B*, **1**, 730.

Devlin, M. J., Clapp, A. C., Gundersen, J. O., Hagmann, C. A. *et al.* (1994), *Ap. J. Lett.*, **430**, L1.

Dumoulin, L., Berge, L., Lesueur, J., Bernas, H. and Chapellier, M. (1993), *J. Low Temp. Phys.*, **93**, 301.

Dvurechenskii, A. V., Dravin, V. A., and Yakimov, A. I. (1988), *JETP Lett.*, **48**, 155.

Edwards, P. P. and Sienko, M. J. (1978), *Phys. Rev.*, **B17**, 2575.

Faran, O. and Ovadyahu, Z. (1988), *Solid State Comm.*, **67**, 823.

Fitzgerald, S. A. and Sievers, A. J. (1994), *J. Chem. Phys.*, **101**, 7283.

Frenkel, J. (1938), *Phys. Rev.*, **54**, 647.

Gang, C., Koppen, H. D., van der Heijden, R. W., de Waele, A.T.A.M. and Gijsman, H. M. (1989), *Sol. State Comm.*, **72**, 173.

Gershenzon, E. M., Gurvich, Yu. A., Mel'nikov, A. P. and Shestakov, L. N. (1991), *Sov. Phys. Semicond.*, **25**, 95.

Ghantmaker, V. F. (1974), *Rep. Prog. Phys.*, **37**, 317.

Ghantmaker, V. F. and Gasparov, V. A. (1973), *Sov. Phys.-JETP*, **37**, 864.

Goldie, D. J., Booth, N. E., Patel, C. and Salmon, G. L. (1990), *Phys. Rev. Lett.*, **64**, 954.

Grannan, S. M., Lange, A. E., Haller, E. E. and Beeman, J. W. (1992), *Phys. Rev. B*, **45**, 4516.

Grey, K. E. (1971), *J. Phys. F*, **1**, 290.

Griffin, M. J. and Holland, W. S. (1988), *Int. Journal of IR and Millimeter Waves*, **9**, 861.

Gurvich, Yu. A., Melnikov, A. P., Shestakov, L. N., and Gershenzon, E. M. (1995), *JETP Lett.*, **61**, 731.

Haller, E. E., Palaio, N. P., Rodder, M., Hansen, W. L. and Kreysa, E. (1984); in Neutron Transmutation Doping of Semiconductor Materials, ed. R. D. Larrabee (Plenum, New York).

Haller, E. E., Palaio, N. P., Hansen, W. L. and Kreysa, E. (1985), *IR Phys.*, **25**, 257.

Haller, E. E., Itoh, K. M., Beeman, J. W., Hansen, W. L. and Ozhogin, V. I. (1994), *SPIE Proc.*, **2198**, 630.

Haller, E. E. (1994), *Infrared Phys. and Tech.*, **35**, 127.

Harris, J. and Jones, R. O. (1979), *J. Chem. Phys.*, **70**, 830.

Hartke, J. L. (1968), *J. Appl. Phys.*, **39**, 4871.

Henisch, H. K. (1984), Semiconductor Contacts: An Approach to Ideas and Models (Clarendon Press, Oxford).

Hill, R. M. (1971), *Philos. Mag.*, **24**, 1307.

Holthaus, M., Ristow, G. H. and Hone, D. W. (1995), *Europhys. Lett.*, **32**, 241.

Ionov, A. N., M. N. Matveev, M. N.,I. S. Shlimak, and R. Rentch, JETP Lett. **45**, 310 (1987).

Itoh, K., Hansen, W. L., Haller, E. E., Farmer, J. W. *et al.*(1993-A), *J. Mater. Res.*, **8**, 1341.

Itoh, K., Hansen, W. L., Haller, E. E., Farmer, J. W. and Ozhogin, V. I. (1993-B), *Mat. Sci. Forum*, **117**, 117.

Itoh, K. (1994), Low Temperature Carrier Transport Properties in Isotropically Controlled Germanium (University of California at Berkeley, Doctoral Thesis).

Jaber, A. M. and Kachlishvili, Z. S. (1989), *Sov. Phys. Semicond.*, **23**, 930.

Jayannavar, A. M. (1989), *Sol. State Comm.*, **69**, 703.

Johnson, R. D., deVries, M. S., Salem, J. R., Bethune, D. S. and Yannoni, C. S. (1992), *Nature*, **355**, 239.

Joslin, C. G., Yang, J., Gray, C. G., Goldman, S. and Poll, J. D. (1993), *Chem. Phys. Lett.*, **208**, 86.

Kamimura, H. and Aoki, H. (1989), The Physics of Interacting Electrons in Disordered Systems (Clarendon Press, Oxford).

Kaplan, S. B., Chi, C. C., Langenberg, D. N., Chang, J. J., Jafarey, S. and Scalapino, D. J. (1976), *Phys. Rev. B*, **14**, 4854.

Katz, A., Abernathy, C. R. and Pearton, S. J. (1990-A), *Appl. Phys. Lett.*, **56**, 1028.

Katz, A., Nakahara, S., Savin, W. and Weir, B. E. (1990-B), *J. Appl. Phys.*, **68**, 4133.

Kenny, T. W., Richards, P. L., Park, I. S., Haller, E. E. and Beeman, J. W. (1989), *Phys. Rev. B*, **39**, 8476.

Kikuchi, K., Suzuki, S., Nakao, Y., Nakahara, N., Wakabayashi, T., Shiromaru, H., Saito, K., Ikemoto, I. and Achiba, Y. (1993), *Chem. Phys. Lett.*, **216**, 67.

Kittel, C. (1986), Introduction to Solid State Physics (John Wiley & Sons, New York).

Kobayashi, K., Nagase, S. and Akasaka, T. (1995), *Chem. Phys. Lett.*, **245**, 230.

Kraus, H., von Feilitsche, F., Jochum, J., Mossbauer, R. L., Peterreins, Th. and Probst, F. (1989), *Phys. Lett. B*, **231**, 195.

Kroto, H. W., Heath, J. R., O'Brien, S. C., Curl, R. F. and Smalley, R. E. (1985), *Nature*, **318**, 162.

Laasonen, K. (1992), *Science*, **258**, 1916.

Lakner, M. and Lohneysen, H. v. (1989), *Phys. Rev. Lett.*, **63**, 648.

Lee, M., Solin, S. A. and Hines, D. R. (1993), *Phys. Rev. B.*, **48**, 11921.

Levin, E. I. and Shklovskii, B. I. (1984), *Sov. Phys. Semicond.*, **18**, 534.

Low, F. J. (1961), *J. Opt. Soc. Am.*, **51**, 1300.

Mack, G. X., Anderson, A. C. and Swinehart, P. R. (1983), *Rev. Scient. Instrum.*, **54**, 949.

Marianer, S. and Shklovskii, B. I. (1992), *Phys. Rev. B*, **46**, 13100.

Mather, J. C. (1982), *Appl. Opt.*, **21**, 1125.

Mather, J. C. (1984-A), *Appl. Opt.*, **23**, 584.

Mather, J. C. (1984-B), *Appl. Opt.*, **23**, 3181.

Matveev, G. A. and Lonchakov, A. T. (1993), *Semiconductors*, **27**, 228.

McMillan, W. L. and Mochel, J. M. (1981), *Phys. Rev. Lett.*, **46**, 556.

Mears, C. A., Labov, S. E. and Barfknecht, A. T. (1993), *Appl. Phys. Lett.*, **63**, 2961.

Meijer, G., deVries, M. S., Hunziker, H. E. and Wendt, H. R. (1990), *Appl. Phys. B.*, **51**, 395.

Mendez, E. E. and Bastard, G. (1993), *Physics Today*, **46(6)**, 34.

Miller, D. (1993), Submillimeter Residual Losses in High-T_c Superconductors (University of California at Berkeley, Doctoral Thesis).

Moseley, S. H., Mather, J. C. and McCammon, D. (1984), *J. Appl. Phys.*, **56**, 1257.

Mostefa, M., Bourbie, D. and Olivier, G. (1991), *Phil. Mag. B*, **63**, 1131.

Mott, N. F. (1967), *Adv. Phys.*, **16**, 49.

Mott, N. F. (1969), *Phil. Mag.*, **19**, 835.

Mott, N. F. and Davis, E. A. (1979), Electron Processes in Noncrystalline Materials (Oxford Press, Oxford).

Mott, N. F. (1993), Conduction in Non-Crystalline Materials (Clarendon Press, Oxford).

Nagase, S., Kobayashi, K., Kato, T. and Achiba, Y. (1993), *Chem. Phys. Lett.*, **201**, 275.

Nagase, S. and Kobayashi, K. (1994), *Chem. Phys. Lett.*, **231**, 319.

Nair and Mitra (1977)

Negri, F., Orlandi, G. and Zerbetto, F. (1992), *Chem. Phys. Lett.*, **189**, 495.

Onari, S., Tada, K. and Arai, T. (1991), *J. Phys. Soc. of Japan*, **60**, 4392.

Orlandi, G., Zerbetto, F. and Fowler, P. W. (1993), *J. Phys. Chem.*, **97**, 13575.

Osofsky, M., Bieri, J. B., LaMadrid, M., Contrata, W. and Mochel, J. M. (1988), *Phys. Rev. B.*, **38**, 12215.

Paalanen, M. A., Graebner, J. E., Bhatt, R. N. and Sachdev, S. (1988), *Phys. Rev. Lett.*, **61**, 597.

Padovani, F. A. and Stratton, R. (1966), *Solid St. Electron.*, **9**, 695.

Parisi, J. (1991), *Phil. Mag. Letters*, **64**, 357.

Phillips, R. T., Mackintosh, A. J., and Yoffe, A. D. (1981), *J. Phys. (Paris) Colloq.*, **42**, C4-869.

Pollak, F. H. (1965), *Phys. Rev.*, **138**, A618.

Pollak, M. and Reiss, I. (1976), *J. Phys. C.*, **9**, 2339.

Pollak, M. (1987), in Energy Transfer Dynamics, ed. T. W. Barrett and H. A. Pohl (Springer-Verlag, New York).

Press, W. H., Flannery, B. P., Teukolsky, S. A. and Vetterling, W. T. (1990), Numerical Recipes in C (Cambridge University Press, Cambridge).

Redfield, D. (1975), *Adv. Phys.*, **24**, 463.

Reggiani, L. and Mitin, V. (1989), *Rivista del Nuovo Cimento*, **12**, 1.

Reif, F. (1965), Fundamentals of Statistical and Thermal Physics (McGraw-Hill, New York).

Rentzsch, R., Shlimak, I. S. and Berger, H. (1979), *phys. stat. sol. (a)*, **54**, 487.

Rhoderick, E. H. (1978), Metal-Semiconductor Contacts (Clarendon Press, Oxford).

Richards, P. L. (1994), *J. Appl. Phys.*, **76**, 1.

Rosenbaum, T. F., Andres, K. and Thomas, G. A. (1980), *Sol. State Comm.*, **35**, 663.

Roukes, M. L., Freeman, M. R., Germain, R. S., Richardson, R. C. and Ketchen, M. B. (1985), *Phys. Rev. Lett.*, **55**, 422.

Schwartz, B. (1969), ed. Ohmic Contacts to Semiconductors (Electrochemical Society, New York).

Shahar, D. and Ovadyahu, Z. (1990), *Phys. Rev. Lett.*, **64**, 2293.

Shinohara, H., Sato, H., Yaito, Y., Ohkohchi, M. and Ando, Y. (1992), *J. Phys. Chem.*, **96**, 3571.

Shklovskii, B. I. (1973), *Sov. Phys. Semicond.*, **6**, 1964.

Shklovskii, B. I. (1976), *Sov. Phys. Semicond.*, **10**, 855.

Shklovskii, B. I. (1979), *Sov. Phys. Semicond.*, **13**, 53.

Shklovskii, B. I. and Efros, A. L. (1984), Electronic Properties of Doped Semiconductors (Springer, Berlin).

Schklovskii, B. I., Levin, E. I., Fritzsche, H. and Baranovskii, S. D. (1990), in Transport, Correlations, and Structural Defects, ed. H. Fritzsche (World Scientific, Singapore).

Silver, E., Labov, S., Goulding, F., Madden, N., Landis, D., Beeman, J., Pfafman, T., Melkonian, L., Millet, I. and Wai, Y. (1989), *Nucl. Inst. and Methods in Phys. Research, Sect. A*, **A277**, 657.

Stareev, G. (1993), *Appl. Phys. Lett.*, **62**, 2801.

Staunton, H. F. and Pollak, F. H. (1967), *Phys. Lett. A*, **25**, 751.

Stevenson, S., Dorn, H. C., Burbank, P., Harich, K., Haynes, J., Kiang, C., Salem, J. R., deVries, M. S., van Loosdrecht, P. Johnson, R., Yannoni, C. and Bethune, D. S. (1994-A), *Analytical Chem.*, **66**, 2675.

Stevenson, S., Dorn, H. C., Burbank, P., Harich, K., Sun, Z., Kiang, C., Salem, J. R., deVries, M. S., van Loosdrecht, P. Johnson, R., Yannoni, C. and Bethune, D. S. (1994-B), *Analytical Chem.*, **66**, 2680.

Sze, S. M. (1981), Physics of Semiconductors (Wiley Interscience, New York).

Talamantes, J., Pollak, M. and Baron, R. (1987), *Journal of Non-Crystalline Solids*, **97**, 555.

Tanaka, S., Alsop, D., Chang, E., Clapp, A. *et al.* (1995), *Astrophysical Lett. and Comm.*, **32**, 223.

Timchenko, I. N., Kasiyan, V. A., Nedeoglo, D. D. and Simashkevich, A. V. (1989), *Sov. Phys. Semicond.*, **23**, 148.

Tremblay, F., Pepper, M., Newbury, R., Ritchie, D., Peacock, D. C., Frost, J. E. F., Jones, G. A. C., and Hill, G. (1989), *Phys. Rev. B*, **40**, 3387.

van Cleef, G. W., Renkes, G. D. and Coe, J. V. (1993), *J. Chem. Phys.*, **98**, 860.

van der Heijden, R. W., Chen, G., de Waele, A. T. A. M., Gijsman, H. M. and Tielen, F. P. B. (1992), *Phil. Mag. B*, **65**, 849.

van der Meer, M., Schuchardt, R. and Keiper, R. (1982), *phys. stat. sol. (b)*, **110**, 571.

van Loosdrecht, P. H. M., Johnson, R. D., de Vries, M. S., Kiang, C-H., Bethune, D. S., Dorn, H. C., Burbank, P. and Stevenson, S. (1994), *Phys. Rev. Lett.*, **73**, 3415.

Wang, N., Wellstood, F. C., Sadoulet, B., Haller, E. E. and Beeman, J. (1990), *Phys. Rev. B*, **41**, 3761.

Wannier, G. H. (1960), *Phys. Rev.*, **117**, 432.

Weaver, J., Chai, Y., Kroll, G., Jin, C., Ohno, T., Haufler, R., Guo, T., Alford, J., Conceicao, J., Chibante, L., Jain, A., Palmer, G. and Smalley, R. (1992), *Chem. Phys. Lett.*, **190**, 260.

Wellstood, F. C., Urbina, C. and Clarke, J. (1994A), *Appl. Phys. Lett.*, **54**, 2599.

Wellstood, F. C., Urbina, C. and Clarke, J. (1994B), *Phys. Rev. B.*, **49**, 5942.

Wennberg, A. K. M., Ytterboe, S. N., Gould, C. M., Bozler, H. M., Klem, J. and Morkoc, H. (1986), *Phys. Rev. B*, **34**, 4409.

Yakimov, A. I., Dvurechenskii, A. V. and Baskin, E. M. (1993), *JETP*, **77**, 113.

Yu, A. Y. C. (1970), *Solid-St. Electron.*, **13**, 239.

Zabrodskii, A. G. and Shlimak, I. S. (1977), *Sov. Phys. Semicond.*, **11**, 430.

Zak, J. (1968), *Phys. Rev. Lett.*, **20**, 1477.

Zammit, C. C., Caplin, A. D., Lea, M. J., Fozooni, P., Kennefick, J. and Saunders, J. (1990), *Physica*, **165-166**, 317.

Zavaritskaya, E. I. (1985), *JETP Lett.*, **41**, 279.

Zhang, J. (1992), Hopping Conduction in Doped Silicon and Germanium: Studies of Their Application as Thermometers for X-Ray Calorimeters (University of Wisconsin at Madison, Doctoral Thesis).

ERNEST ORLANDO LAWRENCE BERKELEY NATIONAL LABORATORY
ONE CYCLOTRON ROAD | BERKELEY, CALIFORNIA 94720

Prepared for the U.S. Department of Energy under Contract No. DE-AC03-76SF00098